

**Universität  
Rostock**



Traditio et Innovatio

# **Modelling and simulation of the electric field distribution of electrostimulative implants for regeneration of mandibular bone defects**

**Dissertation**

**zur**

**Erlangung des akademischen Grades**

**Doktor-Ingenieur (Dr.-Ing.)**

**der Fakultät für Informatik und Elektrotechnik**

**der Universität Rostock**

**vorgelegt von**

Hendrikje Raben, geboren am 07. März 1993 in Schwerin  
aus Rostock

Rostock, 18.03.2024

Tag der Verteidigung: 30.09.2024

**Gutachter**

Prof. Dr. Ursula van Rienen, Universität Rostock

Prof. Dr. Dr. Peer Kämmerer, Universitätsmedizin Mainz

Prof. Dr. Martina Gerken, Christian-Albrechts-Universität zu Kiel





# Abstract

Mandibular defects, for example resulting from tumour resections, significantly impair the quality of life of patients and often require complex surgical procedures. However, autologous bone graft, the gold standard for regenerating these defects, is often associated with complications and prolonged healing processes. Electrical stimulation is a promising alternative method for improving bone healing, but so far it has mainly been used in other anatomical areas, such as the hip. At present, there are no clinically established mandibular electrostimulation implant designs. This dissertation is therefore dedicated to the development of such electrostimulating implants for the regeneration of mandibular defects. These implants aim to provide optimal electric field strengths of 5 to 70 V/m to the defect area. The objective of this thesis is to examine the electric field distribution around the implant and to draw conclusions for the application of the method in oral and maxillofacial surgery. To this end, a detailed, macroscopic 3D model of a minipig mandible with a critical-size bone defect, surrounding soft tissue and an implanted bipolar stimulation implant is created. Furthermore, the dielectric properties of mandibular bone of minipigs are modelled based on own measurements and two different scenarios are distinguished. These scenarios either consider a correction of the measurement data at low frequencies or neglect them. The minipig model is then analysed numerically using the finite element method. The investigation focusses on quantifying the under-, over- and beneficially stimulated volume in the defect region in order to evaluate the success of the electrical stimulation. The electrode length and the stimulation potential are numerically optimised at a stimulation frequency of  $f = 20$  Hz to ensure a maximum region of beneficially stimulated tissue. A further aim of this work is to analyse the influ-

ence of uncertain model parameters on the simulation results using uncertainty quantification. The dielectric properties of the biological tissues and the parameters of the electrode-tissue interface are taken into account. In addition to the minipig model, two simulation models of human mandibles are analysed in order to gain valuable insights into important parameters and aspects of electrical stimulation in this field of application. This doctoral thesis thus contributes to the development of advanced implant designs and the optimisation of electrical stimulation in oral and maxillofacial surgery.

# Zusammenfassung

Unterkieferdefekte, die beispielsweise aus Tumorresektionen resultieren, beeinträchtigen die Lebensqualität der Betroffenen erheblich und erfordern oft komplexe chirurgische Eingriffe. Der Goldstandard zur Regeneration dieser Defekte, autologe Knochentransplantate, gehen jedoch häufig mit Komplikationen und langwierigen Heilungsprozessen einher. Elektrostimulation ist eine vielversprechende alternative Methode zur Verbesserung der Knochenheilung, die bisher jedoch hauptsächlich in anderen anatomischen Bereichen, wie der Hüfte, angewendet wird. Bisher gibt es für den Unterkiefer keine klinisch etablierten Implantatdesigns mit elektrischer Stimulation. Diese Dissertation widmet sich daher der Entwicklung solcher elektrostimulierender Implantate zur Regeneration von Unterkieferdefekten. Diese Implantate sollen den defekten Knochen dabei mit optimalen elektrischen Feldstärken zwischen 5 und 70 V/m versorgen. Ziel der Arbeit ist es, die elektrische Feldverteilung in der Umgebung des Implantats zu analysieren und daraus Schlüsse für die Anwendung der Methode in der Mund-, Kiefer- und Gesichtschirurgie zu ziehen. Hierfür wird zunächst ein detailliertes, makroskopisches 3D-Modell eines Schweineunterkiefers mit einem Knochendefekt kritischer Größe, umgebendem Weichteilgewebe und einem implantierten bipolaren Stimulationsimplantat erstellt. Die dielektrischen Eigenschaften von Unterkieferknochen von Minischweinen werden basierend auf Messungen modelliert und es werden zwei verschiedene Szenarien unterschieden. Diese Szenarien berücksichtigen entweder eine Korrektur der Messdaten bei niedrigen Frequenzen oder vernachlässigen diese. Das Minischwein-Modell wird mittels der Finite-Elemente-Methode numerisch analysiert. Die Untersuchung konzentriert sich darauf, das unter-, über- und nutzbringend stimulierte Volumen in der Defekt-

region zu quantifizieren, um den Erfolg der Elektrostimulation zu bewerten. Dabei werden die Elektrodenlänge und das Stimulationspotential bei einer Stimulationsfrequenz von  $f = 20$  Hz numerisch optimiert, um einen maximalen Bereich mit nutzbringenden Feldstärken zu versorgen. Ein weiteres Ziel dieser Arbeit besteht in der Analyse des Einflusses von unsicheren Modellparametern auf die Simulationsergebnisse durch die numerische Quantifizierung von Unsicherheiten (*Uncertainty Quantification*). Hierbei werden die dielektrischen Eigenschaften der biologischen Gewebe, sowie die Parameter der Elektrode-Gewebe-Grenzfläche berücksichtigt. Zusätzlich zum Minischwein-Modell werden zwei Simulationsmodelle von menschlichen Unterkiefern untersucht, um wertvolle Erkenntnisse über wichtige Parameter und Aspekte der Elektrostimulation in diesem Anwendungsbereich zu gewinnen. Damit trägt die vorliegende Doktorarbeit zur Entwicklung fortschrittlicher Implantatdesigns und zur Optimierung der Elektrostimulation in der Mund-, Kiefer-, und Gesichtschirurgie bei.

# Acknowledgement

The research presented in this thesis was conducted within the SFB 1270 “Electrically Active Implants” – ELAINE and was funded by the Deutsche Forschungsgemeinschaft (DFG, German Research Foundation) – SFB 1270/2 - 299150580, as well as a scholarship by the state graduate funding (*Landesgraduiertenförderung*) of the state Mecklenburg-Western Pomerania.

Many people have accompanied me during my journey towards finishing this thesis. I would like to express my sincere gratitude to the following supporters:

- Prof. Dr. rer. nat. Ursula van Rienen for supervising my work. I am grateful for her guidance, support, and encouragement throughout the journey of this doctoral thesis. Her mentorship provided the critical push needed to complete this work. I appreciate the nurturing and supportive environment she provided, which enabled me to delve into this fascinating research with confidence;
- Prof. Dr. med. Dr. med. dent. Peer Kämmerer and Prof. Dr. Martina Gerken for serving as the second examiners;
- Dr. med. Dr. med. dent. Michael Dau from the Department of Oral and Maxillofacial Plastic Surgery of the University Medical Centre Rostock for hours of productive discussions, always being available in case of questions, and providing easy access to information and valuable contacts to other people;
- my colleagues in the group of Theoretical Electrical Engineering, especially Andrea Andree, Franziska Reimann, Christian Schmidt, Christian Bahls, Julius Zimmermann, Nils Arbeiter, Henning Bathel,

and Jan Philipp Payonk for fruitful discussions and emotional support;

- my family from whom I know that my biggest fans are among them;
- Sen.-Prof. Dr.-Ing. Dirk Timmermann and his team for extensive discussions on the technical realisation of the proposed stimulation unit;
- all “ELAINES” for all collaborative efforts and the nice research atmosphere;
- Andrea Moser for being my wonderful, motivating mentor and for keeping me going in the face of all challenges;
- again my friends and family for their emotional support and their patience.
- Furthermore, I acknowledge the use of Grammarly <https://www.grammarly.com/> and DeepL Write <https://www.deepl.com/write> to improve the quality of the writing in parts of this manuscript.

# Contents

<b>1</b>	<b>Introduction</b>	<b>1</b>
1.1	Background: electrostimulation and its role in addressing critical-size mandibular defects . . . . .	1
1.2	Research focus and rationale of the study . . . . .	3
1.3	New contributions to the field of electrical bone stimulation . . . . .	5
1.4	Research aim and objectives . . . . .	6
1.5	Structure of the thesis . . . . .	6
<b>2</b>	<b>Characteristics of bone and electrical bone stimulation</b>	<b>8</b>
2.1	Anatomy of the mandible bone . . . . .	9
2.2	Critical-size mandibular bone defects and state of the art of their treatment	11
2.3	Bioelectricity and electrical stimulation of bone . . . . .	12
2.3.1	Bioelectricity of bone . . . . .	12
2.3.2	Electrical stimulation of bone . . . . .	14
2.3.3	<i>In vivo</i> and clinical application of electrical stimulation of bone .	18
2.3.4	Open challenges in electrical stimulation of bone and numerical simulation of electrostimulating implants . . . . .	20
<b>3</b>	<b>Theoretical basics</b>	<b>22</b>
3.1	Electromagnetic field theory . . . . .	22
3.2	Finite element method . . . . .	25
3.2.1	Domain discretisation . . . . .	26
3.2.2	Selection of basis functions . . . . .	27
3.2.3	Formulation and solution of the system of equations . . . . .	28
<b>4</b>	<b>Dielectric properties and numerical simulation of bioelectric problems including model uncertainties</b>	<b>30</b>
4.1	Dielectric properties of biological tissues . . . . .	30
4.1.1	Ambiguities in the Gabriel data and their correction . . . . .	31

4.1.2	Literature review: reliable studies reporting the dielectric properties of bone . . . . .	32
4.2	Modelling workflow for the generation of the minipig mandible simulation model . . . . .	36
4.2.1	Anatomical and technical modelling of the electrically stimulated mandible . . . . .	37
4.2.2	Physical modelling of the electrically stimulated mandible . . . .	41
4.2.3	Setup of the boundary value problem . . . . .	47
4.2.4	Finite element simulation and discretisation . . . . .	50
4.3	Uncertainty quantification . . . . .	52
4.3.1	Stochastic problem definition . . . . .	52
4.3.2	Variance-based sensitivity analysis . . . . .	54
4.3.3	Uncertainty quantification methods . . . . .	55
4.3.4	Software used for the uncertainty quantification studies . . . . .	58
<b>5</b>	<b>Results and discussion</b>	<b>60</b>
5.1	Measurement and analysis of the dielectric properties of minipig mandibular bone . . . . .	60
5.1.1	Validating and fitting of the impedance data of minipig mandibular bone . . . . .	61
5.1.2	Dielectric properties of minipig mandibular bone resulting from the fitting procedure . . . . .	63
5.1.3	Discussion . . . . .	65
5.2	Optimisation of the implant parameters . . . . .	67
5.2.1	Optimised electric field distribution in the minipig mandible model	68
5.2.2	Comparison of the optimised electric field distribution in both scenarios . . . . .	71
5.2.3	Comparison of optimisation results with previous findings . . . .	75
5.2.4	Discussion . . . . .	76
5.3	Uncertainty quantification and sensitivity analysis of an electrically stimulated minipig mandible . . . . .	80
5.3.1	Specification of the probabilistic minipig model . . . . .	80
5.3.2	Global sensitivity analysis using Sobol' indices . . . . .	83
5.3.3	Quantification of uncertainties in the model outputs of the electrically stimulated minipig mandible . . . . .	92
5.3.4	Conclusion of the uncertainty quantification analyses . . . . .	100



---

5.4	<i>In vivo</i> validation of the optimised electrostimulating implant . . . . .	101
5.5	Preliminary simulation of human mandible models . . . . .	104
5.5.1	Comparative simulation of separate electrostimulating electrodes and fixation screws . . . . .	104
5.5.2	Preliminary investigation of electrostimulating fixation screws at a mandibular reconstruction plate . . . . .	109
5.5.3	Conclusion on the preliminary human mandible models . . . . .	114
<b>6</b>	<b>Conclusion and outlook</b>	<b>116</b>
6.1	Research objectives . . . . .	116
6.2	Limitations of the studies . . . . .	119
6.3	Recommendations . . . . .	120
6.4	Contributions to knowledge in the field of electrostimulating bone implants	122
<b>A</b>	<b>Fit results and fit statistics for the dielectric properties of minipig bone</b>	<b>124</b>
<b>B</b>	<b>Impact of the stimulation amplitude on the Sobol' indices</b>	<b>129</b>
	<b>Bibliography</b>	<b>133</b>

## Nomenclature

AC	alternating current
BiCGSTAB	biconjugate gradient stabilised method
CAD	computer-aided design
COMSOL	COMSOL Multiphysics®
CPE	constant phase element
CT	computer tomography
DC	direct current
EIS	electrochemical impedance spectroscopy
EQS	electroquasistatic
ETI	electrode-tissue interface
FEM	finite element method
GMRES	generalised minimal residual method
gPC	<i>generalised</i> polynomial chaos
LCP	liquid crystal polymer
MC	Monte Carlo
MRI	magnetic resonance imaging
NURBS	non-uniform rational B-splines
PC	polynomial chaos
PCE	polynomial chaos expansion
PDF	probability density function
QS	quasi-stationary current problem
ROI	region of interest
SGP	stress-generated potential
SOR	successive over-relaxation
STD	standard deviation
STL	stereolithography
UQ	uncertainty quantification
VBSA	variance-based sensitivity analysis
VCM	volume conductor model

# Chapter 1

## Introduction

The objective of this thesis is to develop innovative electrostimulative endoprotheses that aid in the regeneration of large bone defects in the lower jaw (mandible), focusing on modelling and numerical simulation of the problem in an animal model. In this regard, a 3D finite element simulation model of the mandible of a minipig equipped with an electrostimulating implant is being developed and the implant parameters are being optimised for the most beneficial stimulation. This study contributes to current research as electrical stimulation in maxillofacial application areas, such as the mandible, is relatively new and simulation models for optimising stimulation parameters are not yet available. This work provides optimised stimulation parameters and further evaluates the impact of uncertain input parameters using uncertainty quantification (UQ). Additionally, I will determine the dielectric tissue properties of the mandibular bone in minipigs, which are not yet available in the literature. Furthermore, I will present numerical models of electrically stimulated human mandibles, providing a basis for further studies. These models demonstrate the potential for further research in the field of electrical stimulation of bone. Some background information on the electrical stimulation of bone and its potential application in maxillofacial surgery will be given in the next section.

### 1.1 Background: electrostimulation and its role in addressing critical-size mandibular defects

Bone, a living organ, undergoes a constant process of dynamic transformation known as bone remodelling. Electrical stimuli, resulting from mechanical stresses during daily activities, naturally regulate this process. The advantageous effects of electrical stimulation with regards to bone regeneration have been well known since the 1950s [1]. For several decades, electrostimulating procedures have been utilised in orthopaedics to treat different types of bone defects, with the intention of precisely imitating the natural functional stress through low-frequency electric fields. This has led to the development of innovative implants that use electrical stimulation to accelerate bone regeneration, a rapidly growing area of research. In recent years, extensive research has

been conducted in the development of electrically stimulating implants for various applications, including bone fractures or non-unions [2–5]. Kraus established empirically that sinusoidal stimulation at a frequency of 20 Hz, with an electric field range between 5 and 70 V/m, resulted in improved bone growth [6]. There are electrostimulating therapeutic devices available commercially for application in the limbs that are based on the associated Kraus-Lechner method [7]. However, similar devices suitable for application at facial bone defects, including the lower jaw (mandible) (Fig. 1.1 (a)), are currently unavailable. Therefore, the research presented in this thesis is motivated by the need to improve treatment outcomes for patients dealing with significant bone defects, known as critical-size defects, in the mandible. These defects often arise due to trauma or surgical procedures such as tumour resections, leading to significant functional and aesthetic impairments in patients. The clinical significance of large mandibular bone defects is substantial. In Germany alone, over 3400 surgeries for total or partial resection of the mandible were conducted in 2019 [8]. The conventional

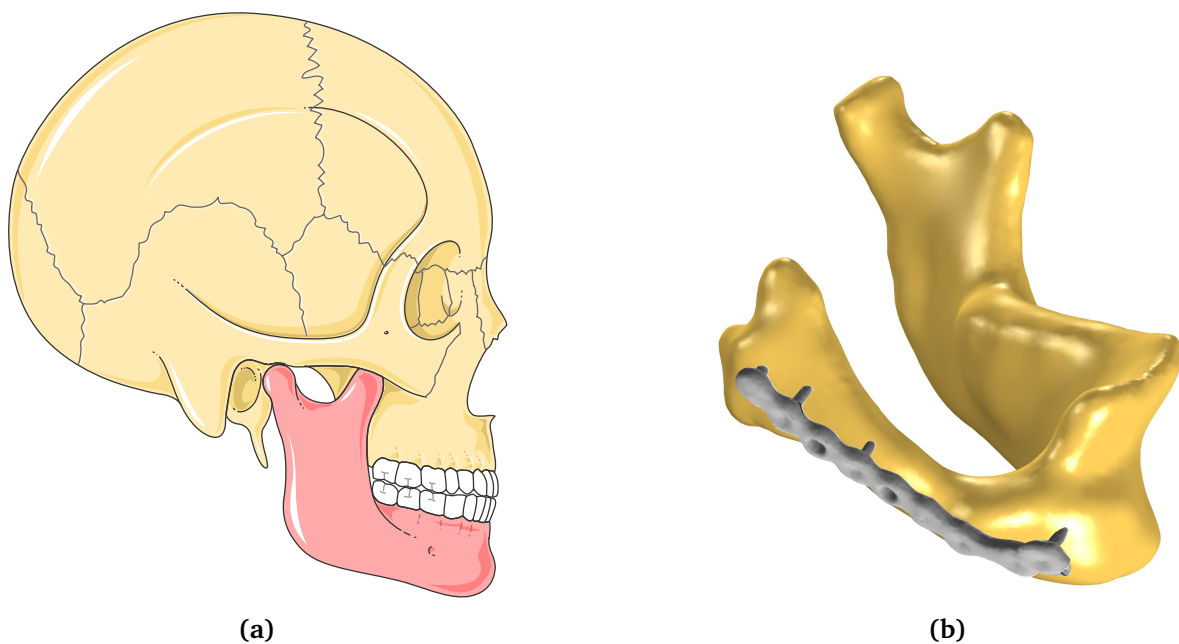


**Figure 1.1:** (a) The location of the human mandible inside the skull is highlighted in red. The figure was partly generated using Servier Medical Art, provided by Servier, licensed under a CC-BY 4.0 license [9]. (b) Exemplary mandible model with a large defect and a titanium reconstruction plate.

methods for healing these defects include titanium reconstruction plates (Fig. 1.1 (b)) in combination with bone grafts [10]. Bone grafts are materials used to replace or repair missing or damaged bone. They can be obtained from the patient's own bone (autologous bone grafts), from other donors, or through the use of artificial bone replacement materials. Regrettably, the conventional approach is associated with prolonged healing time and an increased risk of patient mortality when using the gold standard of autologous bone grafting, which requires a second surgery to graft the

bone material. The incorporation of electrostimulating implants displays potential in enhancing these outcomes.

Electrical stimulation devices for the treatment of major bone defects in the lower jaw are a comparatively new area of research. To date, only Kim et al. have carried out animal experiments [11–13], though without prior numerical optimisation of implant parameters. Moreover, they employed different stimulation parameters than the Kraus-Lechner method, utilising bi-phasic electrical current pulses. Bipolar stimulation electrodes adhering the stimulation parameters established by Kraus [6] have undergone substantial *in vitro* investigation [14–22] as well as numerical analysis [18,23,24]. However, these electrodes have yet to be employed in a large animal model in an *in vivo* setting. This gap will be addressed in the research presented in this thesis, which examines a numerical model of the bipolar electrostimulating electrodes in a minipig mandible as detailed in the research focus presented in the next section.

## 1.2 Research focus and rationale of the study

The research focus of this work is the development and numerical investigation of electrostimulating implants for large defects in the mandible. The regarded electrostimulating setup utilises direct contact stimulation and a bipolar, rod-shaped electrode design as has been used in *in vitro* studies before [14–22]. As the functionality of the electrostimulating system for the mandible first needs to be verified in an animal model, this thesis focuses on developing a detailed numerical model of an electrically stimulated minipig lower jaw. The derived optimal stimulation parameters will be used in subsequent *in vivo* trials. However, I will also address human models to draw first general conclusions on how electrically stimulating implants can be realised in patients.

Numerical modelling is an essential tool in the design process of the aforementioned electrostimulating devices. These models aid in the optimisation of implant parameters, ensuring the previously mentioned beneficial electric field threshold. Most existing stimulation devices are applied empirically or have been developed under rough estimates [6, 25, 26]. However, the actual field distribution within the tissue is unknown and cannot be measured easily. Numerical modelling and simulation, as employed in this work, facilitate the determination of the electric fields and currents in the tissue, thus allowing the design of reliable stimulation devices. Inappropriate electrical stimulation could either have no effect at all or harm the tissue by causing cell death. Therefore, suitable stimulation parameters play a crucial role in electrically stimulating implants. This study aims to optimise these parameters to maximise the effect of beneficial stimulation and hence ensure good healing results. The numerical studies therefore allow to gain important insights prior to *in vivo* validation experiments and subsequently contribute to significantly reducing the number of necessary animal experiments.

For a reliable simulation of the electric field distribution, the dielectric properties of the tissues involved are of utmost importance. Therefore, a further focus of this thesis is on accurately modelling the dielectric properties of the biological tissues involved. Unfortunately, the existing literature lacks any dielectric tissue properties of mandibular bone. Consequently, the dielectric properties of the mandibular bone of minipigs will be determined using electrochemical impedance spectroscopy (EIS). The commonly used tissue database by Gabriel et al. [27–29] has recently undergone reanalysis, indicating ambiguity in interpreting the dielectric tissue properties at low frequencies [30]. To address this issue, numerical simulations of electrostimulating implants for bone regeneration considering the different interpretations are carried out in this thesis.

As the dielectric properties of biological tissues further vary greatly, uncertainty quantification (UQ) studies are conducted to determine the most influential model parameters and input quantities with respect to the uncertainty of the output quantities. This enables identification of which parameters need to be carefully determined for future studies and which can be disregarded in favour of a simplified numerical model.

Systematic research into suitable stimulation parameters is still a very active area of research, e.g., in the SFB 1270 ELAINE.<sup>1</sup> Whereas colleagues in the field of cellular biology concentrate on examining appropriate stimulation parameters *in vitro* or *ex vivo*, this thesis will rely on the stimulation parameters used in commercially available devices found in the literature to establish an electrostimulation implant design. These devices are based on the Kraus-Lechner method [6, 7] (ref. Chapter 2.3.3). The Kraus-Lechner method [6, 7] has been successfully applied in surgical practise in combination with an approved stimulation device that is available on the market. However, the inherently inductive stimulation approach of the Kraus-Lechner method involved a complicated coil setup. Consequently, this setup requires a high level of patient compliance and is not feasible for the application on the jaw. Therefore, in this study, the electrostimulating implant is driven by a small stimulator unit located at the stimulation site itself instead of the coil, with the aim of achieving the same stimulation effect. Thus, the same parameters are used as in the Kraus-Lechner approach but with a different field source. The neglect of the magnetic field is justified based on theoretical considerations (Sec. 3.1). Accordingly, electroquasistatics (EQS) and quasi-stationary current problems (QSSs) are used as approximations in the numerical model. This research aims to establish the initial design of innovative electrostimulative implants for the mandible. Therefore, this study simplifies the numerical model by only considering the entire mandible bone structure at the whole bone scale, and at the meso-scale, distinguishing between cortical and cancellous bone. Furthermore, it should be noted that the simulation of the stimulating unit and cables is not part of this work.

---

<sup>1</sup>The collaborative research centre SFB 1270 ELAINE (<https://www.elaine.uni-rostock.de/en/>) on electrically active implants focuses on improving patient-specific therapies through the development and advancement of innovative electrostimulating implants for bone, cartilage, and deep brain stimulation.

The significance of the research presented here will be outlined in the following section.

### **1.3 New contributions to the field of electrical bone stimulation**

This dissertation focuses on the use of numerical simulations to model electrostimulating implants for the regeneration of mandibular defects and to determine the resulting electric field distribution. These simulations will be used to optimise the design and the parameters of electrostimulating implants. The outcomes of this proof-of-concept investigation have the potential to lead to significant progress in the field of bone regeneration and bring renewed optimism to a large number of patients struggling with severe jaw defects. Furthermore, the inherent scalability of the developed electrostimulation concept could form the basis for extending its benefits to a significantly larger patient population suffering from smaller bone defects, a common issue encountered in dental implantations that require bone augmentation. It is estimated that around 10.7 million dental implant procedures are performed annually worldwide [31], and one in four implants necessitates bone grafting [32,33]. These cases with smaller bone defects could benefit from improved bone regeneration with electrical stimulation in the long term. Accelerating bone growth in patients with impaired defect healing in the jaw could substantially improve their physical and psychological condition and may also reduce the burden on the health care system for such treatments.

Large animal models, such as the minipig, have not yet been studied regarding electrical stimulation in the lower jaw. Additionally, there is currently no numerical minipig model available for large bone defects in the lower jaw. Therefore, this research contributes a 3D computer-aided design (CAD) model of a minipig mandible which will also be useful to other researchers studying, for example, the biomechanical properties of large bone defects. Furthermore, the numerical model will provide optimised implant parameters for innovative electrically stimulating jaw implants that will allow for or promote bone healing. Currently, there are no numerical or even experimental studies on electrical stimulation of large bone defects in human mandibles available. By also considering simplified simulation models of human mandibles, this study will contribute valuable insights for the future development and optimisation of electrostimulating implants for the mandible.

By modelling different scenarios depending on the specific assumptions about the dielectric properties of the tissues, as well as determining the most influential input quantities via uncertainty quantification (UQ), I will contribute important learnings about which quantities should be characterised particularly carefully, both numerically (by adequate models) and experimentally (by accurate measurements).

The research aim guiding the studies, as well as the objectives set to achieve this aim, will be specified in the next section.

## 1.4 Research aim and objectives

The aim of this work is to develop novel electrostimulative endoprotheses for bone regeneration of the lower jaw (mandible), with a focus on modelling and numerical simulation of the problem. To achieve this aim, the following research objectives are addressed in this thesis:

1. Determine the dielectric tissue properties of minipig mandibular bone.
2. Assess the effect of modelling the dielectric tissue properties with and without a correction for electrode effects.
3. Create a 3D finite element model of a minipig mandible with a bipolar electrostimulating implant.
4. Optimise the electric field distribution with respect to the applied stimulation parameters, i.e. electrode length and stimulation voltage, to ensure a maximum volume of beneficially stimulated tissue.
5. Identify the input parameters with the most significant influence and the magnitude of their impact on the simulation results in uncertainty quantification (UQ) studies.
6. Explore potential applications of electrostimulating mandibular implants in humans using simplified human mandible models.

The structure of this thesis will be outlined in the following section.

## 1.5 Structure of the thesis

This thesis is structured into six chapters. Chapter 1 has provided an introduction to the general research focus and a general overview of the aims and objectives of this thesis. Chapter 2 explores the characteristics of bone as a bioelectric tissue and introduces critical-size defects in the mandibular bone and their current treatment. The selection of the minipig as the model considered in this thesis is explained and further details on electrical stimulation of bone as a therapeutic method are presented, as well as current areas of application and current challenges. In Chapter 3, the theoretical basics of electromagnetic field theory and the finite element method (FEM) as the method of choice for simulating the electrically stimulated minipig mandible are introduced. Further methods necessary for the simulation are described in Chapter 4. This Chapter



presents a literature review on the dielectric properties of biological tissues, with particular emphasis on bone, which are of paramount importance for modelling. Moreover, a detailed workflow for creating the numerical model is provided, starting from computer tomography (CT) data, modelling the geometry, defining the physics, setting up the boundary value problem, and solving it with the commercial finite element software COMSOL Multiphysics® (COMSOL). The method of uncertainty quantification (UQ) is presented as a tool to assess the influence of uncertain input parameters on the simulation results. In Chapter 5, the results of this thesis are presented. This includes reporting the measured dielectric properties of minipig mandibular bone used as input parameters in the numerical model. Additionally, the implant parameters, specifically the electrode length and stimulation potential, are optimised and compared to the simulation results of previous studies. The impact of uncertain tissue properties and electrode-tissue interface parameters is also determined and discussed. Chapter 5 also includes a brief summary of the results obtained from applying the established electrostimulating system *in vivo*. Furthermore, preliminary simulation models of human mandibles are introduced and the simulated electric field distribution is examined. The final Chapter 6 features a summary of the thesis as well as an outlook on future research in this area.

Some of the work presented in this thesis has been previously published [34–38]. Therefore, certain sections of this thesis include reformulated material from these publications. Any chapters or sections that contain a substantial amount of material from these works will be clearly identified at the beginning of the respective section.

## Chapter 2

# Characteristics of bone and electrical bone stimulation

In this chapter, I will introduce the structure of bone, with a focus on the mandible (lower jaw). Furthermore, I will discuss critical-size bone defects, the existing therapeutic methods, and the open challenges associated with their treatment. Additionally, I will discuss electrical stimulation as an effective means of improving the treatment of critical-size bone defects in the mandible.

With the exception of a small percentage of water (approximately 10 %), bone is composed of a mineralised organic matrix. This matrix is comprised of both organic (25 % by weight) and inorganic (65 % by weight) phases [39]. The organic phase primarily consists of type I collagen, which plays a vital role in the tensile strength of bone. Minor contributions arise from matrix proteins that assist in mineralisation and bone formation, along with cytokines and growth factors that participate in the differentiation, activation, growth, and turnover of bone cells [40]. The inorganic phase is composed of calcium phosphate, specifically carbonated hydroxyapatite.

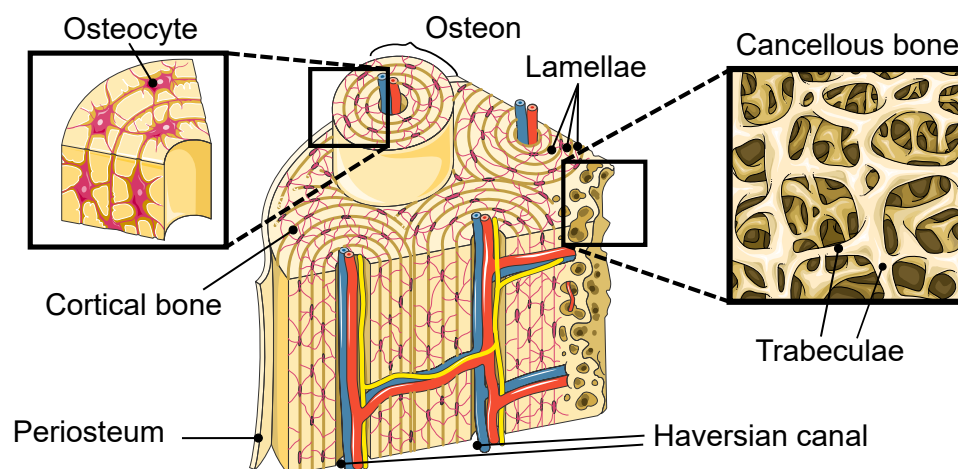


**Figure 2.1:** Schematic structure of bone. The figure was partly generated using *Servier Medical Art*, provided by Servier [41], licensed under CC-BY 4.0.

Currey [42] defined four hierarchy levels present in bone: the nano-scale level is composed of type I collagen fibrils that contain carbonated hydroxyapatite nanocrystals. Secondly, the micro-scale comprises all structures visible under the microscope ( $\approx \mu\text{m}$ ), such as individual mineralised collagen fibres formed by multiple collagen fibrils. Multiple mineralised collagen fibre bundles constitute the so-called lamellae [43] (Fig. 2.1). The lamellae are densely packed with pores that contain osteocytes, i.e. bone cells. The arrangement of the lamellae differs between the two bone types of cortical and cancellous bone. For cortical bone, the lamellae are closely interconnected and arranged concentrically to form osteons. Within the centre of each osteon is a vascular channel called the Haversian canal, which is characterised by electrically conductive soft tissue such as blood, lymph, and nerve fibres [44]. In contrast, the lamellae of cancellous bone are arranged parallel to each other. Together with the osteocytes and mineralised bone matrix, these structures make up the trabeculae. The void between the trabeculae is filled with bone marrow [45]. The third hierarchy level identified by Currey [42] is the meso-scale, which investigates the distinctive structure of cancellous and cortical bone. The fourth and largest hierarchy level, encompassing the whole bone, is the macro-scale. Only the macro- and meso-scale are regarded in this thesis and a brief description of the specific anatomic structure under study, the mandible, will follow in the next section.

## 2.1 Anatomy of the mandible bone

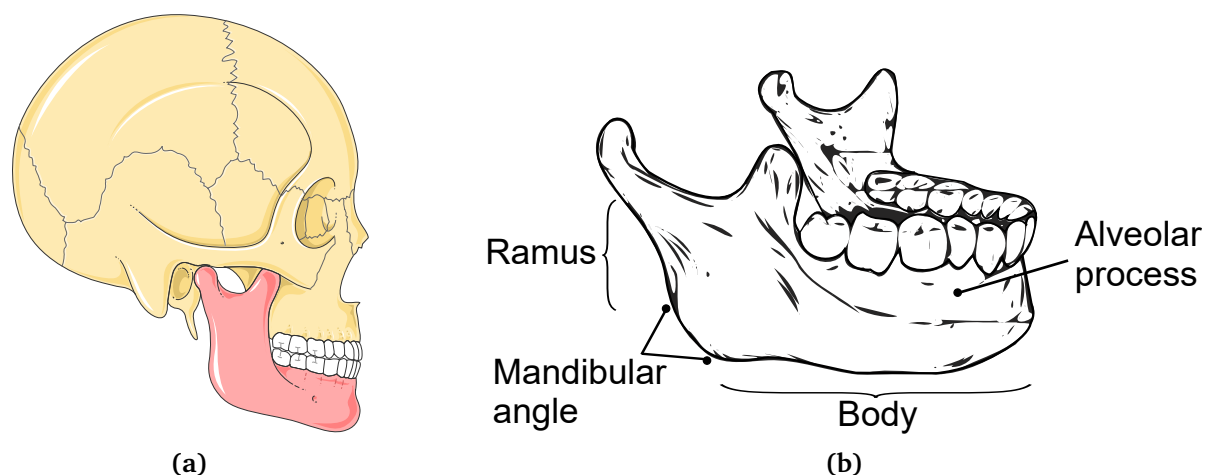


**Figure 2.2:** (a) Location of the human mandible inside the skull. The mandible is highlighted in red (adapted from *Servier Medical Art* [9], provided by Servier, licensed under CC-BY 4.0). (b) Primary components of the mandible (adapted from [46], licensed under CC-BY 4.0. Access for free at <https://openstax.org/books/biology-2e>).

The mandible, also known as the lower jaw, is the only moveable bone of the skull (Fig. 2.2 (a)). It is essential for mastication and facilitates speech articulation in humans. Therefore, any restrictions to its function can considerably reduce the

quality of life of a patient. The mandible comprises a body, the mandibular angle, and the ramus (Fig. 2.2 (b)). The upper boundary of the mandible includes the alveolar process, which is the site where the teeth are embedded [46]. This thesis focusses on the posterior mandible due to its frequent involvement in surgical procedures such as tumour resection.

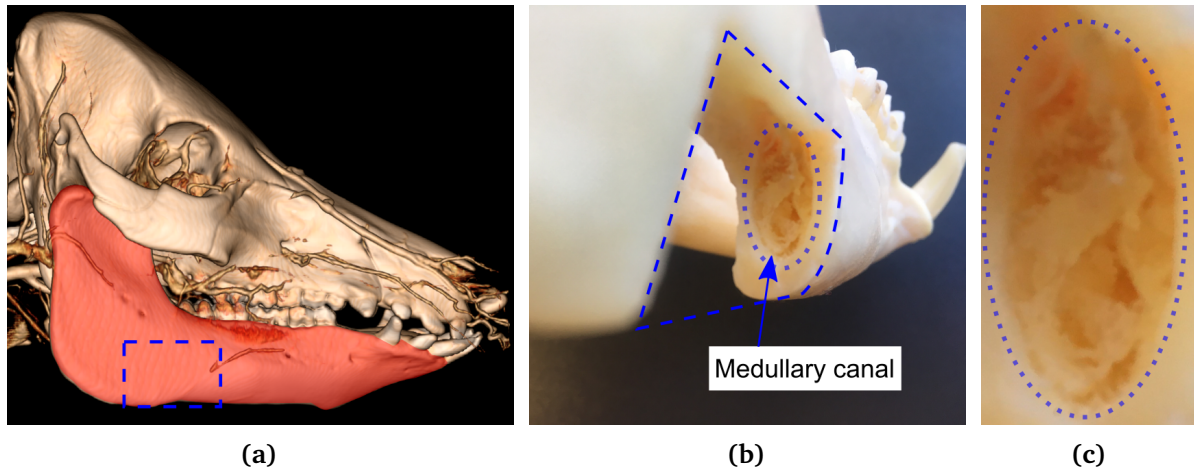


**Figure 2.3:** Anatomy of the minipig mandible. (a) Location of the mandible inside the skull. Shown is a 3D rendering of a minipig skull (adapted from [47], licensed under CC-BY 4.0). The mandible is highlighted in red and the intended defect region is marked with dashed lines. (b) Minipig mandible with defect, allowing the view on the medullary canal (dotted lines) containing cancellous bone. Note that the bone marrow has been removed in the depicted bone model. (c) Enlarged view of the cancellous bone inside the medullary canal.

Before applying new therapeutic devices clinically, they typically undergo *in vitro* and then *in vivo* animal testing to assess their functionality and safety. Therefore, this study aims to investigate the mandible of a minipig (Fig. 2.3 (a)), which is a suitable and common large animal model for subsequent *in vivo* validation studies. These validation studies were conducted in 2021 and their findings have been submitted for review [48]. Lessons learned from the *in vivo* experiments will be addressed in Sec. 5.4. Minipigs are employed as a large animal model for long-term studies in dental and maxillofacial research [47] due to their similarity with the human mandible regarding their shape, size, and anatomy [49]. Additionally, it has been observed that the bone regeneration rate in both the minipig and the human mandible is similar [49, 50].

The mandible displays a complex structure in both humans and minipigs. It is an irregular bone consisting of cancellous bone that is covered with a thin, compact layer of cortical bone (Fig. 2.3 (b)). Cancellous bone is composed of trabeculae and comprises a three-dimensional functional microstructure. This microstructure illustrates that bone grows most strongly in regions of high mechanical stress. Cancellous bone is less dense than cortical bone and possesses a porous, sponge-like structure. It encompasses the medullary cavity (Fig. 2.3 (c)) that is filled with bone marrow [51]. It is worth

emphasising that the morphology of the mandible differs depending on the location: at the posterior joint region, it is fully cortical, but increases in thickness towards the middle, revealing a space filled with cancellous bone and bone marrow on the inside. This region then decreases in width again towards the anterior part of the mandible. Possible defects in these bony structures and their typical clinical treatment are introduced in the next section.

## 2.2 Critical-size mandibular bone defects and state of the art of their treatment

Bone defects in humans can be caused by various factors, including traumatic injury, diseases like osteoporosis or arthritis, tumour resection, and extensive infection [52]. In general, bone is inherently able to repair itself and heal spontaneously. However, in some cases, the defects may be larger than a critical size. In this situation, external therapeutic measures must be taken to allow the bone to heal [10]. These defects are known as critical-size defects. The actual dimensions of this critical size depend on various factors like the anatomic location, species, age, and the surrounding tissue [10]. For the minipig mandible, Ma et al. state that a critical-size defect with preserved periosteum is 6 cm in width [53]. Without preservation of the periosteum, the critical size is 2 cm [53], see Fig. 2.4 (a). In maxillofacial surgery, critical-size defects

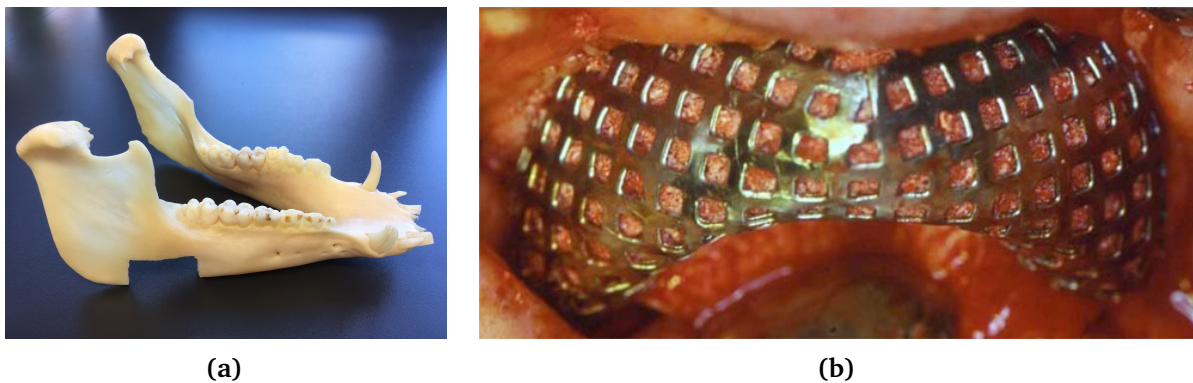


**Figure 2.4:** (a) Deliberately created defect of critical size in the mandible of a minipig for use in animal experiments. (b) Standard treatment of large bone defects in a human patient with a titanium mesh (Figure (b) reproduced from [54], licensed under CC BY-NC 3.0).

occur mainly after partial resection of the mandible due to tumours and are of great clinical relevance, with more than 3100 surgeries per year in Germany alone as of 2019 [55]. The treatment of critical-size defects presents significant challenges due to high complication rates and the frequent requirement for revision surgery [56]. Additionally, according to Nauth et al. [56], there is no consensus on the ideal surgical treatment for critical-size bone defects. Conventionally, these defects are treated with

titanium mesh trays (Fig. 2.4 (b)) or osteosynthesis plates (Fig. 1.1 (b)) that are secured to the remaining bone with screws. These plates are used either alone or in combination with bone graft substitutes. However, relying solely on reconstruction plates often leads to complications, with complication rates as high as 48 % [57], requiring revision surgery. These complications include fracture of the plate or mesh tray, loosening of the fixation screws, or dehiscence [58–61]. The most widely accepted practice for treating critical-size defects is through the use of autologous bone grafts, which are acquired from the bone of the patient such as the fibula or iliac crest [10, 62]. This treatment method has advantages such as the abundance of osteoconductive, osteoinductive, and osteogenetic factors [63]. This treatment can be supported using growth factors [10]. However, the surgery required to harvest the bone graft is associated with high complication rates and morbidity [10]. To avoid subjecting the patient to additional risks associated with a second surgery, this study aims to use electrical stimulation as an alternative treatment approach to achieve faster bone healing and improved fixation of bone and implant. This can further enhance the desired therapy outcome of achieving long-term stability, restored functionality, and aesthetics. In the following sections, I will outline the general principles of electrical stimulation in bone regeneration and then focus specifically on electrical stimulation of the mandible.

## 2.3 Bioelectricity and electrical stimulation of bone

Endogenous electric fields hold an essential role in every cell of the human body. They are involved in action potentials of nerve and muscle fibres and play a crucial role in cell processes such as proliferation, differentiation, and migration [64]. Artificial electrical stimulation has a wide range of applications in imitating these naturally occurring electrical signals, such as neural stimulation like deep brain stimulation (DBS) [65] or cochlear implants [66], wound healing [6], cartilage tissue engineering [67–69], and supporting cancer treatment [70]. The following section will outline the fundamental principles of bioelectricity and stimulation of bone.

### 2.3.1 Bioelectricity of bone

Iwao Yasuda (1909–1983) is widely regarded as a pioneering figure in the field of bone bioelectricity and electrical stimulation of bone. In 1953, he established a clear link between mechanical stress and stimulated bone growth [1]. Moreover, Yasuda also revealed the interrelationship between mechanical stress in bone and the electricity generated by it [1]. By measuring the electric potentials on the surface of a bent long bone, he discovered that the compressed (concave) part of the bone became electronegative, whereas the tensed (convex) areas were electropositive (Fig. 2.5 (a)). He concluded that mechanically induced *electrical* stimuli promote bone regeneration



and, therefore, artificial electrical stimuli could increase bone formation. In the study of Yasuda, experimental confirmation was also found for this hypothesis. In an *in vivo* test, a current of 1  $\mu\text{A}$  was applied to the femoral bone of rabbits over a period of three weeks. Yasuda discovered that new bone was produced, specifically at the negative electrode, while distinctly less bone formed at the positive electrode (Fig. 2.5 (b)). These findings confirmed his hypothesis that electric signals are the fundamental stimuli that promote bone growth [1].

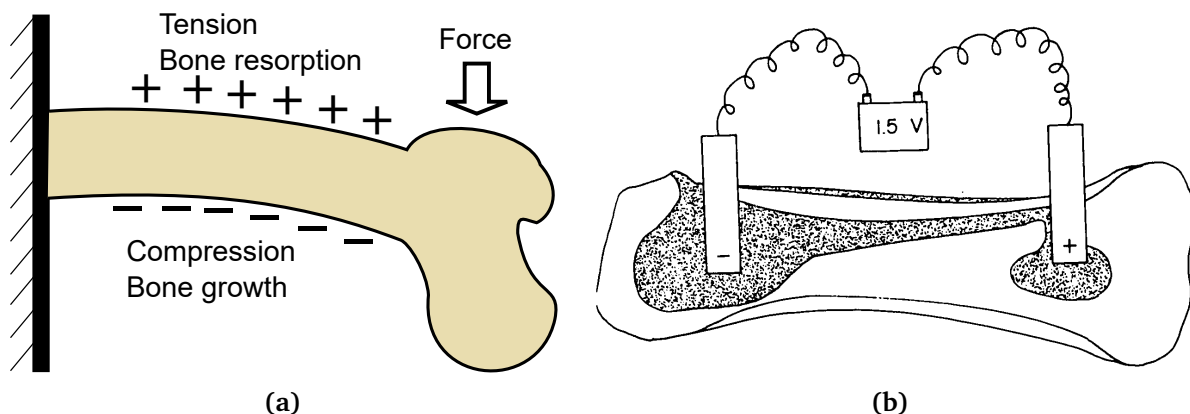


**Figure 2.5:** (a) When a long bone is subjected to mechanical stress, it results in the formation of electric potentials. Compression causes electronegative potentials on the concave side of the bone, while tension yields electropositive potentials on the convex side. Increased bone growth is associated with the concave region, whereas increased bone resorption occurs in the convex region. (b) The application of electrical stimulation to the femoral bone of a rabbit results in increased bone growth (grey areas), especially at the cathode (-). At the anode (+), there is significantly less bone formation. Figure (b) has been reproduced with permission from Wolters Kluwer Health Inc. (Iwao Yasuda, *The Classic. Fundamental Aspects of Fracture Treatment, Clinical Orthopaedics and Related Research*, Vol. 124, p. 5-8, <https://journals.lww.com/c-orthopaedicpractice/pages/default.aspx> [1]).

Since the pioneering research of Yasuda, these bioelectrical interrelationships have been studied extensively. The electric signals observed in bone are generally caused by stress-induced electrical polarisation. These intrinsic electric fields are believed to form the basis for bone remodelling. Stress-generated potentials (SGPs) originating from the piezoelectric properties of bone [71–74] or streaming potentials [75–78] are discussed extensively in the literature. However, the precise mechanisms behind the piezoelectric effect and streaming potentials in bone are not yet fully understood.

The direct piezoelectric effect refers to a change in electrical polarisation and thus the occurrence of an electrical voltage in solids when they are elastically deformed, i.e. strained. The indirect piezoelectric effect occurs when an applied electric field leads to mechanical deformation of the solid [79]. Piezoelectricity occurs only in materials of crystal classes that lack a centre for inversion symmetry, and possess a polar axis in the crystal. In 1957, Fukada and Yasuda observed both the direct and the indirect piezoelectric effect in dry bovine cortical bone [71]. They concluded from

their experiments that the piezoelectric effect is most pronounced when a shearing force is applied to the collagen fibres, causing them to slip past each other [71,80]. In general, the precise nature of the piezoelectric effect in bone has been challenging to characterise. The piezoelectric coefficients of bone and collagen have been reported to vary significantly depending on the measuring method and sample condition [71,73,81–86]. Wieland et al. [87] examined the inverse piezoelectric effect in *trabecular* bovine bone, observing field-dependent strain generated through external electrical stimulation. This strain was large enough to be perceptible for bone cells and may suggest the contribution of the inverse piezoelectric effect to bone remodelling while receiving electrical stimulation [87]. Although there are still uncertainties, there is a consensus that the piezoelectric effect is present in bone. To account for the microstructure of bone, Starkebaum and Korostoff [88] measured SGPs in human and bovine cortical bone samples with microelectrodes. This way, they were able to measure signals down to the osteon level. The researchers determined relatively large fields of approximately 10 to 30 V/m in proximity to the Haversian canals [88]. The field strengths mentioned are comparable in magnitude to those of therapeutically applied electric fields [6], as they are also utilised in this thesis.

In the 1960s, observation on wet bone indicated that the SGPs in bone were not solely related to the piezoelectric effect [89]. Instead, the so-called streaming potentials play a significant role in the electro-mechanical potentials measured in wet bone [85,90]. The streaming potential is an electrokinetic effect that occurs as the result of the flow of extracellular bone fluid. In bone, the liquid located in the inter-cellular spaces contains ions. The application of mechanical stress causes a flow of these ions, creating an electric potential between two points alongside the ion stream [85]. The ratio of the piezoelectric effect and streaming potential depends on the hydration of the material, since water molecules enhance the symmetry of the collagen molecule, thus reducing the piezoelectric effect [85]. This finding implies that the streaming potential is the dominant mechanism under *in vivo* conditions [85]. In current research, the challenge of understanding the bidirectional electromechanical coupling involved in bone remodelling remains [91]. However, it is established that electric fields in bone, generated by piezoelectricity and streaming potentials, initiate these biological processes. Irrespective of the true source of the electric fields that occur naturally in bone, artificial electric fields are utilised for therapeutic purposes. The following section introduces the various methods of application.

### 2.3.2 Electrical stimulation of bone

Following the pioneering research of Yasuda which was presented in the previous section, a number of technologies have been developed with the aim of accelerating bone growth through electrical stimulation [2–5,92]. The fundamental concept behind these approaches is to imitate the electric signals that naturally arise in bones due to SGPs through electrical stimulation. [93]. However, the complex processes involved in bone remodelling and electrically induced bone regeneration are still not



fully understood [94, 95]. There are differences in the mechanisms of action of electrical stimulation for bone regeneration across various stimulation modalities [96]. Essentially, electrical stimulation increases the production of mRNA from DNA. This, in turn, promotes the expression of growth factors [97] which enhance bone healing by promoting cell proliferation [98, 99] and differentiation [96, 100–102]. Furthermore, electrical stimulation encourages bone marrow mesenchymal stem cells to migrate towards the defect site [103]. Electrical stimulation facilitates osteogenesis through various other mechanisms. These mechanisms include the upregulation of intracellular calcium levels [104] and changing the local micro-environment in terms of improved blood circulation and increased pH levels [105]. These changes improve callus formation, mineralisation, and vascularisation at the stimulated defect site, resulting in better treatment outcomes. More specifically, the healing time is reduced or – in cases where the bone would not heal without further treatment – any healing at all is achieved [96]. Biophysical theories have been developed to explain certain aspects of the interaction between electric fields and cells. However, this work specifically examines the macro- and meso-scale, with no consideration for cell-scale processes. Interested readers are referred to works such as [106, 107].

Generally, there are three methods for the application of electrical stimuli. These stimulation modalities comprise direct contact stimulation, capacitive coupling, and inductive coupling. The latter two are non-invasive, whereas direct contact stimulation requires the electrodes to be placed directly at the defect site in an invasive surgery [108]. The stimulation modalities differ in terms of their practicable duration of stimulation and comfort for the patient. Therefore, the question of which stimulation setup with which stimulation parameters is optimal for bone defect regeneration depends on the specific case and is still controversially discussed [109]. This study will examine direct contact stimulation, with the other two stimulation methods being briefly described.

### Direct contact stimulation

Direct contact stimulation<sup>1</sup> is the preferred method for electrostimulation of the implant developed in this thesis. It is an invasive stimulation method that uses surgically implanted electrodes to directly apply the electric field or current to the tissue to be stimulated. Generally, the cathode (negative electrode) is positioned at the defect side, whereas the anode (positive electrode) is preferably placed in the soft tissue [111] (Fig. 2.6 (left)). This arrangement is meant to prevent bone resorption at the anode. In practice however, anatomical conditions such as the thickness of soft tissue often necessitate the anode also being placed in the bone [111]. Currents ranging from five to

---

<sup>1</sup>Note that in the literature this stimulation modality is usually referred to as “direct current stimulation” because direct current (DC, i.e. continuous current) signals are mainly used for stimulation. However, also alternating currents (AC) may be applied with direct electrode-tissue contact. Therefore, I use the more general term “direct contact stimulation” here. I will add the terms DC or AC to clarify which signal form was used in cited studies.

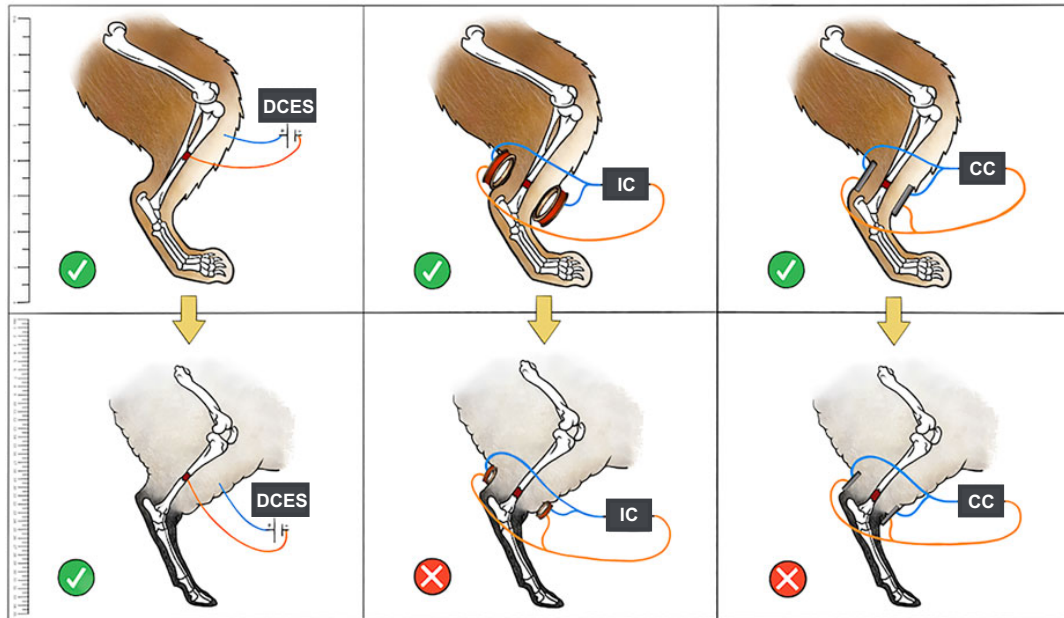


**Figure 2.6:** Schematic illustrating the stimulation modalities used in an animal model, including (left) direct contact electrical stimulation (DCES), whereby one or both stimulation electrodes are surgically implanted into the defect area, (middle) inductively coupled electrical stimulation (IC), where an external induction coil generates a magnetic field that induces an electromagnetic field in the defect region, and (right) capacitively coupled electrical stimulation (CC), where opposite stimulation electrodes are placed on the skin. The main text contains a detailed description of the three stimulation methods. The figures have been adapted from [110] and are licensed under CC BY 4.0.

one hundred microamperes are typically applied [111], with corresponding potentials below 1.5 V to prevent electrolysis [111]. However, these values may differ among the various specific applications. Friedenberget al. [25] observed a dose-response behaviour of the osteogenesis induced by DC direct contact stimulation. They stimulated femoral shafts of rabbits and found that currents within the range of 5–20  $\mu\text{A}$  promoted the formation of new bone, while currents above 20  $\mu\text{A}$  resulted in cell necrosis [25].

In general, the applied potentials in direct contact stimulation may be constant or varying in time, typically with low frequencies below 3 kHz [111]. Although sinusoidal signals with varying frequencies are not commonly employed in direct contact stimulation, they possess the advantage of reducing electrode corrosion. Corrosion can cause the electrode material to wear out quickly and allow the deposition of ions into the tissue, which may be harmful [112, 113]. In AC stimulation, faradic products do not accumulate at the electrode-tissue interface because the electrochemical processes continuously undergo reversal [109, 114]. Bipolar electrodes with directly coupled alternating electric fields have been utilised extensively in *in vitro* experiments in Rostock [16–19]. Recent investigations within the SFB 1270 ELAINE also continue to

explore the potential of these electrodes [20–22]. Consequently, I will employ such bipolar electrodes with directly coupled alternating electric fields in this thesis.

Direct contact stimulation has the particular advantage of stimulating directly at the defect site. Furthermore, patient compliance is high as the stimulation device can be incorporated directly into the bone implant without the need for external primary coils or electrodes, unlike in the inductively or capacitively coupled method. Hence, the direct contact approach enables reliable therapy over an extended period of time. Some authors point out that there are risks associated with invasive treatment methods, such as infections, tissue irritation, inflammation, electrode breakage, and complications associated with a second surgery to remove the electrodes after healing [115, 116]. However, direct contact applications have shown the highest success rates in large animal models [110] and clinical studies [109] as compared to capacitively and inductively coupled applications. Additionally, leaving the implant in the body is planned for the specific application developed in this work, avoiding the need for a second surgery.

### Capacitive coupling

Capacitive coupling is usually a non-invasive stimulation method that involves the use of opposing electrodes on the skin surface [117, 118] (Fig. 2.6 (right)). One of the key benefits of the capacitive stimulation setup is the highly uniform electric field generated between both electrodes. However, due to the significant amount of soft tissue that the potential drops across, the power requirements are much greater in comparison to direct contact stimulation. This holds particularly true for large animal models [110]. Moreover, drawbacks encompass skin irritation and non-compliance of the patient, which impede successful therapy control [119]. Lastly, only a few clinical studies have presented evidence of the beneficial effects of CC stimulation to date [120, 121].

### Inductive coupling

Electric fields in bone can further be induced through inductive, i.e. *electromagnetic* coupling. Inductive stimulation involves placing one or two coils close to the defect site, which generate a time-varying or pulsed electromagnetic field (Fig. 2.6 (middle)) [3, 111]. For the purposes of this thesis, bone defects in the mandible would require the external coil to be positioned around the head. Hence the inductive approach would be accompanied by impaired patient comfort and is further not feasible for long-term *in vivo* experiments. Therefore, inductive coupling was not considered in this thesis.

### 2.3.3 *In vivo* and clinical application of electrical stimulation of bone

The advantageous effect of electrical stimulation on bone regeneration has been demonstrated in numerous *in vitro* and *in vivo* studies [13, 21, 67, 100, 114, 122–126]. In clinical practice, electrical stimulation has been used for bone healing for several decades, dating back to at least the 1980s. Examples include the Magnetodyn® technology [7, 127] and the Biomet® Bone Healing System (Zimmer Biomet, Indiana, IN, United States). Over 15 FDA-approved devices are available as of 2016, listed in [128]. In the following section, the Kraus-Lechner method will be briefly introduced. This technique forms the foundation of the aforementioned Magnetodyn® technology, as well as serving as the basis for the field thresholds examined in this thesis.

#### Electrical stimulation with the Kraus-Lechner method

The stimulation parameters utilised in studies on electrical stimulation of bone are largely used empirically or phenomenologically. This is due to the complex physiological processes involved in bone remodelling which are not yet fully understood, as previously indicated. For instance, empirical evidence shows that low-frequency stimulation with sinusoidal electromagnetic fields between 5 and 70 V/m at frequencies of  $f = 20$  Hz leads to improved healing results in clinical practice [6]. This approach is called the Kraus-Lechner method [7], and has been widely used in orthopaedics [4, 129, 130]. According to this approach, electric field strengths exceeding 70 V/m may result in tissue damage due to overstimulation, whereas field strengths lower than 5 V/m do not facilitate bone regeneration. Accordingly, this field threshold will be employed to optimise the electric field distribution in this work.

The method introduced by Kraus and Lechner [6] has been further developed and specialised. The “bipolar induction screw system” (BISS) was introduced by Mittelmeier et al. [4] and has since become an established practise, particularly for patients with loosened hip endoprostheses or femoral head necrosis. It is noteworthy that the Kraus-Lechner approach originally is an inductive approach. However, as previously mentioned, the primary objective in this work is to ensure optimal patient comfort, and thus, inductive stimulation is not a viable option. Still, as the electric field has the most advantageous effect on bone regeneration, it is assumed that the field threshold proposed by Kraus and the bipolar stimulation electrode introduced by Mittelmeier et al. may be employed for a direct contact stimulation setup like in this study.

The low-frequency approach followed by Kraus and Lechner is particularly supported by the fact that physiological processes in the body take place at low frequencies in the range of 1–20 Hz [131]. For instance, naturally occurring locomotive or chewing forces in humans are typically around 2 Hz [42]. These forces affect the different cells that are involved in bone modelling and remodelling. The hypothesis is that bone cells may respond specifically to stimuli of such physiological frequencies through

the mechano-electrical coupling. This is further supported by research conducted by McLeod et al., who found that extremely low-frequency sinusoidal electric fields ranging from 15 to 30 Hz were most effective in promoting bone regeneration and preventing bone loss [132, 133]. Comparable frequencies of 20–30 Hz are involved in muscle contraction while standing still, suggesting that postural muscle activity plays a role in bone remodelling [133]. The stimulation frequency of 20 Hz is further supported by recent *in vitro* studies. Cell experiments applying an AC sinusoidal signal ( $f = 20$  Hz) on human osteoblasts revealed a voltage-dependent enhancement in cell differentiation [18]. Using the BISS system, electromagnetic fields in combination with additional alternating electric fields at 20 Hz and 700 mV potential difference applied between the screw electrodes demonstrated a favourable effect on the viability and differentiation of bone cells [16].

### **Application of electrical bone stimulation to the lower jaw *in vivo* and clinically**

Only a few studies have considered the *in vivo* or clinical application of electrical stimulation in the mandible. Furthermore, only a few studies analysed this topic *in silico*. *In vivo* and clinical research regarding mandibles that were electrically stimulated showed a rise in bone growth and fracture resistance in comparison to the control group, as outlined in several studies [12, 134–137]. However, most studies indicate that electrical stimulation only initially outperforms the classically treated group [136, 138]. For instance, Masureik and Eriksson used DC currents of 10 and 20  $\mu$ A for healing of human jaw fractures for 10–14 days, employing platinum electrodes [138]. Although they were unable to determine a statistically reliable conclusion, their preliminary clinical study yielded some interesting implications: direct contact stimulation accelerated fracture healing right at the start of treatment. Nevertheless, the difference in fracture mobility between the treated and control group was small after a longer period of six weeks [138]. Note that this study from 1977 is to date the only available clinical study on application of electrical stimulation on the jaw.

Shandler et al. [135] treated relatively small bone defects of 6–8 mm in dog mandibles with an intermittent current ( $f = 0.7$  Hz) for three to five weeks. After three, four, and five weeks, the results showed that the stimulated side had superior healing outcomes compared to the control side. This is in contrast to the study by Masureik and Eriksson [138], where electrical stimulation only initially outperformed the classically treated group. Hakim et al. [137] conducted a study where they combined mandibular distraction osteogenesis in goats with the continuous application of direct current electrical stimulation (10  $\mu$ A). The findings showed an increase in bone growth and fracture resistance when compared with the control group. Zengo et al. [134] also studied the effects of direct current stimulation (3–5  $\mu$ A) in the mandible of beagles, where the electrodes were placed in intact bone without any defects. The study determined that new bone formed particularly around the cathode. On the other hand, increased bone resorption was observed at the anode. Additionally, platinum-iridium electrodes yielded higher rates of bone formation when compared to stainless

steel electrodes. The researchers attributed this finding to faradaic reactions that – in case of stainless steel electrodes – would “compete to some extent with any osteogenic response” [134]. Marino et al. [136] applied direct current stimulation ( $10\text{ }\mu\text{A}$  for two hours per day) to osteotomies ( $7\text{ mm} \times 2\text{ mm}$ ) in the mandibles of rabbits. The acceleration of healing was observed compared to the control group only when the stimulation was applied for four days after surgery, but not when it was applied for the entire investigated healing period of eight days [136].

Electrical stimulation for the treatment of critical-size mandibular bone defects is a relatively new concept, only carried out by Kim et al. thus far [11–13]. They examined the application of electrical stimulation in combination with growth factors to large bone defects in the mandible of rabbits, which served as a small animal model [12]. Two parallel gold electrodes were utilised with charge-balanced biphasic current pulses ( $20\text{ }\mu\text{A}$  amplitude,  $100\text{ }\mu\text{s}$  pulse length, and a frequency of  $100\text{ Hz}$  for 7 days). The researchers observed increased bone formation in the electrically stimulated animals. A few years later, the group of Kim conducted a similar experiment using the same stimulation parameters. However, this time, they used a liquid crystal polymer (LCP) outer box which is suitable for remaining in the body after regeneration [13]. Again, enhanced bone growth was observed in the electrically treated animals. Further, Kim et al. provided a numerical simulation depicting the space derivative of the electric field in the utilised stimulation setup. However, their study lacks details on the numerical analysis and the stimulation parameters were not numerically optimised.

To the best of my knowledge, there have not been any clinical studies investigating the electrical stimulation of large mandibular bone defects. The only study that has examined electrical stimulation in relation to bone defects in a human mandible was carried out by Kamegai et al. [139], who transplanted electrically stimulated periosteum from the tibia into a mandibular defect. Moreover, large animal models, like the minipig, have not yet been investigated for electrical stimulation of the mandible. Therefore, the objective of this thesis research is to fill this research gap by developing reliable electrostimulating implants for proof-of-concept studies in minipigs as a large animal model. The finite element simulation studies carried out are a crucial first step in preparing for *in vivo* experiments with minipigs, which may eventually ease the translation of this technology into clinical applications.

### 2.3.4 Open challenges in electrical stimulation of bone and numerical simulation of electrostimulating implants

Despite the abundance of commercially available electrostimulation devices [128], nevertheless widespread use among clinicians has not been established because clinical outcomes have been equivocal and therefore their efficacy cannot be confidently relied upon [110, 121]. Studies have shown that electrical stimulation is only clearly recommendable for certain orthopaedic indications [128] such as osteotomies and fractures [115]. Furthermore, specific limitations of previous clinical studies include

the heterogeneity of the devices and stimulation protocols used [110] and often the reported stimulation parameters are inconsistent and incomplete [110, 140]. Furthermore, a thorough analysis of the optimal stimulation parameters for the *in vivo* and clinical application of electrical stimulation is yet to be conducted [140]. While electrostimulating devices have been in use for many years in clinical settings, these limitations remain to be resolved. They need to be overcome to enable future evidence-based treatments, rather than continuing to rely on consensus-based approaches. This numerical study aims to develop more reliable electrostimulation devices by identifying optimal stimulation parameters. Combined with well-controlled randomised clinical trials, this will enable the evidence-based development of electrical stimulation implants in the future.

When developing electrostimulating implants for bone regeneration, numerical simulation is a useful tool in the design process as it allows possible stimulation setups to be tested and unfeasible designs to be eliminated at an early stage. Electrostimulating implants for a hip revision system have been developed and numerically optimised in previous literature [23, 141–143]. Additionally, dental implants which are electrically stimulating have been designed and examined *in vivo* [144] and *in silico* [145, 146]. It is worth noting that other groups have not considered large bone voids such as critical-size defects in the mandible in their numerical studies. In previous studies that formed the foundation of this thesis and that I will discuss in Sec. 5.5, preliminary numerical models of electrically stimulated human mandibles were presented [35, 36]. Considering electrostimulating fixation screws, different combinations of activated electrodes and fixation plate designs have been analysed regarding their feasibility for electrostimulation of the human mandible [35]. Using the finite element method, the electric field distribution for multiple implant designs was computed, and it was found that the insulation of the electrodes is a significant factor affecting stimulation impact and power consumption [35]. In another numerical study, different designs of stimulation electrodes were tested in a very simple (i.e. only considering cortical bone in a uniform background material) and preliminary numerical model of a human mandible [36]. The study compared two sites of stimulation: utilising either two fixation screws or one separate electrode for stimulation. The data indicates that additional research is essential to optimise the electrode location and stimulation voltage when using separate stimulation electrodes [36]. Therefore, this dissertation will focus on analysing the effects of different implant and model parameters and subsequently optimising the electric field distribution.

# Chapter 3

## Theoretical basics

This chapter presents the theoretical foundations necessary for the simulation of the electric field distribution of the electrostimulation implant developed in this thesis. It includes a brief description of the underlying electromagnetic field theory and applicable simplifications that are relevant to the specific stimulation frequency and material properties being considered in this thesis. Furthermore, the finite element method (FEM) is briefly introduced as the method of choice for the numerical simulation of the electric field distribution resulting from the electrostimulating implant.

### 3.1 Electromagnetic field theory

Maxwell's equations [147] describe the spatial and temporal evolution of macroscopic electromagnetic fields, forming the basis for determining the electric field distribution of the bioelectric problem presented here. Maxwell's equations in differential form can be stated as follows:

$$\nabla \times \mathbf{E}(\mathbf{r}, t) = -\frac{\partial \mathbf{B}(\mathbf{r}, t)}{\partial t}, \quad (3.1)$$

$$\nabla \times \mathbf{H}(\mathbf{r}, t) = \mathbf{J}(\mathbf{r}, t) + \frac{\partial \mathbf{D}(\mathbf{r}, t)}{\partial t}, \quad (3.2)$$

$$\nabla \cdot \mathbf{D}(\mathbf{r}, t) = \rho(\mathbf{r}, t), \quad (3.3)$$

$$\nabla \cdot \mathbf{B}(\mathbf{r}, t) = 0, \quad (3.4)$$

with the electric field strength  $\mathbf{E}$ , the electric displacement field  $\mathbf{D}$ , the magnetic flux density  $\mathbf{B}$ , the magnetic field strength  $\mathbf{H}$ , the current density  $\mathbf{J}$ , and the charge density  $\rho$ . Assuming that there are no impressed currents and no current of free electric charges, the current density reads

$$\mathbf{J}(\mathbf{r}, t) = \mathbf{J}_L(\mathbf{r}, t) = \sigma(\mathbf{r}, t)\mathbf{E}(\mathbf{r}, t), \quad (3.5)$$

where  $\sigma(\mathbf{r}, t)$  represents the electrical conductivity.



The relationship between the electric displacement field  $\mathbf{D}$  and the electric field  $\mathbf{E}$  in a medium is described by the constitutive equation

$$\mathbf{D}(\mathbf{r}, t) = \varepsilon(\mathbf{r}, t)\mathbf{E}(\mathbf{r}, t) = \varepsilon_0\varepsilon_r(\mathbf{r}, t)\mathbf{E}(\mathbf{r}, t), \quad (3.6)$$

with the vacuum permittivity  $\varepsilon_0$  and the relative permittivity  $\varepsilon_r(\mathbf{r}, t)$ . The dielectric material properties  $\varepsilon_r(\mathbf{r}, t)$  and  $\sigma(\mathbf{r}, t)$  are typically tensor quantities and may depend on both time and the field itself. However, in this thesis, I consider the studied material properties as both linear isotropic and time-invariant.

The electroquasistatic (EQS) approximation of Maxwell's equations has been utilised in this study. I will give only a very condensed overview of the subject, whereas the relevant literature, including [148–151], offers more detailed insights into the topic. The EQS approximation is based on two assumptions: the neglect of propagation effects and the neglect of inductive effects. These assumptions will be further elaborated in the following.

### Neglect of propagation effects

In this dissertation, a device for electrostimulation is designed that provides sinusoidal stimulation at a frequency of  $f = 20$  Hz. At such low frequencies, the electromagnetic fields can be described as slowly varying [149, 152]. More specifically, the wavelength of the fields corresponding to the given frequency is significantly greater than the typical dimension  $L$  of the object being modelled, which is approximately 0.1 m in this thesis. Consequently, the upper frequency limit for inhomogeneous matter can be expressed as [151]

$$\omega_q = \frac{1}{L\sqrt{\varepsilon_{\max}\mu}}, \quad (3.7)$$

where  $\varepsilon_{\max}$  is the maximum permittivity in the system under consideration.  $\mu$  is the permeability which can be assumed to be constant as  $\mu = \mu_r\mu_0$ , with the vacuum permeability  $\mu_0$  and the relative permeability  $\mu_r$ . For most biological tissues and related materials,  $\mu_r \approx 1$  applies. Thus, for the angular frequency  $\omega = 2\pi f$ , wave propagation effects can be disregarded when  $\omega \ll \omega_q$ .

### Neglect of inductive effects

Furthermore, to disregard magnetic induction or eddy currents, i.e.  $-\partial\mathbf{B}(\mathbf{r}, t)/\partial t \approx 0$ , the following condition must be fulfilled

$$\omega \ll \omega_q^2 \frac{\varepsilon_{\max}}{\sigma_{\max}}, \quad (3.8)$$

where  $\sigma_{\max}$  is the maximum conductivity in the system under consideration.

A general criterion for utilising the EQS approximation, which unifies the conditions of negligible wave propagation and magnetic induction, in time-harmonic applications

is given by

$$|kL| \ll 1 \quad \text{with} \quad k = \omega \sqrt{\mu\varepsilon \left(1 - j\frac{\sigma}{\omega\varepsilon}\right)}, \quad (3.9)$$

[152, 153] where  $k$  is the wave number.

As a consequence of neglecting magnetic induction, Eq. (3.1) becomes

$$\nabla \times \mathbf{E}(\mathbf{r}, t) = 0. \quad (3.10)$$

An implication of Eq. (3.10) is that the EQS electric field is a conservative vector field, meaning it is non-rotational. As a result, a scalar potential  $\varphi(\mathbf{r}, t)$  can be defined, such that

$$\mathbf{E}(\mathbf{r}, t) = -\nabla\varphi(\mathbf{r}, t). \quad (3.11)$$

For time-varying fields in general and for harmonic time-dependence (i.e. sinusoidal variation with time) in particular, the method of variable separation can be utilised. Subsequently, it is possible to solve for the Fourier transforms of the electromagnetic fields using the following ansatz:

$$\mathbf{E}(\mathbf{r}, t) = \text{Re}(\underline{\mathbf{E}}(\mathbf{r})e^{j\omega t}), \quad \mathbf{H}(\mathbf{r}, t) = \text{Re}(\underline{\mathbf{H}}(\mathbf{r})e^{j\omega t}). \quad (3.12)$$

$\underline{\mathbf{E}}(\mathbf{r}) = \mathbf{E}(\mathbf{r})e^{j\phi}$  is the complex amplitude or phasor with the phase angle  $\phi$  and the imaginary unit  $j$ .

Inserting the phasor formulation into Maxwell's equations and considering Eq. (3.10) results in:

$$\nabla \times \underline{\mathbf{E}}(\mathbf{r}) = 0, \quad (3.13)$$

$$\nabla \times \underline{\mathbf{H}}(\mathbf{r}) = \underline{\mathbf{J}}(\mathbf{r}, \omega) + j\omega\underline{\mathbf{D}}(\mathbf{r}), \quad (3.14)$$

$$\nabla \cdot \underline{\mathbf{D}}(\mathbf{r}) = \underline{\rho}(\mathbf{r}), \quad (3.15)$$

$$\nabla \cdot \underline{\mathbf{B}}(\mathbf{r}) = 0. \quad (3.16)$$

Equations (3.13) and (3.15) are known as the fundamental EQS equations because  $\underline{\mathbf{E}}$  can be uniquely determined using only them.

Starting from Ampere-Maxwell's law (Eq. (3.14)), taking the divergence of both sides, and utilising Eq. (3.11) and the constitutive relations Eqs. (3.5) and (3.6), the complex Laplace equation is obtained, which resembles the EQS approximation of Maxwell's equations

$$\nabla \cdot \left( [\sigma(\mathbf{r}, \omega) + j\omega\varepsilon_0\varepsilon_r(\mathbf{r}, \omega)] \nabla \underline{\varphi}(\mathbf{r}) \right) = 0. \quad (3.17)$$

This elliptic partial differential equation is solved to obtain the complex electric potential  $\underline{\varphi}(\mathbf{r})$ . Further information on the derivation of Eq. (3.17) can be retraced in publications such as [148, 152, 153].

The expression  $\sigma(\mathbf{r}, \omega) + j\omega\varepsilon_0\varepsilon_r(\mathbf{r}, \omega) = \sigma^* = \sigma' + j\sigma''$  in Eq. (3.17) refers to the complex conductivity  $\sigma^*$ , with the real (conductive) part  $\sigma' = \sigma$  and the imaginary (capacitive) part  $\sigma'' = \omega\varepsilon_0\varepsilon_r$ . In case of

$$\omega\varepsilon_0\varepsilon_r/\sigma \ll 1, \quad (3.18)$$

further simplifications are possible and capacitive effects can be neglected by disregarding the displacement current density  $\mathbf{J}_D(\mathbf{r}, t) = \partial\mathbf{D}(\mathbf{r}, t)/\partial t \approx 0$ . As a result, Eq. (3.17) can be simplified to a quasi-stationary current problem (QS)

$$\nabla \cdot (\sigma(\mathbf{r}, \omega) \nabla \varphi(\mathbf{r})) = 0. \quad (3.19)$$

Note that in this instance, the electric potential  $\varphi(\mathbf{r})$  is real-valued. Nevertheless, consideration of the electrode-tissue interface (Sec. 4.2.2) again results in a complex-valued electric potential  $\underline{\varphi}(\mathbf{r})$ .

In a homogeneous domain, the electric potential resulting from a space charge distribution is given by

$$\varphi(\mathbf{r}) = \frac{1}{4\pi\varepsilon_0} \iiint_V \frac{\rho(\mathbf{r}')}{|\mathbf{r} - \mathbf{r}'|} dV', \quad (3.20)$$

with integration over all charges in the space  $V$  [154]. Equation (3.20) implies that with increasing distance  $|\mathbf{r} - \mathbf{r}'|$  from the field source the electric potential and hence the electric field strength decreases. This allows for simplification of the model by neglecting details in the geometry outside the region of interest (ROI), as demonstrated in Sec. 4.2.1.

## 3.2 Finite element method

With the increased computing power in recent decades, computer-aided computational methods have become commonplace in engineering and the natural sciences. Partial differential equations and ordinary differential equations can describe the majority of physical phenomena. Nevertheless, when presented with highly complex geometries and boundary conditions, such as those found in biological tissues, an exact analytical solution is often not possible, necessitating the use of an approximate numerical solution. Moreover, numerical simulations hold great significance in research areas where experimental data are unavailable or difficult to obtain. The finite element method (FEM) is a numerical technique for the approximate solution of partial differential equations. This approach involves subdividing the computational region into a

finite number of smaller parts, called *elements*. Generally, in FEM the partial differential equations of the model problem are transformed into a system of linear ordinary equations that can be solved numerically. This method facilitates the analysis of complex geometries, such as the electrically stimulated minipig mandible considered in this thesis, and provides an approximate solution for the resulting field distribution. Moreover, FEM permits a resource-efficient design optimisation of the electrostimulating implant, which is also under examination.

The general steps to be considered in the FEM are:

- discretise the model geometry, i.e. divide it into smaller sub-domains;
- approximate the solution through expansion into a set of basis functions;
- apply the weighted residual method, i.e. minimise the residual in variational sense and choosing appropriate weighing functions;
- solve the resulting set of equations for the unknowns.

These steps are further elaborated in the subsequent sections. However, as this work involves the use of a well-established commercial FEM software rather than the development of numerical methods, I will only give a very brief overview of the concept of FEM. Additional information on FEM in general and in electromagnetics can be found in textbooks such as [155–157].

### 3.2.1 Domain discretisation

The fundamental concept of FEM is to decompose the problem domain to be analysed into smaller subdomains of simple geometry and finite size [159], the so-called *elements*. On these finite elements, the equations introduced in Sec. 3.1 are solved approximately. The choice of the shape of the elements depends on the dimension, the specific problem, and other factors. For instance, in simulations of structural mechanics, rectangular (2D) or hexahedral (3D) elements are frequently employed (Fig. 3.1). There are approaches in biomedical FEM modelling, particularly in the field of neuroscience, where the hexahedral finite element mesh is generated directly from the cubic voxel magnetic resonance imaging (MRI) data [160]. This approach requires high-resolution image data for accurate modelling [161]. In contrast, when modelling and simulating biological structures that are not solely based on MRI or CT data, such as in this thesis, tetrahedral elements are usually utilised due to their ability to discretise highly irregular geometries effectively. As a result, they lead to accurate approximations of the true solution, particularly when selecting higher order or curved elements. The elements contain a number of points, the so-called *nodes*. The number of nodes depends on the type and the order of the element. For instance, first-order (linear) Lagrange elements have one node located at each corner of the element (Fig. 3.1 (a)). Second-order (quadratic) Lagrange elements contain additional nodes at the midpoints of the edges, sides, or the centre of the element, depending on the specific element type, see Fig. 3.1

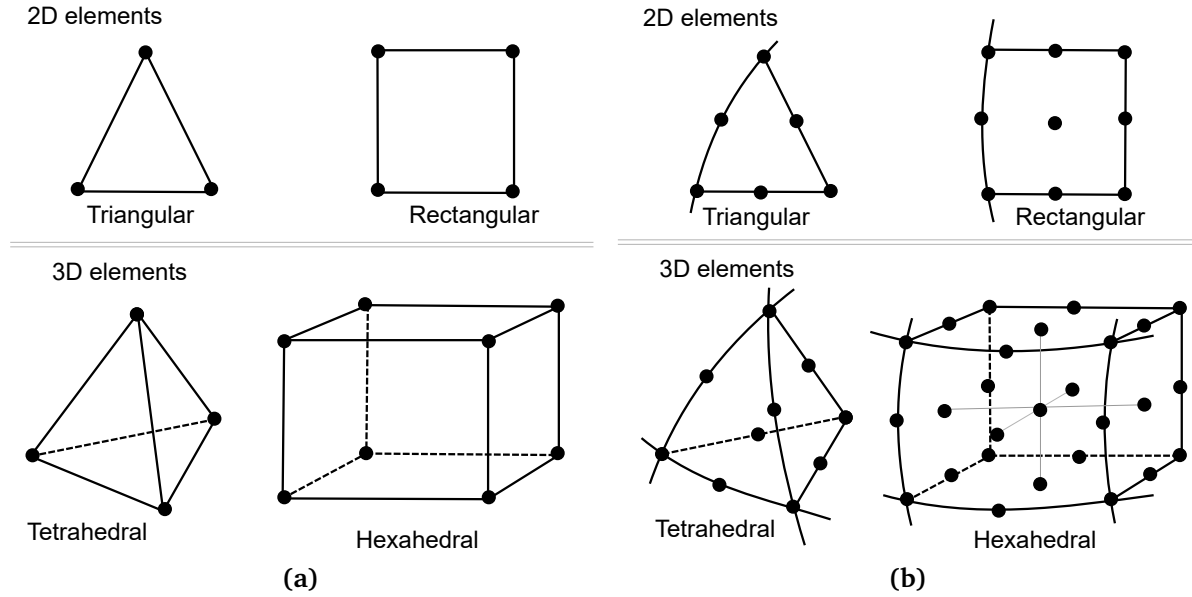


**Figure 3.1:** Examples of (a) linear and (b) quadratic Lagrange elements. The edges of higher order elements might be curved to better represent the geometry as indicated in (b). The figure is redrawn with permission from [158].

(b). By allowing for a more precise approximation of curved geometries, they offer a greater degree of accuracy. A further improvement in approximation of the solution is possible by employing curved mesh elements, i.e. elements capable of resolving the curved model boundary better than straight elements. When utilising the same order for both the geometry representation and the solution representation, e.g., second order as in this study, the elements are referred to as isoparametric.

### 3.2.2 Selection of basis functions

In a second step of the FEM analysis, the approximate solution  $\tilde{\varphi}(\mathbf{r})$  of the unknown electric potential, which is considered in this work, is described piecewise on each of the elements with the help of basis functions  $\psi_i(\mathbf{r})$ :

$$\underline{\varphi}(\mathbf{r}) \approx \tilde{\underline{\varphi}}(\mathbf{r}) = \sum_{i=1}^n f_i \psi_i(\mathbf{r}). \quad (3.21)$$

The basis functions  $\psi_i(\mathbf{r})$  are low-order polynomials that approximate the unknown solution within an element.  $f_i$  represent the unknown coefficients, while  $n$  is the number of nodes in the element. The value of the unknown function at each location within the element is related to the corresponding value  $f_i$  at the nodes by means of the polynomial basis functions  $\psi_i(\mathbf{r})$ . The basis functions are defined at each node of the element. They are non-zero only within the elements that are connected to the corresponding node, and they vanish outside of these elements [157]. The order of the

basis functions represents a compromise between the precision of the calculations and the required computing and memory resources. When using curved elements like in this study, higher-order basis functions are necessary. In this work, the objective is to compute the scalar electric potential  $\varphi(\mathbf{r})$  and therefore quadratic nodal Lagrange basis functions on tetrahedral elements have been used. Other physical quantities, such as the electric field norm, are calculated from this potential in a post-processing step.

### 3.2.3 Formulation and solution of the system of equations

After the discretisation, the system of equations that is to be solved must be formulated. In this work, the Galerkin method is chosen, which belongs to the family of weighted residual methods [159] and the minimum of the residual in a variational sense is determined. The weighing functions  $w_j$  are used to set the weighted average of the residual to zero. In the Galerkin method, these functions are identical to the basis functions ( $w_j(\mathbf{r}) = \psi_j(\mathbf{r})$ ). It should be noted that within the framework of the Galerkin method the determined minimum value denotes the physically exact solution corresponding to the state of minimum energy. The matrix representation of the resulting linear system of equations is as follows

$$\mathbf{A}\mathbf{f} = 0, \quad (3.22)$$

with the  $N \times N$  matrix  $\mathbf{A}$  which is complex-symmetric in the case of the full EQS case (Eq. (3.17)), with  $N$  being the total number of nodes.  $\mathbf{f}$  is the unknown  $N \times 1$  vector containing the  $f_i$  (here corresponding the degrees of freedom of the electric potential  $\varphi(\mathbf{r})$ ). Before solving the system of equations appropriate boundary conditions must be defined. For example, Dirichlet boundary conditions may be used to specify the function values at the boundary of the domain  $\Omega$ , whilst Neumann boundary conditions may specify the derivative of the function [159]. Further details on the particular boundary conditions employed in this study are available in Sec. 4.2.3.

The resulting set of equations is solved numerically using either direct or iterative methods. Direct methods include decomposition methods, such as LU decomposition, which transforms the system matrix into a triangular form [149]. The use of direct solvers is typically a very robust approach that can handle even highly ill-conditioned problems. However, they can be associated with high memory consumption and increased computational time when the number of unknowns is very large, e.g., in the order of a few million as in the model in this thesis. For this reason, direct methods are not used in this work. Iterative methods, on the other hand, start with an estimate of the solution to the unknowns. The solution is then gradually approached until a specified solution tolerance is met. The main advantage of iterative solvers is their memory consumption, which is significantly lower than that of direct solvers for problems of the same size. In addition, FEM yields sparse system matrices (i.e. most of the matrix elements are zero), which makes iterative solvers further suitable. More information

on solution methods and algorithms can be found in textbooks such as [149, 157, 162]. The specific solvers used in this thesis are introduced in Sec. 4.2.4.

In the subsequent chapter, the methods for setting up a bioelectric model will be presented. It is imperative to accurately model the dielectric properties of bone and adjacent tissues to achieve maximal regenerative effects while creating electrical stimulation devices. Therefore, the following section introduces the dielectric properties of biological tissues used in modelling mandible electrical stimulation in the minipig.

## Chapter 4

# Dielectric properties and numerical simulation of bioelectric problems including model uncertainties

The accurate and dependable modelling and simulation of the electric field distribution in a bioelectric model are of significant importance in the development of electrostimulating implants. The following chapter introduces the dielectric properties of biological tissues and bone in particular, which are essential for ensuring accurate simulations of the electric field distribution in the minipig mandible model. I will begin by providing an overview of the characteristics of the dielectric properties of biological tissues and their modelling in the literature. Current research indicates the requirement for corrective measures concerning the commonly-used tissue database. Consequently, the implications of this finding for the modelling of the dielectric properties of bone in this thesis will be explained. Furthermore, I will give an overview of the current state of knowledge on the dielectric properties of bone found in the literature, illustrating the wide range of the values for conductivity and relative permittivity. The modelling workflow used to create the simulation model of the electrically stimulated minipig mandible will also be outlined, building upon the aforementioned overview. This workflow involves several steps, whereby the dielectric tissue properties are considered essential for setting up a reliable model. Lastly, I will present the basic principles of uncertainty quantification (UQ) as a tool to evaluate the influence of variations in the input quantities such as the dielectric tissue properties, which, as mentioned above, have been shown to vary widely.

### 4.1 Dielectric properties of biological tissues

The dielectric properties describe the response of a material to an applied electric field. The conductivity  $\sigma$  and the permittivity  $\varepsilon$  relate to the conduction and polarisation currents, respectively, induced by an electric field that acts on free and bound charges. Biological tissues possess a complex structure, leading to multiple relaxation times and causing the behaviour of their dielectric properties to be highly frequency-dependent. In



an idealised view, the permittivity of tissue subjected to an alternating current stimulus decreases in three major steps with increasing frequency. These steps are referred to as the alpha, beta, and gamma dispersion [163] and are illustrated in Fig. 4.1. The

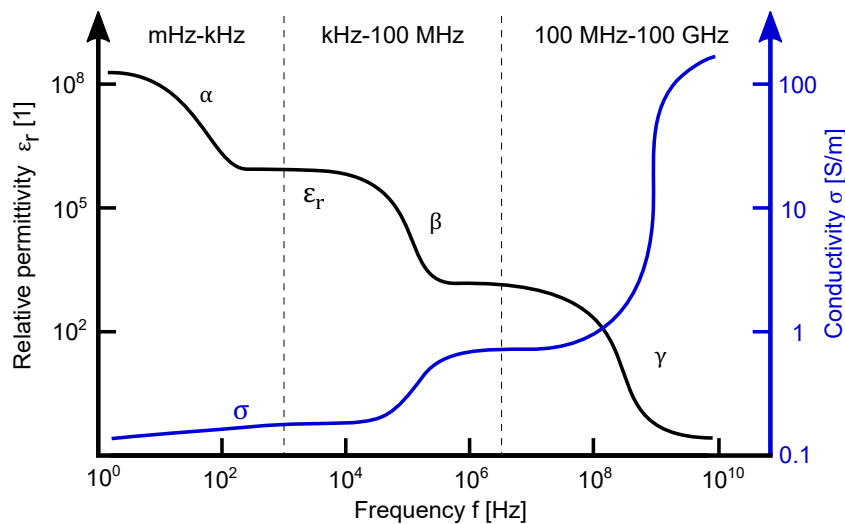


**Figure 4.1:** Schematic representation of the alpha, beta, and gamma dispersion in biological tissues based on [164]. Note that the actual location and extent of the dispersions depends on the specific tissue.

alpha dispersion occurs in the low-frequency regime (mHz–kHz) and is caused, e.g., by ion-counterion diffusion effects at the cell surface [165, 166]. Nonetheless, the origin of the alpha dispersion is still not fully understood and remains subject of ongoing research and debate [167]. For a detailed discussion see also [30]. The beta dispersion is present in the kHz–100 MHz regime and is predominantly caused by the capacitive charging of cell membranes [166, 168]. The gamma dispersion (100 MHz–100 GHz) arises due to dipolar reorientation effects in polar media such as water [166]. The precise location of the steps depends on the specific tissue. Other dispersions, such as the delta dispersion in the lower GHz range, may also occur [27, 166]. In the case of bone, the dielectric properties derived from experimental data and the number and location of the dispersions differ significantly. After a brief and critical review of the widely-used database of Gabriel et al. for modelling the dielectric properties of biological tissues, examples are given in Sec. 4.1.2.

#### 4.1.1 Ambiguities in the Gabriel data and their correction

Many studies on modelling and simulation of electrically stimulated bone [23, 143, 145, 169–178] have employed the literature values of Gabriel et al. [29, 179] (in the following referred to as the “Gabriel data”) for the dielectric properties of bone. However, it should be noted that the Gabriel data for the dielectric properties of bone at low frequencies have not been directly measured but have been derived from a parametric model. The Cole-Cole model [180] is frequently used to describe dielectric

materials that exhibit different relaxation times over a wide frequency range. Gabriel et al. utilised a four-pole Cole-Cole dispersion model by fitting it to experimental data gathered from numerous studies, including ovine, bovine, and human bone samples. For a comprehensive review of the dielectric properties in biological tissues and their modelling, the publications by Gabriel et al. [27–29] provide the reader with useful insights. Recently, Zimmermann and van Rienen [30] have suggested that there may be some ambiguity in the dielectric properties of tissues as measured and modelled in the widely-used Gabriel database. The authors debate whether the assumed Cole-Cole model with four dispersions correctly describes the sole tissue behaviour or whether the data actually also include contributions from the electrode-tissue interface (ETI), especially at lower frequencies [30]. Effects at the ETI such as electrode polarisation often either mask or are erroneously interpreted as the alpha dispersion [165]. Zimmermann and van Rienen suggest omitting the lower-frequency dispersions and utilising an equivalent circuit model to account for the ETI [30]. This correction reduces the relative permittivity – which is for some tissues, including bone, in the order of  $10^6$  and higher in the studies of Gabriel and others [29, 181] – by several orders of magnitude and leads to an almost frequency independent conductivity in the low frequency range [30]. Furthermore, electrode polarisation is present at frequencies up to 10 kHz and beyond [166]. Multiple studies that corrected their data for electrode polarisation provide evidence for the suggested correction, demonstrating that at low frequencies ( $< \text{approximately } 10 \text{ kHz}$ ) the impedance of biological tissues is mainly resistive [30, 182, 183]. Similarly, studies investigating the dielectric properties of bone in particular have found that the conductivity remains constant at low frequencies [184–186].

The outlined ambiguity in the interpretation of the dielectric tissue properties at low frequencies has two consequences for this thesis. Firstly, it is crucial to demand that electrode processes are taken into account when considering the dielectric properties of biological tissues from the literature. In the following section, I will therefore examine the relevant literature on the dielectric properties of bone and address this issue. Secondly, it is important to consider the two possible interpretations suggested by Zimmermann and van Rienen. Accordingly, I will present the specific choices for modelling the dielectric tissue properties in two case scenarios in my numerical model in Sec. 4.2.2.

#### **4.1.2 Literature review: reliable studies reporting the dielectric properties of bone**

Studies have shown that the DC conductivity of bone is roughly proportional to the conductivity of the surrounding fluid, indicating that the conductivity is primarily influenced by the fluid-filled canals within the bone [187]. Nevertheless, given the complex structure and anisotropy of bone, its dielectric properties also rely heavily on various other factors. These factors include species [27, 188], age [189–192], the spe-

cific anatomical location [193], and health conditions such as osteoporosis [194, 195]. Furthermore, the measured dielectric properties depend on the experimental conditions, such as *in vivo* or *ex vivo* measurements [196], temperature [197–199], measurement setup [188], and condition of the samples [188, 200]. This work aims to create a numerical model that closely reflects reality. For this purpose, an extensive review of the available literature on the measurements of the dielectric properties of bone has been carried out. The objective of this review was to identify reliably measured dielectric properties of bone and obtain a comprehensive overview of the range of these properties. The literature research involved examining studies from 1964 to 2021 that considered near-*in-vivo* physiological conditions during the measurements. Consequently, measurements were required to be performed at or close to body temperature ( $T \approx 37^\circ\text{C}$ ) using fresh or *in vivo* samples. It is expected that utilising *in vivo* or freshly excised bone yields more accurate conductivities owing to the presence of vascular tissue and fluids in the bone pores [201]. Several studies were excluded due to their use of *ex vivo*, previously frozen, or long-stored samples or their operation at room temperature (e.g., [181, 193, 198, 202–210]). Due to the low-frequency application considered

Study	bone type	species	frequency range	samples	T [ $^\circ\text{C}$ ]
Tang et al. [201]	cort. & canc.	human	1 Hz–4 MHz	fresh	36.5 $^\circ\text{C}$
Smith and Foster [211]	cort.	rat	1 kHz–13 MHz	fresh	37 $^\circ\text{C}$
Balmer et al. (2016) [184]	canc.	ovine	<1 kHz	<i>in vivo</i>	BT
Balmer et al. (2018) [185]	cort. & canc.	bovine	1 kHz–13 MHz	fresh	BT
Kosterich et al. [187]	cort.	rat	10 Hz–100 MHz	fresh	37 $^\circ\text{C}$

**Table 4.1:** Experimental studies on measuring the conductivity of bone tissue that fit the scope of this work. BT: body temperature. Note that only the studies of Kosterich et al. [187] and Smith and Foster [211] also reported the relative permittivity (for cortical bone). No acceptable study reporting the relative permittivity for cancellous bone was found.

in this work, only studies considering measuring frequencies  $\leq 10\text{ kHz}$  were included. Moreover, differences in results between studies may also be due to electrode polarisation effects at low frequencies which are not easy to compensate for [212]. Therefore, I require the studies to adequately correct for electrode polarisation at low frequencies. Thus, only five out of the original pool of forty-one studies met the aforementioned criteria (refer to Table 4.1). All of these studies employed measures to correct for the ETI in a two-electrode setup (Kosterich et al. [187], Smith and Foster [211], Balmer et al. (2016) [184], Balmer et al. (2018) [185]) or four-electrode setup (Tang et al. [201]). The dielectric properties from the aforementioned studies are displayed in Figs. 4.2 and 4.3. In addition, the Gabriel data [179, 213] are included for comparison purposes. It is noteworthy that Gabriel et al. measured the dielectric properties of bone within the frequency range of 1 MHz–20 GHz. The Gabriel data below 1 MHz are

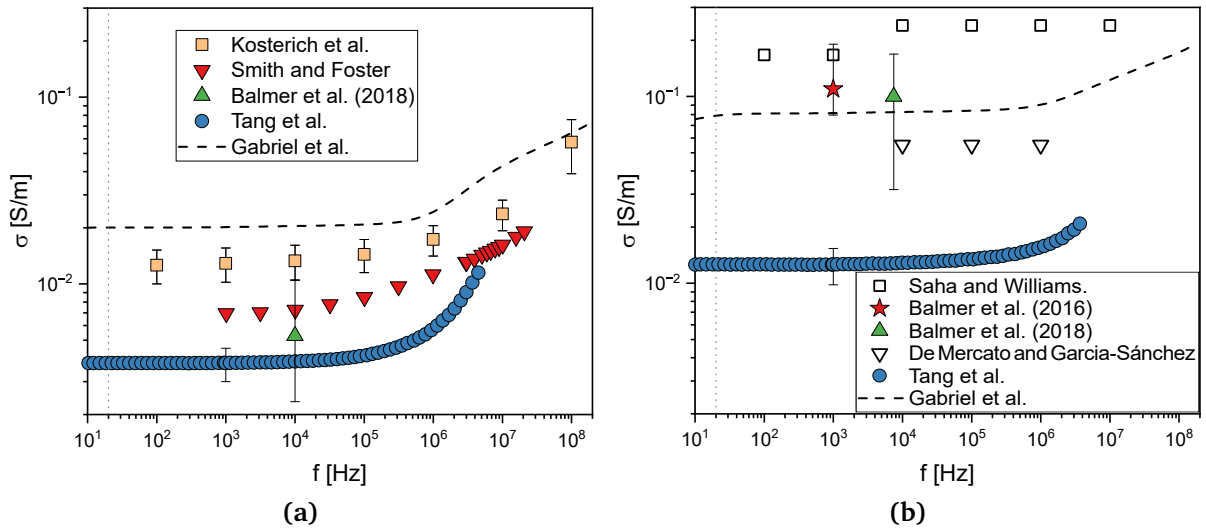


**Figure 4.2:** Electrical conductivity  $\sigma$  of (a) cortical and (b) cancellous bone according to literature that fits the scope of this work (Kosterich et al. [187], Smith and Foster [211], Balmer et al. [184, 185], Tang et al. [201]) and the widely-used Gabriel data [29] for comparison. Note the large discrepancies between the conductivity values reported in different studies. Note that in (b) additionally the data of Saha and Williams [207] and De Mercato and Garcia-Sánchez [205] are shown, which serve as the basis for the parametric Gabriel model at low frequencies. However, they do not meet the requirements formulated in this thesis. The vertical dotted line denotes  $f = 20$  Hz.

based on fitting the measured values from other studies [187, 204, 205, 207, 211] to the parametric four-pole Cole-Cole model.

No suitable data regarding the relative permittivity of cancellous bone was found in the literature. Instead, Fig. 4.3 (b) depicts the experimental data of De Mercato and Garcia-Sánchez [205] and Saha and Williams [207], which serve as the basis for the Gabriel model at lower frequencies. It should be noted that the latter studies typically have limitations such as measurement at room temperature, no consideration of electrode polarisation, or use of frozen samples. Experimental error bars are included if provided in the original study.<sup>1</sup>

Generally, it can be observed that the absolute values of the measured conductivities vary widely in the literature (see Fig. 4.2). Specifically, for cortical bone, the values of the electrical conductivity at frequencies below 1 kHz range from 0.0038 S/m (Tang et al. [201]) to 0.013 S/m (Kosterich et al. [187]). Notably, the Gabriel data show even significantly higher values of 0.02 S/m [29]. For cancellous bone, electrical conductivity values at low frequencies span between 0.013 S/m (Tang et al. [201]) and 0.11 S/m (Balmer et al., 2016 [184]). The Gabriel data fall within this range with 0.08 S/m [29]. These large differences in conductivity may be due to different anatomical origins of

<sup>1</sup>Note that for Kosterich et al. [187] standard errors were given, while the bars for Tang et al. [201] and Balmer et al. [184, 185] display the minimum and maximum range of values obtained.

the samples or different experimental conditions such as the treatment of the sample, or the choice of immersion fluid [201]. Specifically, a small level of saline on the sample surface may enable a shunting effect that leads to the measurement of higher conductivities [201]. Furthermore, the values given for cancellous bone by Tang et al. [201] are from measurements on trilayered skull bone. This type of bone sample contains both cortical and cancellous bone, which results in much lower conductivities compared to values obtained by other authors for completely cancellous bone. Even within the measured values of the same study there can be large variations in the measured data. For example, cancellous samples with a range of bone densities were measured by Balmer et al.. They found significant correlation between bone density and the measured conductivity [184, 185]. Additionally, Fig. 4.2 demonstrates a conductivity that remains almost constant below frequencies of 10 kHz in studies that account for ETI effects. In the Gabriel data, on the other hand, there is a slight decrease in conductivity that is most pronounced for cancellous bone, see Fig. 4.2 (b).

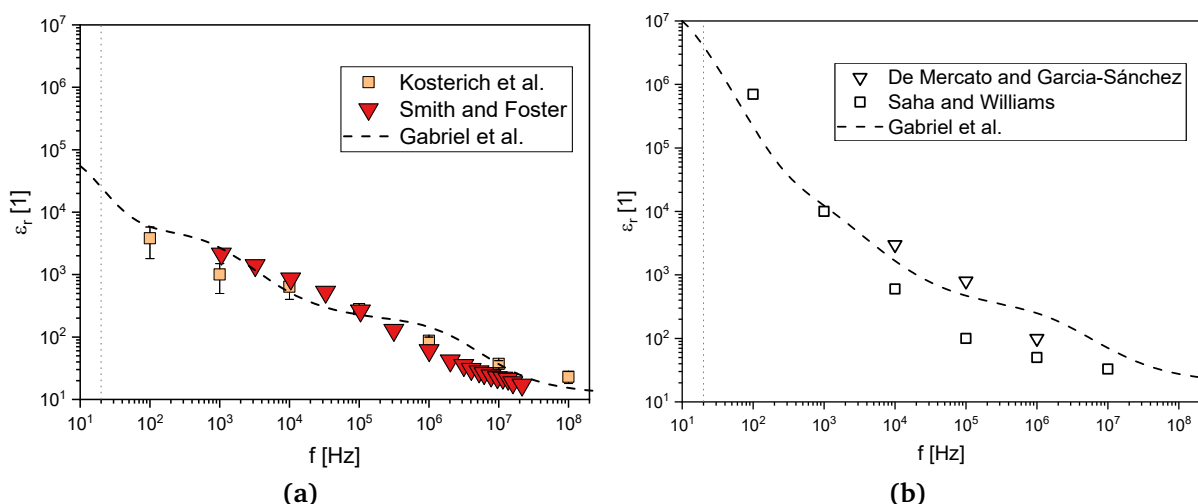


**Figure 4.3:** Relative permittivity  $\epsilon_r$  of (a) cortical and (b) cancellous bone according to literature that fits the scope of this work (Kosterich et al. [187], Smith and Foster [211]). Note that the data of De Mercato and Garcia-Sánchez [205] (measured at room temperature) and Saha and Williams [207] (frozen samples,  $T = 27^\circ\text{C}$ ) do not fully meet the requirements set for usable data. The vertical dotted line denotes  $f = 20$  Hz.

Concerning the relative permittivity of cortical bone, according to the accepted literature, values ranging in the thousands have been reported at frequencies of  $f = 100$  Hz and  $f = 1$  kHz by Kosterich et al. [187]) and Smith and Foster [211] (Fig. 4.3 (a)). The Gabriel data indicate slightly higher values, with a relative permittivity of 25100 at a frequency of 20 Hz. The relative permittivity of cancellous bone (shown in Fig. 4.3 (b)) obtained from ambiguous sources is several orders of magnitude higher in the low-frequency regime, with values of  $\epsilon_r(f = 100 \text{ Hz}) = 7 \cdot 10^5$  (Saha and Williams [207]) and  $\epsilon_r(f = 20 \text{ Hz}) = 4 \cdot 10^6$  (Gabriel et al. [29]). It is unclear whether the observed high relative permittivities are realistic or if they may be a result of an improper mea-

surement setup or uncorrected electrode processes [30]. This pronounced lack of dependable data for cancellous bone and the unavailability of mandibular or minipig bone in any of the reviewed or selected studies motivated a separate measurement. Therefore, the dielectric properties of the mandibular bone of minipigs were measured within the scope of the SFB 1270 ELAINE. Even though these measurements were not ideal due to the use of *ex vivo* and frozen samples,<sup>2</sup> they allow a general assessment of the dielectric properties of minipig mandibular bone. The measurement and analysis is described in Sec. 5.1.

## 4.2 Modelling workflow for the generation of the minipig mandible simulation model

*Parts of this chapter and the corresponding results presented in Sec. 5.2 are based on my publication “Establishment of a numerical model to design an electrostimulating system for a porcine mandibular critical-size defect” [34], which appeared in Applied Sciences.<sup>3</sup> Substantial changes with regard to the publication are addressed in the corresponding sections.*

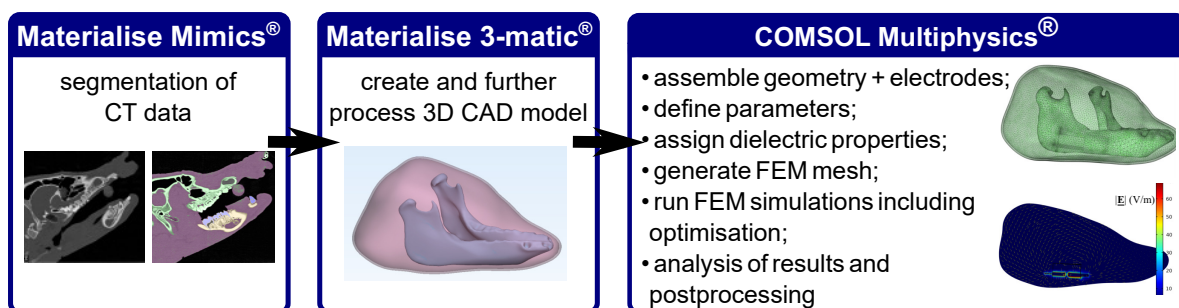


**Figure 4.4:** Schematic process and involved software for generating a numerical model of the electrically stimulated minipig mandible based on computer tomography (CT) data. The involved steps include segmentation of the CT data (left), modelling the 3D computer-aided design (CAD) model of the mandible and surrounding tissues (middle), assembling the tissue model and the electrodes, and setting up the finite element method (FEM) model (right).

To perform a numerical analysis of the electric field distribution stimulated by an electrostimulating implant in an irregular geometric structure such as the lower jaw, a

<sup>2</sup>Regrettably, an improved measurement setup was not available during the completion of this thesis.

<sup>3</sup>Ursula van Rienen, Peer W. Kämmerer, Rainer Bader, and I conceptualised this study. I carried out the modelling, all simulations and the data analysis, prepared the visualisation of the data and wrote the initial draft of the manuscript. Ursula van Rienen, Peer W. Kämmerer, and Rainer Bader supervised the project, acquired the funding, provided methodological guidance, and provided all resources. The data for the published study is available online <https://purl.uni-rostock.de/rosdok/id00002450>.

three-dimensional model of the relevant anatomical region is required. Furthermore, it is necessary to specify the dielectric properties of bone and the surrounding tissues in the considered anatomical region along with appropriate boundary conditions. This enables the simulation of the electric field distribution and the derivation of stimulation parameters required for optimal stimulation success. The steps required to establish a bioelectric numerical model of electrically stimulated biological tissues [106, 214] are outlined below. These steps comprise:

- setting up the anatomical and technical model, i.e. segmenting computer tomography (CT) data and subsequently conducting computer-aided design (CAD) modelling based on the segmentation (Fig. 4.4 (left, middle)). Additionally, modelling of the electrodes and reconstruction plates and screws (if applicable) is undertaken;
- setting up the physical model by assigning the dielectric properties to the anatomical and technical models while also modelling the ETI through an equivalent circuit model (Fig. 4.4 (right));
- setting up the corresponding boundary value problem by defining the required equations for simulating the electric field distribution;
- solving the boundary value problem numerically.

The general steps outlined here are described more comprehensively and specifically with reference to the minipig mandible model in the following sections.

### **4.2.1 Anatomical and technical modelling of the electrically stimulated mandible**

The geometrical model that is subject to the finite element studies was built up from the results of two modelling steps: firstly the anatomical modelling, i.e. creating the model of the defective minipig mandible and its surrounding tissue; secondly, the technical modelling, where technical components like the electrostimulating implant or osteosynthesis plates and screws are created.

#### **Anatomical modelling of the minipig mandible with surrounding tissues**

The anatomical modelling of the minipig mandible was based on CT data of a 17-month-old male Göttingen minipig, as shown in Fig. 4.5 (a) and (b). The CT data consisted of 442 slices, each with  $512 \times 512$  pixels and a pixel spacing of approximately 0.39 mm. The slice thickness was 1 mm and the spacing between the slices was 0.5 mm. By assigning certain thresholds of grey values to the respective biological tissues (namely cortical bone, teeth, and soft tissue – see Fig. 4.5 (c)), the data was segmented to create an initial rough anatomical model (Fig. 4.5 (d)). The image processing software



Materialise Mimics® version 19 was utilised for this purpose. One component of the

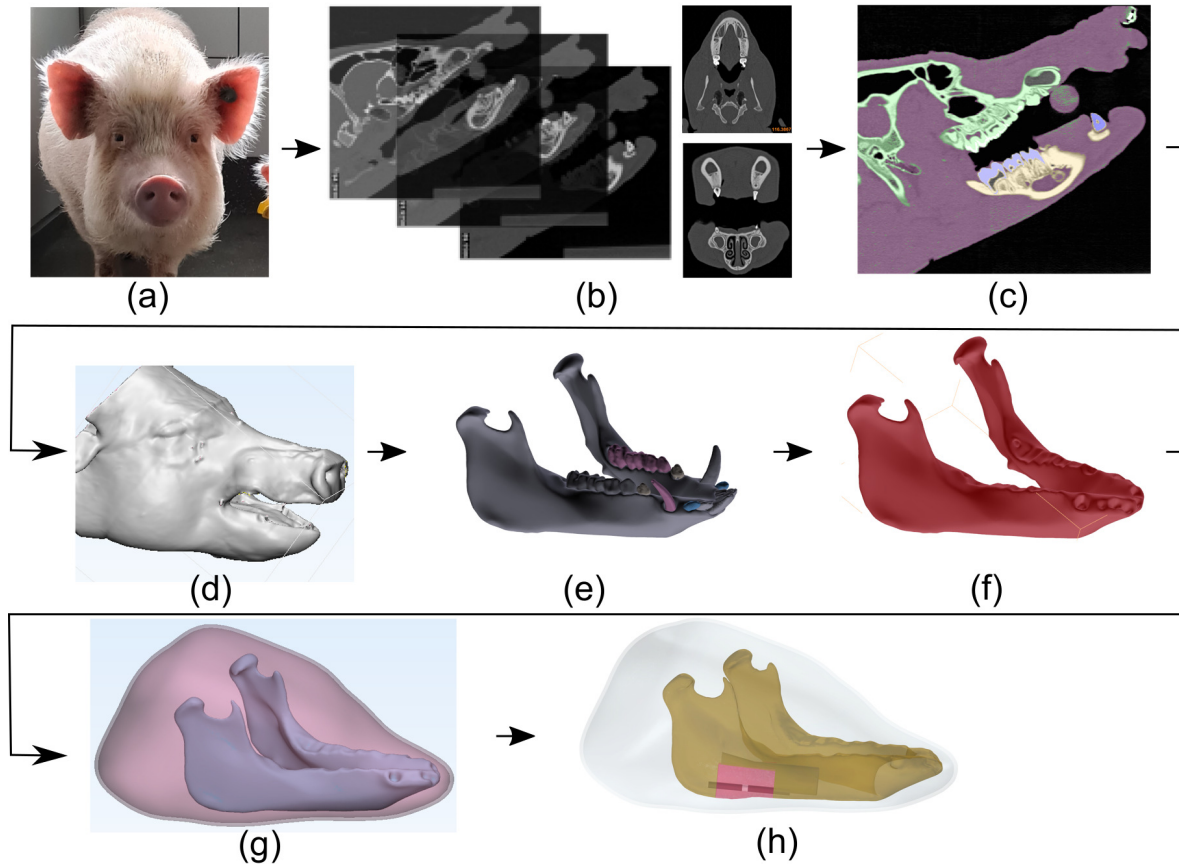


**Figure 4.5:** Workflow for creating the 3D model of a minipig mandible. The process starts with computer tomography (CT) data (b) of a minipig (a). The CT data are then segmented (c), assigning various grey values to different tissues (mandible bone: yellow, teeth: blue, soft tissue: violet, remaining bone: green). Subsequently, a preliminary model of the soft tissue domain (d) and the mandible (not visible) is obtained, which is then further processed and smoothed. The upper part of the head and details of the head are removed. The smoothed mandible still contains teeth (e), which are removed in a further step (f). The preliminary anatomical CAD model is shown in (g), with the mandible bone surrounded by a simplified soft tissue domain and an additional outer layer representing the skin. (h) presents the final 3D model, which includes the anatomical model supplemented by a generic cancellous bone domain and the critical-size defect (highlighted in red), along with the technical model, i.e. the bipolar electrostimulating implant.

anatomical model comprises the mandible bone from which the teeth (Fig. 4.5 (e)) were subtracted. This was done to avoid unnecessarily small details in the geometry, which could lead to problems during the simulation, e.g., due to singularities. This simplification is valid since the field amplitude can easily be estimated to be well below the stimulation threshold in the neighbourhood of the teeth (compare Eq. (3.20)). The resulting coarse anatomical model (stereolithography (STL) file) was imported



into the CAD software Materialise 3-matic® version 11 (Materialise, Leuven, Belgium. <https://www.materialise.com>) to be further processed. The modifications included manually filling larger holes in the geometry object resulting from subtraction of the teeth, wrapping (i.e. automatically filling smaller holes and creating a “watertight” model), smoothing of the surface, and removing other geometric artefacts such as spikes, double or intersecting triangles, and sharp triangles (Fig. 4.5 (f)). The latter modifications were executed automatically using the *Fix Wizard* of Materialise 3-matic®. Furthermore, the surface underwent manual local smoothing to remove additional unwanted and unrealistic geometric features such as small bumps and unevenness of the surface. Finally, the number of triangles describing the STL object was reduced, while preserving the mesh quality.

The tissue domain representing the mucosa was created analogously: first, the coarse STL file resulting after segmentation (Fig. 4.5 (d)) was imported into Materialise 3-matic® and the ears and the upper part of the minipig head were removed to reduce unnecessary computational costs in the later simulations. Notably, the electric fields in this case can also be considered negligible with respect to the stimulation threshold. Next, the wrapping, smoothing, and repairing process was carried out analogously to the bone geometry. As the skin could not be reliably identified on the CT images, an outer shell of uniform thickness was modelled instead. To generate the skin domain, the *hollow* function of Materialise 3-matic® was used to create a shell with a uniform thickness of 2.28 mm equivalent to the skin thickness of the back of a six-months-old minipig [215]. The mucosa and skin objects were uniformly remeshed with a desired edge length of 3 mm. Subsequently, the bone geometry was imported and all domains, including bone, soft tissue, and skin, were merged into a final model object by creating a non-manifold assembly, see Fig. 4.5 (g).

As mentioned previously (cf. Sec. 2.1), the regarded bone region comprises two layers: the outer cortical bone and the cancellous bone in its interior. The cancellous bone was not modelled based on segmentation due to the limited resolution of the CT scan. Instead, I modelled it as a generically shaped object (see Figure 4.5 (h)) directly in the geometry pre-processor of the simulation software COMSOL Multiphysics® version 6.0 (COMSOL AB, Göttingen, Germany. <https://www.comsol.com>), briefly COMSOL from hereon. Additionally, the cancellous bone layer was disregarded in bone areas far away from the so-called ROI. The ROI is defined as the volume inside the defect domain, highlighted in red in Fig. 4.5 (h).

As defined previously (cf. Sec. 2.2), a critical-size defect in minipig mandibles measures at least 2 cm [53]. Based on this and the planned *in vivo* studies, the defect is designed to be approximately 35 mm in width, 20 mm in height, and 15 mm in depth.<sup>4</sup> However, due to the irregular geometry of the mandible, only the width of 35 mm can be considered a fixed value. In surgical practise and in the simulation model, the height of the defect ranges from approximately 17.3 mm (at the anterior) to 21.1 mm (at the posterior). The actual depth of the defect in the simulation model is about 4 mm (at

---

<sup>4</sup>The specifications for the critical size defect have been provided by colleagues in oral and maxillofacial surgery.

the upper posterior) and 21.45 mm (at the upper anterior). The critical-size defect in the angular region of the mandible was modelled in COMSOL by subtracting a cuboid from the cortical bone geometry. In the *in vivo* experiment, the defect is supposed to be filled with granulated autologous bone from the corresponding defect region. Finally, so-called virtual operations were employed to simplify the topological structure of the geometry by creating composite domains and composite faces. This allows for an easier and more regular generation of the finite element mesh.

### Technical modelling of the implant and the mesh tray

The proposed electrostimulating implant to be used in animal studies consists of a cylindrical implant equipped with bipolar stimulation electrodes. The design of the bipolar cylindrical electrode is inspired by the electrode setups commonly employed in *in vitro* investigations conducted in Rostock [14–22], see Fig. 4.6 (a). The suggested

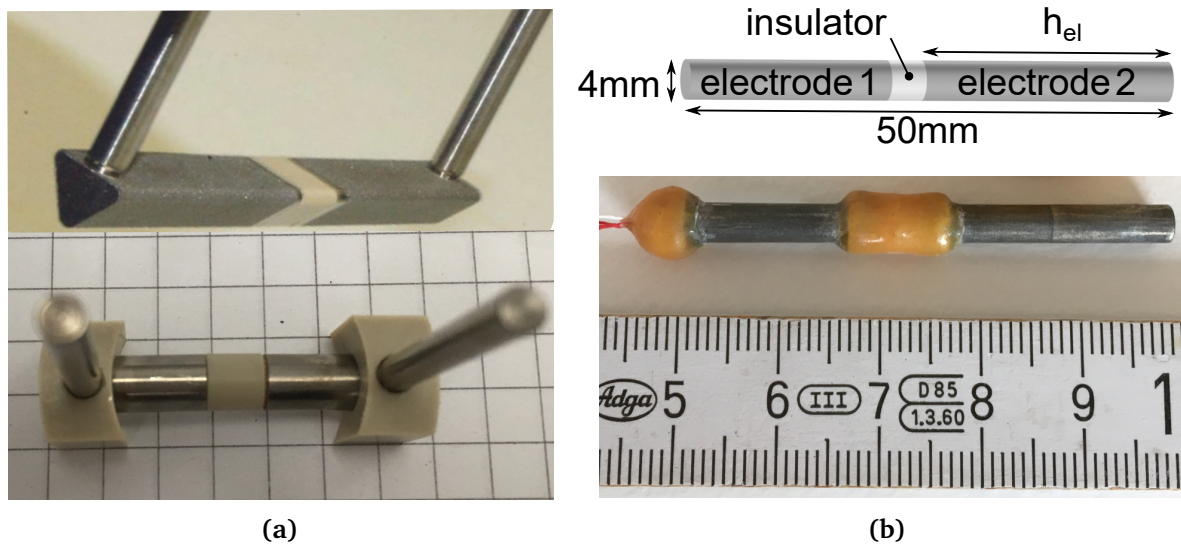


**Figure 4.6:** (a) Bipolar electrostimulating electrodes for *in vitro* applications which inspired the electrode design in this thesis. The top figure was adapted from [18] (licensed under (CC BY 4.0)). (b) Top: electrode design considered in the numerical model in this thesis. electrode 1: posterior electrode, electrode 2: anterior electrode.  $h_{el}$  is the electrode length to be optimised. Bottom: electrostimulating implant used in the *in vivo* experiments. Note that for the *in vivo* experiments, the insulator could only be manufactured in a bulky manner and had to be extended to the cable-leading end of the implant to ensure watertightness. Figure (b) is adapted from my own publication [38].

rod-shaped electrodes are suitable for the irregularly shaped mandible, which is typically narrower at the front and broader at the back.<sup>5</sup> Further advantages of this design are

<sup>5</sup>Other electrode designs, such as three-sided or plate-capacitor-like models, were also simulated but are outside the scope of this work. Instead, the latter are part of ongoing research conducted in the second funding period of the SFB 1270 ELAINE

its comparatively simple fabrication and good comparability with *in vitro* experiments. Moreover, the implant is complemented by a titanium cage (also referred to as *mesh tray*) that keeps the granulated bone material in place. Further, the mesh tray ensures mechanical stability. This is particularly crucial during the *in vivo* experiments as it prevents fracture or other damage to the implant caused by chewing or rubbing of the cheeks.<sup>6</sup> Nevertheless, the technical model only includes the electrostimulating implant, with no geometric modelling of the mesh tray, to decrease the size of the FEM problem. Instead, a floating potential boundary condition (see Chapter 4.2.3) is used to simulate the stabilising Ti6Al4V mesh tray that surrounds the defect domain. The parametrised implant geometry is shown in Fig. 4.6 (b): two electrodes of length  $h_{el}$  (electrode 2) and  $h_{el} - 5$  mm (electrode 1) are separated by an insulator of  $55$  mm  $- 2h_{el}$  length. The electrode length  $h_{el}$  is a fundamental parameter influencing the electric field distribution and hence the regeneration success. Therefore, in addition to the stimulation amplitude, this parameter is optimised to achieve the most favourable electric field distribution (see Sec. 5.2).

In the current study, the technical modelling of the implant design and positioning was performed directly in the geometry module of COMSOL. The initial electrode design, as published in [34], with a pin-shaped posterior end proved to be too complicated to manufacture and was therefore replaced by an extension of the basic cylindrical electrode shape with a diameter of 4 mm and positioned approximately in the centre of the defect region. Furthermore, to account for the limited space in the posterior portion of the mandible, the posterior electrode was reduced by 5 mm resulting in an implant with a total length of 50 mm in this thesis. These modifications were suggested by colleagues from the cranio-maxillofacial surgery department to facilitate manufacturing and improve manageability during surgery [216, 217].

## 4.2.2 Physical modelling of the electrically stimulated mandible

The physical modelling step involves assigning the tissue and material properties to the anatomical and technical model. In this study, it is necessary to assign the dielectric tissue and material properties, i.e. the electrical conductivity  $\sigma$  and the relative permittivity  $\epsilon_r$ , to the respective model domains in order to simulate the electric field distribution resulting from the electric stimulation of the mandible. The tissues considered in this study (see Fig. 4.7) are

- cortical bone representing the outer structure of the mandible;
- cancellous bone inside the mandible and filling the defect;
- mucosa surrounding the bone domains;
- skin surrounding the mucosa domain.

<sup>6</sup>Note that rubbing of the cheeks against objects or other minipigs is a natural behaviour exhibited by minipigs.

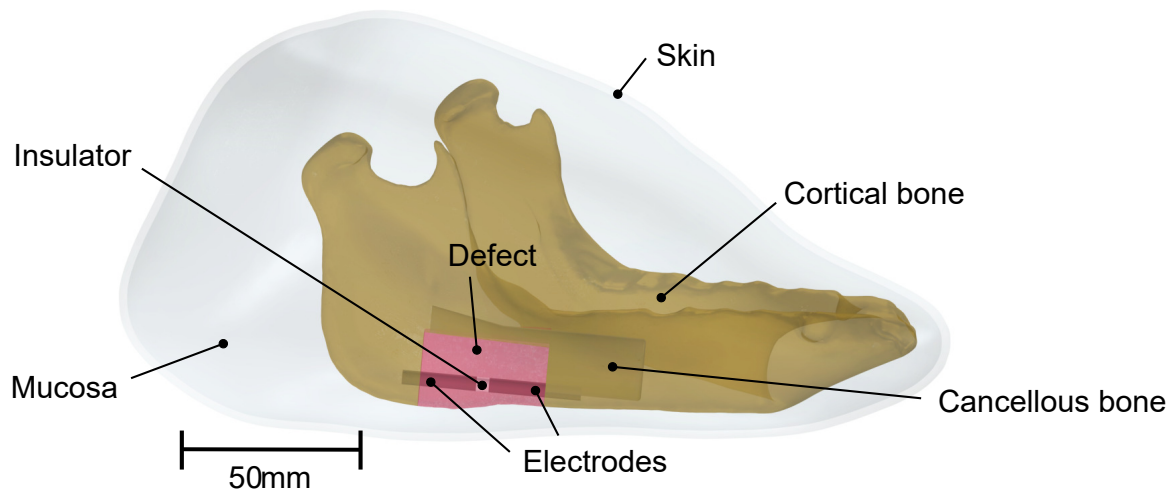


**Figure 4.7:** CAD model of a defective minipig mandible and its surrounding tissues, equipped with an electrostimulating implant. The critical-size defect (region of interest) is highlighted in red. The figure is adapted from my own publication [38].

The dielectric properties of these biological tissues are frequency-dependent and for mucosa and skin their values at the stimulation frequency of  $f = 20$  Hz were calculated via the website of the IT'IS<sup>7</sup> database [218] that is based on the Gabriel data [27–29, 179]. As there are no reliable measurement data on the dielectric properties of mucosa in the low-frequency region [219], using the data of perpendicular muscle is suggested by IT'IS [218] as it resembles similar properties as the mucosa surrounding the jaw bone. This recommendation was applied in this work.

Part of the work presented here has been previously published [34]. The Gabriel data [29] were used for determining the dielectric properties of bone during the publication of that manuscript. During further work on this dissertation project, I initiated measurements to obtain own data on the dielectric properties of cancellous and cortical minipig mandibular bone. These measurements are described in Sec. 5.1. However, there may be some ambiguities in interpreting the data at low frequencies, as discussed earlier (cf. Sec. 4.1.1), which could require correction. Therefore, two important aspects have been enhanced in comparison to the published version of [34]: firstly, the incorporation of our own measurement data for minipig bone; secondly, the implementation of the correction of Zimmermann and van Rienen [30]. This correction and an associated case distinction are detailed in the following section.

<sup>7</sup>Foundation for Research on Information Technologies in Society (IT'IS) <https://itis.swiss/virtual-population/tissue-properties/database/dielectric-properties/>

## Definition of two scenarios for the dielectric tissue properties

Zimmermann and van Rienen [30] suggest that there are two possible interpretations for the Gabriel data on the dielectric properties of biological tissues at low frequencies (cf. Sec. 4.1.1). Either intrinsic tissue properties alone can be attributed to the data, or additional electrode effects may be present in the data. In their research, Zimmermann and van Rienen exclusively apply their correction to the Gabriel data. However, bone is not considered in their study because Gabriel et al. did not directly measure the dielectric properties of bone at low frequencies. Nonetheless, other authors [181, 210, 220, 221] carried out experimental studies on bone that did not account for ETI contributions and as a result, exhibit a significant decrease in conductivity towards lower frequencies. Using such uncorrected data as input in numerical simulations could significantly affect the simulation results. Therefore, I will address this ambiguity by considering two scenarios using either corrected or uncorrected tissue data in my numerical model. This approach will facilitate an evaluation of the influence of these two different model choices, which either rely on the data obtained from the literature and experiments *as they are* or correcting them for possible electrode effects. Therefore, this thesis outlines the two conductivity scenarios as follows:

**EQS<sub>Ga</sub>**: scenario EQS<sub>Ga</sub> regards frequency-dependent low-frequency dielectric properties. Specifically, it employs uncorrected Gabriel data stemming from a 4-Cole-Cole model for mucosa (i.e. perpendicular muscle) and dry skin at  $f = 20$  Hz. For cortical and cancellous bone, uncorrected experimental values from the analysis of own EIS data of minipig mandible bone at  $f = 40$  Hz were used,<sup>8</sup> assuming that the data contain only tissue properties and no electrode effects.

**QS<sub>Zi</sub>**: scenario QS<sub>Zi</sub> involves a low-frequency correction following the recommendations of Zimmermann and van Rienen [30]. Accordingly, the experimental minipig EIS data for cortical and cancellous bone were corrected for electrode polarisation effects by fitting the experimental data to a 2-Cole-Cole model and subtracting the constant phase element (CPE) contribution. The CPE will be introduced in the following subsection. Additionally, Gabriel data for mucosa (i.e. perpendicular muscle) that had been corrected for electrode polarisation as described by Zimmermann and van Rienen [30] were used. The data for skin are the same as for EQS<sub>Ga</sub>, as no electrode polarisation was observed for this tissue type in the study by Zimmermann and van Rienen [30].

The dielectric tissue properties assigned in each scenario are summarised in Table 4.2. The process for determining the dielectric properties of cortical and cancellous bone is described in Sec. 5.1.1. Applying the correction proposed by Zimmermann and van Rienen [30], the capacitive part  $\omega\epsilon_0\epsilon_r$  of the complex conductivity of the tissues in QS<sub>Zi</sub> is less than 1 % of the magnitude of the conductive part  $\sigma$  and thus negligible (Table 4.3). As a result, a quasi-stationary current problem (QS) (Eq. (3.19))

---

<sup>8</sup>Due to the limitations of the instrument used, the minimum frequency measured was 40 Hz and not 20 Hz as suggested by the Kraus-Lechner method (Sec. 2.3.3). However, no significant differences are expected at these frequencies.

Tissue	EQS <sub>Ga</sub>		QS <sub>Zi</sub>	
	$\sigma$ [S/m]	$\varepsilon_r$ [1]	$\sigma$ [S/m]	$\varepsilon_r$ [1]
Cortical bone (own meas.)	0.017	$3.27 \cdot 10^6$	0.027	94560
Cancellous bone (own meas.)	0.05	$1.26 \cdot 10^7$	0.10	341000
Mucosa (perpendicular muscle) [179]	0.207	$2.43 \cdot 10^7$	0.363	18900
Skin [179]	$2 \cdot 10^{-4}$	1140	$2 \cdot 10^{-4}$	1140

**Table 4.2:** Dielectric properties (electrical conductivity  $\sigma$  and relative permittivity  $\varepsilon_r$ ) of the biological tissues utilised in the numerical simulations at  $f = 20$  Hz.

can be considered in this particular case. For scenario EQS<sub>Ga</sub>, the capacitive part of the complex conductivity is in the same order of magnitude as the conductive part for cortical bone, cancellous bone, and mucosa, and therefore cannot be disregarded. Consequently, the full EQS equation (3.17) needs to be considered in this case. Scenario QS<sub>Zi</sub> is considered more realistic because it corrects the measurement data for electrode polarisation that is to be expected at low frequencies as they are regarded here. This correction ensures that only the intrinsic tissue properties are reflected in the derived dielectric properties. An overview of the differences between the two scenarios is given in Fig. 4.8.

Tissue	$\omega\varepsilon_0\varepsilon_r/\sigma$	
	EQS <sub>Ga</sub>	QS <sub>Zi</sub>
Cortical bone	0.2162	0.0039
Cancellous bone	0.2821	0.0038
Mucosa (perpendicular muscle)	0.1303	$5.8 \cdot 10^{-5}$
Skin	0.0063	0.0063

**Table 4.3:** Ratio of the capacitive part ( $\omega\varepsilon_0\varepsilon_r$ ) to the conductive part ( $\sigma$ ) of the complex conductivity based on the different sets of dielectric tissue properties (Table 4.2) that were regarded in the scenarios EQS<sub>Ga</sub> and QS<sub>Zi</sub>. At  $\omega = 2\pi f = 2\pi 20$  Hz, only the QS<sub>Zi</sub> scenario satisfies the condition  $\omega\varepsilon_0\varepsilon_r/\sigma \ll 1$  for all tissues, i.e. the capacitive part is definitely *much* smaller than the conductive part of the complex conductivity. This allows for a quasi-stationary current problem (QS) instead of the full EQS equation to be solved in scenario QS<sub>Zi</sub>. For scenario EQS<sub>Ga</sub>, this condition is only clearly satisfied for skin, while for the other tissues  $\omega\varepsilon$  and  $\sigma$  are of the same order of magnitude and thus this scenario requires the solution of the EQS equation Eq. (3.17).

The electrostimulating implant is constructed from biocompatible materials commonly used in orthopaedics and maxillofacial surgery. The electrodes are composed

	EQS <sub>Ga</sub>	QS <sub>Zi</sub>
Interpretation of EIS data	Sole tissue characteristics	Tissue characteristics and electrode effects
Correction for electrode processes	No	Yes (except skin)
Derived dielectric properties	May include electrode effects	Only include tissue characteristics
Applied approximation of Maxwell's equations	EQS	QS
Assessment of derived dielectric properties	Ambiguous	Closer to reality

**Figure 4.8:** Summary of the differences between the two scenarios EQS<sub>Ga</sub> and QS<sub>Zi</sub> considered in this work, comparing the interpretation of the raw electrochemical impedance spectroscopy (EIS) data, application of a correction of EIS data for electrode processes, the interpretation of the derived dielectric properties ( $\sigma$ ,  $\epsilon_r$ ), the applied approximation of Maxwell's equations justified by the  $\omega\epsilon_0\epsilon_r/\sigma$  ratio (see main text and in Table 4.3), and an evaluation of the credibility of the dielectric properties. Note that no correction for electrode processes was necessary for skin because no electrode polarisation was observed by Zimmermann and van Rienen [30]. QS<sub>Zi</sub> is considered more realistic because it corrects the tissue data for possible electrode effects.

of the titanium alloy Ti6Al4V, while the insulator is made from PEEK (polyether ether ketone). There is a significant contrast in the material properties involved. The conductivity of metal alloys such as Ti6Al4V typically falls within the range of  $10^6$  S/m [222], whereas biological tissues usually have conductivities around  $10^{-1}$  S/m [29], and insulators such as PEEK display a conductivity of  $10^{-12}$  S/m [223]. Therefore, the domains of the electrodes and the insulator were excluded from the simulation and were regarded as terminal and electric insulation boundary conditions instead. This avoids numerical complications arising from a highly ill-conditioned matrix [224].

In addition to the dielectric properties of the biological tissue, electrochemical processes at the electrode-tissue interface must also be considered in the numerical model as they influence the voltage response of the tissue. The upcoming section outlines the modelling of these processes.

### Modelling of the electrode–tissue interface

In the numerical model, the electrochemical processes at the electrode-tissue interface (ETI) between the electrostimulating implant and the conductive tissue must be taken into account since a significant part of the applied potential drops across this interface layer. These processes include the capacitive charging of the electrical

double layer (non-Faradaic processes) as well as the transfer of charges through the interface (Faradaic processes), which determine the ratio of flowing current and the associated voltage drop. Faradaic reactions are usually irreversible and thus alter the chemical composition of the electrode, resulting in corrosion or other degradation of the interface. The electrical double layer is caused by the redistribution of ions in the surrounding electrolyte as they interact with the charged electrode surface. Its pseudocapacitive behaviour is empirically modelled using the so-called constant phase element (CPE) [225]. This implies that a constant phase difference between voltage and current exists, but generally with a larger value than the  $-90^\circ$  that would apply to a pure capacitance. The CPE is described by the equation

$$Z_{\text{CPE}} = K \left( j \frac{\omega}{\omega_0} \right)^{-\beta}, \quad (4.1)$$

where  $K$  represents the ratio of the voltage and current amplitudes,  $j$  is the imaginary unit,  $\omega$  the angular frequency  $\omega = 2\pi f$ , and  $\omega_0 = 1\text{s}^{-1}$  a normalisation frequency to account for proper units of  $\Omega$  for  $Z_{\text{CPE}}$ . The parameter  $\beta = 0 \dots 1$  reflects the frequency dependence of the CPE and how much it deviates from a pure capacitance ( $\beta = 1$ ).  $\beta = 0$  would resemble an ideal resistor. The constant phase is equal to  $-(90 \cdot \beta)^\circ$ .

The ETI is modelled by an equivalent circuit model that is commonly used to model simple systems: a parallel connection of the impedance of a constant phase element  $Z_{\text{CPE}}$  and a charge transfer resistance  $R_{\text{CT}}$  [225, 226], see Figure 4.9. It is worth noting that  $R_{\text{CT}}$  is nonlinear in general, but it can be modelled by an ohmic resistance for small voltage drops [186]. When comparing the values of  $R_{\text{CT}}$  and  $Z_{\text{CPE}}$ , it is evident that within the considered frequency range  $R_{\text{CT}}$  has almost no influence, since  $R_{\text{CT}} \gg Z_{\text{CPE}}$  and thus most of the current flows via  $Z_{\text{CPE}}$ . Therefore, only  $Z_{\text{CPE}}$  was considered for fitting the experimental bone data in the equivalent circuit for the ETI, (see Sec. 4.2.3).<sup>9</sup> The impedance of the tissue  $Z_{\text{Tissue}}$  is defined by its dielectric properties  $\sigma$  and  $\varepsilon_r$  (see Sec. 5.1.1) and the geometric dimensions of the tissue domains.

Thus, each of the two ETIs of the bipolar electrode is described by an impedance  $Z_{\text{ETI},i}$  ( $i = 1, 2$ ), with

$$\frac{1}{Z_{\text{ETI},i}} = \frac{1}{Z_{\text{CPE},i}} + \frac{1}{R_{\text{CT},i}} \quad (4.2)$$

$$= \left( \frac{A_{\text{meas}}}{A_{\text{el},i}} K \left( j \frac{\omega}{\omega_0} \right)^{-\beta} \right)^{-1} + \left( \frac{A_{\text{meas}}}{A_{\text{el},i}} R_{\text{CT}} \right)^{-1}. \quad (4.3)$$

In Eq. (4.3), the contributions to the impedance have been scaled with respect to the surface area of the measuring electrode used in electrochemical impedance spectroscopy (EIS) measurements from the literature with  $A_{\text{meas}} = 314 \text{ mm}^2$  [227] and the surface

<sup>9</sup>Note that  $R_{\text{CT}}$  was still included in the simulation studies for completeness. However, it would have had almost no effect on the results if I had left it out.



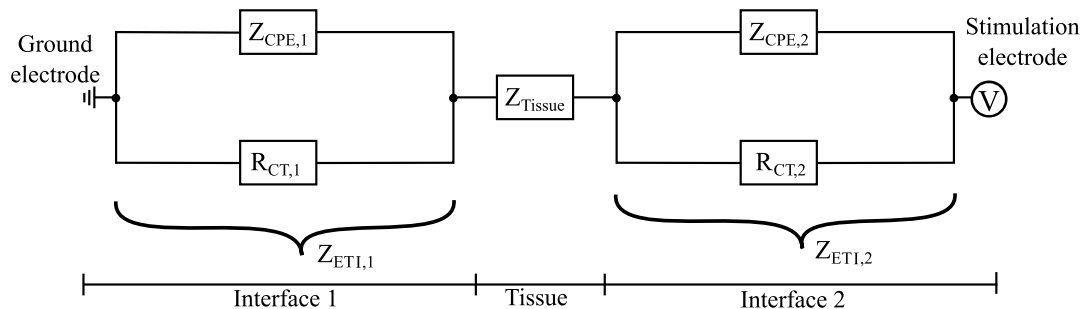


**Figure 4.9:** Equivalent circuit model for the electrode-tissue interface (ETI). The ETI at each electrode is described by an impedance  $Z_{ETI}$  which includes a constant phase element  $Z_{CPE}$  and a charge transfer resistance  $R_{CT}$  in parallel. The tissue properties are described by the impedance  $Z_{tissue}$ , which depends on the dielectric tissue properties and the geometric dimensions of the model domains. The figure is adapted from my own publication [34] (CC BY 4.0 license).

area of the stimulation electrode  $A_{el,i}$  used in the simulations.<sup>10</sup> The value of  $A_{el,i}$  is dependent on the electrode length and has been calculated directly in COMSOL by surface integration. The parameters  $\beta$ ,  $K$ ,  $R_{CT}$  used to model the ETI were derived from EIS measurements of polished titanium specimens [227]. As the interface behaviour primarily depends on the surface structure rather than the material itself, it is safe to assume that the values measured for titanium also give a good approximation for the titanium alloy Ti6Al4V employed here. The values from Lange et al. [227] are  $\beta = 0.95$ ,  $K = (Y_0[1/F])^{-\beta} \Omega = (38.95 \cdot 10^{-6})^{-0.95} \Omega = 15453 \Omega$ ,  $R_{CT} = 137.7 \text{ k}\Omega$ . Note that in EIS measurements, it is more common to use the capacitance parameter  $Y_0$  instead of the parameter  $K$ , which was utilised by Richardot and McAdams [225].

### 4.2.3 Setup of the boundary value problem

In Sec. 3.1, the requirements for the EQS approximation were introduced. These requirements are met for both scenarios considered in this work, see Fig. 4.10. Consequently, the equation to be solved for scenario EQS<sub>Ga</sub> is given by Eq. (3.17). For scenario QS<sub>Zi</sub>, it was also demonstrated that the conditions for a QS are fulfilled (see Sec. 4.2.2), hence Eq. (3.19) can be regarded.

The boundary conditions applied in this model are summarised in Fig. 4.11. At the electrode surfaces, Dirichlet boundary conditions are applied, with the stimulation potential to be optimised  $\varphi_{stim} \neq 0$  at the surface of the anterior electrode and with

<sup>10</sup>During the work on this thesis, I had no opportunity to experimentally characterise the electrochemical properties of the minipig stimulation electrodes. Hence, the literature data from Lange et al. [227] was used.

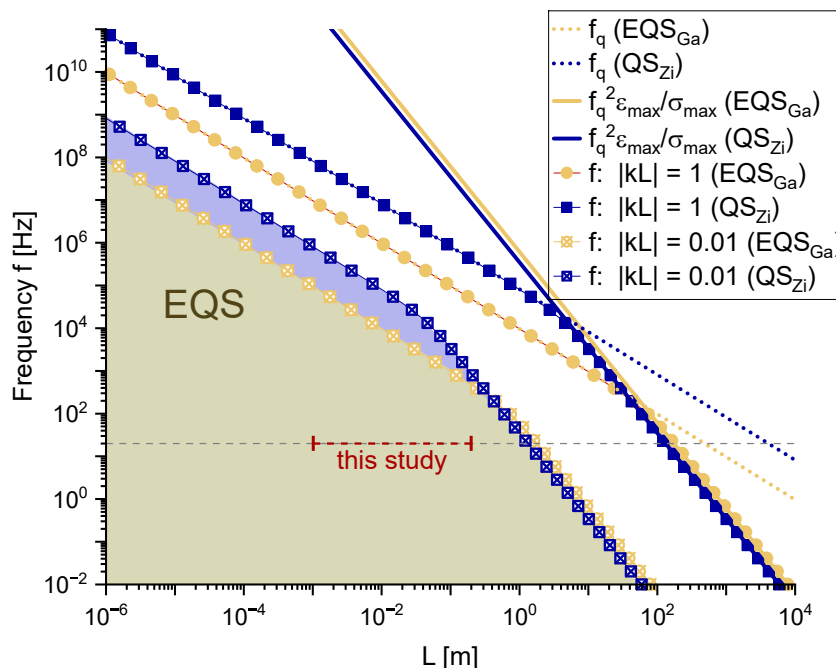


**Figure 4.10:** Valid regime for the electroquasistatic (EQS) approximation (highlighted in beige for scenario EQS<sub>Ga</sub> and in blue/beige for QS<sub>Zi</sub>). The characteristic length of the modelled object is denoted by  $L$  and ranges from  $10^{-3}$  to  $2 \cdot 10^{-1}$  m in this study. The stimulation frequency considered in this work is  $f = 20$  Hz (dashed horizontal line), and for the biological tissues investigated  $\varepsilon_{r,\max} = 2.43 \cdot 10^7$  and  $\sigma_{\max} = 0.207$  S/m (EQS<sub>Ga</sub>) and  $\varepsilon_{r,\max} = 3.41 \cdot 10^5$  and  $\sigma_{\max} = 0.363$  S/m (QS<sub>Zi</sub>) applies.  $f_q$  indicates the limit for negligible wave propagation,  $f_q^2 \varepsilon_{\max} / \sigma_{\max}$  is the indicator for negligible magnetic induction, and  $|kL|$  combines both effects (cf. Sec. 3.1). For  $|kL| \ll 1$ , the EQS approximation is valid. For the tissues, stimulation frequency, and model size regarded here, this is clearly the case (see bold dashed line “this study”). EQS would also be applicable for higher stimulation frequencies up to about 1 kHz. Please note that, for practical reasons, this figure uses the frequency  $f$ , instead of the angular frequency  $\omega$  ( $\omega = 2\pi f$ ).

ground potential at the surface of the posterior electrode:

$$\underline{\varphi}(\mathbf{r}) = \varphi_{\text{stim}} \quad \text{at electrode 1 (anterior electrode),} \quad (4.4)$$

$$\underline{\varphi}(\mathbf{r}) = 0 \quad \text{at electrode 2 (posterior electrode).} \quad (4.5)$$

Homogeneous Neumann boundary conditions are assigned to the surfaces of the skin and insulator domains,

$$\mathbf{n} \cdot \mathbf{J} = 0, \quad (4.6)$$

where  $\mathbf{n}$  denotes an outward oriented vector normal to the boundary.

In surgical practice, a titanium mesh tray serves as an additional stabilisation of the bone, but it also has an impact on the resulting electric field distribution. To simplify

the model and decrease the computation time, the mesh tray has not been explicitly modelled; instead it has been regarded as a floating potential boundary condition at the lateral and lower border of the defect region (see Fig. 4.11). The floating potential boundary condition employs an unknown for the constant potential  $\underline{\varphi}_0$  on the boundary of the mesh tray  $\Gamma_M$ , which is determined by the solver. This boundary condition implies that the tangential electric field is zero and the electric field is perpendicular to the boundary [228]

$$\int_{\Gamma_M} \sigma \frac{\partial}{\partial n_M} \underline{\varphi}(\mathbf{r}) dS = I_0 = 0, \quad \underline{\varphi}(\mathbf{r}) = \underline{\varphi}_0. \quad (4.7)$$

The value of the resulting potential depends on the integral source current  $I_0$ . In this study,  $I_0$  is considered to be zero, indicating that no net current is flowing through the surface, and the boundary is acting as an unconnected perfect conductor. This is a valid approximation because the conductivity of the mesh tray is several orders of magnitude greater than that of the surrounding tissue. Comparative simulations that I performed on a simplified model setup (not shown) demonstrated that the relative difference in the electric field norm in comparison to a fully modelled mesh tray is less than 3 % but the reduction in CPU time is 45 %.

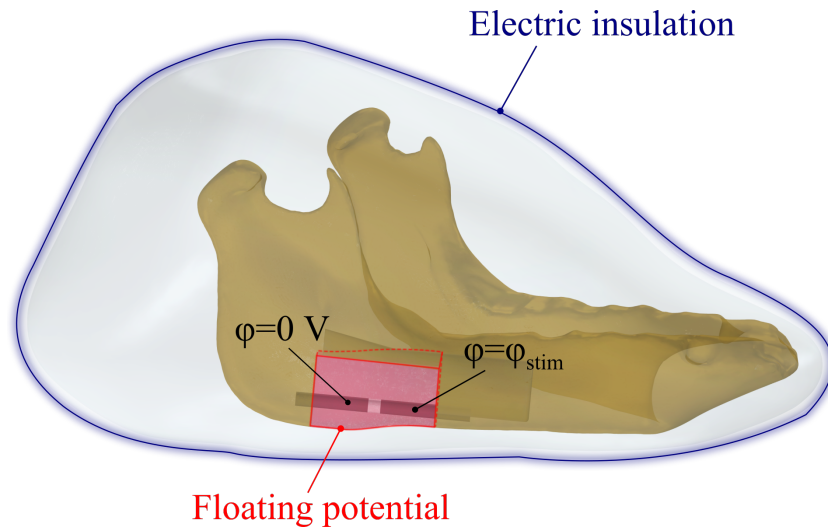


**Figure 4.11:** Boundary conditions applied in the simulation model: Dirichlet boundary conditions were assigned to the surfaces of both electrodes (black), homogeneous Neumann boundary conditions were assigned to the surface of the skin (blue), and a floating potential boundary condition was assigned to the surface enclosing the defect region (red).

Considering the mentioned boundary conditions, Eqs. (3.17) resp. (3.19) are solved for the complex electric potential  $\underline{\varphi}(\mathbf{r})$ . Using this value, the complex amplitude of the electric field strength  $\underline{\mathbf{E}} = -\nabla \underline{\varphi}$  can be derived. Finally, the electric field norm  $|\underline{\mathbf{E}}|$  that is used to rate the stimulation impact is computed.

#### 4.2.4 Finite element simulation and discretisation

The commercial finite element software COMSOL Multiphysics® (COMSOL) version 6.0 was used for modelling and simulation in this thesis. The software presents a variety of benefits, including a user-friendly intuitive graphical interface, built-in powerful and very flexible meshing algorithms, a variety of implemented boundary conditions, a large selection of good solvers and decent post-processing and visualisation capabilities. Furthermore, the *Optimisation module* and the *Design module* allow for direct manipulation of the geometry inside the software. I utilised the *Electric Currents* and *Electrical Circuit* interfaces within the *ACDC module* to solve the EQS approximation of Maxwell's equations (Eq. (3.17)) and the QS (Eq. (3.19)). The ETI was modelled via an *Electrical Circuit* interface at each electrode. The equivalent circuit illustrated in Fig. 4.9 comprised a ground node and an impedance  $Z_{ETI,1}$  (Eq. (4.3)) at the posterior electrode, as well as a ground node, an impedance  $Z_{EDL,2}$ , and a voltage source  $\varphi_{stim}$  at the anterior electrode. The *Electrical circuit* interface solves Kirchhoff's circuit laws to determine the voltages and currents at each circuit element. These laws relate to the conservation of electrical charges and energy in electrical circuits and can be derived from Maxwell's equations. In particular, Kirchhoff's current law states that the sum of the currents entering a junction is equal to the sum of the currents leaving it. Kirchhoff's voltage law indicates that the sum of voltages in a closed loop in a circuit is zero [229].

The electrical circuit and the terminal boundary condition are linked through an *External-I-Terminal*, which applies a voltage relative to ground to the circuit node, i.e. the surface of the electrodes. To optimise the stimulation parameters, the *Optimisation module* of COMSOL was used. Further details on this optimisation will be provided in Sec. 5.2.

Quadratic Lagrange elements were used on a tetrahedral mesh to approximate the dependent variable in the model – in this case, the electric potential  $\varphi$ . The meshing algorithm in COMSOL first meshes all surfaces of the modelled object. This mesh is then used to initiate the tetrahedral volume mesh. For intersecting elements, their dimensions are adjusted to maintain isotropy, with similar edge lengths and angles to the greatest extent possible. This is achieved while ensuring moderate transitions between smaller and larger elements. On the basis of a mesh convergence study I ensured that the electric energy  $W_{el}$  in the entire computational domain only marginally changed by less than 0.008 % upon further refining the mesh compared to the finest mesh resolution employed (Fig. 4.12). Moreover, I ensured that the mesh quality is high (close to 1), especially in the region of interest (ROI). The applied finite element mesh consisted of approximately 1.07 million tetrahedral elements resulting in approximately 1.47 million degrees of freedom solved for (Fig. 4.13).

The large numerical problem considered with more than one million degrees of freedom makes the use of direct solvers impractical due to high memory consumption and long computation times (see Sec. 3.2.3). Therefore, iterative solvers were used in this work. The EQS problem (Eq. (3.17)) results in a complex-symmetric system matrix. Consequently, the computations for scenario EQS<sub>Ga</sub> were carried out using the

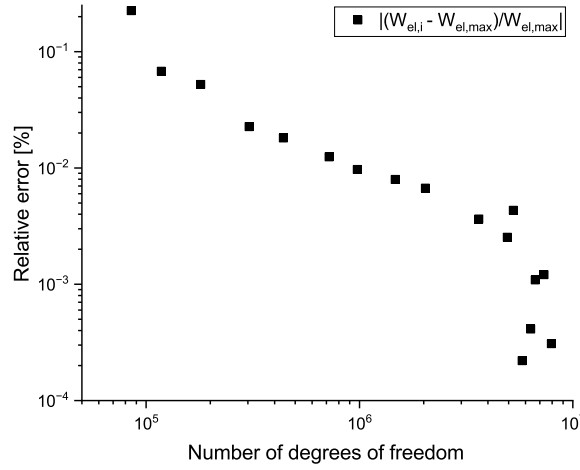


**Figure 4.12:** Relative error in the electric energy  $W_{el}$  in dependence on the number of degrees of freedom solved for. The relative error of each mesh realisation  $i$  is computed with respect to the finest mesh resolution with maximum degrees of freedom.

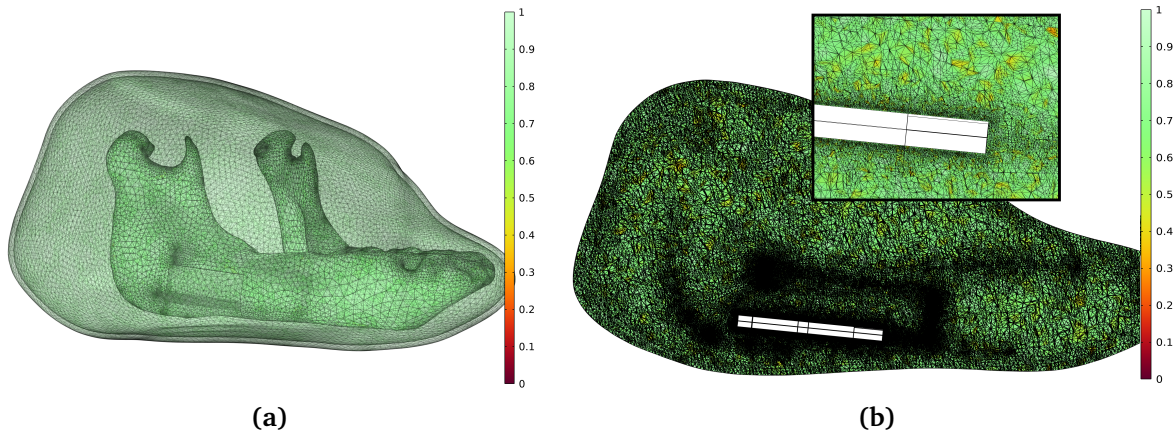


**Figure 4.13:** Finite element mesh and mesh quality (quality measure: skewness) for the electrically stimulated minipig model. (a) Volume mesh and (b) mesh in a slice through the defect region. Note that the implant is not shown as it was excluded from the computational domain.

biconjugate gradient stabilised method (BiCGSTAB), which is suitable for solving such problems and is thus implemented as the default solver in COMSOL. A relative tolerance of  $\text{tol} = 1 \cdot 10^{-3}$  and a factor of  $\rho = 400$  in the error estimation of COMSOL were utilised. For scenario  $QS_{Zi}$ , the generalised minimal residual method (GMRES) [230], another iterative solver, was utilised. GMRES was chosen because it is a memory efficient and fast solver for large numerical models. It has also a more regular convergence behaviour than BiCGSTAB and proved to be 16 % faster than BiCGSTAB in test simulations. However, no such speedup was observed in the models with  $EQS_{Ga}$ , hence the default BiCGSTAB solver was used. Again, a relative tolerance of  $\text{tol} = 1 \cdot 10^{-3}$  and a factor of  $\rho = 400$  in the error estimate of COMSOL were used. In the implementation within COMSOL, the solvers in both scenarios are accelerated by the algebraic multi-

grid method. Furthermore, the successive over-relaxation (SOR) method is used as presmoothing and backward SOR (SORU) as a postsmoothing.

The computations were performed on a Windows workstation with  $24 \times 3.00$  GHz CPU and 256 GB RAM. The simulation time for one run was approximately 81 s on the chosen mesh for EQS<sub>Ga</sub> and 67 s for QS<sub>Zi</sub>. To achieve the desired optimality tolerance in the optimisation study, 50 (EQS<sub>Ga</sub>) and 51 (QS<sub>Zi</sub>) simulation runs were required.

### 4.3 Uncertainty quantification

*Parts of this section were taken from the manuscript “Addressing model uncertainties in finite element simulation of electrically stimulated implants for critical-size mandibular defects”, which appeared in IEEE Transactions on Biomedical Engineering [38].<sup>11</sup>*

In computational modelling, deterministic models are typically utilised whereby fixed input values are employed. However, in most realistically modelled applications a stochastic system must be employed instead of a deterministic system. This is due to input properties being subject to individual variation, intrinsic variability, measurement errors, or insufficient measurement accuracy. Further sources of uncertainty may arise from a lack of data or knowledge on specific parameters. These uncertainties can affect, for example, material properties, the geometry, or boundary conditions in the simulation model. The uncertainties of input parameters are propagated through the numerical model and can therefore have a significant impact on the simulation output. The aim of uncertainty quantification (UQ) studies is therefore to quantify the uncertainties in the model output given the variations in the input data. Statistical moments, such as the mean or variance, are employed to describe the formerly unknown distribution  $\rho_Y$  of the model output. Further goals of UQ studies are to understand the impact of parameters and to rank their importance [231]. By doing so, parameters with negligible influence on the output variance can be disregarded in further UQ studies, simplifying the numerical model.

#### 4.3.1 Stochastic problem definition

When statistical variations of the parameters occur within a model, those parameters should be described with a probability distribution, rather than a fixed, deterministic value (see Fig. 4.14). This enables quantification of the uncertainty propagation through the model. Probability distributions for uncertain parameters are derived from measurements, parameter estimations, or expert judgements and are described using

---

<sup>11</sup>I conceptualised the study, carried out all simulations and the data analysis, prepared the figures, and wrote the first draft of the manuscript. Ursula van Rienen initiated and supervised the project and provided methodological guidance. Ursula van Rienen and Peer W. Kämmerer acquired the funding and provided all resources.

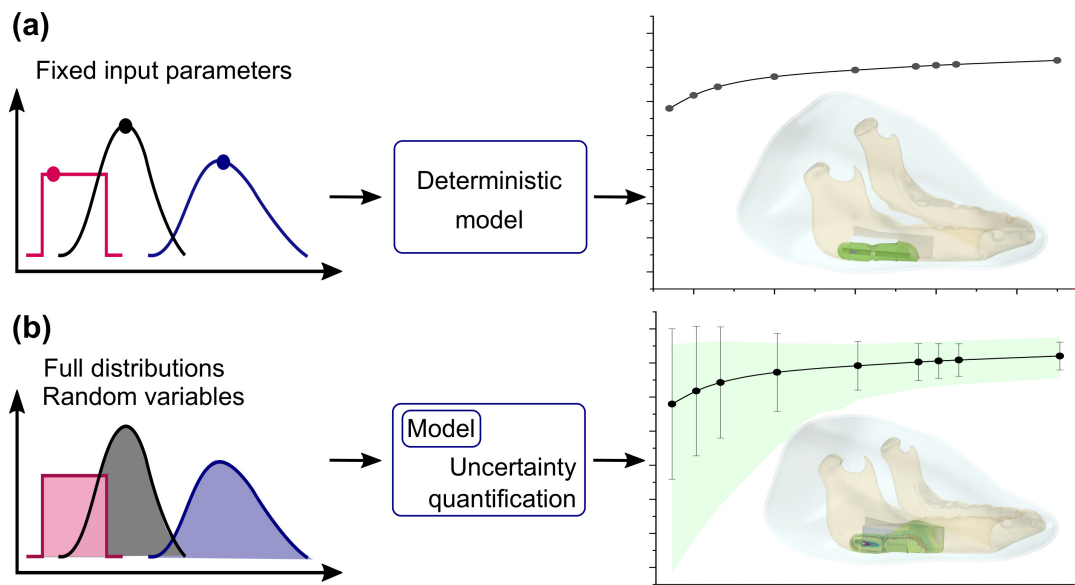


**Figure 4.14:** Principle of uncertainty quantification (UQ) applied to a deterministic model. (a) In a traditional deterministic model, fixed input parameters are considered, resulting in a distinct model output. (b) In a UQ analysis, uncertain inputs are introduced as random variables, and their probability distribution is fed into the model. As a result, the original deterministic problem then becomes a stochastic problem and the output is characterised by a range of possible values.

probability density functions (PDFs). Examples of uncertain parameters in bioelectric modelling are the electrical conductivity  $\sigma$ , the relative permittivity  $\varepsilon_r$ , or the parameters of the electrode-tissue interface (ETI).

I consider a model  $\mathcal{M}$  with both deterministic and uncertain input parameters

$$Y = \mathcal{M}(\mathbf{W}, \mathbf{X}), \quad (4.8)$$

with  $L$  deterministic (i.e. fixed) input parameters  $\mathbf{W} = [W_1, W_2, \dots, W_L]$  and  $M$  uncertain input parameters that are collected in a random vector  $\mathbf{X} = [X_1, X_2, \dots, X_M]$ . The model produces the output  $Y$  with an unknown probability density function  $\rho_Y$ . In the probabilistic setting [232, 233], the uncertain parameters  $X_i$  can be described by PDFs  $\rho_{X_i}$ . In the multivariate case with several uncertain input parameters, these parameters are described by a joint PDF  $\rho_{\mathbf{X}}$ . Assuming independent uncertain parameters, the joint probability density function is the product of the univariate probability density functions  $\rho_{X_i}$

$$\rho_{\mathbf{X}} = \prod_{i=1}^M \rho_{X_i}. \quad (4.9)$$

Important stochastic measures that can be derived from a UQ study are the mean and the variance of the model output  $Y$ . For a random variable  $Y$  with output space  $\Omega_y$ , the

mean value is defined as

$$\mu_Y = \mathbb{E}[Y] = \int_{\Omega_Y} y \rho_Y(y) \, dy, \quad (4.10)$$

where  $y$  is a random realisation of  $Y$  and  $\rho_Y$  is the (formerly unknown) probability density function of the model output [234]. The mean value corresponds to the expected value of the model output.

The variance  $\mathbb{V}[Y]$  is defined as

$$\mathbb{V}[Y] = \text{STD}_Y^2 = \int_{\Omega_Y} (y - \mathbb{E}[Y])^2 \rho_Y(y) \, dy \quad (4.11)$$

and is a measure of the dispersion of  $Y$  around the mean [234]. STD is the standard deviation, a metric that has the same unit as the random variable.

The input parameters that have the greatest impact on the output variance can be identified through sensitivity analysis. In the following section, a variance-based sensitivity analysis (VBSA) method [235, 236] is described in more detail.

### 4.3.2 Variance-based sensitivity analysis

Conducting a sensitivity analysis enables the determination of how variance in the input variables manifests in the output of a model. Furthermore, it facilitates the identification of which input parameters have the most significant impact on the variance of the quantities of interest. The Sobol' indices [235] are frequently employed to characterise the sensitivity of a model. They can be used to quantitatively determine which parameters contribute more to the total variation of the outputs and, in contrary, which parameters are less influential. They decompose the total variance of a quantity of interest into sums of contributions of the different input parameters. The Sobol' indices originally stem from the so-called Sobol' decomposition that is used to estimate the sensitivity of a model to different variables or groups of variables. For a detailed explanation of the Sobol' decomposition, readers are directed to the original works of Ilya Meyerovich Sobol' [235, 237, 238]. The primary concept is to express the model output as an expansion into summands of increasing dimensions [237]. This way, the total variance of a model with  $M$  independent input parameters can also be expressed as a decomposition into sums of partial variances. The global sensitivity indices or *Sobol' indices* are defined as the ratios of the partial variances  $D_{i_1 \dots i_s}$  to the total variance  $D$

$$S_{i_1 \dots i_s} = \frac{D_{i_1 \dots i_s}}{D}, \text{ with } 1 \leq i_1 < \dots < i_s \leq M. \quad (4.12)$$

Hence, each Sobol' index  $S_{i_1 \dots i_s}$  denotes how much of the total variance is due to the uncertainties in the input parameter set  $\{i_1 \dots i_s\}$ . The Sobol' indices are non-negative



and for  $M$  independent input parameters their sum is equal to one [239]:

$$\sum_{s=1}^M \sum_{i_1 < \dots < i_s} S_{i_1 \dots i_s} = \sum_{i=1}^M S_i + \sum_{1 \leq i < j \leq M} S_{ij} + \dots + S_{12 \dots M} = 1. \quad (4.13)$$

The Sobol' indices are defined at various orders, with first order Sobol' indices  $S_i$  quantifying the direct effect that a single parameter  $X_i$  alone has on the model variance. In this context, a small  $S_i$  implies that there will be only slight changes in the model output due to variations in the parameter  $X_i$ , whilst larger values indicate a more significant impact on the output variance. The sum of the first order Sobol' indices cannot exceed one and only equates to one if there are no interactions among the parameters [239]. An interaction in the field of statistics means that the effect of one input parameter on the output variable depends on the value of another input parameter [240].

When there are interactions present in the model, the total Sobol' indices  $S_{T_i}$  are important. They characterise the sensitivity stemming from interactions between a given parameter  $X_i$  and all combinations of the other parameters from the complementary set  $\mathbf{X}_{ci}$ , as well as first order effects [241]:

$$S_{T_i} = S_i + S_{i,ci} = 1 - S_{ci}. \quad (4.14)$$

$S_{ci}$  is the sum of all  $S_{i_1 \dots i_s}$  not containing the index  $i$ . The sum of Eq. (4.14) across all input parameters  $i$  cannot be less than one but generally sums to more than one, as it contains each first order effect once and each interaction term multiple times. It only equals one in the absence of interactions [239]. Greater first order Sobol' indices indicate stronger individual parameter effects, whereas greater total Sobol' indices suggest stronger overall parameter influence, including interactions. The differences between first order and total Sobol' indices emphasise the significance of parameter interactions in influencing the output. The subsequent sections will describe the calculation of the above statistical measures using UQ methods.

### 4.3.3 Uncertainty quantification methods

Numerous methods for UQ exist, differing in accuracy and efficiency based on the number of uncertain parameters and mathematical problems being considered. The most frequently used approaches are the Monte Carlo (MC) method and the polynomial chaos (PC) method. The MC method involves repeated deterministic evaluations of the model, taking into account the statistical properties of the random variables. Statistical information such as the mean and variance can then be calculated from the resulting set of solutions. One benefit of using the MC method is its independence from the number of uncertain parameters [234]. However, a considerable disadvantage of this approach is its slow convergence rate  $\mathcal{O}(K^{-1/2})$ , with  $K$  being the number of model runs [234]. Hence, it takes a large number of model evaluations for the solution statistic

to converge. Thus, the MC method can be very computationally expensive. This is not acceptable for complex 3D FEM models that require increased computational cost even for single runs, as is the case in this study.

In contrast, a highly efficient and now one of the most widely used methods is the PC method [233, 234, 242]. This approach utilises orthogonal polynomial basis functions to approximate the problem in terms of a so-called surrogate model. This surrogate model allows to derive approximations for statistical measures such as mean, variance, and sensitivity indices analytically and very efficiently [236]. The convergence of the PC method is much faster than the convergence of the MC method [243] under certain assumptions on the smoothness of the output functions. Practically speaking, this means that fewer model runs of the FEM model are necessary with the PC method compared to the MC method, resulting in significantly reduced computational costs. However, it should be noted that the PC technique outperforms the MC method only for a moderate number of uncertain parameters of up to  $M \approx 20$  [243]. As the numerical model studied in this thesis possesses a maximum of  $M = 7$  uncertain parameters, the PC method has been adopted to estimate the uncertainties. Further explanation of the theoretical framework of the generalised polynomial chaos approach is provided in the subsequent section.

### Generalised polynomial chaos expansion

The approach of describing a statistical process with a functional approximation using polynomials was first described by Wiener [244]. Wiener used exclusively Hermite polynomials to depict a Gaussian process. The so-called polynomial chaos expansions (PCEs) for estimating uncertainties have been further extended to other polynomials and hence other input distributions by Xiu and Karniadakis [233]. The *generalised* polynomial chaos (gPC) method considers particular polynomials that correspond to the specific distribution of the random variables. Here, I provide a short introduction to

Distribution	PDF $f_X$	Polynomial	Support range
Normal	$\frac{1}{\sqrt{2\pi}} e^{-\frac{x^2}{2}}$	Hermite	$[-\infty, \infty]$
Uniform	$\frac{1}{2}$	Legendre	$[-1, 1]$

**Table 4.4:** Selected distribution, probability density function (PDF), and corresponding orthogonal polynomials in this study. Adapted from [245].

the theory of the gPC technique. For a more detailed description, please refer to the original work by Xiu and Karniadakis [233, 234]. Revisiting the model  $\mathcal{M}$  introduced in Chapter 4.3.1, there exists a polynomial orthogonal basis for  $\mathcal{M}$  based on assumptions about the input distributions  $\rho_{X_i}$ . The specific assumptions and conditions required for the described relations here can be reviewed in great detail in [233, 246]. Following

the formulation of Xiu [234], the model  $\mathcal{M}$  is approximated by a PCE

$$Y = \mathcal{M}(\mathbf{W}, \mathbf{X}) \approx \hat{\mathcal{M}}(\mathbf{W}, \mathbf{X}) = \sum_{\mathbf{i}=0}^N c_{\mathbf{i}}(\mathbf{W}) \Phi_{\mathbf{i}}(\mathbf{X}), \text{ with } N = N_p - 1, \quad (4.15)$$

with orthogonal polynomials  $\Phi_{\mathbf{i}}(\mathbf{X})$  and a priori unknown coefficients  $c_{\mathbf{i}}(\mathbf{W})$ . The expansion coefficients  $c_{\mathbf{i}}(\mathbf{W})$  are to be determined and depend only on the deterministic inputs  $\mathbf{W}$ . The expansion is truncated after  $N_p$  terms. Here,  $\mathbf{i} = (i_1, \dots, i_M) \in \mathbb{N}_0^M$  is a multi-index with  $|\mathbf{i}| = i_1 + \dots + i_M$ . In the multivariate case with  $M$  uncertain input variables, the tensor product of the univariate gPC polynomials forms the  $M$ -variate gPC polynomial basis functions:

$$\Phi_{\mathbf{i}}(\mathbf{X}) = \phi_{i_1}(X_1) \cdots \phi_{i_M}(X_M), \quad 0 \leq |\mathbf{i}| \leq N, \quad (4.16)$$

In the gPC method, the polynomials are orthogonal with respect to the joint probability density function  $\rho_{\mathbf{X}}$ , ensuring efficient computation. Different polynomials are chosen for different input distributions. Table 4.4 summarises the distributions employed for modelling uncertain input parameters, the corresponding probability density functions, and the corresponding polynomials in this study.

The number of expansion factors  $N_p$  depends on the number of uncertain inputs  $M$  and the order  $p$  of the PCE [243]

$$N_p = \binom{M+p}{p}. \quad (4.17)$$

Using a higher order  $p$  of PC basis functions improves the accuracy of the approximation but also requires more computations.

In the UQ toolbox used in this study (Uncertainpy [247], see Sec. 4.3.4), the orthogonal polynomials are generated by the three-term discretised Stieltjes recursion [247–250]. To determine the polynomial coefficients, the point collocation method is employed. This method will be briefly introduced in the following section. For further information, please refer to Xiu [234].

### Estimation of the polynomial chaos expansion coefficients

To determine the expansion coefficients  $c_{\mathbf{i}}$  of the polynomial expansion (Eq. (4.15)), the point collocation method is used. It is a robust method that is generally recommended for use with the applied UQ toolbox Uncertainpy [247] and is therefore also used in this study. The point collocation method enforces the polynomial approximation to be equal to the model at the collocation nodes. Uncertainpy employs the recommendation of Hosder et al. [251] and uses  $2(N_p + 1)$  collocation nodes.  $N_p$  is the number of expansion factors, see Eq. (4.17). Note that the number of collocation nodes equals the number of simulation runs as the model is computed at each collocation node.

Hammersley sampling [252] is used to sample the collocation nodes from the joint probability density function  $\rho_{\mathbf{x}}$ . Regression methods are necessary to solve the resulting set of linear equations for the polynomial coefficients  $c_i$ . Tikhonov regularisation [253] is the method utilised by Uncertainpy for this purpose.

After determining the expansion coefficients, the statistical measures can be analytically derived in a post-processing step [236]. Additionally, the PC method can efficiently estimate both the first order and total Sobol' indices [236, 243, 247].

The mean corresponds to

$$\mathbb{E}[\mathcal{M}] \approx \mathbb{E}[\hat{\mathcal{M}}] = c_0. \quad (4.18)$$

The variance is calculated by

$$\mathbb{V}[\mathcal{M}] \approx \mathbb{V}[\hat{\mathcal{M}}] = \sum_{i=1}^N \gamma_i c_i^2, \quad (4.19)$$

where  $\gamma_i = \mathbb{E}[\Phi_i^2(Y)]$  is a normalisation factor [234].

Furthermore, also the Sobol' indices are directly derived from the PCE coefficients [236, 243]. The 5th and 95th percentiles, and hence the 90 % prediction interval, are estimated by applying the MC method to the surrogate model  $\hat{\mathcal{M}}$ . This involves calculating a large number of MC samples based on the surrogate model. In contrast to performing the MC method for UQ on the numerical model itself, the MC sampling of the surrogate model is not computationally demanding.

#### 4.3.4 Software used for the uncertainty quantification studies

Research in the field of computational bioelectric engineering has explored the use of UQ in a range of areas, including electrostimulating hip revision systems [174], cartilage tissue engineering [254, 255], deep brain stimulation [256–259], and cochlear implants [260]. The utilisation of UQ has gained significant attention in recent years due to the improved computational power and subsequent advancements in the field. Various commercial and open-source software options are available for engineers to conveniently apply UQ tools [247, 261, 262] to their specific problems without requiring an in-depth understanding of the mathematical theory behind it [233, 242, 244, 263] or dealing with the computational implementation challenges. Most of these toolboxes are well-established within their field of application. Therefore, it is highly recommended [264] to utilise pre-existing toolboxes.

For the UQ studies in this work, a modified version<sup>12</sup> of the open source Python toolbox Uncertainpy (version 1.2.3) [247] was used to compute the statistical measures and perform sensitivity analysis based on Sobol' indices. Originally designed for

<sup>12</sup><https://github.com/j-zimmermann/uncertainpy/tree/1.2.0.1>

computational neuroscience, Uncertainpy is also broadly applicable to other areas of study. For instance, it has been used to characterise uncertainties in the numerical modelling of electrically stimulated cells [254, 255, 265] or deep brain stimulation in a rodent model [256]. Uncertainpy uses global, non-intrusive methods and is based on Chaospy [250, 266], an established open source Python toolkit with UQ functionalities, in particular PCE and advanced MC methods.

To enable the application of UQ in this study, a programming interface between the finite element software COMSOL and the Python UQ toolbox Uncertainpy has to be established. COMSOL is interconnected to MATLAB® via LiveLink™ for MATLAB®. The communication between Uncertainpy and COMSOL is set up by establishing a Python-MATLAB API (Application Programming Interface). This is achieved via the MATLAB Engine API for Python. With this Python package, MATLAB® can be called as a computational engine.

# Chapter 5

## Results and discussion

In the following, the derivation of the dielectric tissue properties of minipig mandibular bone derived from electrochemical impedance spectroscopy (EIS) measurements is described. These quantities are then further used for the numerical simulation and optimisation of the electric field distribution in the computational model of an electrically stimulated minipig mandible. Expanding on this, the optimised field distributions for the two distinct scenarios considered within this dissertation will be presented. Uncertainty quantification (UQ) studies investigating the influence of uncertain input parameters on the model results are subsequently provided. Finally, preliminary simulation results of electrically stimulated human mandible models give an outlook on possible clinical applications of electrostimulating systems for the regeneration of facial bone defects.

### 5.1 Measurement and analysis of the dielectric properties of minipig mandibular bone

As an alternative to the widely-used Gabriel data, own measurements of the dielectric properties of minipig mandible bone have been performed.<sup>1</sup> The bone samples originated from two animals and they were stored in a freezer at  $-20^{\circ}\text{C}$  for a week for organisational reasons. Prior to impedance spectroscopy measurements they were placed in an incubator with  $T = 37^{\circ}\text{C}$  to allow for measurements at approximately body temperature. Due to experimental limitations, direct measurements inside the incubator were not feasible at that time. Sample preparation and EIS measurements follow the procedure described in [181]. The measurements were taken in the frequency range of  $f = 40\text{ Hz} - 5\text{ MHz}$ . Due to the limitations of the used measurement device, the minimum frequency measured was 40 Hz and not 20 Hz as suggested in the employed

---

<sup>1</sup>I initiated the measurements, coordinated the sample transfer, and analysed the measurement data. I thank Dr. rer. nat. Wenzuo Wei from ELAINE project A05 for performing the measurements and providing the raw data. In addition, I thank Dr. vet. Mohamed Elhensheri and Daniel Wolter (Department of Oral and Maxillofacial Surgery, University Medical Centre Rostock) for providing and preparing the bone specimens.

Kraus-Lechner method (refer to Sec. 2.3.3). Nonetheless, no significant differences are anticipated at these frequencies. The validation and further analysis of the derived data is described in the next section.

### 5.1.1 Validating and fitting of the impedance data of minipig mandibular bone

The dielectric properties of cortical and cancellous bone were determined through EIS measurements on the mandibular bone of minipigs in the frequency range of 40 Hz–5 MHz. Prior to deriving these properties from the measured impedance data, the measurement data were checked for compliance with the Kramers-Kronig relationships, which connect the real and imaginary components of the impedance, to ensure validity of the experimental data [168]. It was accomplished by means of a so-called Lin-KK test [267] that is implemented in *ImpedanceFitter* [268]. In this test, the EIS data are fitted to an equivalent circuit model consisting of an ohmic resistor that is in series with several RC elements. Further, a capacitance (for the electrode-tissue interface (ETI)) and an inductance (for lead inductances) can be regarded additionally if necessary. For further information on the method see [267] or [30]. Only data adhering to the Kramers-Kronig relations were considered for the further analysis described in Sec. 5.1.2. In some instances, the Lin-KK test indicated that the data were valid within a limited frequency range only. In these cases, the data underwent fitting after a subsequent second Lin-KK test, which proved their validity in the determined restricted frequency range. The described testing procedure resulted in 32 valid data sets for cancellous bone and five data sets for cortical bone. Measuring the dielectric properties of cortical bone posed several challenges. The cortical bone samples taken from the posterior part of the mandible had an uneven surface, making it more difficult to obtain accurate measurements. Furthermore, a buildup of liquids potentially rendered a significant portion of this data unusable.

The raw measurement data of the minipig bone deduced from two-electrode measurements may include electrode effects. For instance, the straight line in the Nyquist plot depicted in Fig. 5.1 could indicate the presence of a constant phase element (CPE) impedance that models the ETI effects. However, these electrode effects cannot be unambiguously defined and quantified reliably without further measurements that are beyond the scope of this thesis. Nonetheless, it is possible to correct the data to some extent by considering the pseudocapacitive double layer at the ETI as a CPE and subtracting it from the total impedance. Therefore, the valid data sets were fitted to an equivalent circuit comprising a two Cole-Cole (2CC) model in series with a CPE following the aforementioned recommendations by Zimmermann and van Rienen [30]. Using this approach, the measuring data are described by the impedance

$$Z = Z_{2CC} + Z_{CPE} = \frac{1}{j\varepsilon_{r,2CC}\omega c_0} + K \left( j \frac{\omega}{\omega_0} \right)^{-\beta}, \quad (5.1)$$

with the complex relative permittivity  $\varepsilon^*$  and the cell constant  $c_0 = \varepsilon_0 A/t$  that can be calculated based on the area of the EIS electrode  $A$  and the sample thickness  $t$ . For the 2CC model, the complex relative permittivity corresponds to

$$\varepsilon_{r,2CC}^* = \varepsilon_r - \frac{j\sigma}{\omega\varepsilon_0} = \varepsilon_\infty + \sum_{i=1}^2 \frac{\Delta\varepsilon_i}{1 + (j\omega\tau_i)^{a_i}} - \frac{j\sigma_{DC}}{\omega\varepsilon_0}, \quad (5.2)$$

where  $\varepsilon_\infty$  is the high-frequency limit of the permittivity,  $\Delta\varepsilon_i$  is the magnitude of the  $i$ th dispersion,  $\tau_i$  is the mean relaxation time of the  $i$ th dispersion, the parameter  $a_i \in [0, 1]$  characterises the broadening of the dispersion, and  $\sigma_{DC}$  is the static conductivity of the tissue [30].  $\varepsilon_\infty$ ,  $\Delta\varepsilon_i$ ,  $\tau_i$ ,  $a_i$ ,  $\sigma_{DC}$ ,  $K$ , and  $\beta$  are regarded as fit parameters.

A charge transfer resistance was not included in the fitted equivalent circuit as it had no discernible impact on the fit result, and furthermore, displayed high fitting uncertainties during test analyses. As the measured impedance values varied greatly with frequency, a weighting algorithm was used to improve the fit. The fitting parameters are given in the Appendix A. The validity testing of the experimental data and the fitting of equivalent circuit models to them was carried out using the open source Python package *ImpedanceFitter* version 2.0.3 [268].

The hypothesis that the experimental data can be fitted by a 2CC model, as motivated by Zimmermann and van Rienen [30], is further supported by the fact that two dispersions were clearly visible in most of the Nyquist plots of the samples (Fig. 5.1). The fit results and the fit statistics are provided in Tables A.1 to A.4 in the Appendix. The derived dielectric properties are presented in the next section.

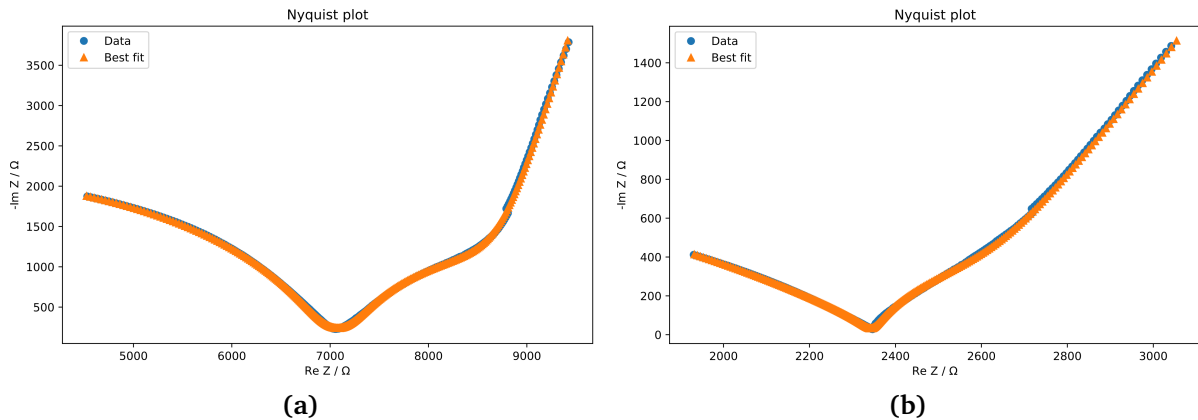


**Figure 5.1:** Exemplary Nyquist (imaginary and real part of the impedance  $Z$ ) plots for minipig bone samples. (a) cortical bone, (b) cancellous bone. Shown are the experimental data (Data) and the 2CC fit (Best Fit). The covered frequency range is 40 Hz–5 MHz. High frequencies are on the left, low frequencies on the right of the plot. The straight line that is particularly evident in (a) indicates the presence of electrode polarisation, which is modelled by a constant phase element (CPE) impedance.



### 5.1.2 Dielectric properties of minipig mandibular bone resulting from the fitting procedure

The dielectric properties resulting from the 2CC fits after correction for the CPE are shown in Figs. 5.2 and 5.3 in comparison with the original measurement data and the literature values introduced in Sec. 4.1.2. Upon analysing the 2CC results, the electrical conductivity is almost frequency-independent at low frequencies (Fig. 5.2). This is in contrast to the uncorrected experimental minipig conductivity data, where there is a pronounced decrease in conductivity with decreasing frequency. In comparison to the literature data, the determined conductivities of minipig cortical bone are slightly higher, which could be due to a variety of possible factors, as introduced in Sec. 4.1.2. However, the cancellous bone conductivity is comparable to the data of Balmer et al. and the Gabriel data. The properties of cancellous bone are particularly crucial for this thesis as

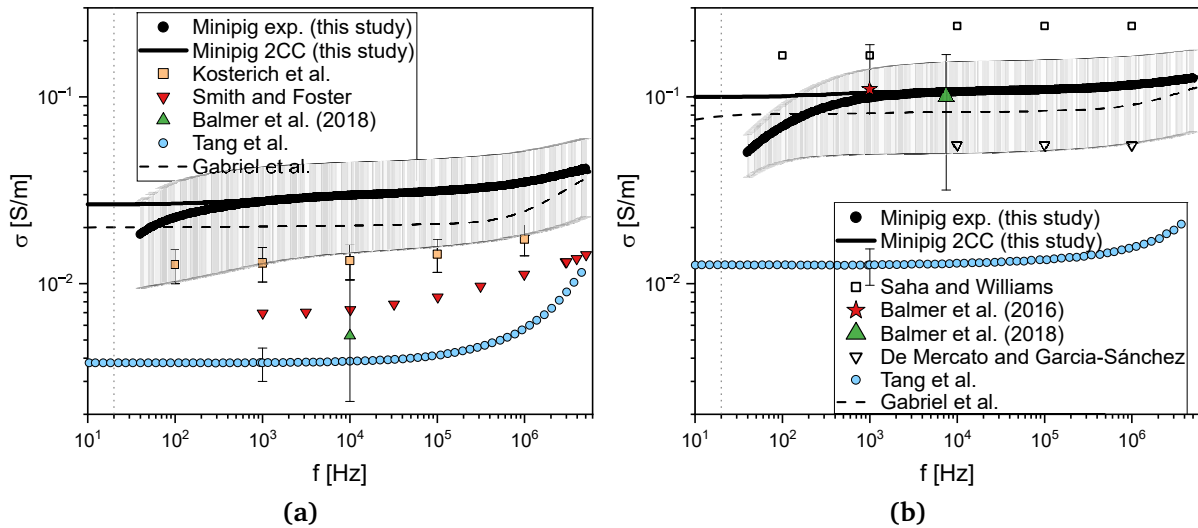


**Figure 5.2:** Electrical conductivity  $\sigma$  of (a) cortical and (b) cancellous bone according to own measurement data (Minipig exp.) and comparison with literature data (Kosterich et al. [187], Smith and Foster [211], Balmer et al. [184,185], Tang et al. [201], Gabriel et al. [29], Saha and Williams [207], and De Mercato and Garcia-Sánchez [205]). The experimental standard deviations are indicated in grey. In addition to the experimental raw data (Minipig exp.), the data corrected for electrode polarisation are given (Minipig 2CC).

the defect area is filled with this tissue. For cancellous bone, the determined conductivity is very similar to the data obtained by Balmer et al. at 1 kHz and 10 kHz [184, 185] (Fig. 5.2 (b)). This applies to both the corrected and uncorrected minipig data. However, it is apparent that the uncorrected data for cancellous bone conductivity decreases at frequencies below 10 kHz. Consequently, notable discrepancies can be observed in comparison to the Balmer data and the corrected experimental data at lower frequencies. Therefore, the uncorrected conductivity of minipig mandibular bone at the lowest measurement frequency (40 Hz) is even lower ( $\sigma = 0.05$  S/m) than the ambiguous Gabriel data ( $\sigma = 0.08$  S/m).

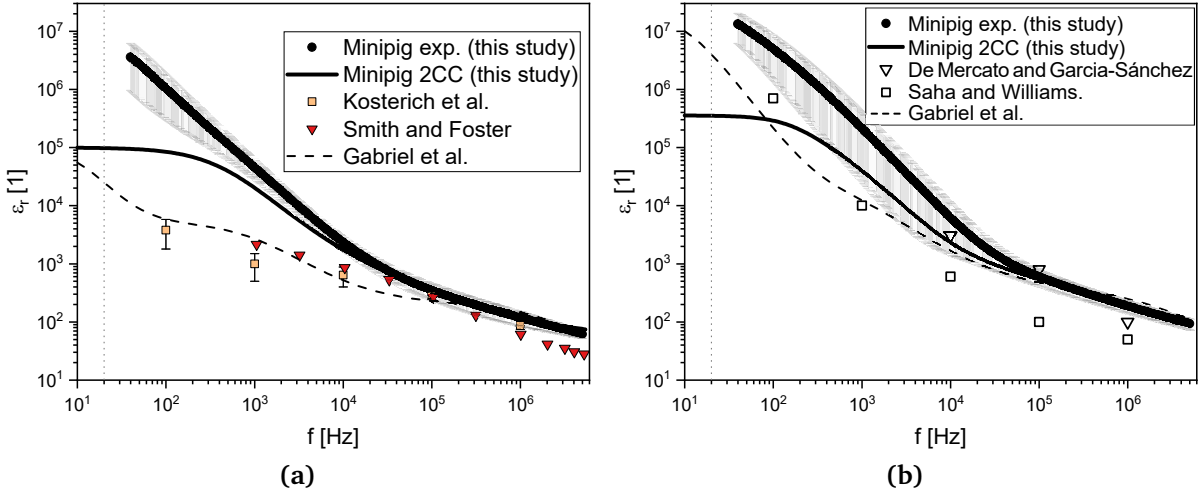


**Figure 5.3:** Relative permittivity  $\varepsilon_r$  of (a) cortical and (b) cancellous bone according to own measurement data (Minipig exp.) and comparison with literature data (Kosterich et al. [187], Smith and Foster [211], Gabriel et al. [29], Saha and Williams [207], and De Mercato and Garcia-Sánchez [205]). The experimental standard deviations are indicated in grey. In addition to the experimental raw data (Minipig exp.), the data corrected for electrode polarisation are given (Minipig 2CC).

The corrected fits of the relative permittivity of cancellous bone have characteristic dispersions in the range of about 160 Hz–2.3 kHz and 12 kHz–1.7 MHz. These ranges align with the ranges of the alpha and beta dispersion, which were introduced in Sec. 4.1 [166]. The experimentally obtained uncorrected relative permittivity of cancellous bone in this study is strikingly high at low frequencies (Fig. 5.3 (b)). To some extent it exceeds that of Gabriel by several orders of magnitude and exceeds  $10^7$  below 100 Hz. Thus, the condition (3.18) is not fulfilled in this case and the full EQS equation (3.17) has to be considered (see Sec. 4.2.2). For the relative permittivity of cortical bone, the situation is similar. Still, the values of  $\varepsilon_r$  are approximately one order of magnitude lower than those of cancellous bone. The agreement between the measured data (both uncorrected and corrected) and the data by Kosterich et al. [187] and Smith and Foster [211] is satisfactory down to frequencies of approximately 30 kHz. At lower frequencies, even the corrected data exceed the literature data by one to two orders of magnitude.

The mean values of the dielectric properties of cortical and cancellous minipig mandibular bone at a frequency of  $f = 40$  Hz are summarised in Table 5.1. Following correction, the conductivity of cortical bone is 1.6 times higher than the uncorrected data, and for cancellous bone it is twice as high. Conversely, the corrected relative permittivity values for cortical and cancellous bone are 34.6 and 37.0 times lower, respectively. The values obtained from the uncorrected measurement data (Minipig exp.), as well as the data corrected for electrode polarisation (Minipig 2CC), are subsequently implemented in the simulations of the scenarios EQS<sub>Ga</sub> and QS<sub>Zi</sub>, respectively. Refer to Table 4.2 for more information.

Tissue/Material	Minipig exp.		Minipig 2CC	
	$\sigma$ [S/m]	$\varepsilon_r$ [1]	$\sigma$ [S/m]	$\varepsilon_r$ [1]
Cortical bone	0.017	$3.27 \cdot 10^6$	0.027	94560
Cancellous bone	0.05	$1.26 \cdot 10^7$	0.10	341000

**Table 5.1:** Dielectric properties (electrical conductivity  $\sigma$  and relative permittivity  $\varepsilon_r$ ) derived from EIS measurements of cortical and cancellous minipig mandibular bone at  $f = 40$  Hz. Given are values for uncorrected data (Minipig exp.) and data corrected for electrode polarisation (Minipig 2CC). These correspond to scenarios EQS<sub>Ga</sub> and QS<sub>Zi</sub>, respectively.

### 5.1.3 Discussion

The comparison between the dielectric properties of bone determined experimentally in this work and those reported in the literature revealed significant disparities, particularly for the cortical bone samples. However, the experimental outcomes of this work and the literature showed a good agreement for cancellous bone. Further research is necessary to determine whether the observed discrepancies between our measurements and the literature data stem from inherent tissue variations of the particular tissues in question (Kosterich et al. [187] and Smith and Foster [211] utilised cortical rat femur) or are instead caused by deficiencies in our available experimental methods. It is feasible that one of the two (or more) dispersions observable in the Nyquist plots (ref. Sec. 5.1.1) could be an artefact caused by the handling of the sample or the measurement device itself. For instance, air pockets present in the samples could be a probable cause of the issue. Additionally, in some samples, both highly insulating phases (teeth) and conductive phases (cancellous bone) were present, potentially resulting in two or more dispersions. Furthermore, there were technical issues resulting in small jumps in the data (Fig. 5.1) that made several of the datasets unusable, especially when these jumps occurred in the middle of the frequency spectrum. In some instances, a portion of the dispersions may be resolved even with the jumps, albeit at the risk of distorting the resulting dielectric properties. In light of these limitations, future studies require an improved measurement setup and sample preparation. Additionally, models that incorporate only a single Cole-Cole dispersion should be considered.

I have considered the measurements of Balmer et al. [184, 185], Smith and Foster [211], Kosterich et al. [187], and Tang et al. [201] to be reliable. However, they did not include jaw or minipig bone samples. Therefore, our own research makes a crucial contribution to determining the precise dielectric properties of the minipig model, enhancing its validity. However, the data obtained from the EIS measurements on mandibular bone of minipigs did not meet the standards I set for the research quality in my preceding literature review (cf. Sec. 4.1.2). Although I was successful

in obtaining measurements from the desired anatomical region and species at body temperature, the samples collected were not fresh as required for reliable studies. In contrast, the minipig experiments necessitated the utilisation of initially frozen, thawed, and reheated samples (at a temperature of roughly  $T = 37^\circ\text{C}$ ) in a measuring system that consisted of three electrodes.<sup>2</sup> Therefore, to improve the measurement procedure in the future, it is imperative to carefully organise and coordinate the procedures.

Acquiring bone samples from minipigs poses further significant challenges. Ethical considerations make it unfeasible to obtain these animals solely for bone tissue extraction. Therefore, samples must be obtained opportunistically during other experiments when suitable animals are available for bone extraction. A measurement procedure that is as seamless as possible would then have to be established, including:

- sample extraction a few minutes post mortem;
- avoid exposure of the samples to air and prevent them from drying out, e.g., by covering them with gauze soaked in physiological saline [269];
- cutting the samples into slices immediately after sample extraction; using low cutting speed [181] to avoid thermal damage such as denaturation of proteins and keep the tissues wet with physiological saline during cutting;
- ensuring thorough documentation by taking photographs of all samples, documenting the anatomical origin and the dimensions (i.e. thickness) of every sample, and documenting the orientation of the samples towards the bone axis;
- immediately transport the samples to the measurement lab; transport the cut samples in  $40^\circ\text{C}$  Ringer's solution with bicarbonate buffer (oxygen saturated) [270];
- immediately perform EIS measurements under controlled conditions directly inside an incubator at  $T = 37^\circ\text{C}$  and with relatively high humidity [201, 269];
- measure each sample multiple times and average to reduce measurement errors;
- finish each EIS measurement as quickly as possible to minimise moisture loss or the effect of the humidity of the environment [181];
- conduct a calibrating *cell measurement*, i.e. a measurement with a standard solution, shortly before or after the actual measurement with a specimen because electrode impedance changes with time and use [203].

To sum up, further research is necessary to address the hurdles associated with measuring the dielectric properties of bone and to identify potential factors causing discrepancies in the measured values. *In vivo* measurements, as employed by Balmer et al. [184], are a desirable approach, but they are very challenging to perform and involve additional ethical concerns. The uncertainty of the obtained dielectric properties can

---

<sup>2</sup>The measurement setup consisted of two electrodes for measuring and one guard electrode to reduce stray capacitance. Further details can be found in [181].

be addressed with uncertainty quantification (UQ) studies. These will be discussed in detail in Sec. 5.3. However, before that, the optimisation of the electrostimulation implant with deterministic input parameters will be presented in the next section.

## 5.2 Optimisation of the implant parameters

The stimulation parameters, namely the electrode length  $h_{el}$  and the stimulation voltage  $\varphi_{stim}$  must be optimised to attain the most effective electric stimulation within the bone defect as the region of interest (ROI). To this end, a goal function was defined with respect to the volume of stimulated tissue in the ROI. Based on the findings of Kraus [6], certain areas in the defective volume can be characterised as either beneficially stimulated, overstimulated, or understimulated, depending on the electric field norm  $|\underline{E}|$ . Specifically, the term “beneficially stimulated” refers to  $5 \text{ V/m} \leq |\underline{E}| \leq 70 \text{ V/m}$ , whereas overstimulation would correspond to  $|\underline{E}| > 70 \text{ V/m}$ , and understimulation would imply  $|\underline{E}| < 5 \text{ V/m}$  [6]. Therefore, the volumes of beneficially, under-, and overstimulated tissue correspond to

$$V_{bene} : \quad 5 \text{ V/m} \leq |\underline{E}| \leq 70 \text{ V/m}, \quad (5.3)$$

$$V_{under} : \quad |\underline{E}| < 5 \text{ V/m}, \quad (5.4)$$

$$V_{over} : \quad |\underline{E}| > 70 \text{ V/m}. \quad (5.5)$$

These stimulated volumes are determined by volume integration in COMSOL.

To optimise the stimulation parameters for the most beneficial electric field distribution, the goal defined in this study is to maximise the volume of beneficially stimulated tissue in the ROI while minimising the volumes of under- and overstimulated tissue. Maximising the volume of beneficially stimulated tissue ( $V_{bene}$ ) is equivalent to minimising the volume where no beneficial stimulation is present ( $\bar{V}_{bene}$ ), i.e. understimulation or overstimulation occurs:

$$V_{bene} \Rightarrow \max \quad \Leftrightarrow \bar{V}_{bene} \Rightarrow \min, \quad (5.6)$$

$$V_{under} \Rightarrow \min, \quad (5.7)$$

$$V_{over} \Rightarrow \min. \quad (5.8)$$

Accordingly, the regarded goal functions are

$$\bar{f}_{bene} = s_{bene} \bar{V}_{bene}, \quad (5.9)$$

$$f_{under} = s_{under} V_{under}, \quad (5.10)$$

$$f_{over} = s_{over} V_{over}, \quad (5.11)$$

and their sum is to be minimised in order to achieve the best possible stimulation effect. The goal functions are scaled with scaling factors  $s_{bene} = s_{under} = 4 \cdot 10^{-5}$ ,  $s_{over} =$

$2 \cdot 10^{-4}$  so that they are in the order of magnitude of one.<sup>3</sup> This ensures the stability of the optimisation methods of COMSOL. Overstimulation is detrimental as it may cause tissue damage and therefore should be avoided in particular. Consequently, goal function Eq. (5.11) is weighed by a five times larger factor.

The optimisation studies were based on two control variables – the electrode length  $h_{el}$  and the stimulation amplitude  $\varphi_{stim}$ . These variables were optimised through the use of the *Optimization module* in COMSOL, with the Nelder-Mead-Simplex algorithm [271, 272] being employed for this purpose. An optimality tolerance of 0.001 was set to represent the relative accuracy in the final values of the scaled control variables. The derivative-free Nelder-Mead-Simplex algorithm explores the design space around the current iterate by evaluating the goal function. Transformations are applied on the point of the simplex with the poorest goal function value. If no further improvement of the goal function is achieved with relative increments of the scaled control variables greater or equal to the tolerance, the optimisation iteration is terminated. In this thesis, the stimulation amplitude was optimised between the lower and upper bounds of the control variable  $\varphi_{stim} = 0.2 \dots 4 \text{ V}$  with an initial value of  $\varphi_{stim} = 0.2 \text{ V}$ .<sup>4</sup> I defined a scaling factor of 2 V to ensure that this control variable is in the order of magnitude of 1, enabling the optimisation algorithm to function properly. Initial values, scales and bounds of the control variables are summarised in Table 5.2. In the same way, a lower bound of 10 mm and an upper bound of 27 mm were specified for  $h_{el}$ , with an initial value of 20 mm and a scaling factor of 10 mm. These optimisation settings have been employed in both considered model scenarios (see Sec. 4.2.2). The results of the optimisation are explained in detail in the following section.

Control variable	Initial value	Scale	Lower bound	Upper bound
$h_{el}$	20 mm	10 mm	10 mm	27 mm
$\varphi_{stim}$	0.2 V	2 V	0.2 V	4 V

**Table 5.2:** Initial values, scaling factors, and bounds of the control variables  $h_{el}$  and  $\varphi_{stim}$  for optimising the electric field distribution in scenarios EQS<sub>Ga</sub> and QS<sub>Zi</sub>.

### 5.2.1 Optimised electric field distribution in the minipig mandible model

Analysing the volume of stimulated tissue shows that the optimal electrode configuration for maximising the volume of beneficially stimulated tissue and minimising overstimulation in the defect domain differs significantly for the two scenarios considered. Specifically, in scenario EQS<sub>Ga</sub>, the determined optimised configuration is

<sup>3</sup>Initially, the volumes of stimulated tissue are in the order of  $10^{-6} \text{ m}^3$ , so scaling is necessary.

<sup>4</sup>All voltages and currents are presented as zero to peak values in this thesis.

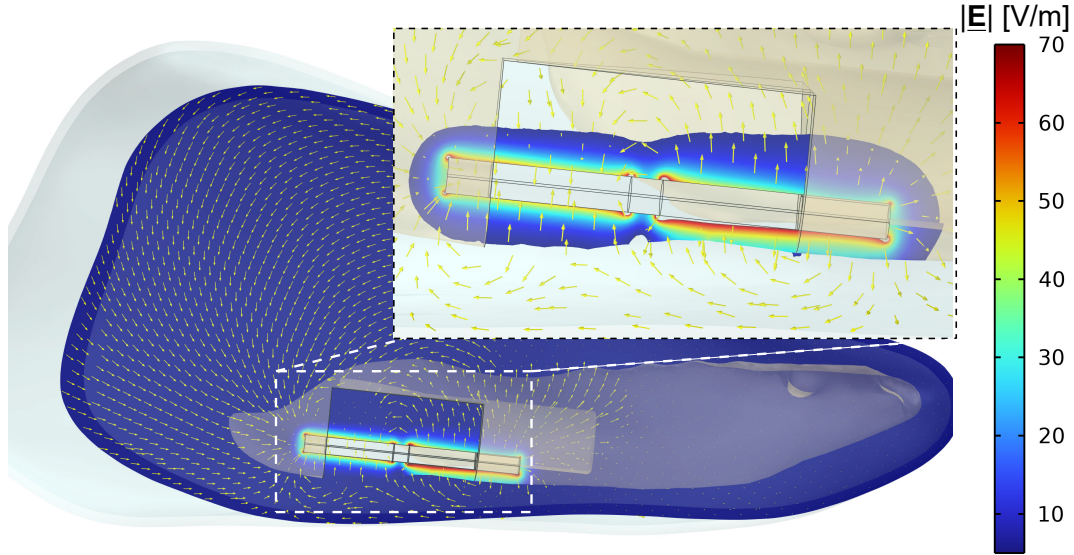


**Figure 5.4:** Simulated electric field norm  $|\mathbf{E}|$  in a slice through the electrically stimulated minipig mandible for the optimised scenario EQS<sub>Ga</sub> ( $h_{el} = 25.714$  mm and  $\varphi_{stim} = 0.41$  V). The scale is bounded for field strengths between 5 and 70 V/m and the arrow length of the electric field lines is normalised. Refer to the inset for visualisation of the beneficially stimulated region in the plane. The defect material is omitted in the inset for better visualisation. At a distance of about 10 mm from the electrode, the electric field norm has dropped below 3 V/m. The distance between the electrode surface and the upper edge of the defect is approximately 12 mm, the width of the defect is 35 mm. Adapted from [38].

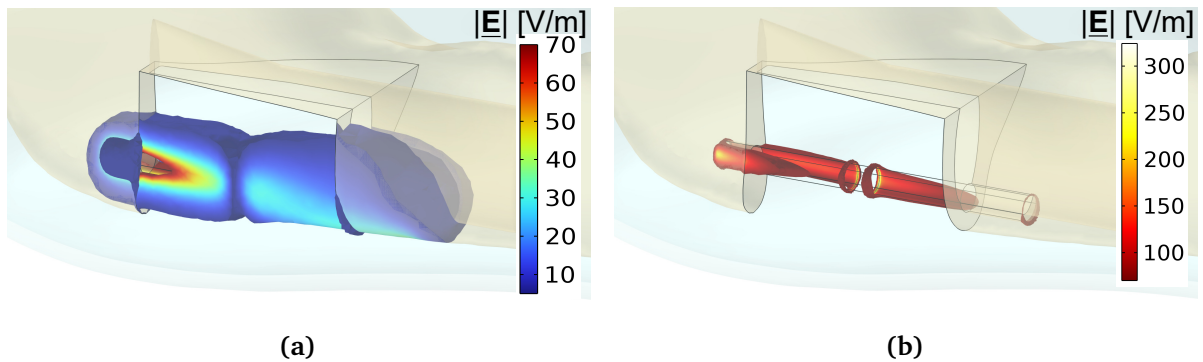


**Figure 5.5:** Volumes with beneficially (a) and overstimulated (b) tissue around the electrostimulating implant in EQS<sub>Ga</sub>. Note the different scale for the overstimulated region. Maximum field amplitudes of over 500 V/m are reached at the electrode-insulator interface. To ensure better visualisation, the defect material has been omitted.

$h_{el} = 25.7$  mm and  $\varphi_{stim} = 0.41$  V. For scenario QS<sub>Zi</sub>, a similar electrode length  $h_{el} = 25.9$  mm but a 50 % larger stimulation amplitude of  $\varphi_{stim} = 0.60$  V was found to be optimal (Table 5.3). The optimised electrode configuration resulted in a terminal current of 0.9 mA for EQS<sub>Ga</sub> and a value that is almost twice as large ( $I_{term} = 1.7$  mA)

for  $QS_{Zi}$ . The impedance of the system is also noticeably different with  $455\ \Omega$  for  $EQS_{Ga}$  and  $354\ \Omega$  for  $QS_{Zi}$ . These significant differences are a result of the distinct sets of dielectric tissue properties used in the two scenarios.<sup>5</sup> Scenario  $QS_{Zi}$  includes a correction of the tissue data for electrode effects and therefore results in substantially higher conductivities compared to  $EQS_{Ga}$  (Table 4.2).<sup>6</sup> These higher conductivities lead to the observed the higher current and smaller impedance in  $QS_{Zi}$ .

Scenario	$h_{el}$ [mm]	$\varphi_{stim}$ [V]	$I_{term}$ [mA]	$ Z $ [ $\Omega$ ]
$EQS_{Ga}$	25.7	0.41	0.9	455
$QS_{Zi}$	25.9	0.60	1.7	354

**Table 5.3:** Optimised electrode configuration in terms of the electrode length  $h_{el}$  [mm] and the stimulation voltage  $\varphi_{stim}$ . Additionally, the corresponding terminal current  $I_{term}$  flowing through the system and the impedance  $|Z|$  of the system in scenarios  $EQS_{Ga}$  and  $QS_{Zi}$  are provided.

Figure 5.4 displays the simulated electric field norm  $|\underline{E}|$  and the electric field lines in a vertical slice of the mandible bone through the defect region (defect width 35 mm) and electrodes (electrode diameter 4 mm) for the optimised scenario  $EQS_{Ga}$ . The situation is very similar in scenario  $QS_{Zi}$ , therefore it is not shown here. Note that the colour legend only extends from 5–70 V/m to highlight the thresholds for beneficial bone stimulation. The electric field extends all around the electrodes, where it reaches the desired values between 5 and 70 V/m. Still, it also decreases rapidly with increasing distance from the electrodes because the conductivity of the tissue is comparatively high.

The determined beneficial stimulation volume has a dumbbell shape surrounding the electrodes, as depicted in Fig. 5.5 (a). The extension of this shape is restricted by the floating potential boundary condition around the defect boundary, resembling a metal, i.e. highly conducting, stabilisation mesh tray. At the posterior part of the mandible, the beneficial stimulation volume reaches at least 4 mm into the tissue. As the field is not limited by the mesh tray at its open sides in longitudinal direction of the defect, here, the beneficial stimulation volume extends further into the soft tissue. Additionally, it is generally observable that the volume of beneficially stimulated tissue evolves asymmetrically around the stimulation electrodes such that it is significantly greater in the anterior region of the defect. This is attributed to the abundance of the less conductive cortical bone next to the cancellous bone domain. However, at a distance of about 10 mm from the electrode, the electric field norm has dropped below 3 V/m. The distance between the electrode surface and the upper edge of the defect is

<sup>5</sup>I would like to emphasise that  $QS_{Zi}$  is *not* an approximation of  $EQS_{Ga}$ , as the two scenarios are based on the different sets of dielectric tissue properties mentioned above.

<sup>6</sup>Note that specifically the corrected tissue data in scenario  $QS_{Zi}$  make the QS approximation of Maxwell's equation possible, see Sec. 4.2.2, page 42.



approximately 12 mm. The region with overstimulation ( $|\underline{E}| > 70 \text{ V/m}$ ) is limited to a small area ( $< 1 \text{ mm}$ ) directly around the electrodes and is located mainly towards the sides of the mesh tray Fig. 5.5 (b).

As previously stated, both scenarios, i.e.  $\text{EQS}_{\text{Ga}}$  and  $\text{QS}_{\text{Zi}}$ , yield relatively similar results in terms of the optimised electric field distribution. However, there will be an examination of the minor distinctions in the next section.

### 5.2.2 Comparison of the optimised electric field distribution in both scenarios

Overall, the optimised configurations for both scenarios, namely  $\text{EQS}_{\text{Ga}}$  and  $\text{QS}_{\text{Zi}}$ , generate highly comparable proportions of under-, beneficially and overstimulated tissue in the defect region, as shown in Table 5.4. In each scenario, roughly half of the defect volume is beneficially stimulated, while slightly more than 50 % of the volume is understimulated. In terms of total numbers, the volume of beneficially stimulated tissue is only  $0.4 \text{ mm}^3$  greater in  $\text{QS}_{\text{Zi}}$  compared to  $\text{EQS}_{\text{Ga}}$ . The amount of overstimulated tissue is small at 2.12 % ( $\text{EQS}_{\text{Ga}}$ ) and 2.07 % ( $\text{QS}_{\text{Zi}}$ ). As a result, the volume of overstimulated tissue in the defect region is only  $3.0 \text{ mm}^3$  greater in  $\text{EQS}_{\text{Ga}}$  than in  $\text{QS}_{\text{Zi}}$ . Figure 5.6 illustrates the volume of beneficially stimulated tissue for the optimised configuration of both scenarios. It underlines the very similar extent of beneficially stimulated tissue in both scenarios. The same applies to the overstimulated volume (as shown in Fig. 5.7) and the understimulated volume (not depicted).

Scen.	$V_{\text{under}} [\text{mm}^3]$	$V_{\text{bene}} [\text{mm}^3]$	$V_{\text{over}} [\text{mm}^3]$	$V_{\text{under}} [\%]$	$V_{\text{bene}} [\%]$	$V_{\text{over}} [\%]$
$\text{EQS}_{\text{Ga}}$	2787.9	2603.0	116.9	50.62	47.26	2.12
$\text{QS}_{\text{Zi}}$	2790.5	2603.4	113.9	50.66	47.27	2.07

**Table 5.4:** Volume of under- ( $V_{\text{under}}$ ), beneficially ( $V_{\text{bene}}$ ), and overstimulated ( $V_{\text{over}}$ ) tissue in the defect region for the considered scenarios  $\text{EQS}_{\text{Ga}}$  and  $\text{QS}_{\text{Zi}}$  in  $\text{mm}^3$  and in % of the total defect volume.

For the analysis of the deterministic, optimised electrode configuration for  $\text{EQS}_{\text{Ga}}$  and  $\text{QS}_{\text{Zi}}$ , the electric field norm  $|\underline{E}|$  is plotted along three lines perpendicular to the electrode surface as a function of the distance to the upper electrode surface (Fig. 5.8). Since there are only minor differences in the course of the field strength in both scenarios, only the result for  $\text{QS}_{\text{Zi}}$  is shown in Fig. 5.8 (a).

In Fig. 5.8 (b) it can be seen that the course of the electric field norm  $|\underline{E}|$  is only slightly different for the two scenarios. Only for the middle line,  $|\underline{E}|$  is noticeably higher for  $\text{QS}_{\text{Zi}}$  (max.  $5 \text{ V/m}$ ) than for  $\text{EQS}_{\text{Ga}}$ . The value of  $|\underline{E}|$  is higher in the left portion of

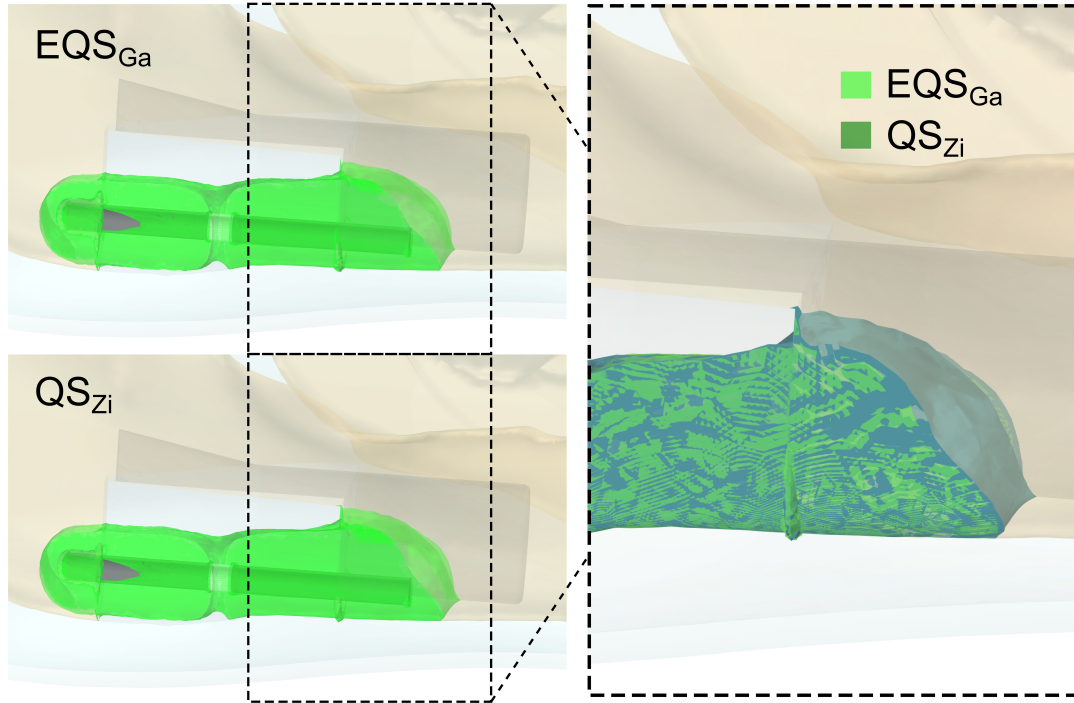


**Figure 5.6:** Visualisation of the volume of beneficially stimulated tissue ( $5 \text{ V/m} \leq |\mathbf{E}| \leq 70 \text{ V/m}$ ) for both optimised scenarios. Top left:  $\text{EQS}_{\text{Ga}}$ , bottom left:  $\text{QS}_{\text{Zi}}$ . Inset on the right: superimposed plot of both scenarios. Note that the extent of the beneficial volume differs only slightly (see inset). For  $\text{QS}_{\text{Zi}}$ , the beneficially stimulated volume in the defect region is  $0.4 \text{ mm}^3$  greater than in  $\text{EQS}_{\text{Ga}}$ .

the defect region for both scenarios, but it attenuates more quickly and to lower field strengths on the right portion of the defect region (Figure 5.8 (b)). In the middle line, the overall field strengths is lowest due to the dumbbell-shaped distribution of the field around the bipolar stimulation electrodes.

Furthermore, it is interesting to note the impact of the irregular model geometry on the field strength (Fig. 5.8 (a)). For the part below the electrode ( $\Delta x < 0$ ), the location of the mesh tray (i.e. floating potential boundary condition) is particularly noticeable: from left to right (i.e. from the posterior to the anterior part of the defect), the distance from the electrode to the mesh tray is smaller, and the field diminishes accordingly at smaller distances from the electrode. The field strength at the lower electrode surface (negative  $\Delta x$  values) is higher at the right (anterior) electrode (approximately  $75 \text{ V/m}$   $\text{EQS}_{\text{Ga}}$ ,  $78 \text{ V/m}$   $\text{QS}_{\text{Zi}}$ ) than at the left (posterior) electrode surface (approximately  $49 \text{ V/m}$   $\text{EQS}_{\text{Ga}}$ ,  $51 \text{ V/m}$   $\text{QS}_{\text{Zi}}$ ). The middle cut line displays even lower field strengths ( $24 \text{ V/m}$   $\text{EQS}_{\text{Ga}}$ ,  $28 \text{ V/m}$   $\text{QS}_{\text{Zi}}$ ) attributed to the dumbbell-shaped field distribution around the bipolar electrodes. However, the differences for the upper electrode surface (positive  $\Delta x$  values) are less pronounced. When comparing the electric field norm for both scenarios in the immediate vicinity of the electrode (as illustrated in Fig. 5.8 (b)), significant disparities only emerge for the middle cut line. Specifically, the field norm for  $\text{QS}_{\text{Zi}}$  exceeds that of  $\text{EQS}_{\text{Ga}}$  by approximately  $8 \text{ V/m}$  at the electrode surface. However,

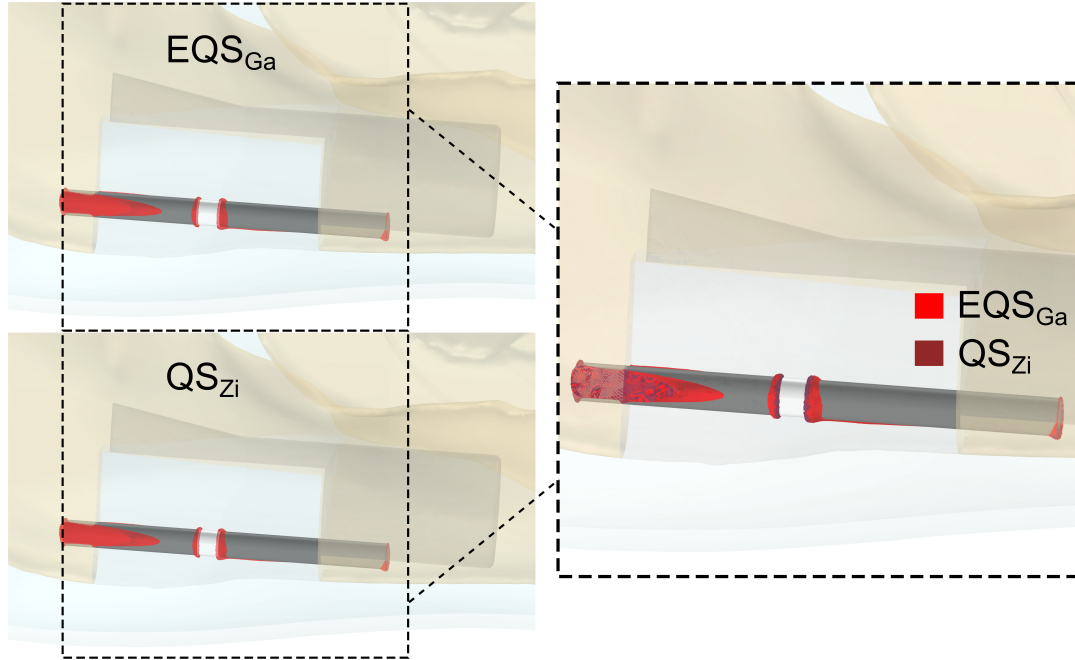


**Figure 5.7:** Visualisation of the volume of overstimulated tissue ( $|E| > 70 \text{ V/m}$ ) for both optimised scenarios. Note that the extent of the beneficial volume differs only slightly (see inset). For  $\text{EQS}_{\text{Ga}}$ , the overstimulated volume in the defect region is  $3.0 \text{ mm}^3$  greater than in  $\text{QS}_{\text{Zi}}$ .

this disparity fades with increasing distance from the electrode. At  $\Delta x = 5.5 \text{ mm}$ , the outcomes for both scenarios are indistinguishable.

Because the same properties are used to model the cancellous bone above the upper edge of the defect as in the defect region, and due to the irregular shape of the cancellous part and its increasing height towards the left, different  $\Delta x$  values are observed for the side above the electrodes where the field strength approaches zero (see Fig. 5.8 (a)). In this instance, a steep increase in field strength is observable as a consequence of the material boundary towards the less conductive cortical bone. An anticipated, albeit small, rise in field strength at the boundary of cancellous and cortical bone is only observable for the right electrode at a distance of approximately 12 mm. However, for the left electrode, the field has already decreased significantly due to the greater distance between the material boundary and the electrode. Therefore, the field change cannot be identified in the chosen representation.

I will now examine the distribution of the electric field throughout the whole 3D minipig model. As expected, the electric field strength decreases rapidly as the distance from the electrodes increases in the defect region (Fig. 5.9). Analysis of the maximum and minimum electric field magnitudes in the other model domains, i.e. spongiosa (cancellous bone domain), cortical bone, mucosa, and skin, reveals that the level of considerable electric field strength in the tissue domains of the mucosa and the skin

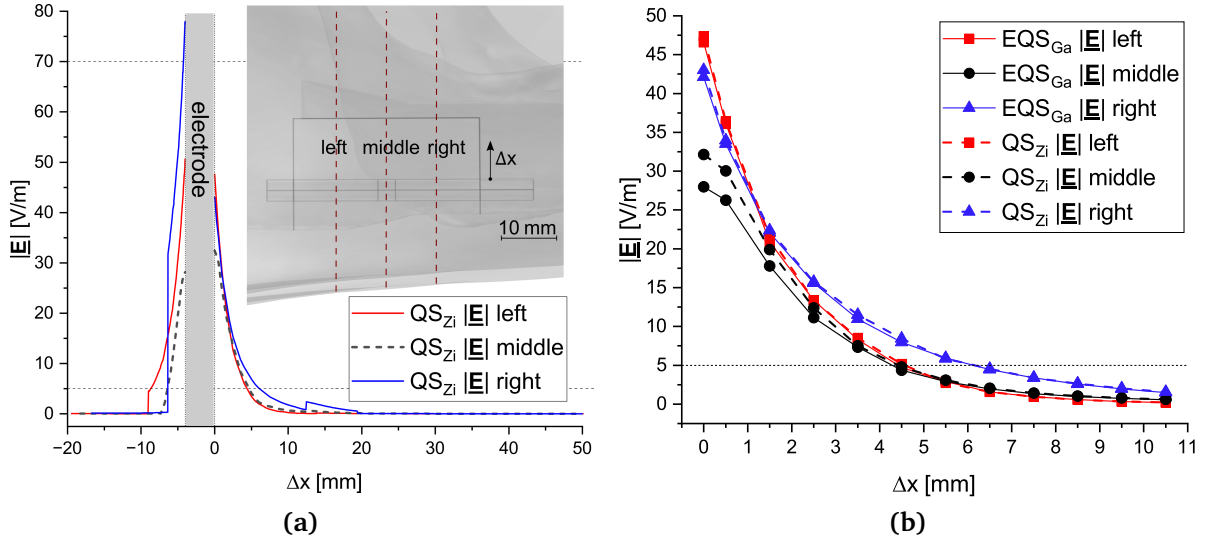


**Figure 5.8:** Electric field norm  $|\underline{E}|$  simulated along three lines perpendicular to the electrode surface. The inset in (a) displays the position of these lines in the left (posterior), middle, and right (anterior) portion of the defect. (a) Exemplary plot for  $QS_{Zi}$  regarding a broad range of distances to the electrode surface. (b) Comparative plot of the electric field strength curve for both considered scenarios ( $EQS_{Ga}$  straight line,  $QS_{Zi}$  dashed line). The course of  $|\underline{E}|$  differs only slightly for both scenarios. The dotted lines indicate the region of beneficially stimulated tissue ( $5 \text{ V/m} \leq |\underline{E}| \leq 70 \text{ V/m}$ ).

Domain	$EQS_{Ga}$			
	$ \underline{E} _{\max}$ [V/m]	$ \underline{E} _{\min}$ [V/m]	$V_{\text{bene}}$ [mm <sup>3</sup> ]	$V_{\text{over}}$ [mm <sup>3</sup> ]
Defect	534	0.0123	2603	117
Spongiosa	167	0.005	509	0.1
Cortical bone	486	0.0022	1895	20
Mucosa	49	$3.8 \cdot 10^{-4}$	44	0
Skin	1	0.0016	0	0

**Table 5.5:** Maximum ( $|\underline{E}|_{\max}$ ) and minimum ( $|\underline{E}|_{\min}$ ) values of the electric field norm  $|\underline{E}|$  and volumes of beneficially stimulated ( $V_{\text{bene}}$ ) and overstimulated ( $V_{\text{over}}$ ) tissue in the different model domains for scenario  $EQS_{Ga}$ . The maximum values are usually located next to the electrode (defect, cortical bone, spongiosa) or next to mesh tray (mucosa). The maximum and minimum values for scenario  $QS_{Zi}$  were in the same order of magnitude and are not given here for the sake of brevity.

is insignificant (Table 5.5). In both the spongiosa domain (509 mm<sup>3</sup>) and the cortical bone domain (1895 mm<sup>3</sup>), there is substantial stimulation at beneficial field strengths. The volume of overstimulated tissue in these domains, however, is not significant. It is important to note that no field ranges exist to determine potential harmful or beneficial

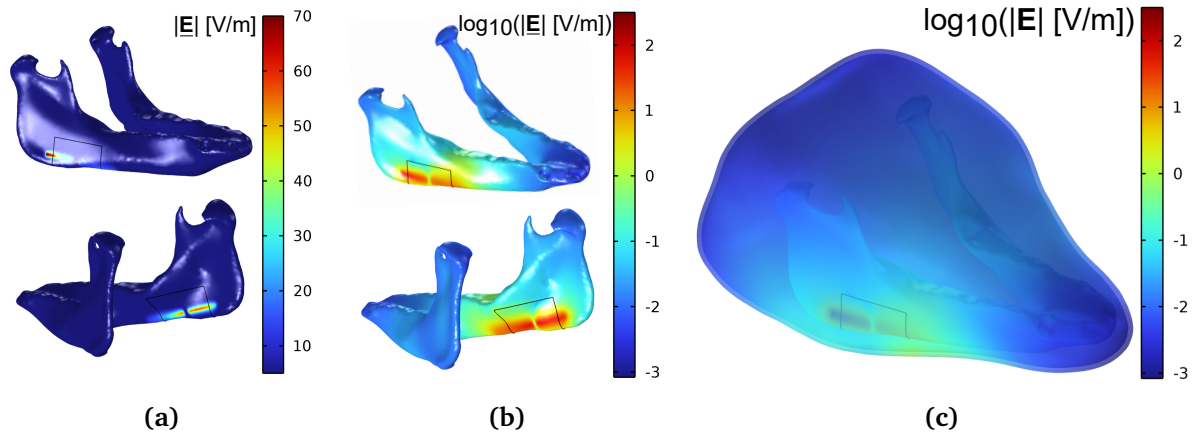


**Figure 5.9:** Norm of the electric field strength  $|E|$  in (a), (b) the cortical bone and (c) the whole minipig model. Note the logarithmic scale in (b) and (c) as the electric field strength decreases rapidly with increasing distance from the electrodes.

field values in tissues other than bone. Whether a specific stimulation signal has negative effects on the tissue also depends on the electrode material, the signal form, and the frequency [273]. No literature thresholds were discovered for this particular situation in this dissertation. Consequently, the 5–70 V/m threshold defined for bone was also employed for the other tissues. Based on this assumption, it can be deduced that there will be only little harm to adjacent tissues with the optimised electrode configuration in EQS<sub>Ga</sub> (Table 5.5) and QS<sub>Zi</sub> (not shown due to very similar results). Nonetheless, the actual nature of any potential effects of this particular stimulation design on the surrounding soft tissue can only be revealed through *in vivo* trials [273].

### 5.2.3 Comparison of optimisation results with previous findings

The optimisation results stemming from the two conductivity scenarios studied in this thesis (EQS<sub>Ga</sub> and QS<sub>Zi</sub>) will also be compared to two additional cases. The first case compares to the optimisation results from my paper, Raben et al. [34], which used a preliminary version of the numerical minipig model. The model did not utilise own bone measurement data but only employed *uncorrected* Gabriel data [29] for the dielectric tissue properties and had a slightly different electrode design, incorporating a 1 cm long fixation pin with 1 mm diameter at the end of the posterior electrode. Secondly, the outcomes of using the optimised electrode parameters from Raben et al. [34], along with tissue properties utilised in scenario QS<sub>Zi</sub> of this thesis will be

Case	$h_{\text{el}}$ [mm]	$\varphi_{\text{stim}}$ [V]	$V_{\text{under}}$ [%]	$V_{\text{bene}}$ [%]	$V_{\text{over}}$ [%]
EQS <sub>Ga</sub>	25.7	0.41	50.62	47.26	2.12
QS <sub>Zi</sub>	25.9	0.60	50.66	47.27	2.07
Raben et al. [34]	25.0	0.52	48.75	48.96	2.29
Raben et al.   QS <sub>Zi</sub>	25.0	0.52	53.89	44.79	1.32

**Table 5.6:** Optimised electrode configuration (electrode length  $h_{\text{el}}$  and the stimulation voltage  $\varphi_{\text{stim}}$ ) and corresponding percentage of under-, beneficially, and overstimulated volumes in the defect region for different optimised model cases, including the scenarios considered in this thesis (EQS<sub>Ga</sub> and QS<sub>Zi</sub>). Note that the model in Raben et al. [34] differed from the model regarded in this thesis by employing a slightly different electrode design. All models significantly differ from each other by using different sets of dielectric tissue properties.

presented (referred to as “Raben et al. | QS<sub>Zi</sub>”).<sup>7</sup> This enables the evaluation of the effects of the previously uncorrected tissue properties applied in [34].

Table 5.6 displays the percentages of under-, beneficially, and overstimulated volume in the defect region for each of the four cases. In general, the results indicate similar proportions of stimulated tissue across all four compared scenarios. Approximately one half of the defect volume is understimulated, while slightly less than one half is beneficially stimulated. The volume of overstimulated tissue falls within the range of 1.3–2.3 % with the least amount of overstimulation observed in Raben et al. | QS<sub>Zi</sub>. However, here also the percentage of beneficially stimulated tissue was 2.5 percentage points lower than in the models established in this thesis. Therefore, it is possible that the volume of beneficially stimulated tissue during *in vivo* application was slightly smaller than anticipated in [34]. Still, the differences in stimulated volumes are too small to significantly impact the overall successful outcome of the *in vivo* animal studies.

## 5.2.4 Discussion

From the volume plot of the beneficially and overstimulated volumes (Fig. 5.5), it is evident that the fixation mesh has a significant impact. When the distance between the implant and the fixation mesh is small, the electric field reaches critically high values. This is because the equipotential mesh tray with the applied floating potential boundary condition can be considered as an additional electrode. For practical applications, it is therefore advisable to ensure that the fixation mesh is kept at an appropriate distance from the electrode. Additionally, it must be ensured that the fixation mesh is

<sup>7</sup>I would like to remind the reader that scenarios EQS<sub>Ga</sub> and QS<sub>Zi</sub> are based on different sets of dielectric properties, either including a correction for electrode processes (QS<sub>Zi</sub>) or not (EQS<sub>Ga</sub>). The respective sets of dielectric properties in turn allow either for applying the EQS or QS approximation, see Table 4.3.

sufficiently stable so that it does not deform when the animals perform their normal activities, such as chewing and rubbing their cheeks. Otherwise, the deformed mesh tray could result in increased and harmful electric field strengths or even a shorted electrode. Deformed mesh trays were observed during the *in vivo* animal study [48], which could have contributed to the suboptimal bone growth results in the defect region (see Sec. 5.4). Evidently, the titanium mesh selected by the oral and maxillofacial surgeons was insufficiently robust. Consequently, future studies will give specific focus to the development of mechanically stable electrostimulating implants and improved implant designs. For instance, other researchers have employed LCP, a biomaterial that possesses a mechanical strength comparable to that of bone, to stabilise their electrostimulation system in a small animal model (rabbit) [13]. I am contributing to a similar approach currently being advanced in the SFB 1270 ELAINE, with a particular focus on the development of reliably stable, load-bearing implants based on the titanium alloy Ti6Al4V.

By specifying strict weighting of the objective function for overstimulation, in the optimised setting only 2.1 % of the tissue receives potentially harmful field strengths greater than 70 V/m. It is favourable that the simulated volume of overstimulated tissue is generally much smaller than the volume of beneficially stimulated tissue. Otherwise, the related tissue damage would undo the healing impact of the electric stimulation in certain regions of the defect. However, it was observed that the desired field threshold between 5 and 70 V/m is not only achieved in the bone, but also in the soft tissue. The consequences of this need to be carefully studied in the *in vivo* experiments as the impact of such fields on soft tissue is not exactly known.

Forcing the optimisation to avoid overstimulation further resulted in a relatively low optimal stimulation amplitude of about  $\varphi_{\text{stim,opt}} = 0.41 \text{ V}$  ( $\text{EQS}_{\text{Ga}}$ ) and  $\varphi_{\text{stim,opt}} = 0.60 \text{ V}$  ( $\text{QS}_{\text{Zi}}$ ). This is also favourable in terms of ensuring a long battery life for the animal experiments. Additionally, Liboff et al. [196] observed significant electrolysis at stimulation potentials exceeding 1 V. Hence, it is advisable to refrain from utilising voltages as high as this in the proposed electrostimulating devices. As per [274] (reproduced in [275]), AC electric currents with peak values greater than 0.71 mA in the frequency range of 15 to 100 Hz are perceivable by humans. Therefore, the computed currents of 0.9 mA ( $\text{EQS}_{\text{Ga}}$ ) and 1.7 mA ( $\text{QS}_{\text{Zi}}$ ), which flow between the electrode and the tissue, may be physically perceivable. Nevertheless, the values of the electric currents obtained in this thesis are considerably lower than the muscular response threshold (5 mA [274]). As a result, the electric currents in the optimised stimulation setup can be considered suitable for long-term stimulation. However, only *in vivo* experiments can reveal the actual impact.

With regard to possible heat generation, the implant can be considered as safe: The phenomenon of heat production by an electric current passing through a resistance is known as *Joule heating* or *resistive heating*. The heat dissipation resulting from electrical stimulation could affect bone healing. Previous research indicated that a modest increase in temperature (hyperthermia) can facilitate bone formation [276, 277]. Conversely, temperatures exceeding 47 °C were associated with increased bone



resorption in rabbits [278]. In preliminary studies beyond the scope of this work, I numerically estimated the time-dependent temperature increase and heat generation near the electrostimulating implant. The model was simplistic in the sense that the uncorrected tissue properties of Gabriel et al. [29] were used and no ETI was considered. The frequency-transient studies indicate that electrical stimulation with  $\varphi_{\text{stim}} = 1.2 \text{ V}$  at  $f = 20 \text{ Hz}$  for 50 minutes causes a temperature increase of merely 0.1 K in the initial temperature of  $37^\circ\text{C}$ . Therefore, it is unlikely that severe tissue heating will occur, particularly since the applied stimulation voltage also was considerably higher than in this study.

It could be argued that given the achieved optimal outcome with approximately 50 % beneficially stimulated tissue in the defect region, further improvements are required, leading to the exploration of alternative electrode designs. I am actively contributing to this ongoing exploration of alternative electrode designs within the SFB 1270 ELAINE. Such an iterative refinement process, which in this work included several design modifications of the bipolar electrodes, of the design in consultation with collaborating colleagues is a crucial step in the development of an optimised electrostimulating implant. Nonetheless, the original rationale behind employing the bipolar electrode design was to ensure comparability with *in vitro* setups. Additionally, the clinical effectiveness of the bipolar electrode design for avascular necrosis of the femoral head has been demonstrated [279].<sup>8</sup>

To this end, it is further crucial to emphasise the need for interdisciplinary discussions on the findings with colleagues involved in developing the stimulation unit and conducting *in vivo* trials. In this regard, it is important to not only focus on the maximum volume of beneficially stimulated tissue but also to be aware of the associated power consumption of the implant. This is particularly important because batteries will be used for power supply in the experiments. These batteries have a limited lifespan that varies based on their capacity and the power required to drive the stimulation signal. Therefore, it may be necessary to strike a balance between optimal stimulation volume and energy usage. The stimulator that will drive the stimulation signal in the *in vivo* experiments, *STELLA Bone* [280, 281], is powered by a CR2450 button cell with a nominal capacity of  $Q = 620 \text{ mAh}$ . With  $Q = 1/\sqrt{2}It$ , such a battery could enable 974 hours ( $\text{EQS}_{\text{Ga}}$ ) or 516 hours ( $\text{QS}_{\text{Zi}}$ ) of stimulation. *In vivo*, the electrical stimulation is intended to be applied thrice a day for 45 minutes over a period of three to six weeks, equivalent to a total of 47 to 95 hours of treatment. Based on these numbers, it is evident that the selected battery can reliably meet the required energy demand, while also accounting for a safety margin.

Furthermore, the impedance of the system under consideration is a crucial parameter for its technical implementation. In this study, the impedance of the system falls within the range of 350–450  $\Omega$  (Table 5.3). For scenario  $\text{QS}_{\text{Zi}}$  with corrected tissue properties, the impedance of the system is markedly low due to the higher tissue conductivities (Table 4.2). Therefore, a higher current is needed to achieve the desired optimal region

<sup>8</sup>It should be noted that in this particular application of the so-called ASNIS III s-series™ screw, the electrical stimulation is achieved inductively.



of beneficially stimulated tissue. Driving such high currents could create technical challenges in the development of the stimulator required to power the electrostimulating implant, as experimental studies by colleagues on a very simplified stimulation setup for dimensioning the stimulator suggested impedances in the order of  $2\text{ k}\Omega$  [280]. As a result, the output stage of the stimulation unit may not be capable of driving the much higher current. Furthermore, the lower impedance necessitates a greater battery capacity. Therefore, future research needs to address these limitations by performing accurate experimental impedance characterisation in a setup that simulates real-world conditions, i.e. using the stimulation electrodes and surrounding tissues that would be present in an *in vivo* situation.

### 5.3 Uncertainty quantification and sensitivity analysis of an electrically stimulated minipig mandible

*Parts of this section have been published in the manuscript “Addressing model uncertainties in finite element simulation of electrically stimulated implants for critical-size mandibular defects”, which appeared in IEEE Transactions on Biomedical Engineering [38].<sup>9</sup>*

In the previous chapters, the electric stimulation system for bone regeneration in a critical-size defect of a minipig mandible was introduced and optimised. Nevertheless, both the lack of reliable measurement data and the intrinsic variations in the dielectric properties of biological tissues, as discussed in previous chapters, can significantly affect the reliability of the simulated electric field distribution. In addition, the parameters of the electrode-tissue interface are subject to considerable variability. To assess how uncertainties in the input data affect the predictions of the model, uncertainty quantification (UQ) methods described in Sec. 4.3 are utilised. For the sake of brevity, the UQ studies will only consider the influence of uncertain dielectric tissue properties and parameters of the electrode-tissue interface (ETI). The impact of variations in technical parameters like electrode length or stimulation amplitude will not be directly addressed in the UQ studies described here. However, a brief overview of how different values of these parameters impact the stimulated volumes is given in the context of parameter studies.

The present study employs the *generalised* polynomial chaos (gPC) method to evaluate the impact of uncertain dielectric properties on the simulated electrically stimulated volumes and further output quantities. This is achieved by computing the Sobol’ sensitivity indices and other relevant statistical measures. The following section describes the above analysis in detail.

#### 5.3.1 Specification of the probabilistic minipig model

Regarding the dielectric tissue properties in particular, sources of uncertainty include measurement uncertainties, biological variability over time, variations in conductivity across different bone regions due to the anatomical structure, and physiological conditions, as introduced in Chapter 4.1. For the minipig model, uncertain dielectric tissue properties were considered for cortical and cancellous bone, mucosa, and skin, as well as uncertain ETI parameters  $R_{CT}$ ,  $Y_0$ , and  $\beta$ . The UQ studies were conducted for both scenarios outlined in Sec. 4.2.2, page 42, with different sets of uncertain parameters being examined for each scenario. This was necessary because relative permittivities

---

<sup>9</sup>Ursula van Rienen, Peer W. Kämmerer, and I conceptualised the study. I carried out all simulations and the data analysis, wrote the initial draft of the manuscript and prepared the visualisation of the data. Ursula van Rienen initiated and supervised the project and provided methodological guidance. Ursula van Rienen and Peer W. Kämmerer acquired the funding and provided all resources.

were only modelled in EQS<sub>Ga</sub>. The electrode length and stimulation voltage in each scenario were chosen according to the optimised values as given in Table 5.3.

In order to quantify the impact of uncertainties in the dielectric tissue properties on the computed output quantities, it is necessary to define reasonable probability distributions for the uncertain parameters. I conducted extensive literature research on how to statistically model the dielectric properties of biological tissues. However, there appears to be no consensus on the specific type of distribution to be used in modelling these tissues. Due to the limited amount of data available, UQ studies that involve material or tissue properties often assume normal [255, 260, 282] or uniform distributions [174, 254, 257–259, 283–285]. The latter is used particularly often as it represents a “worst-case scenario” [174, 257, 258] with all parameter values having the same probability. Nevertheless, a bell-shaped distribution would naturally be expected for biological materials [286]. Some studies use beta distributions, but often without a detailed explanation of this choice in general or of the choice of the distribution parameters [256, 286].

Ideally, the distribution type and its parameters should be derived from experimental data. This ensures trustworthy analyses as the distribution characteristics heavily influence the UQ results. Following the statistical analysis of own measurement data of cancellous minipig mandibular bone, the dielectric tissue properties were modelled with normal distributions. The Shapiro-Wilk test [287] was used to prove that these measurement data can be described by normal distributions.<sup>10</sup> This test is particularly appropriate for small sample sizes with  $n < 50$ , as in the present investigation ( $n = 32$  for cancellous bone).<sup>11</sup> To describe the normal distributions for the dielectric properties of bone, I chose the mean values from the experiment (Table 5.1). The mean values for the dielectric properties of mucosa and skin were retrieved from Gabriel et al. [29], taking into account the correction for electrode polarisation where appropriate (scenario QS<sub>Zi</sub>). The standard deviations (STDs) for all tissue conductivities were selected so that STD/mean = 25 %. This is similar to [187], where STD/mean = 20 %. I assumed uniform distributions for the relative permittivities as a worst-case scenario, with a variation of  $\pm 50$  % around the mean value. This resulted in a relative input uncertainty of STD/mean  $\approx 28.9$  %.<sup>12</sup>

In preliminary UQ studies for QS<sub>Zi</sub>, the parameters  $\sigma_{\text{skin}}$ ,  $\sigma_{\text{muc}}$ , and  $R_{\text{CT}}$  were found to have almost no effect on the simulation results: the sum of their Sobol’ indices was generally less than 0.0005 for all analysed output quantities (refer to Fig. 5.14 and 5.15). As a result, these input parameters were excluded from the UQ studies for EQS<sub>Ga</sub>. Instead, the influence of the relative permittivities  $\varepsilon_{\text{r,cort}}$ ,  $\varepsilon_{\text{r,muc}}$ , and  $\varepsilon_{\text{r,canc}}$  was investigated in EQS<sub>Ga</sub>.

<sup>10</sup>I thank Dr. Piotr Putek for providing the statistical analysis.

<sup>11</sup>Unfortunately, statistical conclusions could not be drawn from the data for cortical bone due to its very small sample size ( $n = 5$ ). Nevertheless, the dielectric properties of cortical bone were also assumed to be normally distributed.

<sup>12</sup>Note that in case of the uniform distribution  $\text{STD} = (U - L)/\sqrt{12}$ , with  $U$  and  $L$  the upper and lower bounds of the distribution, respectively.

The parameters of the electrode-tissue interface ( $\beta$ ,  $Y_0$ , and  $R_{CT}$ ) were modelled using uniform distributions in order to account for a worst-case scenario due to unknown variations: during extensive literature research, I found that the reported parameter values differ significantly depending on the particular electrode material and surface properties (for  $Y_0$  and  $n$  [227, 288–291]; for  $R_{CT}$  [227, 288, 292, 293]). No detailed characterisation of the electrochemical and surface properties of the used electrodes is currently available, so I assumed uniform distributions with a variation of  $\pm 50\%$  for  $Y_0$  and  $R_{CT}$ . This decision is justified to cover a wide range of values due to possible changes of the electrode during the stimulation period, such as corrosion or deposition of calcium phosphate [24]. For  $\beta$ , I assumed that variations may reach as low as 0.7, as reported by Tamilselvi et al. [288] following apatite deposition. This can be compared to the deposition of calcium phosphate observed at similar electrodes during *in vitro* experiments [24]. The uncertain parameters assumed in each scenario, along with their corresponding distributions, are presented in Tables 5.7 (QS<sub>Zi</sub>) and 5.8 (EQS<sub>Ga</sub>). The remaining deterministic parameters were set to their nominal values as stated in Table 4.2.

Tissue	Distribution	Explanation
$\sigma_{canc}$	$\mathcal{N}(0.1003, 0.0251)$ S/m	Own measurements; assumed STD/mean = 25 %
$\sigma_{cort}$	$\mathcal{N}(0.0267, 0.0067)$ S/m	Own measurements; assumed STD/mean = 25 %
$\sigma_{skin}$	$\mathcal{N}(2.0, 0.5) \cdot 10^{-4}$ S/m	[29, 30]; assumed STD/mean = 25 %
$\sigma_{muc}$	$\mathcal{N}(0.363, 0.091)$ S/m	[30]; assumed STD/mean = 25 %
$R_{CT}$	$\mathcal{U}(138.0, 39.8)$ k $\Omega$	[227]; assumed $\pm 50\%$ variation
$Y_0$	$\mathcal{U}(19.5, 58.4)$ $\mu$ F	[227]; assumed $\pm 50\%$ variation
$\beta$	$\mathcal{U}(0.7, 1)$	[288]

**Table 5.7:** Assumed distributions for the electric conductivities and the electrode-tissue interface (ETI) parameters in scenario QS<sub>Zi</sub>. The normal distribution is denoted by  $\mathcal{N}$  and the uniform distribution is denoted by  $\mathcal{U}$ . The simulations were carried out for the optimised electrode configuration with  $h_{el} = 25.9$  mm and  $\varphi_{stim} = 0.60$  V.

In this study, the default settings of Uncertainpy [247] were used: fourth order polynomials (Hermite polynomials for the normally distributed input parameters and Legendre polynomials for input parameters following a uniform distribution, see Sec. 4.3.3) were used and the point collocation method with  $2(N_p + 1)$  collocation nodes was applied. This corresponds to 662 model runs in the case of  $M = 7$  uncertain parameters. I considered  $10^4$  PCE-MC samples for sampling the surrogate model  $\hat{\mathcal{M}}$  and determining the 5th and 95th percentiles and the 90 % prediction interval. The subsequent section presents the results obtained from the UQ analysis.

Tissue	Distribution	Explanation
$\sigma_{\text{canc}}$	$\mathcal{N}(0.0498, 0.0125)$ S/m	Own measurements; assumed STD/mean = 25 %
$\sigma_{\text{cort}}$	$\mathcal{N}(0.0168, 0.0042)$ S/m	Own measurements; assumed STD/mean = 25 %
$\varepsilon_{r,\text{canc}}$	$\mathcal{U}(6.3, 18.9) \cdot 10^6$	Own measurements; assumed $\pm 50$ % variation
$\varepsilon_{r,\text{cort}}$	$\mathcal{U}(1.6, 4.9) \cdot 10^6$	Own measurements; assumed $\pm 50$ % variation
$\varepsilon_{r,\text{muc}}$	$\mathcal{U}(12.2, 36.5) \cdot 10^6$	[29]; $\pm 50$ % variation
$Y_0$	$\mathcal{U}(19.5, 58.4)$ $\mu\text{F}$	[227]; assumed $\pm 50$ % variation
$\beta$	$\mathcal{U}(0.7, 1)$	[288]

**Table 5.8:** Assumed distributions for the dielectric properties and the electrode-tissue interface (ETI) parameters in scenario EQS<sub>Ga</sub>. The normal distribution is denoted by  $\mathcal{N}$  and the uniform distribution is denoted by  $\mathcal{U}$ . The simulations were carried out for the optimised electrode configuration with  $h_{\text{el}} = 25.7$  mm and  $\varphi_{\text{stim}} = 0.41$  V.

### 5.3.2 Global sensitivity analysis using Sobol' indices

In this research, a global sensitivity analysis was carried out using Sobol' indices to evaluate the influence of different input parameters on the output functions, as explained in Chapter 5.3. The considered output quantities are the volumes of under-, beneficially, and overstimulated tissue in the defect region ( $V_{\text{under}}$ ,  $V_{\text{bene}}$ ,  $V_{\text{over}}$ , as defined in Sec. 5.2) for both considered scenarios EQS<sub>Ga</sub> and QS<sub>Zi</sub>. Additionally, the terminal current  $I_{\text{term}}$  and the norm of the electric field  $|\mathbf{E}(P_1)|$  at an exemplary point  $P_1$  in the defect region at a distance of 3.5 mm from the electrode surface were taken into account. The position of  $P_1$  within the defect region is depicted in Fig. 5.11. For a comprehensive overview of the impact of the parameters on the output, also the standard deviation (STD) as well and the 5th and 95th percentile were computed.

When examining the first order Sobol' indices, I found that the input parameters exhibit different levels of influence on the output variables. The study demonstrates that in both conductivity scenarios the CPE parameter  $\beta$  is the most influential parameter for all considered output quantities, contributing about half of the output variance (see Fig. 5.10 and Fig. 5.11 in which the statistical metrics are presented exemplarily for scenario EQS<sub>Ga</sub>). The capacitance parameter  $Y_0$  is an additional influential quantity, accounting for ca. 21–28 % of the total variance. The impact of the conductivity of cancellous bone  $\sigma_{\text{canc}}$  is comparatively smaller, with first order sensitivity indices typically in the range of 0.5–0.12. The precise contributions vary depending on the different output quantities and the scenario considered. For instance, for  $I_{\text{term}}$  in EQS<sub>Ga</sub>, the contribution of  $\sigma_{\text{canc}}$  with  $S_{\sigma_{\text{canc}}} = 0.26$  is even larger than that of  $Y_0$  ( $S_{Y_0} = 0.22$ ). Additionally, in QS<sub>Zi</sub>  $\sigma_{\text{canc}}$  has a similarly large impact on the electric field norm as  $Y_0$  ( $S_{\sigma_{\text{canc}}} = 0.22$  and  $S_{Y_0} = 0.23$ , see Fig. 5.15 (d)). From their small Sobol' indices it is evident that the parameters  $\varepsilon_{r,\text{cort}}$ ,  $\varepsilon_{r,\text{muc}}$ ,  $\varepsilon_{r,\text{canc}}$ , and  $\sigma_{\text{cort}}$  (EQS<sub>Ga</sub>) as well as  $\sigma_{\text{cort}}$ ,  $\sigma_{\text{muc}}$ ,  $\sigma_{\text{skin}}$ , and  $R_{\text{CT}}$  (QS<sub>Zi</sub>) have a negligible impact on all considered output quantities. As

a result, these parameters could be assigned constant values to simplify the model in future studies. A more detailed comparison of the uncertainties in both examined scenarios will be presented in the subsequent section. Presently, I will concentrate on the situation in scenario EQS<sub>Ga</sub>.

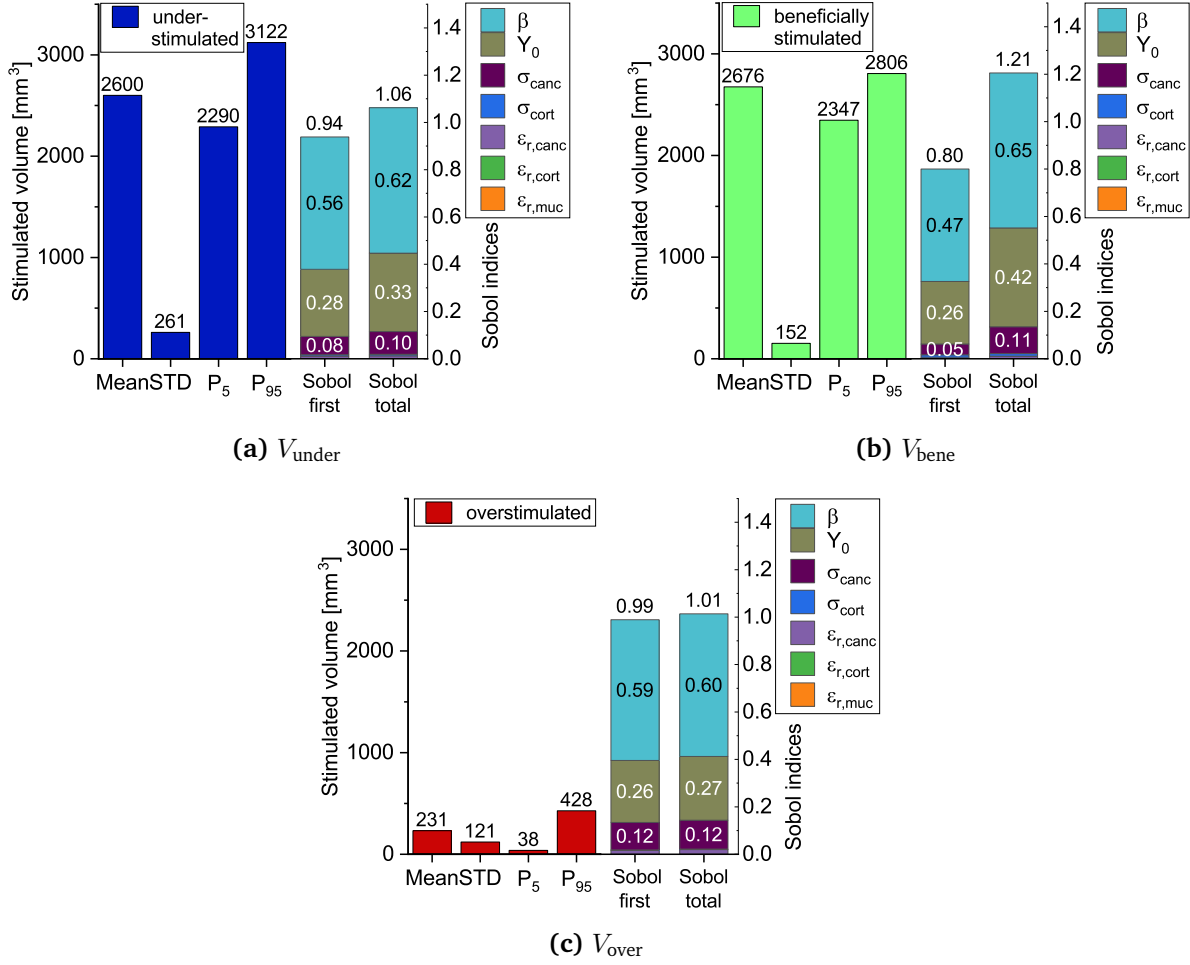


**Figure 5.10:** Statistical metrics (mean, standard deviation (STD), 5th (P5) and 95th percentile (P95)) and Sobol' indices (First order and total Sobol' indices) for the (a) under-stimulated, (b) beneficially stimulated, and (c) overstimulated tissue in the defect region in scenario EQS<sub>Ga</sub>. The dominant impact of the parameters  $\beta$  and  $Y_0$  is evident.  $\sigma_{\text{canc}}$  has an observable impact, while  $\sigma_{\text{cort}}$  and the relative permittivities  $\epsilon_r$  are negligible. Especially for the beneficially stimulated volume, the sum of the total Sobol' indices is significantly greater than one, suggesting interaction effects.

A distinct difference between the first order and total Sobol' index of a parameter indicates interactions between this parameter and the other parameters. Another indicator of the presence of interactions is that the sum of the first order Sobol' indices is significantly less than one. Simultaneously, the sum of the total Sobol' indices is significantly greater than one. As illustrated in Fig. 5.10, the difference between the first order and total Sobol' indices for the parameters  $\beta$ ,  $Y_0$ , and  $\sigma_{\text{canc}}$  is particularly significant in relation to  $V_{\text{bene}}$ . This implies that these parameters have a notable impact

on this output quantity due to both direct and interaction effects. It also suggests that the interactions between  $\beta$ ,  $Y_0$ ,  $\sigma_{\text{canc}}$  and the other input parameters play a vital role in determining the output variability. However, it should be noted that the overall uncertainty in  $V_{\text{bene}}$  is relatively low, with  $\text{STD}/\text{mean} \approx 5.7\%$ , indicating that the actual variations resulting from parameter interactions are not expected to be very pronounced. The interactions are mostly evident for  $V_{\text{bene}}$  as specific combinations of parameter values may cause the set field threshold of  $5 \text{ V/m} \leq |\underline{\mathbf{E}}| \leq 70 \text{ V/m}$  to be surpassed either upwards or downwards, resulting in a variation in the volume of beneficial stimulation. For  $V_{\text{under}}$  and  $I_{\text{term}}$ , only minor interaction effects are apparent, with  $\sum_i S_{T_i} \approx 1.06$ . The interaction effects for  $V_{\text{over}}$  and  $|\underline{\mathbf{E}}(P_1)|$  are negligible.

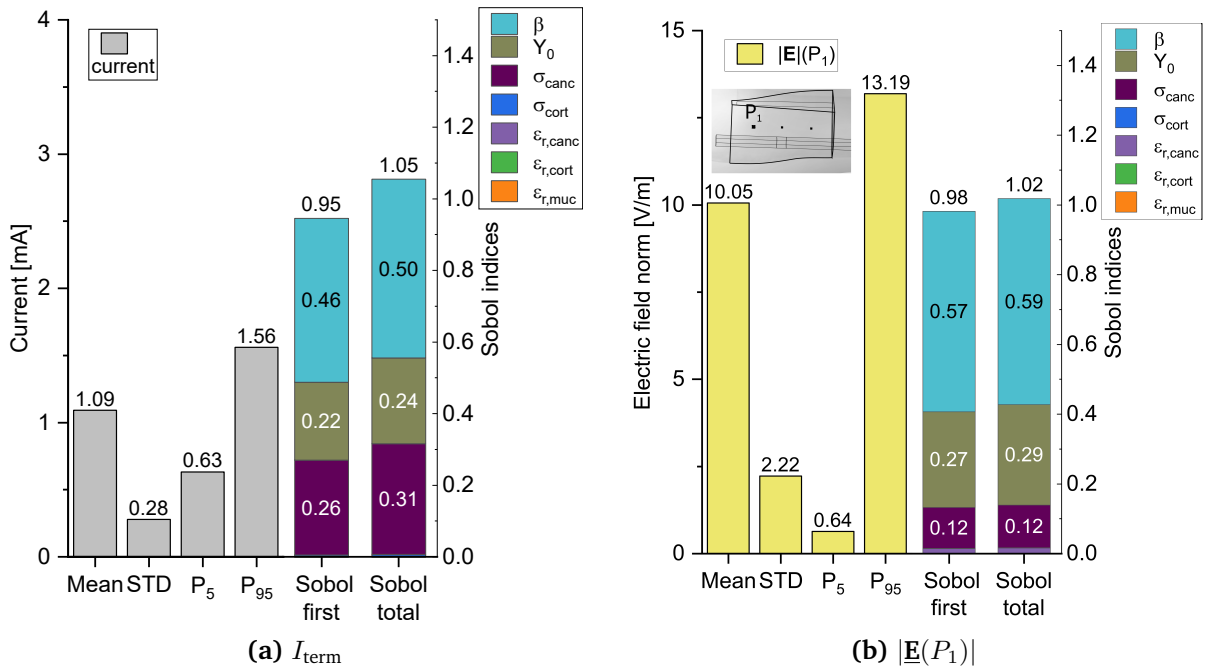


**Figure 5.11:** Statistical metrics (mean, standard deviation (STD), 5th (P5) and 95th percentile (P95)) and Sobol' indices (First order and total Sobol' indices) for the (a) terminal current  $I_{\text{term}}$  and (b) the electric field norm  $|\underline{\mathbf{E}}(P_1)|$  in point  $P_1$  in EQS<sub>Ga</sub>. The dominant contribution of the parameters  $\beta$  and  $Y_0$  is evident.  $\sigma_{\text{canc}}$  has an observable impact, while  $\sigma_{\text{cort}}$  and the relative permittivities  $\epsilon_r$  are negligible. For  $I_{\text{term}}$ , the sum of the total Sobol' indices is slightly greater than one, implying the possibility of interaction effects. In (b), the location of the point  $P_1$  is indicated. Statistical metrics and Sobol' indices for the other displayed points were very similar to that of  $P_1$ , so they are not shown separately.

The UQ studies in this thesis were carried out for scenarios EQS<sub>Ga</sub> and QS<sub>Zi</sub>. The following section will examine the similarities and differences concerning the uncertainties in both of these scenarios.

### Impact of the conductivity scenario on the statistical metrics and the Sobol' indices

Both scenarios defined in this thesis considered different sets of uncertain input parameters and different total parameter ranges, e.g., for the cancellous bone conductivity  $\sigma_{\text{canc}}$  (Sec. 5.3.1). As a result, a direct comparison between the two scenarios is neither feasible nor intended. Instead, the individual outcomes of both scenarios aim to provide insight into the impacts of uncertain input quantities.

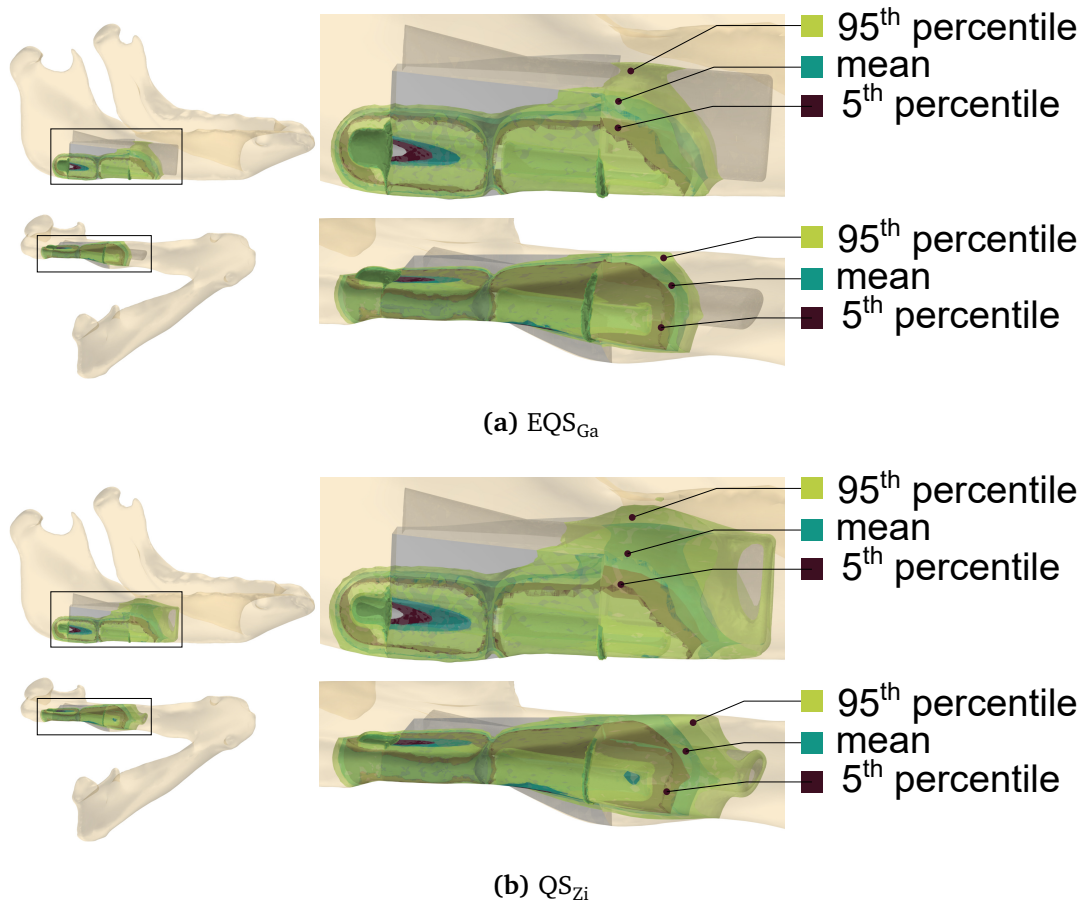


**Figure 5.12:** Exemplary visualisation of the beneficially stimulated tissue ( $5 \text{ V/m} \leq |\mathbf{E}| \leq 70 \text{ V/m}$ ) in the probabilistic model in (a) EQS<sub>Ga</sub> and (b) QS<sub>Zi</sub>. Shown are the 95th percentile, the mean, and the 5th percentile. Figure adapted from [38].

In Fig. 5.12 and Fig. 5.13 the 95th percentile, mean, and 5th percentile of the beneficially and overstimulated volume are illustrated for both of the optimised scenarios. The aforementioned dumbbell-shaped electric field distribution is again evident, and the asymmetry in the beneficial electric field distribution is even more pronounced than in the deterministic models. The 5th percentile of the beneficially stimulated volume resembles a relatively narrow region around the electrode, penetrating approximately 4–5 mm into the defect tissue in both scenarios. For the mean value in scenario QS<sub>Zi</sub>, the beneficially stimulated volume reaches ca. 5–10 mm into the defect tissue. For the



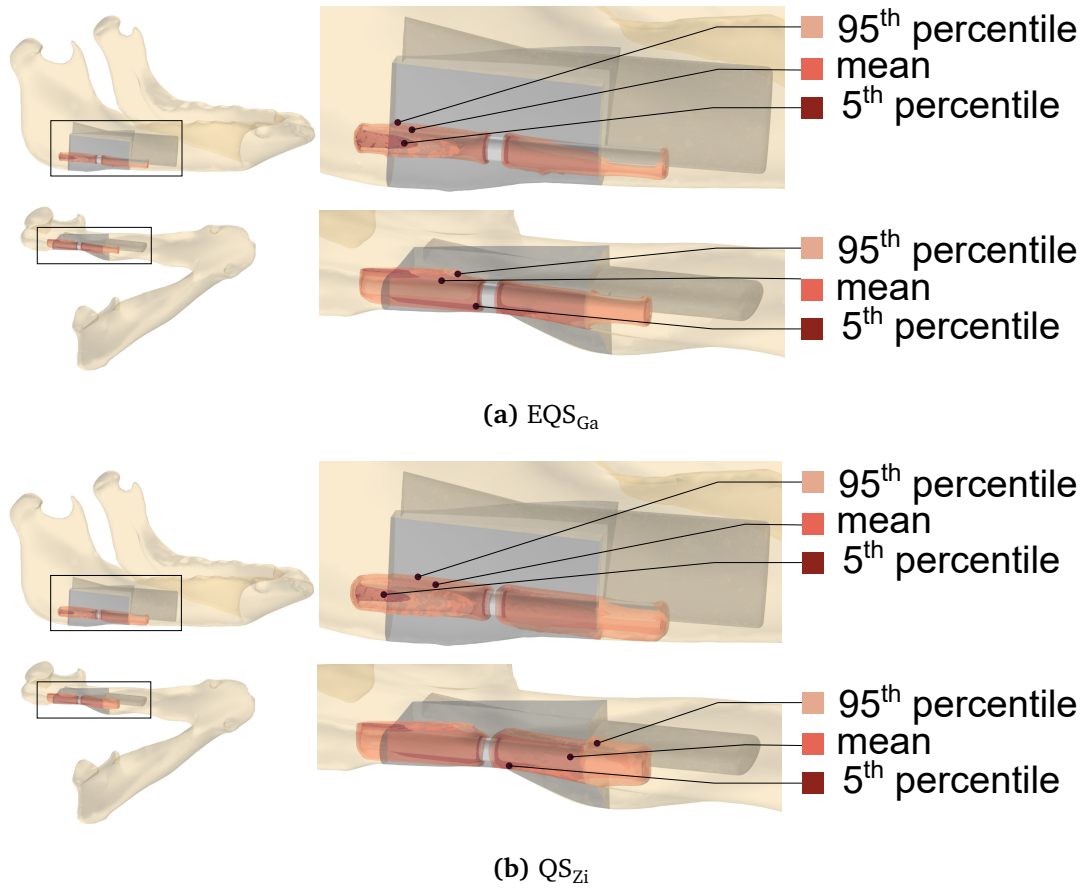


**Figure 5.13:** Exemplary visualisation of the overstimulated tissue ( $|\mathbf{E}| > 70 \text{ V/m}$ ) in the probabilistic model in (a) EQS<sub>Ga</sub> and (b) QS<sub>Zi</sub>. Shown are the 95th percentile, the mean, and the 5th percentile. Figure adapted from [38].

95th percentile this amounts to roughly 5.5–12 mm, which corresponds to the entire height of the defect region at the anterior side of the defect. The values for scenario EQS<sub>Ga</sub> are slightly smaller. The 5th percentile and the mean of the overstimulated volume cover only parts of the electrodes and are mainly located to the sides of the mesh tray in both scenarios. However, the 95th percentile indicates that almost the complete surface area of the electrodes is overstimulated. The overstimulated volume extends to around 0.3 mm (top and bottom of the electrodes) and 1 mm (sides of the electrodes) into the tissue. Table 5.9 presents the mean values of the stimulated volumes, the current, and  $|\mathbf{E}(P_1)|$  in both scenarios. The beneficially stimulated volume and  $|\mathbf{E}(P_1)|$  are similar across both scenarios, with slightly larger values in scenario QS<sub>Zi</sub>. The larger beneficially stimulated volume resulting from QS<sub>Zi</sub> is desirable as this scenario takes into account electrode processes and is thought to be closer to reality, see Sec. 4.2.2. However, this scenario may result in considerably more overstimulation, specifically 57% more than in EQS<sub>Ga</sub>. In addition, the current in QS<sub>Zi</sub> is more than double of the value of EQS<sub>Ga</sub>, resulting in an increased demand for electrical energy.

In comparison to the deterministic results (Tables 5.3 and 5.4), the mean values of the stimulated volumes obtained from the UQ results in both scenarios demonstrate a minor increase in  $V_{\text{bene}}$  and  $V_{\text{over}}$  and a corresponding decrease in  $V_{\text{under}}$ , as stated in Table 5.10. The total volume of overstimulated tissue in the probabilistic models is roughly two ( $\text{EQS}_{\text{Ga}}$ ) and three times ( $\text{QS}_{\text{Zi}}$ ) larger than in the deterministic case. Nonetheless, the corresponding increase in overstimulation as a percentage of the total defect volume may remain tolerable, with an increase of 2.1 % for  $\text{EQS}_{\text{Ga}}$  and 4.5 % for  $\text{QS}_{\text{Zi}}$ . Additionally, there are notable differences observed in the terminal current  $I_{\text{term}}$ . Specifically, in the probabilistic case, the mean of  $I_{\text{term}}$  is 21 % ( $\text{EQS}_{\text{Ga}}$ ) and 36 % ( $\text{QS}_{\text{Zi}}$ ) greater, indicating higher energy demands.

Output quantity	Mean		[%]	
	$\text{EQS}_{\text{Ga}}$	$\text{QS}_{\text{Zi}}$	$\text{EQS}_{\text{Ga}}$	$\text{QS}_{\text{Zi}}$
$V_{\text{under}}$	2600 mm <sup>3</sup>	2428 mm <sup>3</sup>	47.2 %	44.1 %
$V_{\text{bene}}$	2676 mm <sup>3</sup>	2718 mm <sup>3</sup>	48.6 %	49.3 %
$V_{\text{over}}$	231 mm <sup>3</sup>	362 mm <sup>3</sup>	4.2 %	6.6 %
$I_{\text{term}}$	1.09 mA	2.31 mA	–	–
$ \underline{\mathbf{E}}(P_1) $	10.05 V/m	11.61 V/m	–	–

**Table 5.9:** Mean values of the uncertain volumes of under- ( $V_{\text{under}}$ ), beneficially ( $V_{\text{bene}}$ ), and overstimulated ( $V_{\text{over}}$ ) tissue in the defect region,  $I_{\text{term}}$ , and  $|\underline{\mathbf{E}}(P_1)|$  for the considered scenarios  $\text{EQS}_{\text{Ga}}$  and  $\text{QS}_{\text{Zi}}$ . The stimulated volumes are given in mm<sup>3</sup> and as a percentage of the entire defect volume. The uncertain input parameters regarded in the different scenarios are provided in Tables 5.7 and 5.8.

Output quantity	$\text{EQS}_{\text{Ga}}$		$\text{QS}_{\text{Zi}}$	
	$\Delta$	$\Delta$ [%]	$\Delta$	$\Delta$ [%]
$V_{\text{under}}$	-187.9 mm <sup>3</sup>	-3.4 %	-362.5 mm <sup>3</sup>	-6.6 %
$V_{\text{bene}}$	73.0 mm <sup>3</sup>	1.3 %	114.6 mm <sup>3</sup>	2.1 %
$V_{\text{over}}$	114.1 mm <sup>3</sup>	2.1 %	248.1 mm <sup>3</sup>	4.5 %
$I_{\text{term}}$	0.19 A	21 %	0.61 A	36 %

**Table 5.10:** Difference  $\Delta = X_{\text{UQ}} - X_{\text{det}}$  with respect to the deterministic models (see Table 5.4) for the volume of under- ( $V_{\text{under}}$ ), beneficially ( $V_{\text{bene}}$ ), and overstimulated ( $V_{\text{over}}$ ) tissue in the defect region and the current  $I_{\text{term}}$ . Note that the difference in volume is given in mm<sup>3</sup> and in % of the total defect volume.

In addition to the larger volume of overstimulated tissue in  $\text{QS}_{\text{Zi}}$ , also the standard deviation and 95th percentile are significantly higher (Fig. 5.14 (e) and (f)). In terms

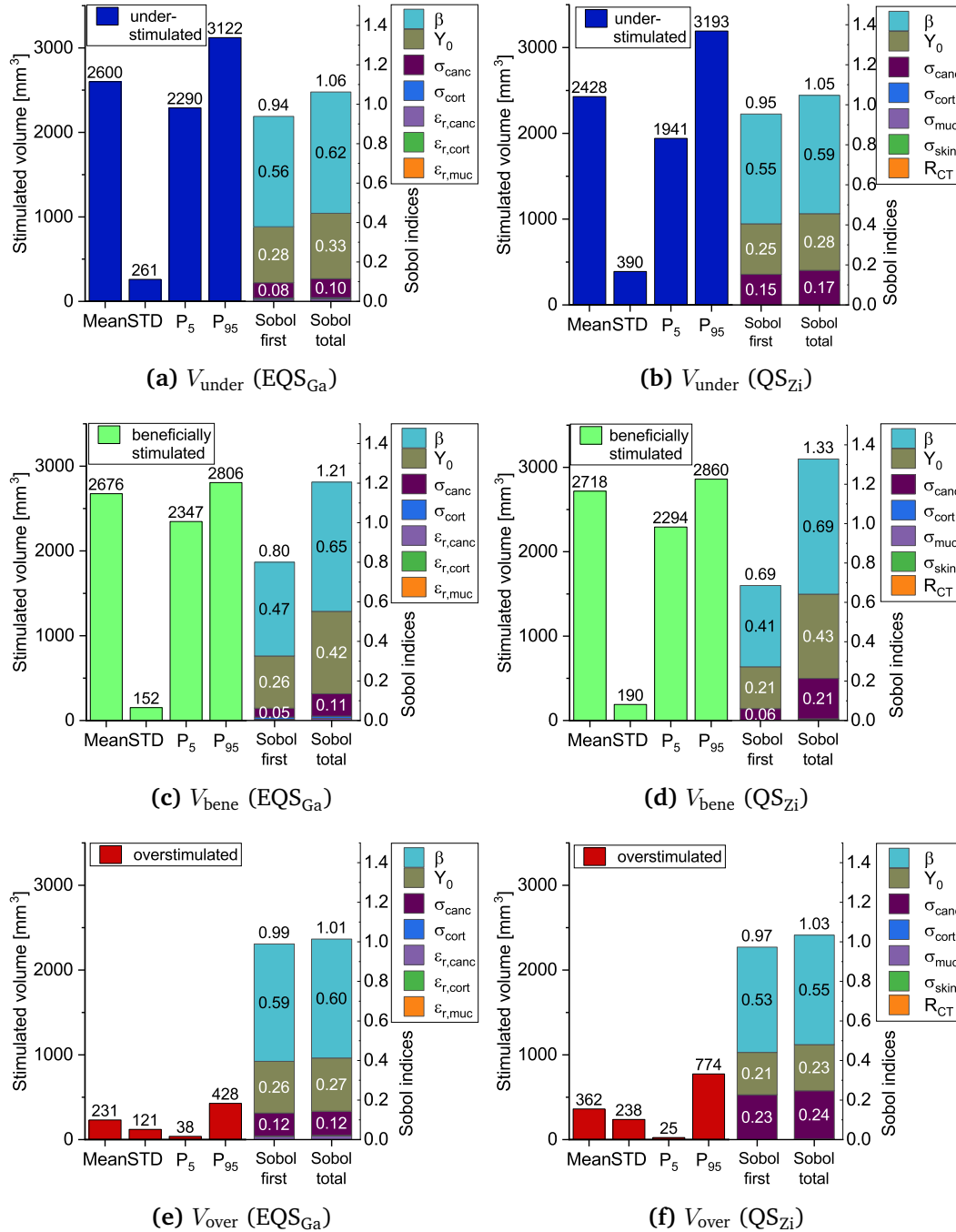


**Figure 5.14:** Comparison of the statistical metrics (mean, standard deviation (STD), 5th (P<sub>5</sub>) and 95th percentile (P<sub>95</sub>)) and Sobol' indices (first order and total Sobol' indices) for the (a), (b) understimulated, (c), (d), beneficially stimulated, and (e), (f) overstimulated tissue in the defect region in scenario EQS<sub>Ga</sub> ((a), (c), (e)) and scenario QS<sub>Zi</sub> ((b), (d), (f)). Figure adapted from [38].

of the beneficially stimulated tissue, both scenarios yield similar outcomes with QS<sub>Zi</sub> having somewhat larger mean and 95th percentile values (Fig. 5.14 (c), (d)). Similar

findings with more significant differences are obtained for the understimulated volume (Fig. 5.14 (a), (b)). A noteworthy finding is that the range of stimulated volumes, i.e. the difference between the 5th and the 95th percentile, is greater for  $QS_{Zi}$  than for  $EQS_{Ga}$  (Figs. 5.14 and 5.15).

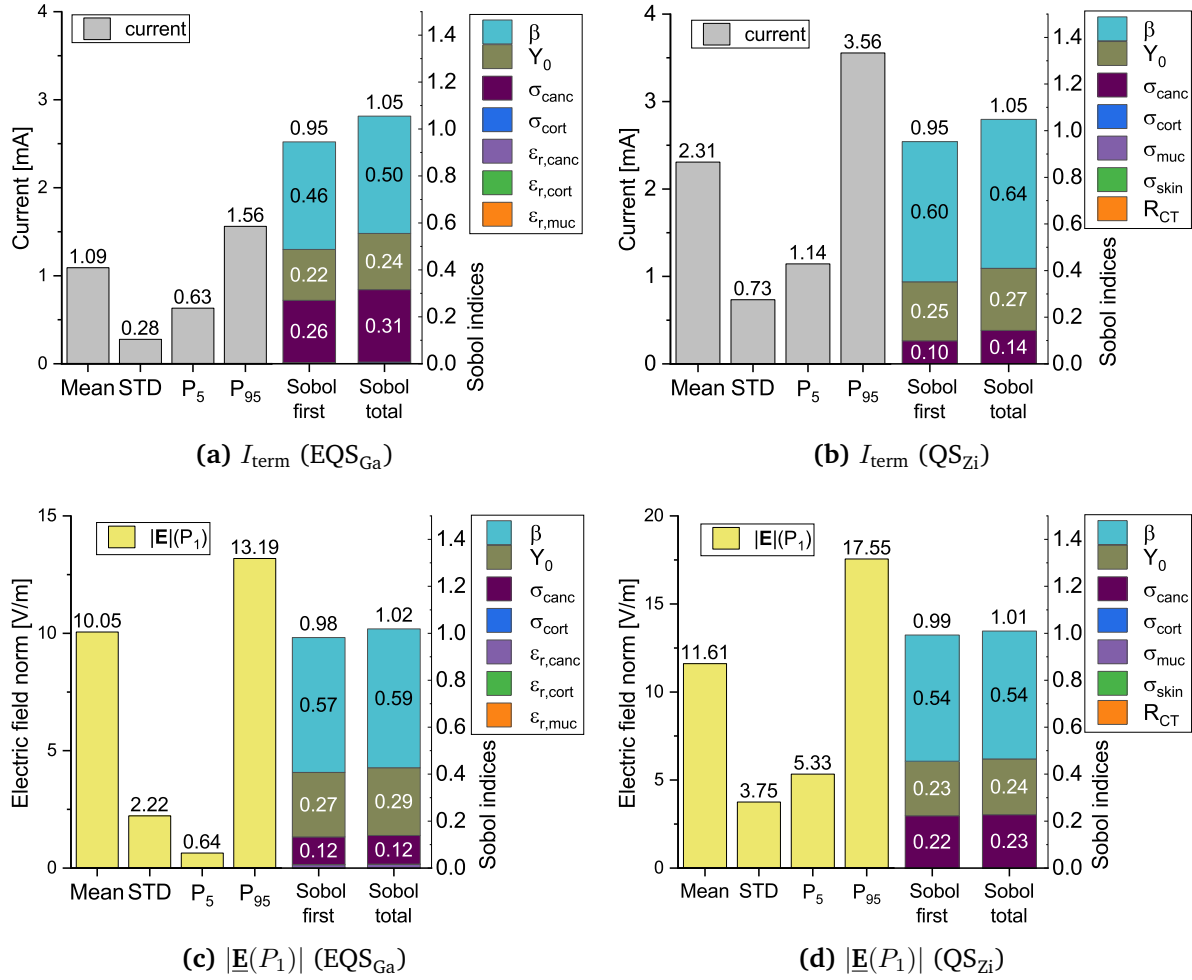


**Figure 5.15:** Comparison of the statistical metrics (mean, standard deviation (STD), 5th (P<sub>5</sub>) and 95th percentile (P<sub>95</sub>)) and Sobol' indices (first order and total Sobol' indices) for (a), (b) the terminal current  $I_{term}$  and (c), (d) the electric field norm  $|\underline{E}(P_1)|$  in point  $P_1$  in  $EQS_{Ga}$  ((a), (c)) and  $QS_{Zi}$  ((b), (d)). Figure adapted from [38].

In both scenarios analysed, the overall importance of the various input parameters is similar with  $\beta$ ,  $Y_0$ , and  $\sigma_{canc}$  being the most influential parameters as per the Sobol' indices, see Fig. 5.14 and Fig. 5.15. For the majority of output quantities, there are only minor differences in the absolute numbers. Comparing the Sobol' indices in both scenarios, the most significant differences are apparent for the output quantities  $I_{term}$  and  $|\underline{E}|$ . Additionally, for  $\sigma_{canc}$  there are significant differences between the Sobol' indices of the scenarios for all output quantities.

For the input parameter  $\beta$ , the behaviour in both scenarios is largely comparable. The most striking differences are in the output quantity  $I_{term}$ :  $\beta$  has a significantly

greater influence on  $I_{\text{term}}$  in  $QS_{Zi}$ . On the other hand, the Sobol' indices for  $\sigma_{\text{canc}}$  are over twice as high in  $EQS_{Ga}$  when compared to  $QS_{Zi}$ , with an accordingly smaller impact of  $\beta$  and  $Y_0$ . However, considering the standard deviations in both scenarios and multiplying them by the Sobol' indices, the resulting value is approximately 0.073 mA in both cases. This indicates that the total impact of  $\sigma_{\text{canc}}$  in both examined scenarios is in fact comparable and that Sobol' indices should always be analysed with reference to the standard deviation.

For the beneficially stimulated tissue as an output quantity, the difference between the total Sobol' index and the first order Sobol' index is greater in  $QS_{Zi}$  than in  $EQS_{Ga}$  for all regarded uncertain input parameters. This implies more pronounced interactions in  $QS_{Zi}$  than in  $EQS_{Ga}$ .

## Discussion

The findings of this sensitivity analysis, i.e. the high sensitivity with respect to the CPE parameters  $\beta$  and  $Y_0$ , highlight the importance of a careful characterisation of the electrode material. Otherwise, even relatively small variations in the input parameters could lead to large variations in the volume of stimulated tissue, as suggested by the results of this global sensitivity analysis. Furthermore, the considerable sensitivities of  $I_{\text{term}}$  with respect to  $\sigma_{\text{canc}}$  ( $EQS_{Ga}$ ) and of the electric field norm with respect to  $\sigma_{\text{canc}}$  ( $QS_{Zi}$ ) indicate that it is essential to accurately measure the conductivity of the bone or bone replacement material in the defect volume. This is required to model the electrostimulating setup precisely, enabling cooperation partners to design the electrostimulating circuitry appropriately. The aforementioned aspect is particularly crucial since the stimulator, along with its electronics, requires designing for a specific impedance range [280]. As a result, it can only deliver a limited amount of current.

Compared to the deterministic studies, the mean values of the stimulated volumes from the UQ studies show only slight differences. Considering the uncertainties assumed in this work, the overall stimulation success is not compromised in the probabilistic setting. However, due to substantial differences in the current, the stimulator should be designed to accommodate a wider range of currents with the ability to make adjustments if necessary. Alternatively, a precise experimental characterisation of the relevant input parameters is required to reduce these uncertainties.

Caution should be exercised when comparing both scenarios, as they were established at different levels of stimulation amplitude and considered distinct sets of uncertain input parameters. Nevertheless, the sum of the Sobol' indices of the input quantities considered in both scenarios ( $\beta$ ,  $Y_0$ ,  $\sigma_{\text{canc}}$ ,  $\sigma_{\text{cort}}$ ) is greater than 98.3 % of the sum of all Sobol' indices for all output quantities in both scenarios. Therefore, the comparative findings are easily appreciable. Additionally, both scenarios represent similar levels of under-, beneficially, and overstimulated tissue. Consequently, based on the previous comparison of the scenarios, it can be concluded that in  $QS_{Zi}$ , which

may be closer to the actual conditions, even more attention must be paid to the careful characterisation of the tissue and electrode properties.

Due to the novelty of the numerical simulation of electrically stimulating lower jaw bone implants, there are only a few studies in the literature that allow a limited comparison. Other researchers investigating UQ studies of electrically active implants in various applications often examine dissimilar output quantities [256, 286, 294] and different electrode and model geometries [255, 283]. However, there is evidence that supports some of the findings obtained in this thesis: for instance, Schmidt et al. evaluated the uncertainty in the conductivities of head tissues for the application in transcranial stimulation [258]. The determined Sobol' indices for the sensitivity of the stimulation amplitudes revealed the presence of interactions between the skin and skull conductivity. In another study, Schmidt et al. [283] performed a sensitivity analysis for an electrostimulating hip revision system and determined the Sobol' indices for two tissue conductivities for the optimally stimulated region. They noted that parameter interactions were negligible in this case. However, their study did not consider ETI parameters, which are significant according to the findings of this thesis and may prove crucial in the assessment of interactions. Indeed, uncertainties in the ETI parameters were investigated in a further study by the same author [294] focusing on deep brain stimulation: their findings suggest that the investigated output quantities were minimally impacted by variations in the ETI parameters, which differs from the outcome of this study. However, their study referred to the voltage response and the volume of tissue activated as output quantities. These quantities substantially differ from the output quantities addressed in this thesis and thus provide an explanation for the discrepancy.

After determining the input parameters with the greatest impact through sensitivity analysis, I will proceed to quantify the magnitude of the resulting uncertainties in the following section.

### 5.3.3 Quantification of uncertainties in the model outputs of the electrically stimulated minipig mandible

The relative standard deviation  $STD_r = \frac{STD}{\mu}$  is used to quantify the uncertainties in the considered model outputs in both scenarios. Again, I consider the optimised configuration of each scenario here, as summarised earlier in Table 5.3.

From Table 5.11 it is evident that the volume of beneficially stimulated tissue  $V_{bene}$  is only marginally affected by uncertain model parameters, with uncertainties of 5.69 % ( $EQS_{Ga}$ ) and 7.00 % ( $QS_{Zi}$ ). The most significant uncertainties in the optimised electrode configuration are present in the volume of overstimulated tissue  $V_{over}$  with uncertainties of 52.18 % ( $EQS_{Ga}$ ) and 65.81 % ( $QS_{Zi}$ ). There are slightly smaller, yet significant uncertainties ranging from 22–32 % present in the terminal current  $I_{term}$

Output quantity	STD <sub>r</sub> [%]	
	EQS <sub>Ga</sub>	QS <sub>Zi</sub>
$V_{\text{under}}$	10.04	16.06
$V_{\text{bene}}$	5.69	7.00
$V_{\text{over}}$	52.18	65.81
$I_{\text{term}}$	25.48	31.78
$ \underline{\mathbf{E}}(P_1) $	22.10	32.33

**Table 5.11:** Uncertainty in terms of the relative standard deviation  $\text{STD}_r = \text{STD}/\mu$  in the output quantities  $V_{\text{under}}$ ,  $V_{\text{bene}}$ ,  $V_{\text{over}}$ ,  $I_{\text{term}}$ , and  $|\underline{\mathbf{E}}(P_1)|$  for the optimised electrode configurations in the scenarios EQS<sub>Ga</sub> and QS<sub>Zi</sub>. The uncertain input parameters regarded in the different scenarios are provided in Tables 5.7 and 5.8.

and the electric field norm  $|\underline{\mathbf{E}}(P_1)|$ . The output quantities of interest generally exhibited higher uncertainties in QS<sub>Zi</sub>. This was due to the different parameter distributions used in both scenarios, as previously mentioned.

### Impact of the stimulation amplitude on the model uncertainties

To assess the effect of different stimulation amplitudes, e.g., due to technical tolerances of the stimulation unit, UQ was also performed for stimulation voltages that are 20 % lower than the initial, optimised values of both scenarios. Moreover, in order to investigate the effect of even higher stimulation amplitudes, as used in *in vitro* experiments in the SFB 1270 ELAINE [19, 20], voltages of up to 1 V (EQS<sub>Ga</sub>) and 1.5 V (QS<sub>Zi</sub>) were applied.

Fig. 5.16 illustrates that the resulting uncertainty varies considerably over a wide range of stimulation voltages for the different output quantities considered. For instance, in Fig. 5.16 (b) it can be seen that with increasing stimulation amplitude, both the STD and the 90 % prediction interval as well as the uncertainty in terms of STD/mean decrease for beneficially stimulated tissue. In contrast, these quantities show an increase for the under- and overstimulated volume (refer to Fig. 5.16 (a) and (c)). The uncertainty for the beneficially stimulated volume is comparatively low, with STD/mean ranging between 8.2 % and 1.3 %. The volume of overstimulated tissue increases as the stimulation voltage rises, leading to greater overstimulation. Additionally, both the STD and the 90 % prediction interval experience substantial increases, whereas STD/mean decreases (see Fig. 5.16 (c)). The uncertainty for this output quantity is very high, with values of up to 70.2 % (QS<sub>Zi</sub>) and 57.6 % (EQS<sub>Ga</sub>), which decrease to still considerable uncertainties at higher stimulation voltages (30.8 % in QS<sub>Zi</sub> and 25.0 % in EQS<sub>Ga</sub>). The level of uncertainty in QS<sub>Zi</sub> generally exceeds that of EQS<sub>Ga</sub> by more than 20 percentage points.

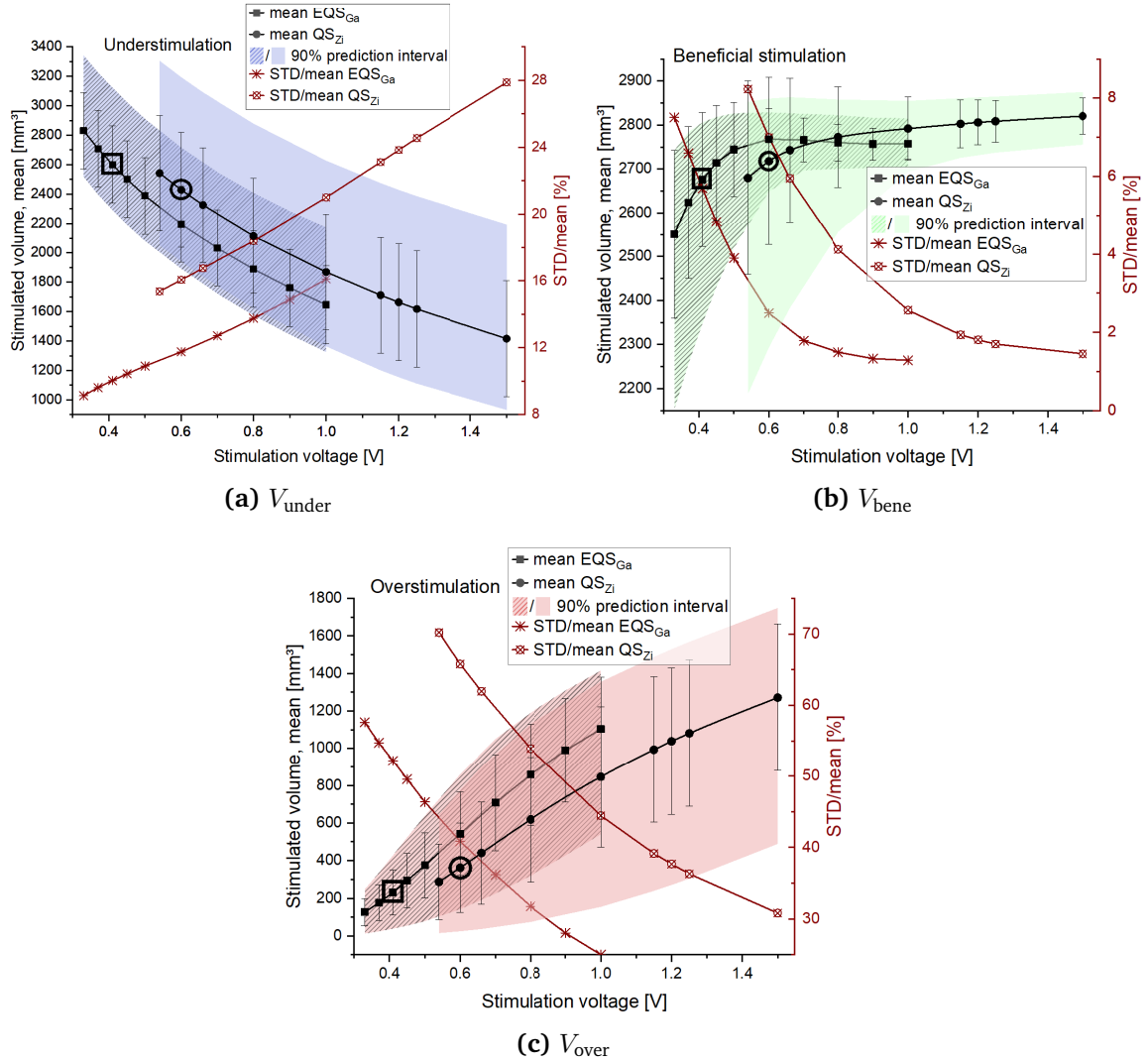


**Figure 5.16:** Stimulated volumes ((a) understimulated  $V_{\text{under}}$ , (b) beneficially stimulated  $V_{\text{bene}}$ , (c) overstimulated  $V_{\text{over}}$ ) in the defect region for different stimulation voltages in scenarios EQS<sub>Ga</sub> and QS<sub>Zi</sub> and the corresponding uncertainty of the quantity of interest in terms of STD/mean. The error bars indicate the standard deviation (STD). The coloured area corresponds to the 90 % prediction interval (line pattern for EQS<sub>Ga</sub>, no line pattern for QS<sub>Zi</sub>). The optimal stimulation voltages of each scenario are indicated with a bold frame. Note the different scales in (a), (b), and (c).

In Figure 5.16 (a) it is evident that the uncertainty of the understimulated volume has moderate values that range between 9.1 % and 27.9 %. The STD and the 90 % prediction interval increase only slightly with increasing stimulation voltage, while STD/mean increases linearly and significantly. At 1.5 V for QS<sub>Zi</sub> it reaches 27.9 %. The uncertainty in EQS<sub>Ga</sub> is approximately five percentage points lower than in QS<sub>Zi</sub>. The 90 % prediction interval and standard deviations for QS<sub>Zi</sub> are marginally wider than those for EQS<sub>Ga</sub>.



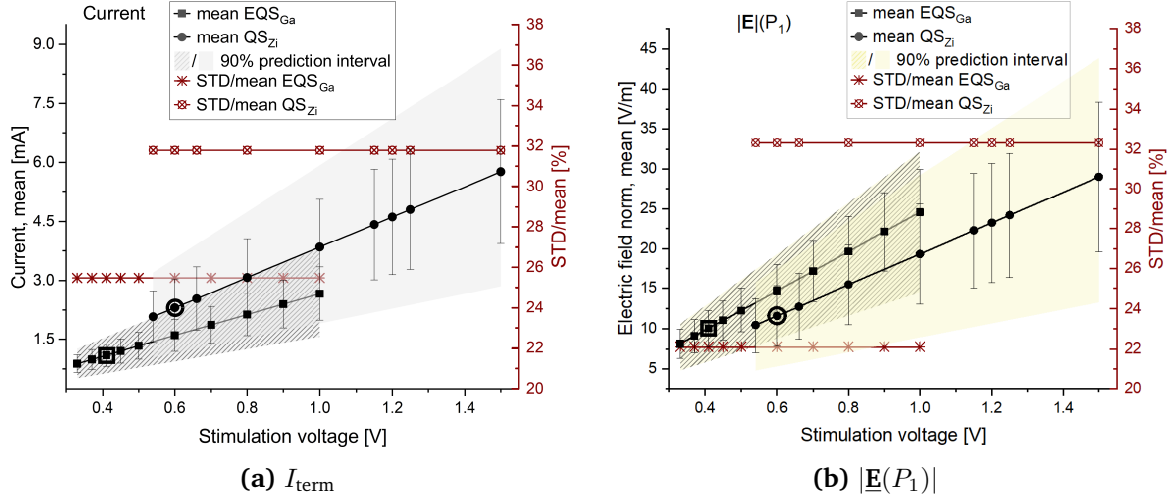


**Figure 5.17:** (a) Terminal current  $I_{\text{term}}$  and (b) norm of the electric field strength in point  $P_1$  ( $|\underline{E}(P_1)|$ ) for different stimulation voltages in  $\text{EQS}_{\text{Ga}}$  and  $\text{QS}_{\text{Zi}}$  and the corresponding uncertainty of the quantity of interest in terms of STD/mean. The error bars indicate the standard deviation (STD). The coloured area corresponds to the 90 % prediction interval (line pattern for  $\text{EQS}_{\text{Ga}}$ , no line pattern for  $\text{QS}_{\text{Zi}}$ ). The optimal stimulation voltages of each scenario are indicated with a bold frame.

As expected, both  $I_{\text{term}}$  and  $|\underline{E}(P_1)|$  increase linearly as the voltage increases (see Fig. 5.17). Additionally, the STDs and the 90 % prediction interval also exhibit higher values with increasing stimulation voltage, with notably greater values observed in  $\text{QS}_{\text{Zi}}$ . In both scenarios, the relative uncertainty STD/mean remains constant because the current and electric field norm are linearly dependent on the stimulation voltage.

The stimulation amplitude also shows an interesting effect on the sensitivity of the beneficially stimulated tissue, where further input parameters such as  $\sigma_{\text{cort}}$  and  $\sigma_{\text{muc}}$  seem to become more influential with respect to the uncertainty of the output quantities with increasing stimulation amplitude, as indicated by significantly increased Sobol' indices. However, when interpreting these results in the context of the drastically decreasing STD shown in Fig. 5.16 (b), no significant variations in the output are expected (see Appendix B). The impact of the stimulation amplitude on the Sobol' indices is negligible in both over- and understimulated tissue, with only a slight difference of a few percentage points.

### Quantified impact of individual parameter variations

The previously described UQ studies enable the estimation of the effect of a set of uncertain input parameters on the model output. To evaluate how the variation in a single parameter affects the volume of stimulated tissue, parametric studies with a variation of only one parameter at a time were performed for both scenarios. The

parameters investigated were those with the most significant impact on the output variance, i.e.  $\beta$ ,  $Y_0$ , and  $\sigma_{\text{canc}}$ . Additionally, the stimulation voltage and the electrode length  $h_{\text{el}}$  were varied parametrically. The parameter values for  $\beta$  and  $Y_0$  encompass the range selected in the UQ studies (Tables 5.7 and 5.8). The chosen range for  $\sigma_{\text{canc}}$  is mean  $\pm 3$  STD. Only one parameter was varied during each parametric study, whereas all others remained set to their initial values (see Table 4.2).

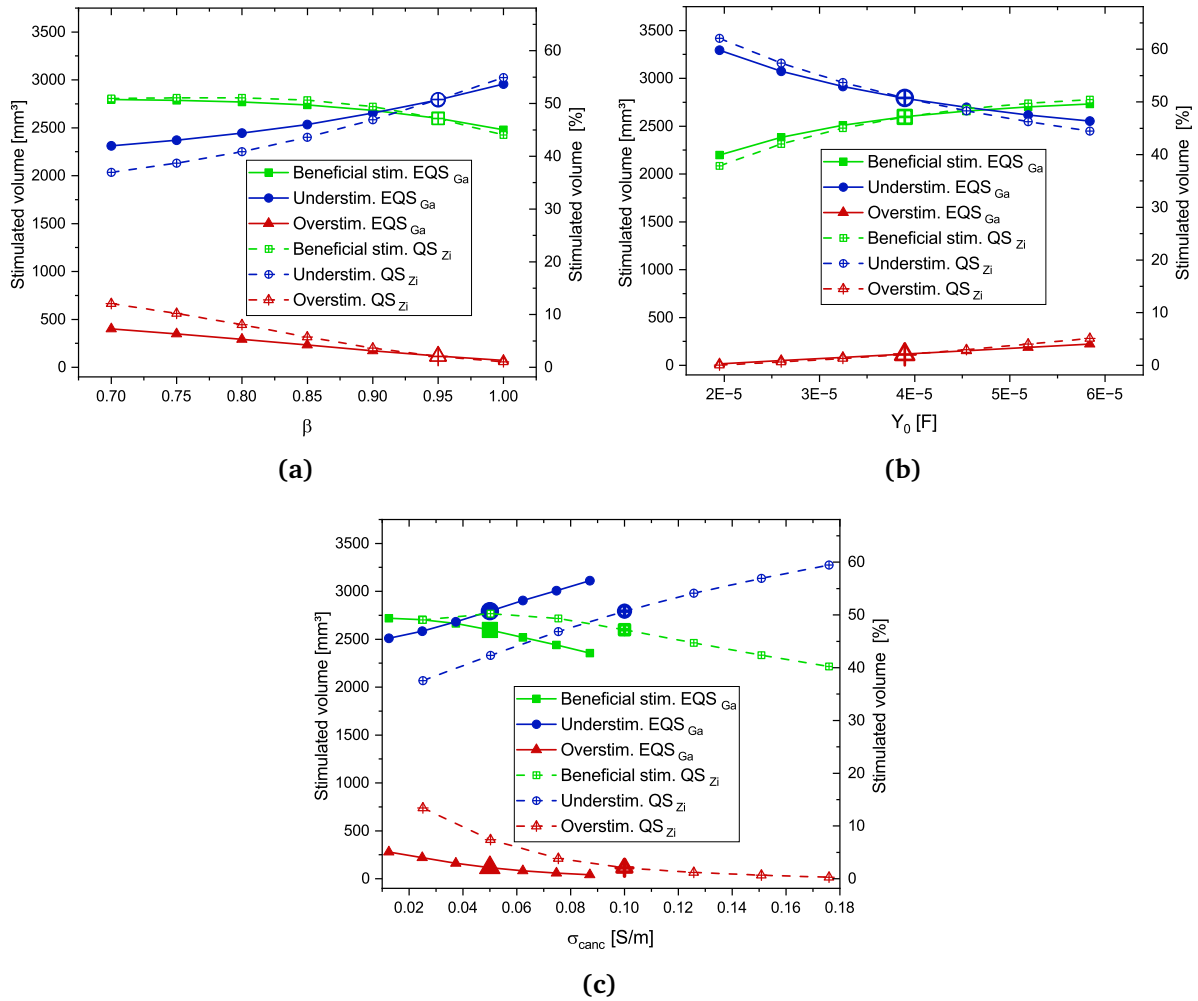


**Figure 5.18:** Impact of parametric variation of the most significant (with respect to the output uncertainty) input parameters on the beneficially, under-, and overstimulated volumes in the defect region. (a)  $\beta$ , (b)  $Y_0$ , (c)  $\sigma_{\text{canc}}$ . Solid lines: EQS<sub>Ga</sub>; dashed lines: QS<sub>Zi</sub>. Stimulated volumes are given in mm<sup>3</sup> (left y-axis) and in % of the whole defect volume (right y-axis). The optimised parameter values are marked with enlarged symbols.

Fig. 5.18 (a) demonstrates that with increasing  $\beta$ , there is a similar decrease in the volume of beneficially stimulated tissue for both scenarios. Within the regarded range of  $\beta \in (0.7, 1)$ , the volume of beneficially stimulated tissue decreases by approximately six percentage points of the total defect volume. At the same time, the understimulated

volume increases while the overstimulated volume decreases with increasing  $\beta$ . These observations can be accounted for by the enhanced CPE impedance resulting from a larger  $\beta$  and, consequently, an increased ETI impedance (as described in Eqs. (4.1) and (4.3)). For  $\beta = 0.7$ , the over- and understimulated volumes attained in  $QS_{Zi}$  are notably greater and less than those reached in  $EQS_{Ga}$ , respectively. Conversely, for  $\beta = 1$ , both scenarios produce similar stimulated volumes. This observation can be explained by the higher stimulation voltage applied in  $QS_{Zi}$  compared to  $EQS_{Ga}$ . As  $\beta$  approaches 0.95 – the configuration for which both scenarios were optimised – the curves of stimulated volumes approach each other. If  $\beta$  was reduced by 0.05 in the vicinity of the initial value of 0.95, it would only lead to underestimation of the beneficial and overstimulated volume by about 2–3 % of the total defect volume. However, a drastically reduced  $\beta = 0.7$  alone could lead to an overstimulated volume that is significantly increased by ten percentage points of the total defect volume for  $QS_{Zi}$ .

Extended usage of electrostimulating electrodes may lead to the formation of calcium phosphate deposits on the electrode surface [24]. During the analysis of the corrosion behaviour of Ti6Al4V in a simulated body fluid (SBF) solution, which contains calcium ions and phosphate ions, Tamilselvi et al. observed a decline in  $\beta$  from an initial value of 0.85 to 0.7 after a span of 15 days [288]. A comparable reduction in  $\beta$  can be anticipated for the electrodes considered in this thesis. This particularly applies to the fact that calcium phosphate deposition has been observed *in vitro* on similar stimulation electrodes [24]. Consequently, it can be inferred that a noticeable rise in overstimulated tissue of around ten percentage points may arise if  $\beta$  reduces from 0.95 to 0.7 when considering  $QS_{Zi}$  (Fig. 5.18 (a)). In this case it would be necessary to reduce the stimulation amplitude.

Varying the capacitance parameter  $Y_0$  alone leads to an increase in the overstimulated and beneficially stimulated volume, while the understimulated volume decreases (Fig. 5.18 (b)). There are only minor differences between the two scenarios. Throughout the optimisation and UQ studies, the capacitance parameter  $Y_0$  of a polished titanium specimen was utilised. A rougher electrode surface would result in a multiple of the assumed parameter value [227], which exceeds even the range considered in the parameter studies. Therefore, a simulation with the parameter values  $\beta = 0.64$ ,  $Y_0 = 271 \mu F$ ,  $R_{CT} = 2.65 k\Omega$  from [227] for a vacuum plasma sprayed titanium surface was considered as an extreme example for comparison purposes for the optimised  $QS_{Zi}$  case. The test simulation revealed that 50 % of the tissue in the defect region was beneficially stimulated, while 19 % was overstimulated, and 31 % was understimulated. The overstimulation, which is significantly higher in comparison to the maximum 2.3 % with polished titanium (Table 5.6), is the most noteworthy outcome. The significant degree of overstimulation would require reoptimisation of the stimulation parameters.

The absence of a proper electrode characterisation during the simulation studies for this thesis constitutes a significant source of uncertainty that I addressed through the utilisation of UQ. However, the variation in input parameters may be too extensive to be practically managed with UQ, as stated above. Therefore, future studies should

address this issue by accurately characterising the electrochemical properties of the electrode material or by defining additional case scenarios for the development of electrostimulating implant designs. To the best of my knowledge, there have been no studies carried out to investigate how the ETI parameters of electrostimulating bone implants change over time. In this context, it would be highly desirable to carry out investigations, ideally through the direct monitoring of electrostimulation *in vivo* using impedance spectroscopy methods, to gain further insight. However, it remains uncertain as to whether such a setup could be technically realised. Nevertheless, these technical aspects merit further discussion with experts for future research.

Recent studies suggest that the electrical properties of bone, e.g., increasing bone resistance, can be used as an indicator for bone fracture healing [295,296]. Consequently, it can be assumed that the electrical conductivity in the defect area decreases during bone regeneration. In this study, smaller  $\sigma_{\text{canc}}$  lead to an increase in both beneficially and overstimulated tissue (Fig. 5.18 (c)). In EQS<sub>Ga</sub>, the increases in  $V_{\text{bene}}$  and  $V_{\text{over}}$  are comparable, whereas in QS<sub>Zi</sub> the overstimulation increases significantly more than the beneficial stimulation, reaching up to 13 % of the defect volume for  $\sigma_{\text{canc}} = 0.025 \text{ S/m}$ . Therefore, it may be advisable to decrease the amplitude of stimulation during the physical treatment to prevent tissue damage. Revisiting the range of cancellous bone conductivity values found in the literature (Fig. 5.2), and considering that Balmer et al. [185] measured conductivity values down to 0.03 S/m, this situation seems realistic and the change of the stimulation effect during the entire treatment duration should be taken into account. In the case of *in vivo* experiments, this duration could last from three to six weeks. I conclude that an appropriate modification of the stimulation parameters is imperative to ensure proper stimulation during the entire therapy. More precisely, decreasing the conductivity in the defect region indicated that, for the same amplitude of the signal driving the stimulation, a higher percentage of the defect region could be stimulated beneficially. This implies that a lower stimulation potential would be sufficient to achieve the same volume of beneficially stimulated tissue. However, there was also a significant increase in overstimulation observed in this situation. Therefore, the optimal stimulation unit should employ closed-loop stimulation using real-time biosignal processing [297,298], which can monitor changes in tissue impedance and can prevent harmful tissue overstimulation by adjusting the stimulation signal accordingly. As the flowing current decreases during the healing progress, the power consumption is also reduced. This could potentially extend the lifespan of the battery of the stimulator.

Fig. 5.19 (a) shows that varying the electrode length  $h_{\text{el}}$  over a wide range has the most profound effect on the stimulated volumes. Increasing  $h_{\text{el}}$  from 10 mm to around 24 mm leads to a linear increase of  $V_{\text{bene}}$  from approximately 10 % to about 45 % of the defect volume. Conversely,  $V_{\text{under}}$  declines from about 90 % to about 52 %. For even larger electrode lengths, the increase in  $V_{\text{bene}}$  and the decrease in  $V_{\text{under}}$  become less pronounced and are even slightly reversed for  $h_{\text{el}} > 26 \text{ mm}$ . This is due to the less distinct but continuous increase in  $V_{\text{over}}$ , which also extends beyond  $h_{\text{el}} > 26 \text{ mm}$ . However, the percentage of overstimulated tissue is relatively small, with a maximum

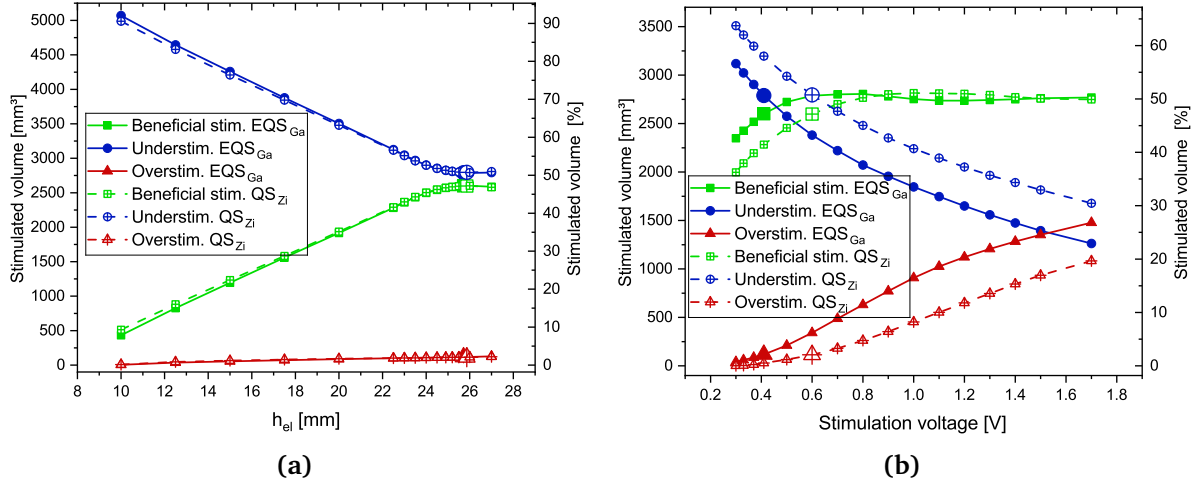


**Figure 5.19:** Impact of parametric variation of (a) the electrode length  $h_{el}$  and (b) the stimulation voltage on the beneficially, under-, and overstimulated volume in the defect region. Solid lines:  $\text{EQS}_{Ga}$ ; dashed lines:  $\text{QS}_{Zi}$ . Stimulated volumes are given in  $\text{mm}^3$  (left y-axis) and in % of the whole defect volume (right y-axis). The optimised parameter values are indicated with enlarged symbols.

of 2.3 % at  $h_{el} = 26.7$  mm. Both scenarios produce almost identical outcomes. The findings that minor adjustments to the electrode length can result in significant changes to the stimulated volume are consistent with those of Su et al. [23]. The authors conducted analogous parameter studies on a bipolar stimulation screw and observed substantial effects of screw length on the stimulated volume [23].

Fig. 5.19 (b) illustrates that a similar trend as for the electrode length can be observed for the stimulation voltage  $\varphi_{stim}$ . Initially,  $V_{bene}$  increases and then remains relatively stable within the 0.8–1.7 V range for both scenarios. At the same time,  $V_{over}$  continuously rises with increasing stimulation voltage, increasing the likelihood of tissue damage. For instance, using higher stimulation voltages, such as  $\varphi_{stim} = 1.2$  V and  $\varphi_{stim} = 1.7$  V, would result in a four-fold and ten-fold increase in overstimulated volume, respectively, when compared to the optimised stimulation voltage of  $\varphi_{stim} = 0.6$  V in  $\text{QS}_{Zi}$ . However, the amount of beneficially stimulated volume would only rise by approximately 8.1 % and 5.8 %, respectively, in these cases. It is concluded that monitoring the stimulation voltage cautiously and maintaining it at a low level is necessary to prevent tissue damage during application.

It is worth noting that  $V_{under}$  is considerably larger whereas  $V_{over}$  is smaller in  $\text{QS}_{Zi}$  compared to  $\text{EQS}_{Ga}$ . As a consequence, the more realistic<sup>13</sup>  $\text{QS}_{Zi}$  leads to reduced risk of tissue damage which may result from unintentionally increased stimulation potentials, such as those arising from technical errors.

<sup>13</sup> $\text{QS}_{Zi}$  includes a correction of electrode processes and is therefore closer to reality than  $\text{EQS}_{Ga}$ , see Sec. 4.2.2.

Parameter	$V_{\text{under}}$	$V_{\text{bene}}$	$V_{\text{over}}$
$\beta$	$\nearrow$	$\searrow$	$\searrow$
$Y_0$	$\searrow$	$\nearrow$	$\nearrow$
$\sigma_{\text{canc}}$	$\nearrow$	$\searrow$	$\searrow$
$h_{\text{el}}$	$\searrow \searrow$	$\nearrow \nearrow$	$\nearrow$
$\varphi_{\text{stim}}$	$\searrow$	$\nearrow \rightarrow$	$\nearrow$

**Table 5.12:** Trend of under- ( $V_{\text{under}}$ ), beneficially ( $V_{\text{bene}}$ ), and overstimulated ( $V_{\text{over}}$ ) volumes with increasing individual parameter values for  $\beta$ ,  $Y_0$ ,  $\sigma_{\text{canc}}$ ,  $h_{\text{el}}$ , and  $\varphi_{\text{stim}}$ . Two arrows indicate a more pronounced increase or decrease.

Table 5.12 shows that the overall tendency of the stimulated volumes with individually varied input parameters is comparable for both examined scenarios. Increasing  $\beta$  or  $\sigma_{\text{canc}}$  causes an increase in  $V_{\text{under}}$  and a decrease in  $V_{\text{bene}}$  and  $V_{\text{over}}$ . Conversely, the opposite effect is noticeable for  $Y_0$ ,  $h_{\text{el}}$ , and  $\varphi_{\text{stim}}$ .

Further simulations (not shown) that varied the relative permittivity of cancellous bone  $\varepsilon_{r,\text{canc}}$  within a large range from  $3 \cdot 10^5$  to  $2 \cdot 10^7$  (EQS<sub>Ga</sub>) indicated only a minute reduction in beneficially stimulated tissue (2.1 %), an increase in understimulated tissue (3.3 %), and a decrease in overstimulated tissue (1.2 %). This finding supports the UQ result of the negligible impact of the relative permittivity.

### 5.3.4 Conclusion of the uncertainty quantification analyses

The UQ studies presented here revealed that the parameters of the ETI,  $\beta$  and  $Y_0$ , as well as the conductivity of cancellous bone,  $\sigma_{\text{canc}}$ , are the most influential quantities with respect to the output variance. Accordingly, these quantities should be measured accurately to ensure reliable simulation results. As the sensitivity in beneficially stimulated volume is affected by changes in the stimulation voltage, future studies should directly consider the stimulation voltage as an uncertain input variable to draw further conclusions on its significance. This also applies to the electrode length, which in parameter studies has shown to influence the stimulation outcome significantly.

The UQ results indicate higher portions of overstimulated tissue and higher currents than the deterministic studies. Further, the highest relative uncertainty resulted for the overstimulated volume. These characteristics were especially pronounced for the more realistic scenario QS<sub>Zi</sub>, where the beneficial field strength reaches further into the tissue than in EQS<sub>Ga</sub>. While the latter aspect is desirable, the aforementioned overstimulation and increased energy demand due to higher currents may pose risk of tissue damage and further practical challenges. Therefore, as stated above, a careful characterisation of the dielectric tissue properties and the ETI is crucial to reduce these uncertainties and enable reliable modelling.

In this work, the stimulation parameters were optimised using deterministic input parameters and the UQ studies were then performed separately as a first step towards a reliable implant design. However, robust optimisation [299], where uncertainties are incorporated directly into optimisation procedure, is desirable in future studies. This can further ensure optimal performance of the electrostimulating implant across a range of possible scenarios or uncertainties.

The electrode design established within the framework of this thesis was applied in *in vivo* experiments with minipigs. The subsequent section will provide a brief overview of the findings obtained from these experiments.

## 5.4 *In vivo* validation of the optimised electrostimulating implant

In this thesis, an electrostimulation implant was developed for direct contact electrical stimulation to enhance early bone growth and healing of critical-size mandibular defects. To investigate its feasibility, *in vivo* studies were performed in minipigs. The results of this study are yet unpublished but are submitted for review [48].<sup>14</sup> The study examined six adult Aachener minipigs with critical-size mandibular defects. Twelve implants were placed, with six being electrostimulating and six serving as the control group. The electrostimulation protocol consisted of three 45-minute sessions per day using a sinusoidal stimulation voltage with a frequency of 20 Hz and a peak value of 0.5 V. The stimulation implant used had an electrode length of 25 mm (refer to Fig. 5.20). These stimulation parameters are based on the numerical optimisation studies described in my previous publication [34].

After three weeks, the animals that received electrical stimulation exhibited a significantly greater amount of newly formed bone in the middle of the defect (region S2, Fig. 5.20) and in the residual cortical bone at the posterior end of the implant (region S3, Fig. 5.20), particularly within a distance of ca. 1.5–2 mm around the implant, compared to the control group (Table 5.13). In the middle of the defect (S2), there was also better vascularisation and improved immune response observed compared to the control group. Thus, the regenerative potential of the numerically optimised electrode configuration could be validated in specific regions of the defect *in vivo*. In particular, these results suggest that an existing osseous environment can significantly enhance bone regeneration around the electrostimulation implant [48]. However, no statistically significant difference could be observed for new bone growth, vascularisation, and immune response in the region of the interface between the residual cancellous bone and the anterior part of the defect (region S1, Fig. 5.20), i.e. in the absence of viable osseous cells or scaffolds near the implant [48]. Therefore,

<sup>14</sup>I contributed to the electrode design and stimulation parameters used in the *in vivo* study, revised parts of the manuscript, and provided input on potential explanations for the observed limitations.

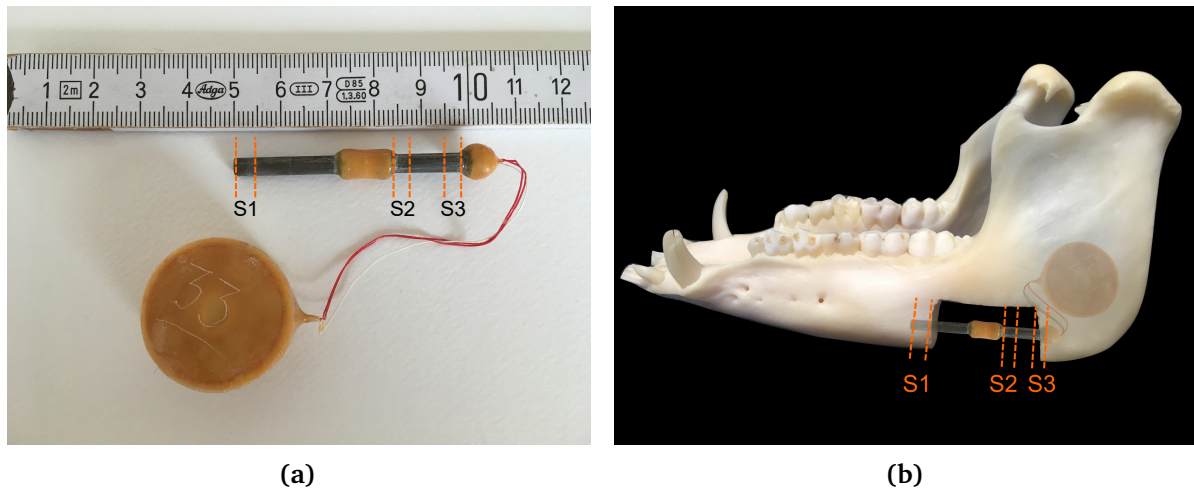


**Figure 5.20:** (a) Electrostimulating implant and stimulator used in the *in vivo* experiments with minipigs and regarded regions for bone growth assessment. S1: interface between the residual cancellous bone and the anterior part of the defect; S2: middle of the defect; S3: residual cortical bone. Note that for the *in vivo* experiments, the insulator could only be manufactured in a bulky manner and had to be extended to the cable-leading end of the implant to ensure watertightness. (b) Visualisation of the electrostimulating implant placed in the minipig mandible.

Region	New bone formation [%]		<i>p</i>
	ESTIM	Control	
S1	$28.2 \pm 4.4$	$27.5 \pm 9.3$	0.817
S2	$27.8 \pm 9.7$	$20.2 \pm 8.7$	0.055
S2 (1.5 mm)	$42.7 \pm 5.5$	$31.2 \pm 4.8$	0.012
S3	$45.4 \pm 4.3$	$28.8 \pm 3.3$	$< 0.001$

**Table 5.13:** New bone formation in specific regions (S1, S2, S3, see Fig. 5.20) of the defect obtained in *in vivo* experiments with minipigs in the stimulated (ESTIM,  $n = 6$ ) and control group ( $n = 6$ ) within a region of interest of 3 mm around the electrode [48]. Mean and standard deviation as well as the *p*-value are given. Region S2 did not show significantly ( $p \leq 0.05$ ) enhanced new bone formation in the whole considered region, but only in a subregion at a radial distance of 1.5 mm around the electrode.

the use of electrical stimulation alone to promote regeneration in critical-size bone defects was assessed to be limited [48]. The identified limitations highlight the need for an improved surgical approach that incorporates the conventional “triad of tissue engineering” [300] consisting of cells, biomaterials, and biochemical factors [48]. The combination of tissue engineering and electrical stimulation, particularly the use of electrical stimulation on tissue-engineered scaffolds loaded with mesenchymal



stem cells, may be a promising approach for future research [48]. In some animals, deformation of the titanium mesh used to surround the defect was observed, suggesting that it was not stable enough. Future studies should therefore employ load-bearing and biomechanically optimised implant designs to improve this aspect. Despite the observed limitations, the described *in vivo* study lays the foundation for future research towards the clinical application of electrically stimulating implants for the regeneration of large mandibular bone defects.

The numerical studies focused on in this thesis indicated a different set of optimised electrode parameters compared to those used in the *in vivo* experiments and published in my previous publication [34] (Table 5.6, see also Sec. 5.2.3). This was due to the newly gained information on the dielectric tissue properties of the minipig mandible and their low-frequency correction [30]. In particular, the application of a higher stimulation amplitude, such as that resulting from the optimisation in this work including the correction of the dielectric tissue properties ( $QS_{zi}$ ) may have improved the *in vivo* results. In addition, alternative electrode designs with opposing electrodes, somewhat similar to [13], could improve the percentage of beneficially stimulated tissue in future studies.

The UQ studies conducted in this thesis (refer to Sec. 5.3.2) highlighted the significant impact of the ETI parameters and the electrical conductivity in the defect region on the uncertainty in the volume of stimulated tissue. The small sample size considered in the *in vivo* study and the intrinsic variability in tissue properties between individual animals may therefore have resulted in further limitations. In addition, variations in body temperature can cause changes in electrical conductivity [198]. Given these uncertain and variable tissue and material properties, different optimal stimulation parameters may have been optimal, highlighting the need for careful characterisation of tissue properties and robust optimisation in future studies.

So far, modelling and simulation have been conducted for the numerical model of an electrically stimulated minipig mandible. Subsequently, preliminary simulations of similar electrostimulating devices for human mandible models will be presented in the following section.

## 5.5 Preliminary simulation of human mandible models

*Parts of this chapter were taken from the publication “Preliminary Numerical Study on Electrical Stimulation at Alloplastic Reconstruction Plates of the Mandible”, which appeared in Scientific Computing in Electrical Engineering [36].<sup>15</sup> Reproduced with permission from Springer Nature.*

In this thesis, the minipig model has been studied extensively to ensure proper transfer of the electrode design into *in vivo* trials. Nevertheless, the initial motivation for developing electrostimulating implants for mandibular bone defects were human models. Thus, several human models were established and studied in preliminary studies prior to the minipig studies. Therefore, the following section presents two numerical investigations of the human mandible which further support the application of electrostimulating jaw implants.

### 5.5.1 Comparative simulation of separate electrostimulating electrodes and fixation screws

The initial rationale behind using electrostimulative implants for mandibular bone defects originated from patients receiving tumour therapy and consequent resection of significant amounts of the mandibular bone. Based on the CT data of a patient who underwent a comparable therapy and received bone substitute material and titanium reconstruction plates [59], a 3D numerical model was established to examine electrostimulation implants in this area of application for the first time.

#### Modelling and simulation of the electrostimulated human jaw model

Based on sectional images from CT data of a patient with a critical-size defect of the mandible, caused by cancer, the slices were segmented using Materialise Mimics<sup>®</sup> version 19 (<http://www.materialise.com>). Subsequently, a CAD model was created for use in a bioelectric simulation model. Figure 5.21 displays exemplary CT slices of the full data set consisting of 302 slices, each with  $512 \times 512$  voxels of dimension  $0.327 \text{ mm} \times 0.327 \text{ mm} \times 0.4 \text{ mm}$ .

Individual grey values were utilised for each tissue or material. Segmentation involved defining grey scale ranges for each substance, including air, soft tissue, bone, and

<sup>15</sup>Ursula van Rienen and Peer W. Kämmerer initiated the study. Together with Ulf Zimmermann, they conceptualised the study and prepared the initial draft of the manuscript. Ursula van Rienen provided methodological guidance. Ulf Zimmermann carried out the initial modelling and first simulations. I significantly improved the segmentation, the modelling of the geometry, and the finite element mesh and substantially revised major parts of the manuscript. I provided improved figures and performed additional simulation studies yielding further results. Ursula van Rienen and Peer W. Kämmerer supervised the project, acquired the funding, and provided all resources.

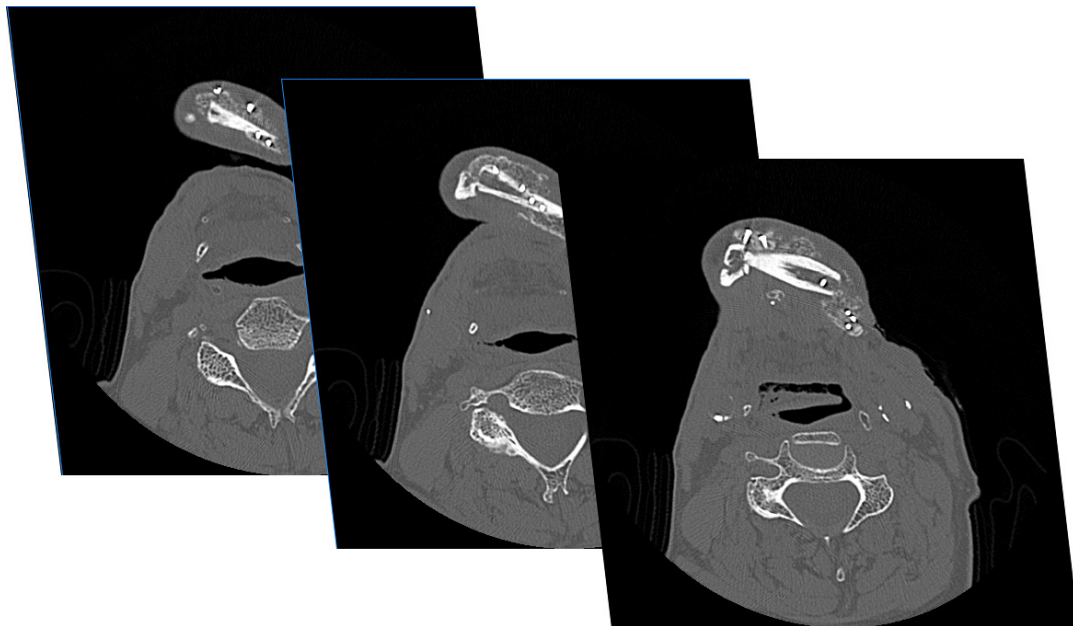


**Figure 5.21:** Slices from a computer tomography (CT) scan of a patient with a critical-size defect of the mandible. Reproduced from [36] with permission from Springer Nature.

metal used for the reconstruction plates and fixation screws. This produces an intermediate, coarsely segmented model. Figure 5.22 (a) shows the 3D model after segmentation. This model was subsequently reduced by removing artefacts and parts that are outside of the region of interest. Thus, nearly all bones, the ears and other small items were removed to minimise the model size. Of all bone tissue, only the jaw bone was kept. As a further step, unwanted geometric features, such as spikes, self-intersections, and small components and holes, were removed from the resulting STL object using the software GEOMAGIC Studio 12 (3D Systems, <https://www.geomagic.com>). After further smoothing, the polygon surface was converted into a non-uniform rational B-splines (NURBS) surface, allowing for an easy import into the simulation software.

Finally, Fig. 5.22 (b) illustrates the anatomical 3D CAD model for which the so-called volume conductor model (VCM) [106] has been established. Note that ultimately the VCM, and thus the problem size, was further reduced so that only the mandible bone in a soft tissue background was modelled. This is sufficient to cover the region of interest, i.e. the volume where the field has not yet decayed to an irrelevant level. This VCM served as a representative model for the subsequent studies.

COMSOL Multiphysics® (COMSOL, <https://www.comsol.com/>, version 5.2a) was used to set up the physical VCM from the anatomical CAD model. The electrical conductivity values were obtained from [29] and are  $7.4 \cdot 10^5$  S/m for titanium (Ti beta-21S), 0.7 S/m for soft tissue, and 0.02 S/m for bone (cortical bone). Sources were defined based on the implanted titanium prosthesis and screws as highlighted in Fig. 5.22 (b). According to the method of Kraus [6], an alternating voltage with a frequency

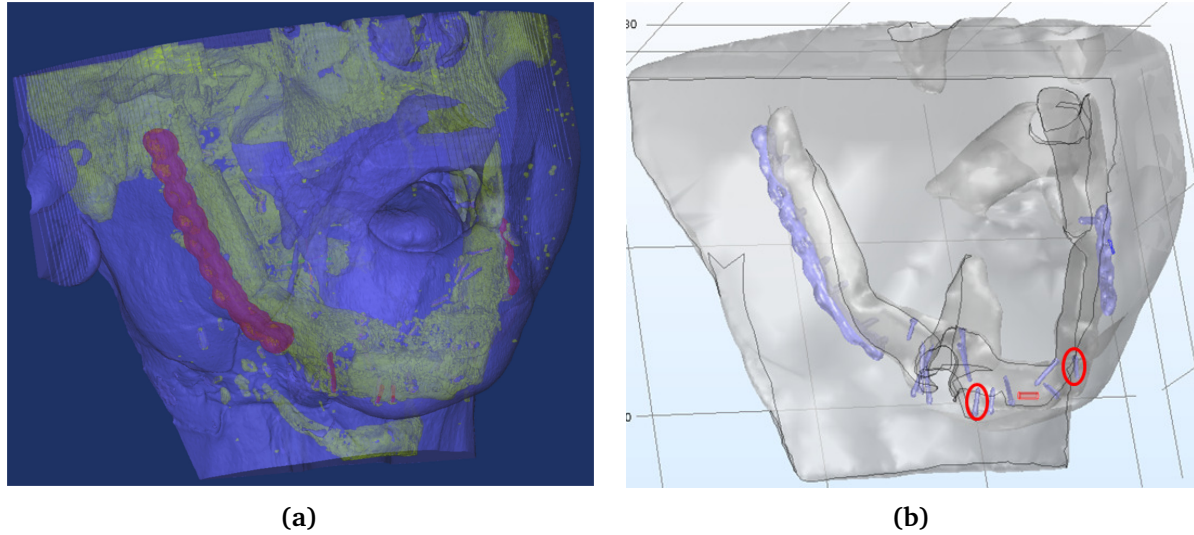


**Figure 5.22:** (a) 3D data after segmentation. This preliminary model differentiates between highly conductive titanium (red), conductive soft tissue (blue), and resistive bone (yellow). (b) Computer-aided design (CAD) model. The metallic implant and the fixation screws are shown in blue. The two screws that are defined as field sources (model 1) as well as the embedded stimulation electrode (model 2) are highlighted. Note that only the relevant part of the bone (the mandible) is kept for the simulation model. Reproduced from [36] with permission from Springer Nature.

of  $f = 20$  Hz was applied to generate electric fields ranging from 5 to 70 V/m (see Sec. 2.3.3).

A quasi-stationary current problem (QS) (Eq. (3.19)) was solved. The boundary conditions were set to Dirichlet boundary conditions with  $\varphi = \pm 0.2$  V at the field-inducing screws, to  $\varphi = 0.4$  V at the central electrode, and to ground potential at the outer posterior boundaries of the bone where the metallic implant would be directly adjacent to the mandible. A Neumann boundary condition was applied to the outer shell of the soft tissue to represent the non-conductive air. The Stationary Current Solver of COMSOL was used to solve this boundary value problem. Based on a mesh convergence study, the preliminary models used approximately 320000 (screws) and 535000 (electrode) tetrahedral mesh elements with an average quality of 0.6 (a value of 1 would refer to equilateral mesh elements). This will be further improved in future works. The resulting problem with 430000 (screws) and 715000 (electrode) degrees of freedom was solved using the conjugate gradient solver with a relative tolerance of  $\text{tol} = 1 \cdot 10^{-3}$  and a factor of  $\rho = 400$  in the error estimate of COMSOL to ensure the desired tolerance even for ill-conditioned problems. A Windows workstation with  $24 \times 3.00$  GHz CPU and 256 GB RAM was used. The computation time for each simulation run for the two models discussed was approximately two minutes, allowing for extensive further parameter and optimisation studies to be carried out in a reasonable time in the future.

## Results and discussion

In this preliminary study, two different stimulation sites are compared. Firstly, in model 1, the stimulation site is located within two screws or nails that are already involved in the implant (see highlight in Fig. 5.22 (b)). Details such as cables are neglected in the simplified models described here. The assigned voltage at the selected screws is  $\varphi_1 = -0.2\text{V}$  and  $\varphi_2 = +0.2\text{V}$ .

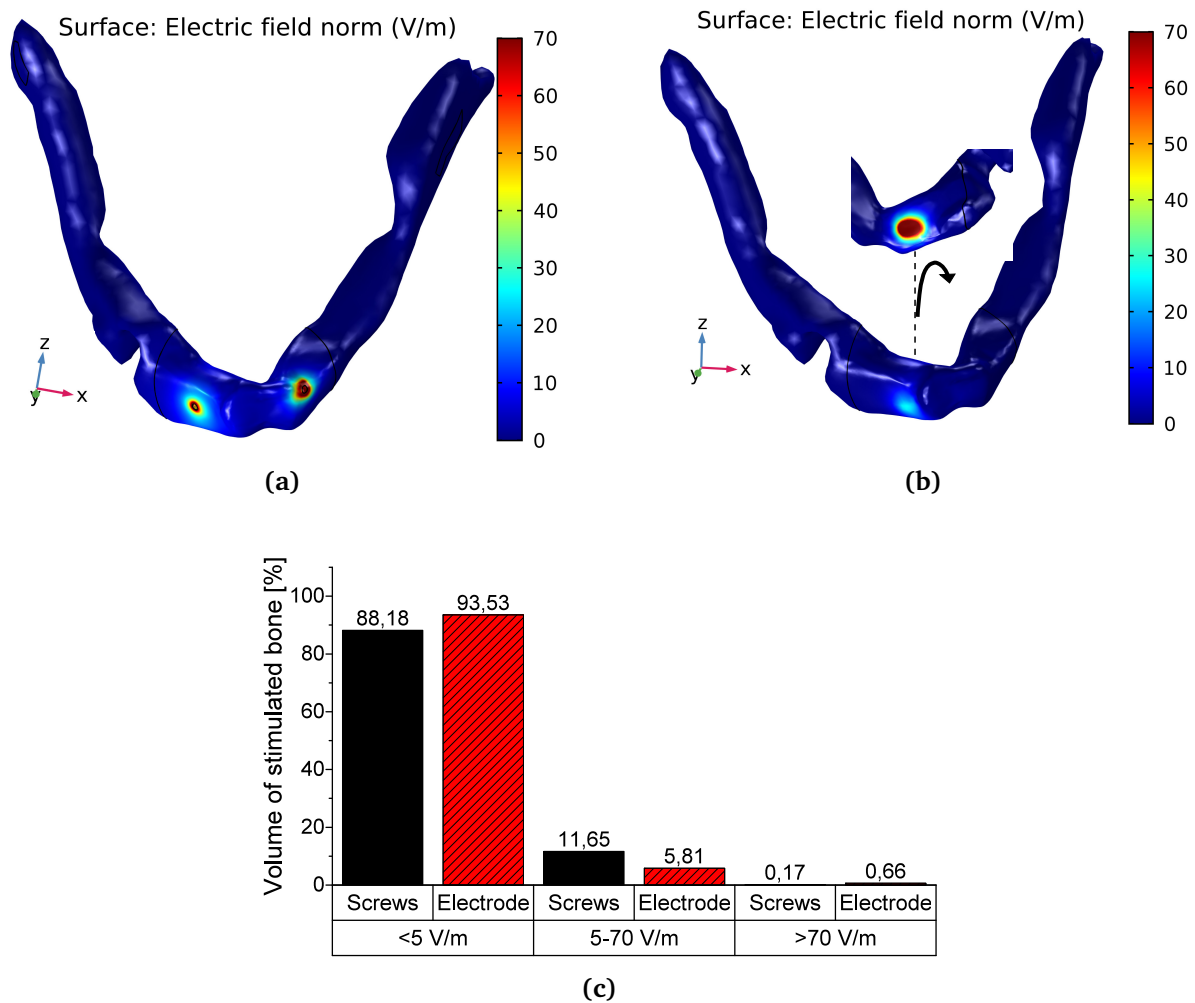


**Figure 5.23:** (a) Model 1: surface plot of the electric field norm on the mandible in the case of two screws as the stimulation site. (b) Model 2: surface plot of the electric field norm on the mandible for a central stimulation site that incorporates an implanted electrode. The inset shows the inner surface of the mandible. (c) Histogram displaying the percentage of understimulated bone ( $|\mathbf{E}| < 5\text{ V/m}$ ), beneficially stimulated bone ( $5\text{ V/m} \leq |\mathbf{E}| \leq 70\text{ V/m}$ ), and overstimulated bone ( $|\mathbf{E}| > 70\text{ V/m}$ ). Reproduced from [36] with permission from Springer Nature.

Fig. 5.23 (a) displays a surface plot of the electric field norm on the mandible surface. It clearly shows that electric field strengths of 70 V/m and more are reached

in the vicinity of the screws, which could lead to an unwanted overstimulation of the adjacent soft tissue. Therefore, a detailed parameter study should be performed in future work to determine if lower stimulation voltages would be applicable for this setup to stay below the 70 V/m limit.

In a second case, model 2, instead of using the screws as a stimulation site, a stimulation electrode was deliberately inserted into the bone. Specifically, a cylinder with a diameter of 2 mm and a height of 5 mm was utilised, as illustrated in Fig. 5.22 (b). The stimulation voltage was  $\varphi = 0.4$  V. Figure 5.23 (b) similarly displays a surface plot of the electric field norm  $|\mathbf{E}|$  on the mandible. In this case, the maximum field strength at the frontal surface remained below 35 V/m. However, Fig. 5.22 (b) reveals a significant area on the inner surface of the mandible where overstimulation with more than 70 V/m occurs.

To compare both stimulation sites, the percentage of beneficially stimulated bone is a good indicator. The histogram in Fig. 5.23 (c) illustrates that the beneficially stimulated percentage of bone volume in the case with two stimulating screws (model 1) is more than twice the percentage of the electrode case (model 2). In addition, the screw configuration results in a slightly smaller unwanted overstimulated volume than the electrode case. However, it should be noted that this finding has some limitations. The smaller volume of beneficially stimulated tissue in model 2 was mainly due to the fact that only one electrode was modelled, in contrast to the two stimulating screws used in model 1. Furthermore, the significant overstimulation observed at the bone surface in model 2 (Fig. 5.23 (b)) might have resulted from the proximity of the electrode to the bone surface. Shifting the electrode towards the centre of the bone could have decreased the overstimulated region. Therefore, further studies should focus on the optimisation of the electrode position and stimulation voltage to ensure optimal stimulation in the defective region with electric field strengths between 5 and 70 V/m [174]. In any case, room for further improvement is expected in both models, as this was only a preliminary study of initial design ideas and a systematic parameter and optimisation study is pending. The optimisation will aim on the stimulation of the individual defective region. From that a region of interest will be defined. Similar to [143], the number and placement of electrodes will be optimised to achieve the highest percentage of optimally stimulated bone in the specified region of interest. This preliminary study demonstrated that stimulation within mandibular defects can provide electric field strengths in the appropriate range to have a positive influence on the intrinsic activation of bone healing properties. These findings are essential for further research involving electrostimulative implants. The long-term vision is to have electrostimulation implants as an adjunct to patient-specific treatment planning.

The establishment of the numerical minipig model that was the main focus of this thesis was motivated by this preliminary study. The VCM of the preliminary human model was improved in the minipig model by differentiating between cortical and cancellous bone and soft tissue, by considering a low-frequency correction of the dielectric tissue properties (scenario QS<sub>zi</sub>), and by increasing the mesh resolution. Furthermore,

the electrode-tissue interface (ETI) was regarded in the minipig model and propagation of parametric uncertainties was addressed through uncertainty quantification (UQ).

### 5.5.2 Preliminary investigation of electrostimulating fixation screws at a mandibular reconstruction plate

*Figures and parts of the text were taken from the publication “Numerical design studies on a novel electrostimulative osteosynthesis system for the mandible” that appeared as a conference proceeding in Current Directions in Biomedical Engineering [35].<sup>16</sup>*

The aim of this study was to investigate different combinations of activated electrode and plate designs with focus on the insulation of the fixation screws and the fitting of the reconstruction plate regarding their influence on the electric field strength and the resulting stimulation impact in the stimulation region. The results suggest that the electrode insulation renders a crucial parameter, which influences substantially the stimulation impact and its power consumption.

#### Computational model

In order to access the electric field distribution in the defective bone area, a volume conductor model of an electrically stimulated mandible based on computer tomography (CT) images of a defective lower jaw and a preliminary bone reconstruction system has been generated. The stimulation impact, which depends on the dielectric properties of the modelled tissue types, the electrode configuration, and stimulation protocol, is determined by computing the electric field strength in the stimulated region using the finite element method.

The CAD model of the mandible was created based on CT images of the mandible of an 18-year-old girl. Registration and segmentation of CT scans were performed using Materialise Mimics®. The resulting surface mesh was further smoothed and processed to a non-uniform rational B-splines (NURBS) surface using GEOMAGIC Studio®. An inner layer of 2.5 mm thickness representing cortical bone was added to the surface model, which was then imported into the simulation software COMSOL Multiphysics® (COMSOL) (COMSOL, <https://www.comsol.com/>, version 5.2a) and combined with the suggested reconstruction system consisting of a titanium reconstruction plate equipped with six electrostimulative fixation screws, each encapsulated by an insulating shell.

<sup>16</sup>Ursula van Rienen, Christian Schmidt, and I conceptualised this study. Karthik Sridhar provided the 3D model of the cortical bone geometry. I created the numerical model with a layered bone structure comprising cortical and cancellous bone, a defective region of interest, and the electrostimulating reconstruction system, and created the visualisation of the model geometry. Christian Schmidt and I carried out the simulations. Christian Schmidt wrote the code for the model analysis and prepared the result plots. I created the initial draft of the manuscript and did the formal analysis. Ursula van Rienen and Christian Schmidt provided methodological guidance. Ursula van Rienen and Peer W. Kämmerer supervised the project, acquired the funding, and provided all resources.



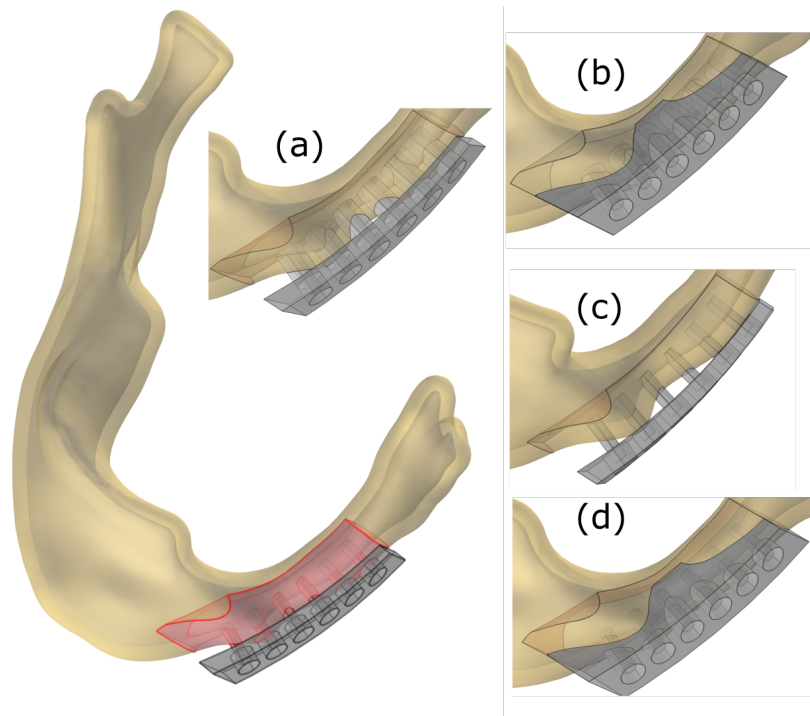


**Figure 5.24:** CAD model of the mandible with the region of interest highlighted in red (left) and four possible stimulation designs: insulated (a), insulated & fitting (b), non-insulated (c), and non-insulated & fitting (d). Figure reproduced from [35] (licensed under CC BY-NC-ND 4.0).

To investigate the effect of the screws' insulation and reconstruction-plate-fitting on the stimulation impact, four different schematic designs have been created (Fig. 5.24). Different lengths of the insulator (only inside the plate ("non-insulated") or reaching into the bone) were considered as well as two different plate designs: firstly, a patient-specific plate closely fitted to the bone (Fig. 5.24 (b),(d)) and, secondly, a generic curved plate, which is not contiguously connected with the bone (Fig. 5.24 (a),(c)). The fixation screws are modelled by cylinders embedded into the reconstruction plate. The model is surrounded by a bounding box filled with soft tissue, resulting in a five-compartment volume conductor model with its isotropic dielectric properties determined from Gabriel et al. [29] (see Table 5.14).

### Finite element simulation

To model the stimulation impact for stimulation signals used in clinical practice [6], sinusoidal voltages with  $f = 20$  Hz are applied to the stimulation electrodes. Considering the applied frequency and the dielectric properties of biological tissue, inductive processes can be neglected in the computation of the electric field strength and the



Material	$\sigma$ [S/m]	$\varepsilon_r$
Cortical bone	0.02	25100
Cancellous bone	0.078902	4020200
Soft tissue (blood)	0.7	5260
Titanium (Ti6Al4V)	$5.6 \cdot 10^5$	1
Insulator	$1 \cdot 10^{-6}$	1

**Table 5.14:** Dielectric properties (electrical conductivity  $\sigma$  and relative permittivity  $\varepsilon_r$ ) at 20 Hz of the modelled materials. For cortical bone, cancellous bone and soft tissue, the properties are taken from [28].

electroquasistatic (EQS) approximation Eq. (3.17) derived from Maxwell's equations can be applied [148].

Stimulation at the active electrodes is modelled by using Dirichlet boundary conditions with a non-zero value at the corresponding fixation screws and a zero value at the exterior boundary of the soft tissue domain, representing ground. The finite element model comprised approximately 1 million tetrahedral mesh cells. The field equation Eq. (3.17) was solved for quadratic basis functions using biconjugate gradient stabilised method and a geometric multigrid preconditioner with a relative tolerance of  $1 \cdot 10^{-6}$ . It was ensured that further mesh refinement would only change the electric field norm in the region of interest by less than 0.2 %.

In order to investigate the influence of different numbers and combinations of active stimulation electrodes, the stimulated volumes in the stimulation region, the required stimulation amplitudes, and the total power consumption for all combinations between one and six active electrodes were determined. The stimulation amplitude for each combination was scaled to a value which provided an average electric field norm of 37.5 V/m in the region of interest (Fig. 5.24), which is the mean of the values of the electric field norm considered as beneficial during the electrical stimulation of bone [6].

## Results

Comparing the four plate designs, a deviation in the electric field norm and region of beneficial stimulation between the models with completely insulated and those with non-insulated fixation screws is noticeable (Fig. 5.25). While the highest field strengths occur in the insulating material, the overall shape of the beneficial stimulation regions is similar. In contrast, increased stimulation in unwanted regions, such as the soft tissue, is noticeable for the non-insulated, non-fitting stimulation system, which results from the direct contact of the electrodes with the soft tissue and its relatively large conductivity compared to bone tissue (Table 5.14). In this case, the high conductivity of the soft tissue leads to a lower electrode impedance. This effect is also visible in a

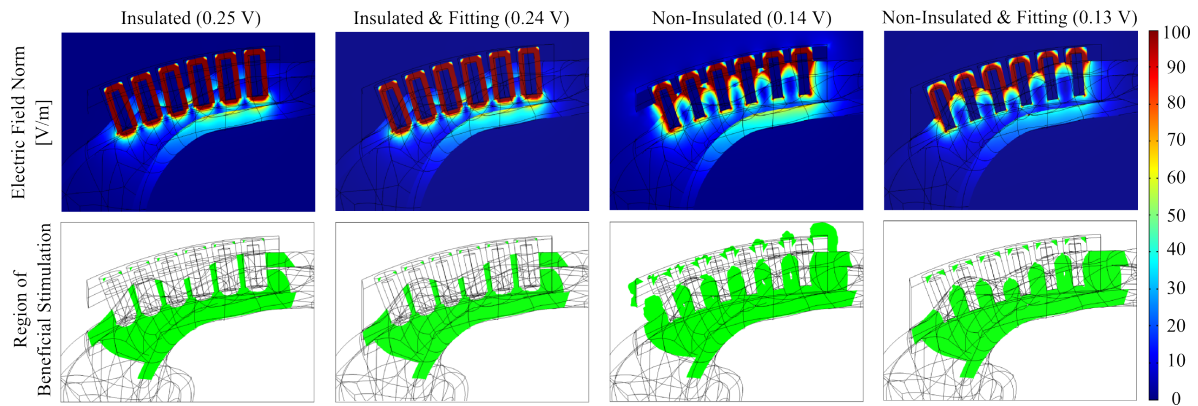


**Figure 5.25:** Electric field norm distribution (top) and region of beneficial stimulation between 5 V/m and 70 V/m (bottom) for a 6-electrode configuration and an applied stimulation amplitude to obtain an average value of 37.5 V/m in the region of interest. Figure reproduced from [35] (licensed under CC BY-NC-ND 4.0).

substantial increase of the total power consumption for the non-insulated, non-fitting model (Fig. 5.26 (a)). In both non-insulated models substantially lower stimulation amplitudes were required to reach the desired field average compared to the models with completely insulated fixation screws. Further, in both insulated models high field strengths with more than 70 V/m occur at the electrode tips that reach into the bone, while comparably less overstimulation at the electrode tips is noticeable in the non-insulated models. For all designs, the required stimulation amplitude and the resulting total power consumption to achieve a mean field strength of 37.5 V/m in the region of interest decreases with the number of active electrodes. The non-insulated model shows a remarkably high power consumption due to the direct contact between the stimulation electrodes and the highly conductive soft tissue. Overall, the lowest power consumption is required in the non-insulated, fitting stimulation system with no direct contact between the stimulation electrodes and the soft tissue. As we are rather interested in the most beneficial number of active electrodes than in their position, the depicted volume ratio represents the percentage of over-, beneficially, and under-stimulated bone tissue in the region of interest averaged over all stimulation configurations for a specific number of active electrodes. It turns out that the more electrodes are active, the more tissue is stimulated beneficially due to the more regular electric field distribution (Fig. 5.26 (b)). It should be noted that the highest overstimulation occurs for the non-insulated designs, which is a direct effect of the contiguous connection between the stimulation electrodes and the bone tissue.

## Discussion and conclusion

As one might expect, prosthesis designs without insulating coating and with only a small number of active stimulation electrodes show large regions of overstimulated tissue with  $|\mathbf{E}| > 70$  V/m (Fig. 5.26 (b)), which is associated with an increased risk of

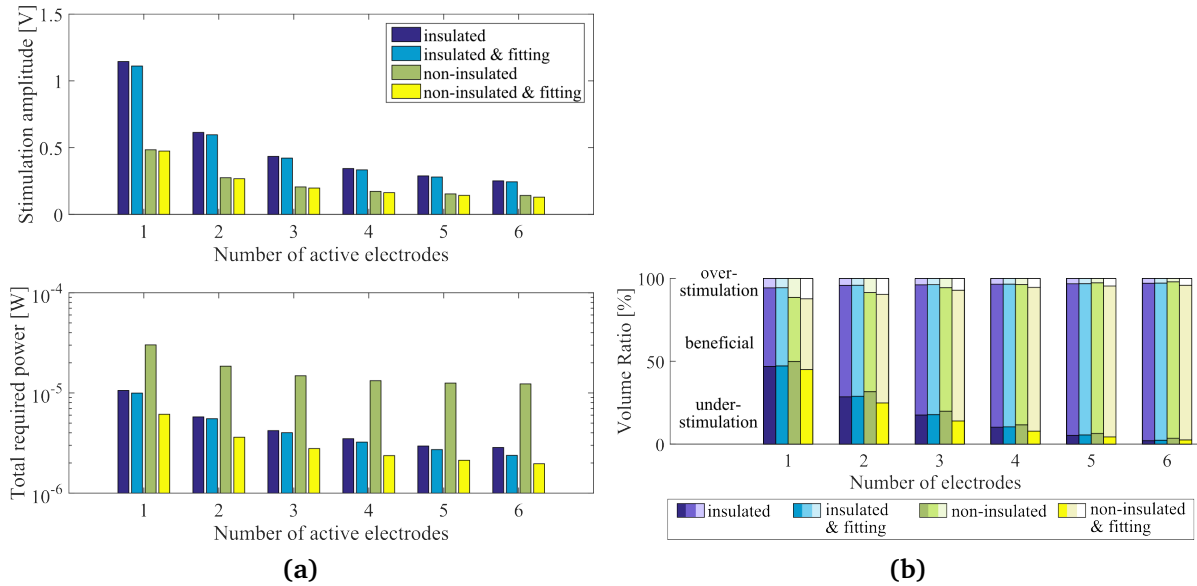


**Figure 5.26:** (a) Stimulation amplitudes (top) and corresponding required power (bottom) for applying an average electric field norm of 37.5 V/m in the region of interest for the different model geometries. (b) Average volume ratios in the region of interest for under-stimulation ( $|\underline{E}| < 5$  V/m), beneficial stimulation ( $5 \text{ V/m} \leq |\underline{E}| \leq 70$  V/m) and over-stimulation ( $|\underline{E}| > 70$  V/m) in dependence of the number of active electrodes for the different model geometries. Figure reproduced from [35] (licensed under CC BY-NC-ND 4.0).

tissue damage. Especially for the non-insulating, non-fitting design, severe damage might result due to direct contact between the stimulation electrodes and the highly conductive soft tissue, which might facilitate harmful electrode-tissue reactions. Therefore, future studies should focus on how to avoid overstimulation when considering fixation screws without a complete insulating coating. As the total required power limits the lifetime of an implanted battery when applying direct electric stimulation, stimulation systems with low power requirement will be preferable. Considering this, the model with only partially insulated fixation screws and non-fitting reconstruction plate renders an inferior design because of its high power consumption and tendency to overstimulation. Thus, in this context, a stimulation system with a higher number of active electrodes is preferential due to its corresponding small power consumption while providing a large region of beneficially stimulated tissue (Fig. 5.26 (a) and (b)). The latter is a result of the more uniform field distribution in the stimulation region. In this study, some simplifications like assigning the dielectric properties of blood to soft tissue and generally assuming isotropic and homogeneous tissue properties within each model compartment are applied. In addition, only one single insulator design with a constant thickness was considered, while the variations in these parameters may as well influence the resulting field distribution. In future studies, the geometrical model will be further refined and especially the impact of the specific tissue properties that may vary from patient to patient and within each compartment will be investigated employing Uncertainty Quantification methods [174].

This preliminary work draws conclusions on how the direct contact between bone and implant as well as different insulator configurations influence the electric field distribution in the stimulation region. Our findings show that prior to *in vivo* experimental studies and clinical trials it is necessary to evaluate the feasibility of different designs of electrostimulation systems to achieve optimal stimulation results while minimising the risk of harmful side effects. Thus, for future mandibular electrostimulation systems we suggest that particular attention should be paid to the insulation of the electrostimulation device against the soft tissue to avoid tissue damage and high power consumption.

### 5.5.3 Conclusion on the preliminary human mandible models

The preliminary human models presented here were employed at the onset of the research on electrostimulating implants for the lower jaw. The initial idea of using electrical stimulation to treat patients with large jaw defects originated in the medical field. Before developing a detailed and optimised minipig simulation model, the simplified human models allowed for an initial assessment of the electric field distribution around electrostimulating implants in the lower jaw. Consequently, the human models shown here were limited in scope, and did not account for correction of dielectric tissue properties nor the electrode-tissue interface (ETI). The animal model was chosen as a priority in this research, as it is only appropriate to thoroughly optimise the human model once the animal model has been successfully used as a proof of principle in *in vivo* studies.

The first valuable implications of the preliminary simulation studies with the human mandible models were twofold. Firstly, I conclude that the electrode configuration in terms of shape, number and location of the electrodes is of utmost importance to ensure favourable electric field strength and distribution, as well as to avoid possibly harmful overstimulation. Secondly, the findings indicate the need to give careful consideration to the design of electrode insulation, as a disadvantageous selection may lead to high power usage, resulting in reduced battery life or increased overstimulation of bone tissue. In this context, it is particularly important to avoid direct contact between the electrode and the highly conductive soft tissue. The bipolar electrode setup employed in the focus of this research was still very simple to allow compatibility with *in vitro* experiments and easy fabrication. In future studies, the implications of the findings could be realised by insulating the portions of the bipolar electrode that are outside the region of interest and in direct contact with healthy bone or soft tissue. However, further numerical investigations on the particular effects of such choices are still pending. Still, future research appears to indicate a shift towards alternative implant designs featuring a design topologically reminiscent of a plate capacitor. These recommendations will be discussed in subsequent sections.

The ETI alters only the amplitude of the electric field and the phase shift but not the field distribution. It can be estimated from the minipig models that the ETI decreases

the field amplitude by approximately 51 % ( $EQS_{Ga}$ ) and 67 % ( $QS_{Zi}$ ), corresponding to only one half or one third of the field norm without the ETI, respectively. Thus, to overcome the ETI and achieve a sufficiently large stimulation range, the stimulation amplitude would need to be increased by a factor of two or three. A similar behaviour and corresponding need for increased stimulation voltages can be expected for the human models.

Simulations of the actual species, specifically the minipig in this study, are crucial as findings cannot be directly transferred from one species to another due to variations in dielectric properties, as previously highlighted (see Sec. 4.1.2). To establish dependable human models in future research, the difficulties of obtaining trustworthy data on the dielectric properties of human mandibular bone are comparable to those discussed in Sec. 5.1.3. These include a challenging measuring procedure owing to organisational issues, as well as significant ethical concerns associated with obtaining access to such bone samples. Using less reliable data, such as samples that are not freshly obtained or that are collected from a different anatomical site, could be a viable compromise for numerically simulating and designing an initial configuration of the electrostimulating system. This will ensure that the system can deliver electrical signals within a specific range. But ultimately, only closed-loop stimulation can address this issue. This will be discussed among other aspects in the following conclusion to the research conducted in this thesis.

# Chapter 6

## Conclusion and outlook

The key findings of the studies outlined in this thesis will be summarised in the following sections. Additionally, I will point out the limitations of the present study that need to be addressed in future research, provide recommendations for this future research, and highlight the contributions to the current state of knowledge in the field of electrostimulating bone implants that this work constitutes.

### 6.1 Research objectives

Large bone defects in the mandible pose a significant challenge in maxillofacial surgery. The risks and disadvantages that are associated with conventional treatments call for alternative approaches. Electrical bone stimulation represents a viable alternative or adjunct for improving therapeutic outcomes. While electrical stimulation devices are already used in clinical practice to enhance regeneration in various anatomical regions, such devices are not yet available for the mandible. To achieve therapeutic success, it is crucial to ensure that stimulation is applied at a therapeutically effective threshold. In this context, the parameters of an electrostimulation implant need to be chosen carefully. Numerical simulations allow the electric field distribution around the electrostimulation implant to be determined and the stimulation parameters to be optimised accordingly. In this way, it is also possible to gain a better understanding of the effects of modifications to the setup. Furthermore, it is possible to draw conclusions on the effects of uncertain material properties, for example during bone healing. Therefore, it can be deduced which aspects are essential for a reliable stimulation. As a result, this research focused on the development of innovative electrostimulative implants for critical-size defects in the mandible. Six main objectives were established to ensure the achievement of the goal of this research:

1. Determine the dielectric tissue properties of minipig mandibular bone.
2. Assess the effect of modelling the dielectric tissue properties with and without a correction for electrode effects.

3. Create a 3D finite element model of a minipig mandible with a bipolar electrostimulating implant.
4. Optimise the electric field distribution with respect to the applied stimulation parameters, i.e. electrode length and stimulation voltage, to ensure a maximum volume of beneficially stimulated tissue.
5. Identify the input parameters with the most significant influence and the magnitude of their impact on the simulation results in uncertainty quantification (UQ) studies.
6. Explore potential applications of electrostimulating mandibular implants in humans using simplified human mandible models.

The first objective was addressed in Sec. 5.1 and was a prerequisite for all subsequent research objectives. Additionally, this research objective was closely linked to objective 2, which referred to two possible interpretations of low-frequency electrochemical impedance spectroscopy (EIS) data, as described in Sec. 4.2.2. This allowed me to determine how the different conductivity scenarios, with or without a low-frequency correction for the electrode processes, affected the simulation and optimisation results. I was able to determine the dielectric tissue properties of the actual species and the specific anatomical location considered in this thesis: the mandibular bone of the minipig. The data obtained for low frequencies, as relevant to this work, differed significantly in both considered scenarios. The conductivity was significantly higher, and relative permittivities were lower after correction for electrode effects. For cancellous bone, the experimentally obtained and corrected data agreed relatively well with the literature, whereas there were more significant discrepancies in terms of higher conductivity obtained for cortical bone. The uncorrected experimental data exhibited a substantial difference by exceeding the literature data for the relative permittivities by several orders of magnitude. This highlights the significance of carrying out such corrective measures. Nonetheless, the obtained measurement data did not meet all of the quality criteria I had previously set, and therefore the measurements need to be improved in future studies. The limitations will be discussed further in Sec. 6.2. The significant variability in values found within the literature indicates that a universal approach to the dielectric properties of bone is unfeasible. Consequently, accounting for the substantial variations caused by factors such as natural variability, sample condition, and measurement aspects is crucial when carrying out numerical simulations. This can be achieved through either uncertainty quantification (UQ) or case distinctions. The second research objective was further closely connected to objectives 1, 4, and 5, as will be illustrated below.

The third research objective, addressed in Sec. 4.2, focussed on presenting the modelling workflow for the development of an electrically stimulated minipig mandible model. As a result, a 3D model of a minipig mandible with a critical-size defect, surrounding soft tissue, and a bipolar electrostimulating implant with variable electrode length was created. This finite element model formed the foundation for extensive numerical studies necessary to address the remaining objectives. The fourth objective

involved the optimisation of the electrostimulating implant for the best possible electric field distribution within the defect region, as described in Sec. 5.2. This objective was closely related to the second objective mentioned above, which comprised determining how the different conductivity scenarios affected the simulation and optimisation results. Ultimately, the optimised stimulation parameters  $h_{el} = 25.7$  mm and  $\varphi_{stim,opt} = 0.41$  V for scenario EQS<sub>Ga</sub> (uncorrected) and  $h_{el} = 25.9$  mm and  $\varphi_{stim,opt} = 0.60$  V for scenario QS<sub>Zi</sub> (corrected) allowed for a beneficial electrical stimulation of roughly one half of the defect volume with only very small regions of overstimulated tissue. Despite the higher voltages and currents resulting from scenario QS<sub>Zi</sub>, I found that the power consumption in both scenarios could be safely delivered throughout the entire treatment time. Moreover, the optimised stimulation voltages have the advantage of being below the level of electrolysis. The corresponding currents may be perceptible, but are substantially lower than currents that would pose a serious risk to the patient.

The fifth objective was to analyse the impact of uncertain input parameters on the model output through the use of uncertainty quantification (UQ). The parameters of the electrode-tissue interface (ETI),  $\beta$ , and  $Y_0$ , as well as the conductivity in the defect region,  $\sigma_{canc}$ , were identified as the most influential input properties with respect to the uncertainty of the output quantities. It could be concluded that uncertainties in the assumed properties of the model may lead to undesired tissue damage due to overstimulation and should be countered by a careful experimental characterisation of the electrode and tissue properties. The volume of overstimulated tissue was the quantity most impacted by the uncertain factors, with over 52 % relative uncertainty. This, alongside the increase in overstimulated volume with increasing stimulation potential, showed the essential need to closely monitor the stimulation potential to avoid tissue harm. With respect to the second research objective in this regard, larger variances in the stimulated volumes and more pronounced parameter interactions were found in scenario QS<sub>Zi</sub>. This, together with the higher mean value of overstimulated tissue, makes thorough parameter characterisation particularly important in this more realistic<sup>1</sup> scenario.

Concerning research objective 6, Sec. 5.5 contained the numerical outcomes of simplified numerical models of electrically stimulated human mandibles. These models and their implications formed the basis for the subsequent simulations of the minipig model. The findings from the human models demonstrated the need to carefully investigate the design of electrodes and the insulating parts of the implant. Every new electrode design should be thoroughly investigated numerically using a model that reflects experimental reality as closely as possible. This is crucial for the development of safe and efficient electrical stimulation devices. In light of these requirements, it is imperative to also acknowledge the limitations that inevitably accompanied this research. Therefore, in the following section, I will examine the limitations of this study and identify challenges that may affect the validity and generalisability of the research findings.

---

<sup>1</sup>QS<sub>Zi</sub> includes a correction of electrode processes and is therefore closer to reality than EQS<sub>Ga</sub>, see Sec. 4.2.2.



## 6.2 Limitations of the studies

One of the most significant obstacles faced by researchers in the field of bioelectric modelling is the general lack of reliable data on the dielectric properties of biological tissues, and the difficulty in obtaining such data through measurements. I have reduced and quantified these uncertainties to ensure that the simulation model produces reliable results: I conducted thorough literature research to procure reliable data, gathered my own measurement data on the mandibular bone of minipigs, and utilised UQ to account for remaining parameter variations. The simulation studies conducted here contribute to explaining the implications of design choices for the electrostimulating implant. However, without precise input data the results can only be viewed as guideline values that are valid within a certain range as determined via case distinctions and UQ.

Another limitation that restricts the reliability of the results presented here concerns the electric field threshold defined for beneficial stimulation of bone. Specifically, the field threshold of 5–70 V/m defined by Kraus [6] was used in this work. As noted in Sec. 6.3, it is feasible that alternative thresholds could lead to better healing results in practical application. Obviously, the stimulation parameters to achieve these thresholds would be different and would need to be optimised accordingly. However, due to the lack of data, currently the 5–70 V/m threshold is the only available option that is supported by clinical evidence for the selected stimulation protocol.

A further limitation is that the same dielectric properties were assumed for the defect region and the remaining cancellous bone domain within the cortical bone. In reality, the dielectric properties of both domains can be different. Initially, it was planned that the cancellous bone material taken from another part of the body will be moulded to fit into the defect and equipped with growth factors. Therefore, the measured dielectric properties of structurally intact bone were regarded here. However, it was only at a later stage of this research that it became clear that the defect would be filled with granulated bone. Therefore, to enhance the reliability of the model in future studies, it is recommended to measure the dielectric properties of granulated bone.

In this study, the ETI parameters of polished titanium in buffered 0.9 % NaCl solution (pH 7.8) [227] were used. EIS measurements on Ti and Ti6Al4V specimens yielded similar results (not published [301]) for both materials. However, it is known that the ETI parameters are highly dependent on the surface properties of the material under consideration, e.g., roughness [227]. For instance, for a vacuum-plasma sprayed specimen, the capacitance parameter  $Y_0$  increases by a factor of about seven and  $\beta$  decreases by one third, compared to polished titanium [227]. Therefore, it is preferable to measure the specific electrode used in this study and obtain the corresponding ETI parameters via electrochemical impedance spectroscopy. As this work intends to establish a simulation model for the electrostimulated mandible in general, this task is deferred to future research. The revised parameters could then be easily incorporated into the established model and provide more reliable results. Recommendations for

addressing this, as well as additional challenges, will be presented in the following section.

### 6.3 Recommendations

In order to improve the reliability of future simulation studies, it is essential to characterise both the dielectric tissue properties as well as the parameters of the ETI through accurate measurements. These measurements should attempt to replicate the real scenario of the electrostimulation implant in use as closely as possible to ensure dependable analyses. Further measurements of the dielectric properties of bone in the low-frequency range are necessary to unambiguously describe this tissue. At present, it remains unclear whether the increase in permittivity at low frequencies as modelled by Gabriel et al. is due to an actual alpha dispersion or simply an artefact of the ETI. However, collecting experimental data to clarify this issue proves challenging because the dielectric properties of truly fresh bone are difficult to measure. In this context, a measurement infrastructure that allows measurements to be made under near *in vivo* conditions is crucial. This infrastructure should include the availability of minipigs, the ability to extract their mandibular bone, and transport it as quickly as possible in a tempered physiological solution to the laboratory for further sample preparation and measurement, as detailed in Sec. 5.1.3. Similar improvements are required to characterise the ETI in future EIS measurements. To achieve this, the original minipig electrodes should be measured in a solution that closely mimics the physiological environment in the mandible. In order to enhance comparability and progress towards a *Digital Twin* [265], *in vivo* EIS measurements are a long-term goal. Regular impedance measurements during the healing process, which causes changes in tissue properties, could then ensure the determination of a consistently favourable stimulation signal. The acquired data can then be fed into the numerical model, and subsequently, the stimulation amplitude can be adjusted in a feedback-controlled manner. This process should include measuring and monitoring the tissue impedance directly through the implanted stimulation electrodes, as suggested by Engel et al. for electrodes similar to the bipolar ones examined in this thesis [302]. Such closed-loop stimulation systems utilise a feedback-control system through real-time biosignal processing. They have thus far mainly been developed for neural and deep brain stimulation applications [297, 298] and are presently under further development within the stimulation platform *STELLA* [281]. Additionally, it is essential to establish a workflow that ensures controlled and monitored electrostimulation through simulation, following the example of Zimmermann and van Rienen [24], while adjusting the stimulation parameters accordingly.

The optimisations and according recommendations have been made based on the hypothesis that the field threshold of 5–70 V/m, which was derived from the stimulation parameters applied in an empirical clinical study of Kraus [6], promotes bone regeneration. Kraus treated necrosis of the femoral head and large defects in

the tibial bone with his stimulation setup [6]. Transferring the stimulation parameters to critical-size defects in the mandible appeared plausible but necessitated further experimental validation through *in vivo* experiments. The recently conducted animal experiments [48] have raised doubts regarding the suitability of the field threshold proposed by Kraus [6]. This prompts the need to consider alternative thresholds or target values for future use. The aim of future studies should therefore be to establish reliable target values and optimal parameter thresholds through *in vitro* and *ex vivo* investigations. To date, most *in vitro* stimulation parameters are used empirically without further justification, rather than being systematically optimised. Electrostimulation systems vary significantly between research groups, highlighting the need for more systematic investigation and optimisation of stimulation parameters, such as signal shape, frequency and amplitude in future research. Furthermore, bioreactors [303–305] have potential for studying the interaction between electric fields and biological tissue *ex vivo*. However, translating *ex vivo* results to *in vivo* conditions is challenging. Nevertheless, this approach is nowadays regarded as necessary to reduce or eliminate ethically questionable animal experiments.

Given the limited portion of tissue that is effectively stimulated by the established bipolar electrode design, another future goal is to further develop the electrode design to ensure a more homogeneous field distribution and increase the amount of beneficially stimulated tissue. I am involved in research in the SFB 1270 ELAINE on such an electrode design featuring opposing plate-shaped electrodes. In addition, a proper stabilisation of the electrode system is essential to prevent failure of the stimulation system due to significant mechanical stress, e.g., during chewing. The bipolar implant design regarded in this thesis is not load-bearing and the titanium mesh with 0.1 mm thickness chosen in practical surgery proved to be insufficiently stable. During the *in vivo* validation experiment with minipigs, a major problem was deformation of the titanium mesh and electrodes due to extensive chewing and rubbing by the animals [48]. To mitigate such complications, the foreseen opposite electrode design will be integrated into a load-bearing outer cage structure to hold the electrodes and bone graft material in place [306]. A similar design with opposing electrodes attached to a stabilising outer cage has been successfully used in animal studies by Kim et al. [11–13]. However, their study did not consider biomechanical optimisation of the cage design, optimisation of the electric field distribution, or incorporation of patient-specific implants, which are integral aspects of our planned research. Load-bearing implant designs may further allow for the investigation of defect cases with total discontinuities, as is typically seen in clinical cases. Therefore, biomechanical analyses of customised construction plates, as presented by, e.g., Narra et. al. [307], could be combined with the electrostimulating setup and electrical optimisation.

As bone has a hierarchical structure, future research should further incorporate multi-scale approaches to enhance the accuracy of the simulation model. It could be argued that such approaches may not significantly affect this specific application, given the presence of granulated bone in the region of interest. However, the impact of the small bone fragments might render effects that are decisive at the micro-scale. I

therefore recommend that future studies should include microscopic details, as already quite simple studies in 2D showed notably increased electric field strengths when considering the bone micro-scale as compared to the macro-scale [308]. Thus, multi-scale models of electrical bone stimulation should be established. These models would facilitate the integration of information from micro-scale simulations into the macro-scale model via appropriate scale-bridging techniques as presented, for instance, by Chopard et al. [309].

Following the presented recommendations for future research, the next section will summarise how the research presented in this thesis and my related publications enhance existing knowledge.

## 6.4 Contributions to knowledge in the field of electrostimulating bone implants

The preliminary human simulation models presented in this thesis showed that electrical stimulation of bone defects in the mandible can provide appropriate electric field strengths that can have a positive effect on bone regeneration [36]. Furthermore, valuable insights were gained into the importance of ensuring proper insulation of the electrodes and avoiding direct contact with soft tissues in order to avoid overstimulation and excessive energy consumption [35]. These studies have provided the basis for the further development and in-depth analysis of electrostimulating systems to address the research gap on electrostimulating implants for mandibular bone defects.

I also contributed to the field of bioelectric modelling by providing previously unavailable data on the dielectric properties of minipig mandibular bone. By comparing different scenarios, I learned that correction of dielectric tissue properties for electrode effects has a large impact on the optimal electrode configuration, as a 50 % higher stimulation amplitude was obtained in the corrected case. Additionally, I have shown that incorporating corrected or uncorrected tissue data significantly affects the variability of the model output, as demonstrated in the UQ studies [38]. This is of great importance for future *in vivo* application and ultimately in the clinic, where a stimulation unit will control and monitor the stimulation signal. With regard to the design of the circuitry, it is important to know the extent of such variations at an early stage of the design process.

The electrostimulating system for the minipig mandible with bipolar stimulation electrodes that was established and optimised in this thesis has significantly contributed to the advancement of future therapies for bone defects in the jaw. The simulation results published in [34] led to a recommendation for the stimulation parameters to be used in the *in vivo* experiments [48] that followed this study. The numerical study combined with the *in vivo* experiments provided proof of concept that it is possible to enhance bone regeneration with an electrically active implant in a critical-size defect.

As such, this study helped to fill the research gap in application of electrical stimulation to large mandibular bone defects in a large animal model. The findings also establish a foundation for the future application of electrostimulation therapy for treating large bone defects. The successful demonstration of the concept in treating critical-size mandibular defects enables the application of the same technique to smaller bone defects, which arise more commonly in standard dental surgeries.

# Appendix A

## Fit results and fit statistics for the dielectric properties of minipig bone

The electrochemical impedance spectroscopy (EIS) data from the mandibular bone of two minipigs were analysed using the Python package *ImpedanceFitter* version 2.0.3 [268] as described in Sec. 5.1. The valid frequency range of the data sets that passed the Lin-KK test, as well as the results of the subsequent parameter estimation are given for each animal in Tables A.1 and A.2. For the parameter estimation, the experimental data were fitted to a Cole-Cole model with two dispersions (2CC) in series with a CPE. A total of 32 data sets for cancellous bone and five data sets for cortical bone were analysed. The data sets 15–20 for animal 1 correspond to cortical bone (Table A.1), while all other data sets refer to cancellous bone. The goodness of the fit is estimated using the reduced chi-square error  $\chi^2_{\nu}$ .  $\chi^2_{\nu}$  and the errors of the parameter estimation for both animals are given in Tables A.3 and A.4.

data set	$f_{\min}$ [Hz]	$f_{\max}$ [MHz]	$c_0$ [pF]	$\varepsilon_{\infty}$	$\Delta\varepsilon_1$	$\Delta\varepsilon_2$	$\tau_1$ [ps]	$\tau_2$ [ns]	$a_1$	$a_2$	$\sigma_{DC}$ [S/m]	$K$ [ $\Omega$ ]	$\beta$
0	200	5	0.04346	26.90	929.82	35478.11	1472186.42	69100.17	0.560	0.951	0.18212	144105.36	0.761
1	150	5	0.04346	28.37	940.32	36739.65	1364566.31	73295.49	0.577	0.952	0.18155	140925.83	0.760
2	200	5	0.04015	35.26	2537.32	516006.13	9674663.04	504130.25	0.585	1.000	0.07767	263774.01	0.899
3	40	5	0.04325	30.31	467.66	1487890.83	350531.24	830192.88	0.603	0.984	0.11774	108570.90	0.766
4	200	5	0.04325	31.60	568.62	1268622.7	371761.89	765141.22	0.617	0.963	0.18406	119248.59	0.720
5	100	5	0.03924	23.96	493.25	8365.09	1169479.9	56430.67	0.495	0.786	0.08928	105466.87	0.744
6	40	5	0.03924	24.80	554.43	258341	1022887.12	341198.66	0.525	0.984	0.08922	121379.38	0.785
7	40	5	0.03607	34.23	948.75	587653.27	1366788.83	676659.22	0.572	0.936	0.11263	122065.17	0.751
8	100	5	0.03607	37.16	841.27	232933.18	1067926.00	512590.95	0.602	0.908	0.10873	71679.69	0.650
9	200	5	0.04230	35.51	887.71	253593.54	968435.8	257358.23	0.556	0.983	0.17547	68867.74	0.653
10	200	5	0.04230	38.99	1253.41	247803.66	2942717.95	281705.66	0.557	1.000	0.13042	154222.92	0.824
11	200	5	0.04412	25.78	27345.36	38267.79	2413293828	105945.71	0.504	0.987	0.1158	87047.04	0.693
12	50	5	0.04401	30.33	1248.79	74186.41	5236709.69	397735.41	0.570	0.979	0.07940	112402.55	0.779
13	200	5	0.04412	20.79	620.89	130731.11	496815.15	106956.78	0.617	1.000	0.22956	136895.34	0.753
14	150	5	0.04220	42.08	293.56	114071.23	181548.44	110886.17	0.601	0.902	0.15383	124141.63	0.729
15	80	5	0.03915	26.82	159.76	60119.58	431440.71	473880.35	0.523	0.803	0.01731	161737.40	0.585
16	40	5	0.03915	22.87	116.83	104831.33	442664.89	549797.31	0.496	0.845	0.02468	187402.12	0.677
17	40	0.3	0.04335	95.91	134.05	170227.35	368472.99	586820.09	0.980	0.843	0.05094	243214.33	0.814
18	40	5	0.04335	22.12	111.20	115024.29	96288	275567.49	0.632	0.924	0.02402	409932.92	0.846
20	100	0.4	0.03599	71.86	73.36	50749.17	452015.34	287205.63	0.892	0.853	0.01615	326690.16	0.614

**Table A.1:** Result of the fitting procedure described in Sec. 5.1.1 for the Cole-Cole model with two dispersions (2CC) in series with a constant phase element (CPE) for minipig No. 1. Further given are the valid minimum frequencies ( $f_{\min}$ ) and maximum frequencies ( $f_{\max}$ ) as obtained through the Lin-KK test. Data sets 15–20 correspond to cortical bone, whereas all other data sets represent cancellous bone.

data set	$f_{\min}$ [Hz]	$f_{\max}$ [MHz]	$c_0$ [pF]	$\varepsilon_{\infty}$	$\Delta\varepsilon_1$	$\Delta\varepsilon_2$	$\tau_1$ [ps]	$\tau_2$ [ns]	$a_1$	$a_2$	$\sigma_{\text{DC}}$ [S/m]	$K$ [ $\Omega$ ]	$\beta$
0	40	5	0.04282	17.13	476.45	401931.41	2126102.27	773824.17	0.516	0.986	0.04319	137999.41	0.670
1	40	2	0.04282	47.28	351.98	125542.12	909073.39	397721.31	0.597	0.917	0.04311	83014.63	0.628
2	40	5	0.04563	37.3	1891.93	444395.71	12355978.95	992879.99	0.486	0.972	0.08290	106364.18	0.757
3	200	5	0.04563	28.39	1042.91	96428.21	4995563.2	147243.83	0.474	0.985	0.10267	96664.69	0.694
4	40	1	0.04843	44.03	201.42	1223050.68	409600.7	839220.56	0.738	1.000	0.07567	100878.45	0.699
5	100	5	0.04401	32.40	424.09	67062.18	730138.38	133872.2	0.583	0.947	0.05563	27267.38	0.461
6	50	5	0.04401	37.24	210.96	136999.98	255648.27	187039.16	0.632	0.914	0.05206	42280.06	0.559
7	200	1	0.04139	47.08	653.17	760867.37	1053341.65	923614.46	0.593	1.000	0.09795	174850.88	0.726
9	40	4	0.04368	27.15	845.93	221708.82	4364583.4	817426.06	0.529	0.962	0.03983	114819.98	0.797
12	80	5	0.03855	33.51	334.81	259782.25	223339.29	187611.69	0.605	0.922	0.140	117153.16	0.732
13	40	1	0.03855	94.27	225.69	1030258.54	245385.85	708393.66	0.882	0.932	0.09378	64056.18	0.710
14	60	5	0.03855	36.44	394.06	432894.67	357694.86	650692.67	0.553	0.908	0.10066	114470.24	0.794
15	100	5	0.03855	19.62	621.28	260849.59	1775235.66	718322.48	0.468	0.920	0.08079	120847.48	0.729
16	40	2	0.06345	33.21	491.07	82299.22	1649139.84	642898.61	0.545	0.833	0.03641	156598.54	0.880
17	40	3	0.06345	21.17	844.03	69451.83	3771344.94	999635.28	0.601	1.000	0.02553	130397.32	0.815
18	40	5	0.03645	49.09	1190.04	217787.98	2604778.21	708188.2	0.557	0.917	0.05386	83776.23	0.799
19	60	5	0.03645	49.60	1185.60	248613.34	2625228.19	748292.94	0.555	0.919	0.05343	98526.51	0.835

**Table A.2:** Result of the fitting procedure described in Sec. 5.1.1 for the Cole-Cole model with two dispersions (2CC) in series with a constant phase element (CPE) for minipig No. 2. Further given are the valid minimum frequencies ( $f_{\min}$ ) and maximum frequencies ( $f_{\max}$ ) as obtained through the Lin-KK test. All data sets represent cancellous bone.



data set	$\chi^2_\nu$	$\pm\epsilon_\infty$ [%]	$\pm\Delta\epsilon_1$ [%]	$\pm\Delta\epsilon_2$ [%]	$\pm\tau_1$ [%]	$\pm\tau_2$ [%]	$\pm a_1$ [%]	$\pm a_2$ [%]	$\pm\sigma_{DC}$ [%]	$\pm K$ [%]	$\pm\beta$ [%]
0	0.2	1.9	3.3	2.1	6.4	1.6	0.4	0.3	0.0	0.3	0.1
1	1.1	4.0	6.9	4.6	12.8	3.7	0.9	0.6	0.1	0.5	0.1
2	1.1	0.4	4.7	5.2	5.9	1.2	0.3	0.3	0.6	7.3	1.5
3	11.3	6.3	4.3	2.2	8.4	0.9	1.7	0.1	0.3	0.9	0.3
4	0.6	4.2	3.8	4.9	6.7	3.0	1.0	0.2	0.3	1.0	0.2
5	1.4	2.9	8.5	4.2	16.9	5.2	0.9	1.0	0.0	0.3	0.1
6	18.0	6.2	6.3	2.3	15.7	1.5	1.8	0.2	0.1	0.8	0.2
7	12.1	3.2	4.9	3.5	9.7	1.8	0.9	0.1	0.2	0.7	0.2
8	1.3	1.0	2.3	4.1	3.7	1.5	0.3	0.1	0.2	0.8	0.3
9	2.2	5.3	9.2	12.1	17.6	3.7	1.4	0.8	0.7	2.8	0.8
10	0.6	1.1	3.6	4.2	6.8	1.4	0.3	0.2	0.2	2.2	0.5
11	3.0	2883.3	14.7	5703.2	4.9	1.4	1.2	2.0	5.1	1.6	
12	4.6	1.2	5.1	7.1	9.2	4.4	0.4	0.6	0.1	0.7	0.2
13	3.3	17.8	10.2	8.4	19.5	4.4	3.0	0.6	0.3	1.8	0.4
14	1.5	4.5	4.5	2.0	7.8	1.4	2.0	0.1	0.1	0.6	0.1
15	34.4	1.1	2.7	2.9	5.9	1.7	0.9	0.2	0.2	1.4	0.5
16	87.0	2.5	5.8	2.3	14.2	1.6	2.2	0.1	0.1	0.8	0.2
17	4.4	12.0	11.1	1.6	9.6	1.2	5.1	0.1	0.1	0.3	0.1
18	63.2	2.4	1.5	0.6	1.8	0.5	1.0	0.0	0.0	0.6	0.1
20	193.0	5.8	11.2	2.3	5.4	1.5	6.0	0.1	0.2	1.3	0.4

**Table A.3:** Reduced chi-square error  $\chi^2_\nu$  and errors of the parameter fit for the Cole-Cole model with two dispersions (2CC) in series with a constant phase element (CPE) for minipig No. 1.

data set	$\chi^2_\nu$	$\pm\epsilon_\infty$ [%]	$\pm\Delta\epsilon_1$ [%]	$\pm\Delta\epsilon_2$ [%]	$\pm\tau_1$ [%]	$\pm\tau_2$ [%]	$\pm a_1$ [%]	$\pm a_2$ [%]	$\pm\sigma_{DC}$ [%]	$\pm K$ [%]	$\pm\beta$ [%]
0	96.4	5.0	9.6	4.7	22.1	1.8	1.6	0.3	0.5	1.7	0.6
1	23.4	3.1	5.1	2.3	9.7	1.5	1.8	0.1	0.1	0.6	0.2
2	5.2	1.7	10.2	6.7	22.1	2.8	0.6	0.3	0.3	0.9	0.3
3	0.5	1.7	5.5	2.2	13.5	1.1	0.6	0.2	0.1	0.9	0.2
4	3.7	9.4	6.7	1.0	6.5	0.4	4.0	0.1	0.2	0.5	0.2
5	13.0	2.1	3.8	2.4	7.3	1.4	0.9	0.2	0.2	1.2	0.6
6	61.2	4.4	6.6	1.8	11.2	1.4	2.8	0.1	0.2	1.2	0.5
7	0.6	6.8	5.2	4.3	9.3	1.8	1.8	0.3	0.3	1.0	0.2
9	7.6	1.0	2.6	1.9	5.6	1.0	0.3	0.1	0.1	0.9	0.2
12	5.7	6.9	5.3	1.9	9.6	1.3	2.4	0.1	0.1	0.7	0.2
13	7.4	7.7	6.6	1.3	3.7	0.6	3.9	0.0	0.2	0.8	0.3
14	4.8	4.7	4.2	3.2	9.1	1.6	1.8	0.1	0.2	1.0	0.3
15	1.8	3.3	4.7	4.3	12.3	1.5	0.8	0.1	0.2	1.1	0.3
16	1.4	1.4	2.1	1.6	4.2	1.5	0.5	0.1	0.0	0.3	0.1
17	14.5	1.0	1.4	7.7	2.7	3.2	0.2	0.4	0.1	1.4	0.4
18	1.9	0.4	0.9	1.1	1.9	0.7	0.1	0.1	0.0	0.5	0.1
19	1.8	0.4	1.0	1.4	1.9	0.7	0.1	0.0	0.1	1.1	0.3

**Table A.4:** Reduced chi-square error  $\chi^2_\nu$  and errors of the parameter fit for the Cole-Cole model with two dispersions (2CC) in series with a constant phase element (CPE) for minipig No. 2.

## Appendix B

### Impact of the stimulation amplitude on the Sobol' indices

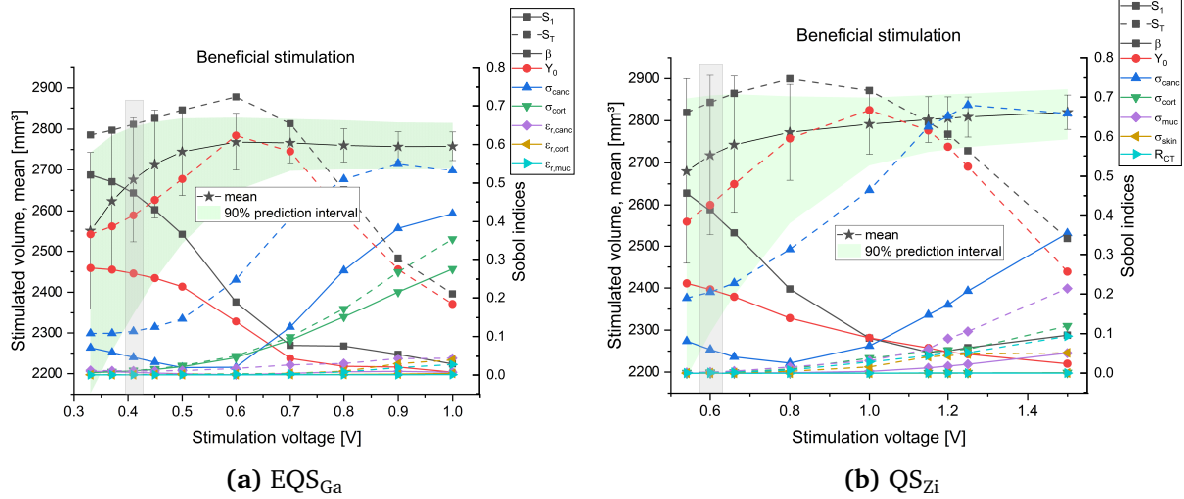


**Figure B.1:** Mean values of the volume of beneficially stimulated tissue ( $5 \text{ V/m} \leq |\underline{E}| \leq 70 \text{ V/m}$ ) inside the defect region and Sobol' indices (first order Sobol' indices  $S_1$  (solid lines) and total Sobol' indices  $S_T$  (dashed lines)) as a function of the stimulation voltage for (a)  $\text{EQS}_{\text{Ga}}$  and (b)  $\text{QS}_{\text{Zi}}$ . Further, the 90 % prediction interval is highlighted in color, while the error bars represent the standard deviation. The optimised configuration is highlighted in grey. Figure adapted from [38].

For both scenarios,  $\text{EQS}_{\text{Ga}}$  and  $\text{QS}_{\text{Zi}}$ , the Sobol' indices (as seen in Figs. B.1 and B.2) exhibit the same overall trend with respect to stimulation voltage. However, the 90 % prediction interval is consistently greater for  $\text{QS}_{\text{Zi}}$ , and the curves for the stimulated volumes show less steep increases and decreases. As the stimulation voltage increases, a notable decrease in the volume of understimulated tissue is observed (Fig. B.2 (c), (d)), while the volume of overstimulated tissue increases significantly with amplified stimulation amplitude (Fig. B.2 (a), (b)). The volume of beneficially stimulated tissue marginally increases and appears to approach a plateau (Fig. B.1).

The extent of the 90 % prediction interval remains relatively constant for the understimulated volume, approximately  $830 \text{ mm}^3$  in scenario  $\text{EQS}_{\text{Ga}}$  and  $1260 \text{ mm}^3$  in

scenario  $QS_{Zi}$ . However, for the beneficially stimulated volume, the 90 % prediction interval decreases from an already relatively narrow value of  $590 \text{ mm}^3$  ( $EQS_{Ga}$ ) and  $665 \text{ mm}^3$  ( $QS_{Zi}$ ) to approximately a quarter of their initial value ( $111 \text{ mm}^3$  ( $EQS_{Ga}$ ) and  $119 \text{ mm}^3$  ( $QS_{Zi}$ )). For overstimulated tissue, the 90 % prediction interval increases significantly from  $236 \text{ mm}^3$  to  $875 \text{ mm}^3$  ( $EQS_{Ga}$ ), and from  $630 \text{ mm}^3$  to  $1261 \text{ mm}^3$  ( $QS_{Zi}$ ).

The narrow 90 % prediction interval of the beneficially stimulated volume suggests it is a robust quantity. Therefore, a large portion of the defective tissue is likely to receive beneficial stimulation across a wide range of stimulation amplitudes, given the assumed uncertainties. However, the results for the overstimulated tissue in the defect region imply that both the 90 % prediction interval as well as the increase in overstimulated volume are much greater, which is an important observation. Therefore, careful monitoring of the applied stimulation voltage is crucial to prevent potential tissue damage resulting from overstimulation.

For the beneficially stimulated tissue, the Sobol' indices exhibit an interesting behaviour with increasing stimulation amplitude (Fig. B.1). The most significant changes can be observed for the input quantities that are already highly influential at the optimised configuration, such as  $\beta$ ,  $Y_0$ , and  $\sigma_{canc}$ . For instance, the impact of the input parameters  $\beta$  and  $Y_0$  is significantly reduced and falls below 0.1 at  $\varphi_{stim} = 0.7 \text{ V}$  in  $EQS_{Ga}$ . Meanwhile, in  $QS_{Zi}$ , this reduction takes place at a higher stimulation amplitude of approximately  $\varphi_{stim} = 1 \text{ V}$ . Furthermore, the total Sobol' indices of  $\beta$  and  $Y_0$  initially increase as the stimulation voltage increases, attain a maximum, and then decrease drastically.

In  $EQS_{Ga}$  and  $QS_{Zi}$ ,  $S_{1,\sigma_{canc}}$  initially experiences a slight decrease and is relatively insignificant up to stimulation voltages of approximately 0.6 V and 1 V, respectively. However, it subsequently increases to 0.42 for 1 V in  $EQS_{Ga}$  (0.36 at 1.5 V in  $QS_{Zi}$ ). Additionally, in both scenarios the total Sobol' index for  $\sigma_{canc}$  is relatively large and demonstrates an increasing tendency with values up to 0.55 ( $EQS_{Ga}$ ) and 0.68 ( $QS_{Zi}$ ) for an increasing stimulation voltage. The findings suggest an increase in interaction effects at higher stimulation amplitudes. This is evidenced by the decrease in the sum of first order indices and the increase in the sum of total order Sobol' indices (not shown). The sum of the total Sobol' indices increases until 0.7 V ( $EQS_{Ga}$ ) and 1.15 V ( $QS_{Zi}$ ) and then decreases.

The influence of  $\sigma_{cort}$  increases with increasing stimulation amplitude from approximately 0.5 V on. Nevertheless, solely in  $EQS_{Ga}$  does  $\sigma_{cort}$  become a significant quantity with respect to the uncertainty of the output quantities at higher stimulation amplitudes and reaches values of up to  $S_{1,\sigma_{cort}} = 0.28$  at  $\varphi_{stim} = 1 \text{ V}$  ( $EQS_{Ga}$ ). In  $QS_{Zi}$ , the total Sobol' index of  $\sigma_{cort}$  increases to values of up to 0.12, while the first order Sobol' index remains below 0.002. Hence, in  $QS_{Zi}$  some impact of uncertain cortical bone conductivity could be expected due to interactions with other input parameters, while in  $EQS_{Ga}$  the individual effect of  $\sigma_{cort}$  on the volume of beneficially stimulated bone could also be substantial. It is worth noting that the total Sobol' index for  $\sigma_{muc}$  also gains

significance at high voltages in  $QS_{Zi}$ , reaching  $S_{T,\sigma_{muc}} = 0.21$  at 1.5 V. However, when interpreting these findings in conjunction with the significantly decreasing standard deviation (Fig. 5.16), it is necessary to approach the observed significance of  $\sigma_{cort}$  and  $\sigma_{muc}$  with caution: the STD/mean ratios for these instances are below 2 % for these cases (where  $\varphi_{stim} = 0.8$  V, 1.2 V, 1.5 V), and therefore no significant variations in the output are anticipated.

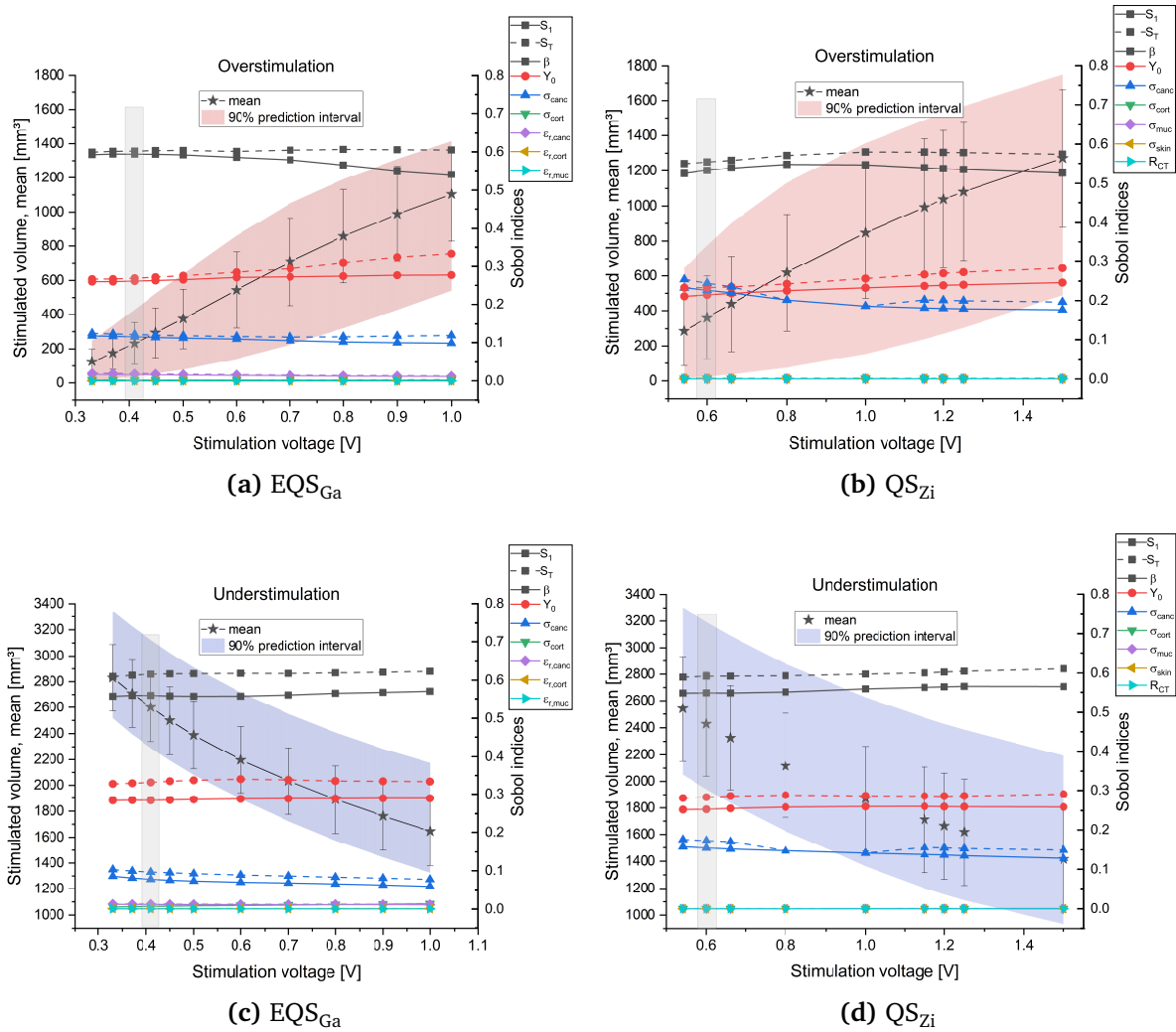


**Figure B.2:** Mean values of the volume of (a), (b) overstimulated tissue ( $|\underline{E}| > 70$  V/m) and (c), (d) understimulated tissue ( $|\underline{E}| < 5$  V/m) inside the defect region as well as Sobol' indices (first order Sobol' indices  $S_1$  (solid lines) and total Sobol' indices  $S_T$  (dashed lines)) as a function of the stimulation voltage for (a), (c)  $EQS_{Ga}$  and (b), (d)  $QS_{Zi}$ . Further, the 90 % prediction interval is highlighted in color, while the error bars represent the standard deviation. The optimised configuration is highlighted in grey. Figure adapted from [38].

The stimulation amplitude has little impact on the Sobol' indices for both over- and understimulated tissue, as depicted in Fig. B.2, with only a few percentage points of difference observed. The first order Sobol' indices for  $\beta$  and  $\sigma_{canc}$  for the overstimulated

tissue experience a slight decrease as the stimulation voltage increases. The decrease is more pronounced for  $\sigma_{\text{canc}}$  in  $\text{QS}_{\text{Zi}}$ . Here, the effect of  $\sigma_{\text{canc}}$  is also greater than in  $\text{EQS}_{\text{Ga}}$ . The Sobol' indices for  $Y_0$  show a slight increase. The sum of the total Sobol' indices for the over- and understimulated volumes in both scenarios remains relatively constant, with variations less than 0.06 (not shown).

Note that the Sobol' indices for the electric field norm  $|\underline{\mathbf{E}}(P_1)|$  and the terminal current  $I_{\text{term}}$  remain constant for different stimulation voltages in the same scenario, due to the linearity of the underlying numerical problem. As a result, they are not shown here. However, this linearity does not apply to the computation of the stimulated volumes, which are evaluated using integrals. Therefore, their Sobol' indices vary for different stimulation voltages.

# Bibliography

- [1] I. Yasuda, “The classic: fundamental aspects of fracture treatment by Iwao Yasuda, reprinted from J. Kyoto Med. Soc., 4:395-406, 1953.” *Clin. Orthop. Relat. Res.*, vol. 124, pp. 5–8, 1977. [Online]. Available: <https://pubmed.ncbi.nlm.nih.gov/340088/>
- [2] K. M. Stürmer and K. P. Schmit-Neuerburg, “Indikation und klinische Ergebnisse der elektromagnetisch induzierten Wechselstromstimulation reaktionsarmer Pseudarthrosen.” *Unfallchirurgie*, vol. 11, no. 4, pp. 197–203, 1985. [Online]. Available: <https://doi.org/10.1007/BF02587960>
- [3] R. K. Aaron, D. M. Ciombor, and B. J. Simon, “Treatment of nonunions with electric and electromagnetic fields.” *Clin. Orthop. Relat. Res.*, no. 419, pp. 21–29, 2004. [Online]. Available: <https://doi.org/10.1097/00003086-200402000-00005>
- [4] W. Mittelmeier, S. Lehner, W. Kraus, H. P. Matter, L. Gerdesmeyer, and E. Steinhäuser, “BISS: concept and biomechanical investigations of a new screw system for electromagnetically induced internal osteostimulation.” *Arch. Orthop. Trauma Surg.*, vol. 124, no. 2, pp. 86–91, 2004. [Online]. Available: <https://doi.org/10.1007/s00402-003-0594-9>
- [5] W. Latham and J. T. Lau, “Bone stimulation. a review of its use as an adjunct.” *Tech. Orthop.*, vol. 26, no. 1, pp. 14–21, 2011. [Online]. Available: <https://doi.org/10.1097/BTO.0b013e31820e66e4>
- [6] W. Kraus, “Magnetic field therapy and magnetically induced electrostimulation in orthopedics.” *Orthopaede*, vol. 13, no. 2, pp. 78–92, 1984. [Online]. Available: <https://pubmed.ncbi.nlm.nih.gov/6203080/>
- [7] W. Kraus and F. Lechner, “Healing of pseudoarthrosis and spontaneous fractures with structure-forming electrodynamic potentials.” *Munch. Med. Wochenschr.*, vol. 114, pp. 1814–9, 1972.
- [8] “DRG-Statistik 2019. Operationen und Prozeduren der vollstationären Patientinnen und Patienten in Krankenhäusern (4-Steller). Key word “5-772 Partielle und totale Resektion der Mandibula”. Statistisches Bundesamt (Destatis), Tech. Rep., 2020. [Online]. Available: <https://www.destatis.de/DE/Themen/Gesellschaft-Umwelt/Gesundheit/Krankenhaeuser/Publikationen/Downloads-Krankenhaeuser/>

- operationen-prozeduren-5231401197014.pdf?\_\_blob=publicationFile (accessed 06.10.2023).
- [9] SMArt image of a skull. Servier Medical Art. (accessed 24.09.2021). [Online]. Available: [https://smart.servier.com/smart\\_image/skull/](https://smart.servier.com/smart_image/skull/)
- [10] E. Roddy, M. R. DeBaun, A. Daoud-Gray, Y. P. Yang, and M. J. Gardner, "Treatment of critical-sized bone defects: clinical and tissue engineering perspectives." *Eur. J. Orthop. Surg. Traumatol.*, vol. 28, no. 3, pp. 351–362, 2018. [Online]. Available: <https://doi.org/10.1007/s00590-017-2063-0>
- [11] J. H. Kim, T. H. Lee, Y. M. Song, I. S. Kim, T. H. Cho, S. J. Hwang, and S. J. Kim, "An implantable electrical bioreactor for enhancement of cell viability." in *2011 Annual International Conference of the IEEE Engineering in Medicine and Biology Society*. IEEE, 2011, pp. 3601–3604, Boston, MA, USA. [Online]. Available: <https://doi.org/10.1109/iembs.2011.6090603>
- [12] J. Kim, H. J. Yang, T. H. Cho, S. E. Lee, Y. D. Park, H. M. Kim, I. S. Kim, Y.-K. Seo, S. J. Hwang, and S. J. Kim, "Enhanced regeneration of rabbit mandibular defects through a combined treatment of electrical stimulation and rhBMP-2 application." *Med. Biol. Eng. Comput.*, no. 12, pp. 1339–1348, 2013. [Online]. Available: <https://doi.org/10.1007/s11517-013-1106-x>
- [13] C. Kim, H. J. Yang, T. H. Cho, B. S. Lee, T. M. Gwon, S. Shin, I. S. Kim, S. J. Kim, and S. J. Hwang, "Implantable electrical stimulation bioreactor with liquid crystal polymer-based electrodes for enhanced bone regeneration at mandibular large defects in rabbit." *Med. Biol. Eng. Comput.*, vol. 58, no. 2, pp. 383–399, 2020. [Online]. Available: <https://doi.org/10.1007/s11517-019-02046-2>
- [14] P. Grunert, A. Jonitz-Heincke, Y. Su, R. Souffrant, D. Hansmann, H. Ewald, A. Krüger, W. Mittelmeier, and R. Bader, "Establishment of a novel in vitro test setup for electric and magnetic stimulation of human osteoblasts." *Cell. Biochem. Biophys.*, vol. 70, no. 2, pp. 805–817, 2014. [Online]. Available: <https://doi.org/10.1007/s12013-014-9984-6>
- [15] Y. Su, D. Klues, W. Mittelmeier, U. van Rienen, and R. Bader, "An automatic approach for calibrating dielectric bone properties by combining finite-element and optimization software tools." *Comput. Methods Biomech. Biomed. Engin.*, vol. 19, pp. 1306–1313, 2016. [Online]. Available: <https://doi.org/10.1080/10255842.2015.1131980>
- [16] B. Hiemer, J. Ziebart, A. Jonitz-Heincke, P. C. Grunert, Y. Su, D. Hansmann, and R. Bader, "Magnetically induced electrostimulation of human osteoblasts results in enhanced cell viability and osteogenic differentiation." *Int. J. Mol. Med.*, vol. 38, pp. 57–64, 2016. [Online]. Available: <https://doi.org/10.3892/ijmm.2016.2590>
- [17] B. Hiemer, M. Krogull, T. Bender, J. Ziebart, S. Krueger, R. Bader, and



- A. Jonitz-Heincke, "Effect of electric stimulation on human chondrocytes and mesenchymal stem cells under normoxia and hypoxia." *Mol. Med. Rep.*, vol. 18, no. 2, pp. 2133–2141, 2018. [Online]. Available: <https://doi.org/10.3892/mmr.2018.9174>
- [18] T. J. Dauben, J. Ziebart, T. Bender, S. Zaatreh, B. Kreikemeyer, and R. Bader, "A novel in vitro system for comparative analyses of bone cells and bacteria under electrical stimulation." *Biomed Res. Int.*, vol. 2016, 2016. [Online]. Available: <https://doi.org/10.1155/2016/5178640>
- [19] F. Sahm, J. Ziebart, A. Jonitz-Heincke, D. Hansmann, T. Dauben, and R. Bader, "Alternating electric fields modify the function of human osteoblasts growing on and in the surroundings of titanium electrodes." *Int. J. Mol. Sci.*, vol. 21, no. 18, p. 6944, 2020. [Online]. Available: <https://doi.org/10.3390/ijms21186944>
- [20] P. W. Kämmerer, V. Engel, F. Plocksties, A. Jonitz-Heincke, D. Timmermann, N. Engel, B. Frerich, R. Bader, D. G. E. Thiem, A. Skorska, R. David, B. Al-Nawas, and M. Dau, "Continuous electrical stimulation affects initial growth and proliferation of adipose-derived stem cells." *Biomedicines*, no. 11, p. 482, 2020. [Online]. Available: <https://doi.org/10.3390/biomedicines8110482>
- [21] F. Sahm, V. Freiin Grote, J. Zimmermann, F. Haack, A. M. Uhrmacher, U. van Rienen, R. Bader, R. Detsch, and A. Jonitz-Heincke, "Long-term stimulation with alternating electric fields modulates the differentiation and mineralization of human pre-osteoblasts." *Front. Physiol.*, vol. 13, 2022. [Online]. Available: <https://doi.org/10.3389/fphys.2022.965181>
- [22] T. Kreller, J. Zimmermann, U. van Rienen, A. R. Boccaccini, A. Jonitz-Heincke, and R. Detsch, "Alternating electric field stimulation: phenotype analysis and osteoclast activity of differentiated RAW 264.7 macrophages on hydroxyapatite-coated Ti6Al4V surfaces and their crosstalk with MC3T3-E1 pre-osteoblasts." *Biomater. Adv.*, p. 213285, 2023. [Online]. Available: <https://doi.org/10.1016/j.bioadv.2023.213285>
- [23] Y. Su, R. Souffrant, D. Kluess, M. Ellenrieder, W. Mittelmeier, U. van Rienen, and R. Bader, "Evaluation of electric field distribution in electromagnetic stimulation of human femoral head." *Bioelectromagnetics*, vol. 35, no. 8, pp. 547–558, 2014. [Online]. Available: <https://doi.org/10.1002/bem.21879>
- [24] J. Zimmermann, F. Sahm, N. Arbeiter, H. Bathel, Z. Song, R. Bader, A. Jonitz-Heincke, and U. van Rienen, "Experimental and numerical methods to ensure comprehensible and replicable alternating current electrical stimulation experiments." *Bioelectrochemistry*, vol. 151, p. 108395, 2023. [Online]. Available: <https://doi.org/10.1016/j.bioelechem.2023.108395>
- [25] Z. B. Friedenber, E. T. Andrews, B. I. Smolenski, B. W. Pearl, and C. T. Brighton, "Bone reaction to varying amounts of direct current." *Surg. Gynecol. Obstet.*, vol. 131, pp. 894–889, 1970. [Online]. Available:

- <https://pubmed.ncbi.nlm.nih.gov/5471542/>
- [26] J. A. Spadaro, "Electrically enhanced osteogenesis at various metal cathodes." *J. Biomed. Mater. Res.*, vol. 16, no. 6, pp. 861–873, 1982. [Online]. Available: <https://doi.org/10.1002/jbm.820160611>
- [27] C. Gabriel, S. Gabriel, and E. Corthout, "The dielectric properties of biological tissues: I. literature survey." *Phys. Med. Biol.*, vol. 41, no. 11, pp. 2231–2249, 1996. [Online]. Available: <https://doi.org/10.1088/0031-9155/41/11/001>
- [28] S. Gabriel, R. W. Lau, and C. Gabriel, "The dielectric properties of biological tissues: II. measurements in the frequency range 10 Hz to 20 GHz." *Phys. Med. Biol.*, vol. 41, no. 11, pp. 2251–2269, 1996. [Online]. Available: <https://doi.org/10.1088/0031-9155/41/11/002>
- [29] S. Gabriel, R. W. Lau, and C. Gabriel, "The dielectric properties of biological tissues: III. parametric models for the dielectric spectrum of tissues." *Phys. Med. Biol.*, vol. 41, no. 11, pp. 2271–2293, 1996. [Online]. Available: <https://doi.org/10.1088/0031-9155/41/11/003>
- [30] J. Zimmermann and U. van Rienen, "Ambiguity in the interpretation of the low-frequency dielectric properties of biological tissues." *Bioelectrochemistry*, vol. 140, p. 107773, 2021. [Online]. Available: <https://doi.org/10.1016/j.bioelechem.2021.107773>
- [31] S. M. Kurtz and J. N. Devine, "PEEK biomaterials in trauma, orthopedic, and spinal implants." *Biomaterials*, vol. 28, no. 32, pp. 4845–4869, 2007. [Online]. Available: <https://doi.org/10.1016/j.biomaterials.2007.07.013>
- [32] V. V. Dam, H. A. Trinh, D. Rokaya, and D. H. Trinh, "Bone augmentation for implant placement: recent advances." *Int. J. Dent.*, vol. 2022, 2022. [Online]. Available: <https://doi.org/10.1155/2022/8900940>
- [33] M. Chiapasco, P. Casentini, and M. Zaniboni, "Bone augmentation procedures in implant dentistry." *Int. J. Oral Maxillofac. Implants*, vol. 24, 2009. [Online]. Available: <https://pubmed.ncbi.nlm.nih.gov/19885448/>
- [34] H. Raben, P. W. Kämmerer, R. Bader, and U. van Rienen, "Establishment of a numerical model to design an electro-stimulating system for a porcine mandibular critical size defect." *Appl. Sci.*, vol. 9, no. 10, p. 2160, 2019. [Online]. Available: <https://doi.org/10.3390/AP9102160>
- [35] H. Raben, C. Schmidt, K. Sridhar, P. W. Kämmerer, and U. van Rienen, "Numerical design studies on a novel electrostimulative osteosynthesis system for the mandible." *Curr. Dir. Biomed. Eng.*, vol. 3, no. 2, pp. 613–617, 2017. [Online]. Available: <https://doi.org/10.1515/cdbme-2017-0128>
- [36] U. van Rienen, U. Zimmermann, H. Raben, and P. W. Kämmerer, "Preliminary numerical study on electrical stimulation at alloplastic reconstruction

- plates of the mandible.” in *Scientific Computing in Electrical Engineering. Mathematics in Industry*, U. Langer, W. Amrhein, and W. Zulehner, Eds., vol. 28. Springer, 2018, St. Wolfgang, Austria. [Online]. Available: [https://doi.org/10.1007/978-3-319-75538-0\\_1](https://doi.org/10.1007/978-3-319-75538-0_1)
- [37] M. Schröder, H. Raben, F. Krüger, A. Ruscheinski, U. van Rienen, A. Uhrmacher, and S. Spors, “PROVenance patterns in numerical modelling and finite element simulation processes of bio-electric systems.” in *2019 41st Annual International Conference of the IEEE Engineering in Medicine and Biology Society (EMBC)*. IEEE, 2019, pp. 3377–3382, Berlin, Germany. [Online]. Available: <https://doi.org/10.1109/EMBC.2019.8856841>
- [38] H. Raben, P. W. Kämmerer, and U. van Rienen, “Addressing model uncertainties in finite element simulation of electrically stimulated implants for critical-size mandibular defects.” *IEEE Trans. Biomed. Eng.*, vol. 71, no. 10, pp. 3055–3068, 2024. [Online]. Available: <https://doi.org/10.1109/TBME.2024.3408076>
- [39] D. B. Burr and M. R. Allen, Eds., *Basic and applied bone biology*, 2nd ed. Boston, MA, USA: Elsevier/Academic Press, 2019. [Online]. Available: <https://doi.org/10.1016/C2016-0-03781-6>
- [40] M. S. Jones and B. Waterson, “Principles of management of long bone fractures and fracture healing.” *Surgery (Oxf.)*, vol. 38, no. 2, pp. 91–99, 2020. [Online]. Available: <https://doi.org/10.1016/j.mpsur.2019.12.010>
- [41] SMArt images of bone structure. Servier Medical Art. (accessed 24.09.2021). [Online]. Available: [https://smart.servier.com/wp-content/uploads/2016/10/Bone\\_structure.pptx](https://smart.servier.com/wp-content/uploads/2016/10/Bone_structure.pptx)
- [42] J. D. Currey, “The structure and mechanics of bone.” *J. Mater. Sci.*, vol. 47, no. 1, pp. 41–54, 2012. [Online]. Available: <https://doi.org/10.1007/s10853-011-5914-9>
- [43] J.-Y. Rho, L. Kuhn-Spearing, and P. Zioupos, “Mechanical properties and the hierarchical structure of bone.” *Med. Eng. Phys.*, vol. 20, no. 2, pp. 92–102, 1998. [Online]. Available: [https://doi.org/10.1016/S1350-4533\(98\)00007-1](https://doi.org/10.1016/S1350-4533(98)00007-1)
- [44] R. Casas and I. Sevostianov, “Electrical resistivity of cortical bone: micromechanical modeling and experimental verification.” *Int. J. Eng. Sci.*, vol. 62, pp. 106–112, 2013. [Online]. Available: <https://doi.org/10.1016/j.ijengsci.2012.09.001>
- [45] F. F. Safadi, M. F. Barbe, S. M. Abdelmagid, M. C. Rico, R. A. Aswad, J. Litvin, and S. N. Popoff, “Bone structure, development and bone biology.” in *Bone pathology*, J. S. Khurana, Ed. Totowa, NJ, USA: Humana Press, 2009, pp. 1–50. [Online]. Available: [https://doi.org/10.1007/978-1-59745-347-9\\_1](https://doi.org/10.1007/978-1-59745-347-9_1)
- [46] P. DeSaix, G. J. Betts, E. Johnson, J. E. Johnson, K. Oksana, D. H. Kruse, B. Poe, J. A. Wise, and K. A. Young, *Anatomy & Physiology*

- 2e., 2nd ed. Houston, TX, USA: OpenStax, 2022. [Online]. Available: <https://openstax.org/details/books/anatomy-and-physiology-2e>
- [47] G. M. Corte, J. Plendl, H. Hünigen, K. C. Richardson, O. Gemeinhardt, and S. M. Niehues, “Refining experimental dental implant testing in the göttingen minipig using 3d computed tomography—a morphometric study of the mandibular canal.” *PLOS ONE*, vol. 12, no. 9, pp. 1–19, 2017. [Online]. Available: <https://doi.org/10.1371/journal.pone.0184889>
- [48] P. Kämmerer, N. Engel, R. Bader, V. Engel, B. Frerich, D. Heimes, J. Kröger, L. Lembke, F. Plocksties, H. Raben, U. van Rienen, A. Springer, D. Timmermann, J. Zimmermann, and M. Dau, “Accelerating early regeneration of critical-size mandibular bone defects through endogenous in vivo electrostimulation.” *Front. Bioeng. Biotechnol.*, 2024, under review.
- [49] J. F. Hoenig, “Das Göttinger Miniaturschwein (GMS) als Versuchstier in der humanmedizinischen osteologischen Grundlagenforschung.” *Z. Zahnärztl. Implantol.*, vol. 9, pp. 244–254, 1993, [Google Scholar]. [Online]. Available: <https://doi.org/10.1111/j.1600-0501.2004.00980.x>
- [50] J. Wiltfang, F. R. Kloss, P. Kessler, E. Nkenke, S. Schultze-mosgau, R. Zimmermann, and K. A. Schlegel, “Effects of platelet-rich plasma on bone healing in combination with autogenous bone and bone substitutes in critical-size defects: an animal experiment.” *Clin. Oral Implants Res.*, vol. 15, no. 2, pp. 187–193, 2004.
- [51] S. L. Thomas von Arx, *Clinical Oral Anatomy*. Switzerland, Springer International Publishing, 2017. [Online]. Available: <https://doi.org/10.1007/978-3-319-41993-0>
- [52] E. Jimi, S. Hirata, K. Osawa, M. Terashita, C. Kitamura, and H. Fukushima, “The current and future therapies of bone regeneration to repair bone defects.” *Int. J. Dent.*, vol. 2012, p. 148261, 2012. [Online]. Available: <https://doi.org/10.1155/2012/148261>
- [53] J.-L. Ma, J.-L. Pan, B.-S. Tan, and F.-Z. Cui, “Determination of critical size defect of minipig mandible.” *J. Tissue Eng. Regen. Med.*, vol. 3, pp. 615–622, 2009. [Online]. Available: <https://doi.org/10.1002/term.203>
- [54] P. P. Poli, M. Beretta, M. Cicciù, and C. Maiorana, “Alveolar ridge augmentation with titanium mesh. a retrospective clinical study.” *Open Dent. J.*, vol. 8, p. 148, 2014. [Online]. Available: <https://doi.org/10.2174/1874210601408010148>
- [55] “The Federal Health Monitoring System, keyword “operations and procedures in hospitals”.” [Online]. Available: [https://www.gbe-bund.de/gbe10/pkg\\_isgbe5.prc\\_isgbe?p\\_uid=gast&p\\_aid=0&p\\_sprache=E](https://www.gbe-bund.de/gbe10/pkg_isgbe5.prc_isgbe?p_uid=gast&p_aid=0&p_sprache=E) (accessed 15.10.2023).
- [56] A. Nauth, E. Schemitsch, B. Norris, Z. Nollin, and J. T. Watson, “Critical-size bone defects: is there a consensus for diagnosis and

- treatment?” *J. Orthop. Trauma*, vol. 32, 2018. [Online]. Available: <https://doi.org/10.1097/bot.0000000000001115>
- [57] M. W. Gielisch, F. Sieberg, D. G. E. Thiem, S. Blatt, D. Heimes, and P. W. Kämmerer, “A novel alloplastic grid reconstruction plate for the mandible - retrospective comparative clinical analysis of failure rates and specific complications.” *J. Maxillofac. Surg.*, vol. 51, no. 7, pp. 448–453, 2023. [Online]. Available: <https://doi.org/10.1016/j.jcms.2023.07.005>
- [58] J. Markwardt, G. Pfeifer, U. Eckelt, and B. Reitemeier, “Analysis of complications after reconstruction of bone defects involving complete mandibular resection using finite element modelling.” *Onkologie*, vol. 30, pp. 121–126, 2007. [Online]. Available: <https://doi.org/10.1159/000098848>
- [59] P. Kämmerer, M. Klein, M. Moergel, M. Gemmel, and G. Draenert, “Local and systemic risk factors influencing the long-term success of angular stable alloplastic reconstruction plates of the mandible.” *J. Craniomaxillofac. Surg.*, vol. 42, pp. e271–e276, 2014. [Online]. Available: <https://doi.org/10.1016/j.jcms.2013.10.004>
- [60] P. Sadr-Eshkevari, A. Rashad, S. A. Vahdati, A. Garajei, B. Bohluli, and P. Maurer, “Alloplastic mandibular reconstruction: a systematic review and meta-analysis of the current century case series.” *Plast. Reconstr. Surg.*, vol. 132, pp. 413e–427e, 2013. [Online]. Available: <https://doi.org/10.1097/prs.0b013e31829ad0d9>
- [61] H. Yamada, K. Nakaoka, T. Sonoyama, K. Kumagai, T. Ikawa, Y. Shigeta, N. Harada, N. Kawamura, T. Ogawa, and Y. Hamada, “Clinical usefulness of mandibular reconstruction using custom-made titanium mesh tray and autogenous particulate cancellous bone and marrow harvested from tibia and/or ilia.” *J. Craniofac. Surg.*, vol. 27, no. 3, 2016. [Online]. Available: <https://doi.org/10.1097/scs.0000000000002472>
- [62] A. H. Schmidt, “Autologous bone graft: is it still the gold standard?” *Injury*, vol. 52, pp. S18–S22, 2021. [Online]. Available: <https://doi.org/10.1016/j.injury.2021.01.043>
- [63] T. W. Bauer and G. F. Muschler, “Bone graft materials: an overview of the basic science.” *Clin. Orthop. Relat. Res.*, vol. 371, 2000. [Online]. Available: <https://doi.org/10.1097/00003086-200002000-00003>
- [64] E.-T. Wang and Z. Min, “Regulation of tissue repair and regeneration by electric fields.” *Chin. J. Traumatol.*, vol. 13, no. 1, pp. 55–61, 2010. [Online]. Available: <https://doi.org/10.3760/CMA.J.ISSN.1008-1275.2010.01.011>
- [65] A. M. Lozano, N. Lipsman, H. Bergman, P. Brown, S. Chabardes, J. W. Chang, K. Matthews, C. C. McIntyre, T. E. Schlaepfer, M. Schulder, Y. Temel, J. Volkmann, and J. K. Krauss, “Deep brain stimulation: current challenges and future directions.” *Nat. Rev. Neurol.*, vol. 15, no. 30683913, pp. 148–160, 2019.

- [Online]. Available: <https://doi.org/10.1038/s41582-018-0128-2>
- [66] S. F. Cogan, "Neural stimulation and recording electrodes." *Annu. Rev. Biomed. Eng.*, vol. 10, no. 1, pp. 275–309, 2008. [Online]. Available: <https://doi.org/10.1146/annurev.bioeng.10.061807.160518>
- [67] L. Massari, F. Benazzo, F. Falez, D. Perugia, L. Pietrogrande, S. Setti, R. Osti, E. Vaienti, C. Ruosi, and R. Cadossi, "Biophysical stimulation of bone and cartilage: state of the art and future perspectives." *Int. Orthop.*, pp. 1–13, 2019. [Online]. Available: <https://doi.org/10.1007/s00264-018-4274-3>
- [68] S. Krueger, A. Riess, A. Jonitz-Heincke, A. Weizel, A. Seyfarth, H. Seitz, and R. Bader, "Establishment of a new device for electrical stimulation of non-degenerative cartilage cells in vitro." *Int. J. Mol. Sci.*, vol. 22, no. 1, p. 394, 2021. [Online]. Available: <https://doi.org/10.3390/ijms22010394>
- [69] R. Vaiciuleviciute, I. Uzieliene, P. Bernotas, V. Novickij, A. Alaburda, and E. Bernotiene, "Electrical stimulation in cartilage tissue engineering." *Bioengineering*, vol. 10, no. 4, p. 454, 2023. [Online]. Available: <https://doi.org/10.3390/bioengineering10040454>
- [70] R. Das, S. Langou, T. T. Le, P. Prasad, F. Lin, and T. D. Nguyen, "Electrical stimulation for immune modulation in cancer treatments." *Front. Bioeng. Biotechnol.*, vol. 9, 2022. [Online]. Available: <https://doi.org/10.3389/fbioe.2021.795300>
- [71] E. Fukada and I. Yasuda, "On the piezoelectric effect of bone." *J. Phys. Soc. Jpn.*, vol. 12, no. 10, pp. 1158–1162, 1957. [Online]. Available: <https://doi.org/10.1143/JPSJ.12.1158>
- [72] C. A. Bassett, "Electrical effects in bone." *Sci. Am.*, vol. 213, no. 4, pp. 18–25, 1965. [Online]. Available: <https://doi.org/10.1038/SCIENTIFICAMERICAN1065-18>
- [73] J. C. Anderson and C. Eriksson, "Piezoelectric properties of dry and wet bone." *Nature*, vol. 227, no. 5257, pp. 491–492, 1970. [Online]. Available: <https://doi.org/10.1038/227491a0>
- [74] W. S. Williams and L. Breger, "Analysis of stress distribution and piezoelectric response in cantilever bending of bone and tendon." *Ann. N. Y. Acad. Sci.*, vol. 238, no. 1, pp. 121–130, 1974. [Online]. Available: <https://doi.org/10.1111/j.1749-6632.1974.tb26782.x>
- [75] C. Eriksson, "Streaming potentials and other water-dependent electrical effects in mineralized tissue." *Ann. N. Y. Acad. Sci.*, vol. 238, no. 1, pp. 321–338, 1974. [Online]. Available: <https://doi.org/10.1111/j.1749-6632.1974.tb26801.x>
- [76] D. Gross and W. S. Williams, "Streaming potential and the electromechanical response of physiologically-moist bone." *J. Biomech.*, vol. 15, no. 4, pp. 277–295,

1982. [Online]. Available: [https://doi.org/10.1016/0021-9290\(82\)90174-9](https://doi.org/10.1016/0021-9290(82)90174-9)
- [77] D. Pienkowski and S. R. Pollack, "The origin of stress-generated potentials in fluid-saturated bone." *J. Orthop. Res.*, vol. 1, pp. 30–41, 1983. [Online]. Available: <https://doi.org/10.1002/jor.1100010105>
- [78] S. R. Pollack, N. Petrov, R. Salzstein, G. Brankov, and R. Blagoeva, "An anatomical model for streaming potentials in osteons." *J. Biomech.*, vol. 17, no. 8, pp. 627–636, 1984. [Online]. Available: [https://doi.org/10.1016/0021-9290\(84\)90094-0](https://doi.org/10.1016/0021-9290(84)90094-0)
- [79] R. Gross and A. Marx, *Festkörperphysik.*, 1st ed. Munich, Germany: Oldenbourg Wissenschaftsverlag, 2012. [Online]. Available: <https://doi.org/10.1524/9783486714869>
- [80] E. Fukada, "Mechanical deformation and electrical polarization in biological substances." *Biorheology*, vol. 5, no. 3, pp. 199–208, 1968. [Online]. Available: <https://doi.org/10.3233/bir-1968-5302>
- [81] A. J. Bur, "Measurements of the dynamic piezoelectric properties of bone as a function of temperature and humidity." *J. Biomech.*, vol. 9, no. 8, pp. 495–507, 1976. [Online]. Available: [https://doi.org/10.1016/0021-9290\(76\)90066-X](https://doi.org/10.1016/0021-9290(76)90066-X)
- [82] A. R. Liboff and M. Furst, "Pyroeffect effect in collagenous structures." *Ann. N. Y. Acad. Sci.*, vol. 238, no. 1, pp. 26–35, 1974. [Online]. Available: <https://doi.org/10.1111/j.1749-6632.1974.tb26777.x>
- [83] G. B. Reinish and A. S. Nowick, "Piezoelectric properties of bone as functions of moisture content." *Nature*, vol. 253, no. 5493, pp. 626–627, 1975. [Online]. Available: <https://doi.org/10.1038/253626a0>
- [84] G. W. Hastings, M. A. ElMessiery, and S. Rakowski, "Mechano-electrical properties of bone." *Biomaterials*, vol. 2, no. 4, pp. 225–233, 1981. [Online]. Available: [https://doi.org/10.1016/0142-9612\(81\)90062-4](https://doi.org/10.1016/0142-9612(81)90062-4)
- [85] G. W. Hastings and F. A. Mahmud, "Electrical effects in bone." *J. Biomed. Eng.*, vol. 10, no. 6, pp. 515–521, 1988. [Online]. Available: [https://doi.org/10.1016/0141-5425\(88\)90109-4](https://doi.org/10.1016/0141-5425(88)90109-4)
- [86] C. Halperin, S. Mutchnik, A. Agronin, M. Molotskii, P. Urenski, M. Salai, and G. Rosenman, "Piezoelectric effect in human bones studied in nanometer scale." *Nano Lett.*, vol. 4, no. 7, pp. 1253–1256, 2004. [Online]. Available: <https://doi.org/10.1021/NL049453I>
- [87] D. C. F. Wieland, C. Krywka, E. Mick, R. Willumeit-Römer, R. Bader, and D. Klues, "Investigation of the inverse piezoelectric effect of trabecular bone on a micrometer length scale using synchrotron radiation." *Acta Biomater.*, vol. 25, pp. 339 – 346, 2015. [Online]. Available: <https://doi.org/10.1016/j.actbio.2015.07.021>

- [88] W. Starkebaum, S. R. Pollack, and E. Korostoff, "Microelectrode studies of stress-generated potentials in four-point bending of bone." *J. Biomed. Mater. Res.*, vol. 13, no. 5, pp. 729–751, 1979. [Online]. Available: <https://doi.org/10.1002/JBM.820130506>
- [89] C. A. Bassett and R. O. Becker, "Generation of electric potentials by bone in response to mechanical stress." *Science*, vol. 137, no. 3535, pp. 1063–1064, 1962. [Online]. Available: <https://doi.org/10.1126/science.137.3535.1063>
- [90] A. C. Ahn and A. J. Grodzinsky, "Relevance of collagen piezoelectricity to "Wolff's Law": a critical review." *Med. Eng. Phys.*, vol. 31, pp. 733–741, 2009. [Online]. Available: <https://doi.org/10.1016/j.medengphy.2009.02.006>
- [91] N. Rosa, R. Simoes, F. D. Magalhães, and A. T. Marques, "From mechanical stimulus to bone formation: a review." *Med. Eng. Phys.*, vol. 37, no. 8, pp. 719–728, 2015. [Online]. Available: <https://doi.org/10.1016/j.medengphy.2015.05.015>
- [92] C. A. L. Bassett and R. J. Pawluk, "Effects of electric currents on bone in vivo." *Nature*, vol. 204, pp. 652–654, 1964. [Online]. Available: <https://doi.org/10.1038/204652a0>
- [93] D. D. Levy, "A pulsed electrical stimulation technique for inducing bone growth." *Ann. N. Y. Acad. Sci.*, no. 1 Electrically, pp. 478–490, 1974. [Online]. Available: <https://doi.org/10.1111/j.1749-6632.1974.tb26814.x>
- [94] J. R. Porter, T. T. Ruckh, and K. C. Popat, "Bone tissue engineering: a review in bone biomimetics and drug delivery strategies." *Biotechnol. Prog.*, vol. 25, no. 6, pp. 1539–1560, 2009. [Online]. Available: <https://doi.org/10.1002/btpr.246>
- [95] L. Leppik, K. M. C. Oliveira, M. B. Bhavsar, and J. H. Barker, "Electrical stimulation in bone tissue engineering treatments." *Eur. J. Trauma Emerg. Surg.*, vol. 46, pp. 231–244, 2020. [Online]. Available: <https://doi.org/10.1007/s00068-020-01324-1>
- [96] J. Simon and B. Simon, "Electrical bone stimulation." in *Musculoskeletal tissue regeneration*, W. S. Pietrzak, Ed. Totowa, NJ, USA: Humana Press, 2008, pp. 259–287. [Online]. Available: [https://doi.org/10.1007/978-1-59745-239-7\\_13](https://doi.org/10.1007/978-1-59745-239-7_13)
- [97] J. C. Gan, D. C. Fredericks, and P. A. Glazer, "Direct current and capacitive coupling electrical stimulation upregulates osteopromotive factors for spinal fusions." *Orthop. J. Harvard Med. School*, vol. 6, pp. 57–59, 2004. [Online]. Available: <http://www.orthojournalhms.org/volume6/pdfs/ms02.pdf>
- [98] I. S. Kim, J. K. Song, Y. L. Zhang, T. H. Lee, T. H. Cho, Y. M. Song, D. K. Kim, S. J. Kim, and S. J. Hwang, "Biphasic electric current stimulates proliferation and induces VEGF production in osteoblasts." *Biochim. Biophys. Acta*, vol. 1763, pp. 907–916, 2006. [Online]. Available: <https://doi.org/10.1016/j.bbamcr.2006.06.007>



- [99] B. Ercan and T. J. Webster, "Greater osteoblast proliferation on anodized nanotubular titanium upon electrical stimulation." *Int. J. Nanomed.*, vol. 3, no. 4, pp. 477–485, 2008. [Online]. Available: <https://doi.org/10.2147/IJN.S3780>
- [100] M. Hronik-Tupaj, W. L. Rice, M. Cronin-Golomb, D. L. Kaplan, and I. Georgakoudi, "Osteoblastic differentiation and stress response of human mesenchymal stem cells exposed to alternating current electric fields." *Biomed. Eng. Online*, vol. 10, p. 9, 2011. [Online]. Available: <https://doi.org/10.1186/1475-925X-10-9>
- [101] M. Eischen-Loges, K. M. C. Oliveira, M. B. Bhavsar, J. H. Barker, and L. Leppik, "Pretreating mesenchymal stem cells with electrical stimulation causes sustained long-lasting pro-osteogenic effects." *PeerJ*, vol. 6, p. e4959, 2018. [Online]. Available: <https://doi.org/10.7717/peerj.4959>
- [102] S. Mobini, L. Leppik, V. T. Parameswaran, and J. H. Barker, "In vitro effect of direct current electrical stimulation on rat mesenchymal stem cells." *PeerJ*, vol. 5, p. e2821, 2017. [Online]. Available: <https://doi.org/10.7717/peerj.2821>
- [103] X. Wang, Y. Gao, H. Shi, N. Liu, W. Zhang, and H. Li, "Influence of the intensity and loading time of direct current electric field on the directional migration of rat bone marrow mesenchymal stem cells." *Front. Med.*, vol. 10, pp. 286–296, 2016. [Online]. Available: <https://doi.org/10.1007/s11684-016-0456-9>
- [104] C. T. Brighton, W. Wang, R. Seldes, G. Zhang, and S. R. Pollack, "Signal transduction in electrically stimulated bone cells." *J. Bone Joint Surg. Am.*, vol. 83-A, no. 10, pp. 1514–1523, 2001. [Online]. Available: <https://doi.org/10.2106/00004623-200110000-00009>
- [105] T. Bodamyali, J. M. Kanczler, B. Simon, D. R. Blake, and C. R. Stevens, "Effect of faradic products on direct current-stimulated calvarial organ culture calcium levels." *Biochem. Biophys. Res. Commun.*, vol. 264, no. 3, pp. 657–661, 1999. [Online]. Available: <https://doi.org/10.1006/BBRC.1999.1355>
- [106] J. Malmivuo and R. Plonsey, *Bioelectromagnetism: Principles and Applications of Bioelectric and Biomagnetic Fields*. Oxford University Press, USA, 1995. [Online]. Available: <https://doi.org/10.1093/acprof:oso/9780195058239.001.0001>
- [107] R. Glaser, *Biophysics: an introduction.*, 2nd ed. Springer Science & Business Media, 2012. [Online]. Available: <https://doi.org/10.1007/978-3-642-25212-9>
- [108] J. T. Ryaby, "Clinical effects of electromagnetic and electric fields on fracture healing." *Clin. Orthop. Relat. Res.*, vol. 355, pp. S205–S215, 1998. [Online]. Available: <https://doi.org/10.1097/00003086-199810001-00021>
- [109] P. J. Nicksic, D. T. Donnelly, N. Verma, A. J. Setiz, A. J. Shoffstall, K. A. Ludwig, A. M. Dingle, and S. O. Poore, "Electrical stimulation of acute fractures: a narrative review of stimulation protocols and device specifications." *Front. Bioeng. Biotechnol.*, vol. 10, no. 879187, 2022. [Online]. Available: <https://doi.org/10.3389/fbioe.2022.879187>

- [110] P. J. Nicksic, D. T. Donnelly, M. Hesse, S. Bedi, N. Verma, A. J. Setiz, A. J. Shoffstall, K. A. Ludwig, A. M. Dingle, and S. O. Poore, "Electronic bone growth stimulators for augmentation of osteogenesis in in vitro and in vivo models: a narrative review of electrical stimulation mechanisms and device specifications." *Front. Bioeng. Biotechnol.*, vol. 10, no. 793945, 2022. [Online]. Available: <https://doi.org/10.3389/fbioe.2022.793945>
- [111] J. Black, *Electrical stimulation: its role in growth, repair and remodeling of the musculoskeletal system*. United States: Westport, Connecticut, USA: Greenwood Press, 1986. [Online]. Available: <https://www.osti.gov/servlets/purl/5963329>
- [112] V. Denaro, A. Cittadini, S. A. Barnaba, L. Ruzzini, L. Denaro, A. Rettino, B. De Paola, N. Papapietro, and A. Sgambato, "Static electromagnetic fields generated by corrosion currents inhibit human osteoblast differentiation." *Spine*, vol. 33, no. 9, pp. 955–959, 2008. [Online]. Available: <https://doi.org/10.1097/BRS.0b013e31816c90b8>
- [113] V. Denaro, N. Papapietro, A. Sgambato, S. A. Barnaba, L. Ruzzini, B. De Paola, A. Rettino, and A. Cittadini, "Periprosthetic electrochemical corrosion of titanium and titanium-based alloys as a cause of spinal fusion failure." *Spine*, vol. 33, no. 1, pp. 8–13, 2008. [Online]. Available: <https://doi.org/10.1097/BRS.0b013e31815e3978>
- [114] C. A. Bassett, R. J. Pawluk, and A. A. Pilla, "Acceleration of fracture repair by electromagnetic fields. a surgically noninvasive method." *Ann. N. Y. Acad. Sci.*, vol. 238, pp. 242–262, 1974. [Online]. Available: <https://doi.org/10.1111/j.1749-6632.1974.tb26794.x>
- [115] C. Khatua, D. Bhattacharya, and V. K. Balla, "In situ electrical stimulation for enhanced bone growth: a mini-review." *Med. Dev. Sens.*, vol. 3, no. 4, p. e10090, 2020. [Online]. Available: <https://doi.org/10.1002/mds3.10090>
- [116] M. Griffin and A. Bayat, "Electrical stimulation in bone healing: critical analysis by evaluating levels of evidence." *Eplasty*, vol. 11, p. e34, 2011. [Online]. Available: <https://www.ncbi.nlm.nih.gov/pmc/articles/PMC3145421/>
- [117] C. T. Brighton, W. J. Hozack, M. D. Brager, R. E. Windsor, S. R. Pollack, E. J. Vreslovic, and J. E. Kotwick, "Fracture healing in the rabbit fibula when subjected to various capacitively coupled electrical fields." *J. Orthop. Res.*, vol. 3, pp. 331–340, 1985. [Online]. Available: <https://doi.org/10.1002/jor.1100030310>
- [118] C. T. Brighton and S. R. Pollack, "Treatment of recalcitrant non-union with a capacitively coupled electrical field. a preliminary report." *J. Bone Joint Surg. Am.*, vol. 67, pp. 577–585, 1985. [Online]. Available: <https://doi.org/10.2106/00004623-198567040-00012>
- [119] J. J. Cook, N. J. Summers, and E. A. Cook, "Healing in the new millennium: bone stimulators: an overview of where we've been and where we may be

- heading.” *Clin. Podiatr. Med. Surg.*, vol. 32, no. 1, pp. 45–59, 2015. [Online]. Available: <https://doi.org/10.1016/j.cpm.2014.09.003>
- [120] A. Muttini, M. Abate, N. Bernabò, F. Cavani, R. Mingozzi, U. Tosi, M. Cadossi, S. Setti, S. Giannini, and R. Leone, “Effect of electric current stimulation in combination with external fixator on bone healing in a sheep fracture model.” *Vet. Ital.*, 2014. [Online]. Available: <https://doi.org/10.12834/VetIt.271.963.2>
- [121] M. B. Bhavsar, Z. Han, T. DeCoster, L. Leppik, K. M. C. Oliveira, and J. H. Barker, “Electrical stimulation-based bone fracture treatment, if it works so well why do not more surgeons use it?” *Eur. J. Trauma Emerg. S.*, vol. 46, no. 2, pp. 245–264, 2020. [Online]. Available: <https://doi.org/10.1007/s00068-019-01127-z>
- [122] C. Shuai, W. Yang, S. Peng, C. Gao, W. Guo, Y. Lai, and P. Feng, “Physical stimulations and their osteogenesis-inducing mechanisms.” *Int. J. Bioprinting*, vol. 4, no. 2, 2018. [Online]. Available: <https://doi.org/10.18063/ijb.v4i2.138>
- [123] Z. Schwartz, B. J. Simon, M. A. Duran, G. Barabino, R. Chaudhri, and B. D. Boyan, “Pulsed electromagnetic fields enhance BMP-2 dependent osteoblastic differentiation of human mesenchymal stem cells.” *J. Orthop. Res.*, vol. 26, no. 9, pp. 1250–1255, 2008. [Online]. Available: <https://doi.org/10.1002/jor.20591>
- [124] G. Jin and G. Kim, “The effect of sinusoidal AC electric stimulation of 3D PCL/CNT and PCL/ $\beta$ -TCP based bio-composites on cellular activities for bone tissue regeneration.” *J. Mater. Chem. B*, vol. 1, no. 10, pp. 1439–1452, 2013. [Online]. Available: <https://doi.org/10.1039/C2TB00338D>
- [125] L. M. Bins-Ely, E. B. Cordero, J. C. M. Souza, W. Teughels, C. A. M. Benfatti, and R. S. Magini, “In vivo electrical application on titanium implants stimulating bone formation.” *J. Periodontal Res.*, vol. 52, no. 3, pp. 479–484, 2017. [Online]. Available: <https://doi.org/10.1111/jre.12413>
- [126] L. Leppik, H. Zhihua, S. Mobini, V. T. Parameswaran, M. Eischen-Loges, A. Slavici, J. Helbing, L. Pindur, K. M. C. Oliveira, M. B. Bhavsar *et al.*, “Combining electrical stimulation and tissue engineering to treat large bone defects in a rat model.” *Sci. Rep.*, vol. 8, no. 1, p. 6307, 2018. [Online]. Available: <https://doi.org/10.1038/s41598-018-24892-0>
- [127] “Neue Magnetodyn GmbH.” [Online]. Available: <https://magnetodyn.de/en/> (accessed 09.06.2022).
- [128] J. M. Khalifeh, Z. Zohny, M. Macewan, M. Stephen, W. Johnston, P. Gamble, Y. Zeng, Y. Yan, and W. Z. Ray, “Electrical stimulation and bone healing: a review of current technology and clinical applications.” *IEEE Rev. Biomed. Eng.*, pp. 217–232, 2018. [Online]. Available: <https://doi.org/10.1109/rbme.2018.2799189>
- [129] C. Windisch, W. Kolb, E. Röhner, M. Wagner, A. Roth, G. Matziolis, and A. Wagner, “Invasive electromagnetic field treatment in osteonecrosis of the femoral head: a prospective cohort study.” *Open Orthop. J.*, vol. 8, no. 24987486, pp. 125–129,

2014. [Online]. Available: <https://doi.org/10.2174/1874325020140515001>
- [130] A. Ganzlin, “Retrospektive Erfassung des funktionellen und radiologischen Outcome nach operativer Behandlung der aseptischen Knochennekrose des Hüftkopfes.” Ph.D. dissertation, Department of Orthopaedics, University Medical Center Rostock, Rostock, Germany, 2017. [Online]. Available: [https://doi.org/10.18453/rosdok\\_id00002602](https://doi.org/10.18453/rosdok_id00002602)
- [131] S. Weinbaum, S. C. Cowin, and Y. Zeng, “A model for the excitation of osteocytes by mechanical loading-induced bone fluid shear stresses.” *J. Biomech.*, vol. 27, no. 3, pp. 339–360, 1994. [Online]. Available: [https://doi.org/10.1016/0021-9290\(94\)90010-8](https://doi.org/10.1016/0021-9290(94)90010-8)
- [132] K. J. McLeod and C. T. Rubin, “The effect of low-frequency electrical fields on osteogenesis.” *J. Bone Joint Surg. Am.*, vol. 74, no. 6, pp. 920–929, 1992. [Online]. Available: <https://doi.org/10.2106/00004623-199274060-00014>
- [133] M. W. Otter, K. J. McLeod, and C. T. Rubin, “Effects of electromagnetic fields in experimental fracture repair.” *Clin. Orthop. Relat. Res.*, vol. 355, pp. S90–S104, 1998. [Online]. Available: <https://doi.org/10.1097/00003086-199810001-00011>
- [134] A. N. Zengo, C. A. Bassett, G. Prountzos, R. J. Pawluk, and A. Pilla, “In vivo effects of direct current in the mandible.” *J. Dent. Res.*, vol. 55, pp. 383–390, 1976. [Online]. Available: <https://doi.org/10.1177/00220345760550031601>
- [135] H. S. Shandler, S. Weinstein, and L. E. Nathan, “Facilitated healing of osseous lesions in the canine mandible after electrical stimulation.” *J. Oral Surg.*, vol. 37, pp. 787–792, 1979. [Online]. Available: <https://pubmed.ncbi.nlm.nih.gov/290769/>
- [136] A. A. Marino, B. D. Gross, and R. D. Specian, “Electrical stimulation of mandibular osteotomies in rabbits.” *Oral Surg. Oral Med. Oral Pathol.*, vol. 62, no. 1, pp. 20–24, 1986. [Online]. Available: [https://doi.org/10.1016/0030-4220\(86\)90065-4](https://doi.org/10.1016/0030-4220(86)90065-4)
- [137] I. E. El-Hakim, A. M. A. Azim, M. F. A. El-Hassan, and S. M. Maree, “Preliminary investigation into the effects of electrical stimulation on mandibular distraction osteogenesis in goats.” *Int. J. Oral Maxillofac. Surg.*, vol. 33, no. 1, pp. 42–47, 2004. [Online]. Available: <https://doi.org/10.1054/IJOM.2003.0445>
- [138] C. Masureik and C. Eriksson, “Preliminary clinical evaluation of the effect of small electrical currents on the healing of jaw fractures.” *Clin. Orthop. Relat. Res.*, vol. 124, pp. 84–91, 1977. [Online]. Available: <https://doi.org/10.1097/00003086-197705000-00012>
- [139] A. Kamegai, M. Mori, and S. Inoue, “Mandibular reconstruction using electrically stimulated periosteum.” *J. Maxillofac. Surg.*, vol. 18, no. 1, pp. 8–13, 1990. [Online]. Available: [https://doi.org/10.1016/S1010-5182\(05\)80597-9](https://doi.org/10.1016/S1010-5182(05)80597-9)

- [140] E. Pettersen, J. Anderson, and M. Ortiz-Catalan, “Electrical stimulation to promote osseointegration of bone anchoring implants: a topical review.” *J. Neuroeng. Rehabil.*, vol. 19, no. 1, p. 31, 2022. [Online]. Available: <https://doi.org/10.1186/s12984-022-01005-7>
- [141] D. Kluess, R. Souffrant, R. Bader, U. van Rienen, H. Ewald, and W. Mittelmeier, “A new concept of an electrostimulative acetabular revision system with patient individual additional fixation.” in *4th European Conference of the International Federation for Medical and Biological Engineering*, J. Vander Sloten, P. Verdonck, M. Nyssen, and J. Haueisen, Eds. Antwerp, Belgium: Springer, 2009, pp. 1847–1850, Antwerp, Belgium. [Online]. Available: [https://doi.org/10.1007/978-3-540-89208-3\\_440](https://doi.org/10.1007/978-3-540-89208-3_440)
- [142] D. Klüß, R. Souffrant, E. Ewald, U. van Rienen, R. Bader, and W. Mittelmeier, “Acetabuläre Hüftendoprothese mit einer Vorrichtung zur Elektrostimulation des Knochens Deutsches Patent- und Markenamt.” Deutsches Patent- und Markenamt. German Patent DE202 008 015 661 U1, Nov. 26, 2008, (accessed 09.11.2023). [Online]. Available: <https://register.dpma.de/DPMAREgister/pat/register?AKZ=2020080156610>
- [143] C. Potratz, D. Kluess, H. Ewald, and U. van Rienen, “Multiobjective optimization of an electrostimulative acetabular revision system.” *IEEE Trans. Biomed. Eng.*, vol. 57, pp. 460–468, 2010. [Online]. Available: <https://doi.org/10.1109/TBME.2009.2030961>
- [144] J. K. Song, T. H. Cho, H. Pan, Y. M. Song, I. S. Kim, T. H. Lee, S. J. Hwang, and S. J. Kim, “An electronic device for accelerating bone formation in tissues surrounding a dental implant.” *Bioelectromagnetics*, vol. 30, pp. 374–384, 2009. [Online]. Available: <https://doi.org/10.1002/bem.20482>
- [145] B. Delenda, R. Bader, and U. van Rienen, “Modeling and simulation of platelet reaction and diffusion towards an electro-stimulating dental implant.” in *37th Annual International Conference of the IEEE Engineering in Medicine and Biology Society (EMBC)*. IEEE, 2015, pp. 2584–2587, Milan, Italy. [Online]. Available: <https://doi.org/10.1109/EMBC.2015.7318920>
- [146] A. S. Beheshtiha and U. Nackenhorst, “Computational simulation of piezo-electrically stimulated bone remodeling surrounding teeth implant.” *Proc. Appl. Math. Mech.*, vol. 15, no. 1, pp. 111–112, 2015. [Online]. Available: <https://doi.org/10.1002/pamm.201510046>
- [147] J. C. Maxwell, *A Treatise on Electricity and Magnetism*. New York, NY, USA: Cambridge University Press, 1873, vol. 1. [Online]. Available: <https://doi.org/10.1017/CBO9780511709333>
- [148] R. Plonsey and D. B. Heppner, “Considerations of quasi-stationarity in electrophysiological systems.” *Bull. Math. Biophys.*, vol. 29, pp. 657–664, 1967. [Online]. Available: <https://doi.org/10.1007/BF02476917>

- [149] U. van Rienen, *Numerical Methods in Computational Electrodynamics - Linear Systems in Practical Applications.*, ser. Lecture Notes in Computational Science and Engineering. Berlin, Germany: Springer, 2001, vol. 12. [Online]. Available: <https://doi.org/10.1007/978-3-642-56802-2>
- [150] H. A. Haus and J. R. Melcher, *Electromagnetic fields and energy*. Englewood Cliffs, NJ, USA: Prentice Hall, 1989.
- [151] H. K. Dirks, “Quasi-stationary fields for microelectronic applications.” *Electr. Eng.*, vol. 79, no. 2, pp. 145–155, 1996. [Online]. Available: <https://doi.org/10.1007/BF01232924>
- [152] U. van Rienen, J. Flehr, U. Schreiber, and V. Motrescu, “Modeling and simulation of electro-quasistatic fields.” in *Modeling, Simulation, and Optimization of Integrated Circuits. ISNM International Series of Numerical Mathematics.*, K. Antreich, R. Bulirsch, A. Gilg, and P. Rentrop, Eds., vol. 146. Basel, Switzerland: Birkhäuser, 2003, pp. 17–31, Oberwolfach, Germany. [Online]. Available: [https://doi.org/10.1007/978-3-0348-8065-7\\_2](https://doi.org/10.1007/978-3-0348-8065-7_2)
- [153] U. van Rienen, J. Flehr, U. Schreiber, S. Schulze, U. Gimsa, W. Baumann, D. G. Weiss, J. Gimsa, R. Benecke, and H.-W. Pau, “Electro-quasistatic simulations in bio-systems engineering and medical engineering.” *Adv. Radio Sci.*, vol. 3, pp. 39–49, 2005. [Online]. Available: <https://doi.org/10.5194/ARS-3-39-2005>
- [154] J. D. Jackson, *Classical electrodynamics.*, 3rd ed. New York, NY, USA: John Wiley & Sons, 2021.
- [155] W. Hackbusch, *Elliptic differential equations: theory and numerical treatment.*, 2nd ed., ser. Springer Series in Computational Mathematics. Berlin, Germany: Springer, 2017, vol. 18. [Online]. Available: <https://doi.org/10.1007/978-3-662-54961-2>
- [156] X.-Q. Sheng and W. Song, *Essentials of computational electromagnetics*. Singapore: John Wiley & Sons, 2012. [Online]. Available: <https://doi.org/10.1002/9780470829646>
- [157] J.-M. Jin, *The finite element method in electromagnetics.*, 3rd ed. Hoboken, NJ, USA: John Wiley & Sons, 2015.
- [158] “Detailed explanation of the finite element method (FEM).” COMSOL Multiphysics, 2017. [Online]. Available: <https://www.comsol.com/multiphysics/finite-element-method> (accessed 11.10.2023).
- [159] P. I. Thomas Rylander, Anders Bondeson, *Computational Electromagnetics*. New York, NY, USA: Springer, 2012. [Online]. Available: <https://doi.org/10.1007/978-1-4614-5351-2>
- [160] J. S. Giudice, W. Zeng, T. Wu, A. Alshareef, D. F. Shedd, and M. B. Panzer, “An analytical review of the numerical methods used for finite element modeling of

- traumatic brain injury.” *Ann. Biomed. Eng.*, vol. 47, no. 9, pp. 1855–1872, 2019. [Online]. Available: <https://doi.org/10.1007/s10439-018-02161-5>
- [161] M. Rullmann, A. Anwander, M. Dannhauer, S. K. Warfield, F. H. Duffy, and C. H. Wolters, “EEG source analysis of epileptiform activity using a 1 mm anisotropic hexahedra finite element head model.” *NeuroImage*, vol. 44, no. 2, pp. 399–410, 2009. [Online]. Available: <https://doi.org/10.1016/j.neuroimage.2008.09.009>
- [162] Y. Saad, *Iterative methods for sparse linear systems.*, 2nd ed. Philadelphia, PA, USA: Society for Industrial and Applied Mathematics (SIAM), 2003. [Online]. Available: <https://doi.org/10.1137/1.9780898718003>
- [163] H. P. Schwan, “Electrical properties of tissue and cell suspensions.” in *Advances in biological and medical physics*. Burlington, MA, USA: Elsevier Science, 1957, vol. 5, pp. 147–209. [Online]. Available: <https://doi.org/10.1016/B978-1-4832-3111-2.50008-0>
- [164] H. P. Schwan, “Electrical properties of tissues and cell suspensions: mechanisms and models.” in *Proceedings of 16th Annual International Conference of the IEEE Engineering in Medicine and Biology Society*. IEEE, 1994, pp. A70–A71, Baltimore, MD, USA. [Online]. Available: <https://doi.org/10.1109/IEMBS.1994.412155>
- [165] H. G. L. Coster, T. C. Chilcott, and A. C. F. Coster, “Impedance spectroscopy of interfaces, membranes and ultrastructures.” *Bioelectrochem. Bioenerg.*, vol. 40, no. 2, pp. 79–98, 1996. [Online]. Available: [https://doi.org/10.1016/0302-4598\(96\)05064-7](https://doi.org/10.1016/0302-4598(96)05064-7)
- [166] S. Grimnes and O. G. Martinsen, *Bioimpedance and Bioelectricity Basics.*, 3rd ed. Boston, MA, USA: Elsevier/Academic Press, 2014. [Online]. Available: <https://books.google.de/books?id=v3EuUjoqwkC>
- [167] P. Bertemes-Filho, “Electrical impedance spectroscopy,” in *Bioimpedance in Biomedical Applications and Research*, F. Simini and P. Bertemes-Filho, Eds. Cham, Switzerland: Springer International Publishing, 2018, pp. 5–27. [Online]. Available: [https://doi.org/10.1007/978-3-319-74388-2\\_2](https://doi.org/10.1007/978-3-319-74388-2_2)
- [168] K. R. Foster and H. P. Schwan, “Dielectric properties of tissues and biological materials: a critical review.” *Crit. Rev. Biomed. Eng.*, vol. 17, pp. 25–104, 1989. [Online]. Available: <https://pubmed.ncbi.nlm.nih.gov/2651001/>
- [169] A. Barchanski, H. De Gersem, E. Gjonaj, and T. Weiland, “Impact of the displacement current on low-frequency electromagnetic fields computed using high-resolution anatomy models.” *Phys. Med. Biol.*, vol. 50, pp. N243–N249, 2005. [Online]. Available: <https://doi.org/10.1088/0031-9155/50/19/N02>
- [170] R. Field and M. Ghovanloo, “Simulation of the capacitive double layer at the interface between microelectrodes and cortical tissue using COMSOL Multiphysics and SPICE modeling.” in *Proc. COMSOL Users Conf.*, 2006, Paris, France. [Online]. Available: <https://www.researchgate.net/>

- [171] J. D. Gomez-Tames, J. Gonzalez, and W. Yu, "A simulation study: effect of the inter-electrode distance, electrode size and shape in transcutaneous electrical stimulation." in *2012 Annual International Conference of the IEEE Engineering in Medicine and Biology Society*. IEEE, 2012, pp. 3576–3579, San Diego, CA, USA. [Online]. Available: <https://doi.org/10.1109/EMBC.2012.6346739>
- [172] M. Prodanović, J. Malešević, M. Filipović, T. Jevtić, G. Bijelić, and N. Malešević, "Numerical simulation of the energy distribution in biological tissues during electrical stimulation." *Serb. J. Electr. Eng.*, vol. 10, no. 1, pp. 165–173, 2013. [Online]. Available: <https://doi.org/10.2298/SJEE1301165P>
- [173] U. Zimmermann and U. van Rienen, "On the optimization of the hip stem for an electrostimulative hip revision system." in *2014 XXXIth URSI General Assembly and Scientific Symposium (URSI GASS)*. IEEE, 2014, Beijing, China. [Online]. Available: <https://doi.org/10.1109/URSIGASS.2014.6930126>
- [174] C. Schmidt, U. Zimmermann, and U. van Rienen, "Modeling of an optimized electrostimulative hip revision system under consideration of uncertainty in the conductivity of bone tissue." *IEEE J. Biomed. Health. Inf.*, vol. 19, pp. 1321–1330, 2015. [Online]. Available: <https://doi.org/10.1109/JBHI.2015.2423705>
- [175] C. Vanegas-Acosta Juan, V. Lancellotti, and Z. A.P.M., "A mathematical framework for predicting thermal damage during bone electrostimulation." *COMPEL Int. J. Comput. Math. Electr. Electron. Eng.*, vol. 34, no. 4, pp. 1085–1100, 2015. [Online]. Available: <https://doi.org/10.1108/COMPEL-09-2014-0241>
- [176] G. Cosoli, L. Scalise, G. Tricarico, E. P. Tomasini, and G. Cerri, "An innovative therapy for peri-implantitis based on radio frequency electric current: numerical simulation results and clinical evidence." in *Conf. Proc. IEEE Eng. Med. Biol. Soc.*, vol. 2016. IEEE, 2016, pp. 5652–5655, Orlando, FL, USA. [Online]. Available: <https://doi.org/10.1109/EMBC.2016.7592009>
- [177] C. Gabriel and A. Peyman, "Dielectric properties of biological tissues; variation with age." in *Conn's Handbook of Models for Human Aging*, 2nd ed., J. L. Ram and P. M. Conn, Eds. Boston, MA, USA: Elsevier/Academic Press, 2018, ch. 69, pp. 939–952. [Online]. Available: <https://doi.org/10.1016/B978-0-12-811353-0.00069-5>
- [178] U. Zimmermann, C. Ebner, Y. Su, T. Bender, Y. D. Bansod, W. Mittelmeier, R. Bader, and U. van Rienen, "Numerical simulation of electric field distribution around an instrumented total hip stem." *Appl. Sci.*, no. 15, p. 6677, 2021. [Online]. Available: <https://doi.org/10.3390/app11156677>
- [179] C. Gabriel, "Compilation of the dielectric properties of body tissues at RF and microwave frequencies." Occupational and Environmental Health Directorate, Radiofrequency Radiation Division, Brooks Air Force Base, Texas, USA, techreport 19960618013, 1996. [Online]. Available: <https://apps.dtic.mil/sti/pdfs/ADA309764.pdf> Associated website <http://niremf>.



ifac.cnr.it/docs/DIELECTRIC/home.html.

- [180] K. S. Cole and R. H. Cole, "Dispersion and absorption in dielectrics I. alternating current characteristics." *J. Chem. Phys.*, vol. 9, no. 4, pp. 341–351, 1941. [Online]. Available: <https://doi.org/10.1063/1.1750906>
- [181] W. Wei, F. Shi, and J. F. Kolb, "Impedimetric analysis of trabecular bone based on Cole and linear discriminant analysis." *Front. Phys.*, vol. 8, no. 576191, 2021. [Online]. Available: <https://doi.org/10.3389/fphy.2020.576191>
- [182] N. K. Logothetis, C. Kayser, and A. Oeltermann, "In vivo measurement of cortical impedance spectrum in monkeys: implications for signal propagation." *Neuron*, vol. 55, no. 5, pp. 809–823, 2007. [Online]. Available: <https://doi.org/10.1016/j.neuron.2007.07.027>
- [183] M. R. Stoneman, M. Kosempa, W. D. Gregory, C. W. Gregory, J. J. Marx, W. Mikkelsen, J. Tjoe, and V. Raicu, "Correction of electrode polarization contributions to the dielectric properties of normal and cancerous breast tissues at audio/radiofrequencies." *Phys. Med. Biol.*, vol. 52, no. 22, pp. 6589–6604, 2007. [Online]. Available: <https://doi.org/10.1088/0031-9155/52/22/003>
- [184] T. W. Balmer, J. Ansó, E. Muntane, K. Gavaghan, S. Weber, A. Stahel, and P. Büchler, "In-vivo electrical impedance measurement in mastoid bone." *Ann. Biomed. Eng.*, pp. 1–11, 2016. [Online]. Available: <https://doi.org/10.1007/s10439-016-1758-4>
- [185] T. W. Balmer, S. Vesztergom, P. Broekmann, A. Stahel, and P. Büchler, "Characterization of the electrical conductivity of bone and its correlation to osseous structure." *Sci. Rep.*, vol. 8, no. 1, p. 8601, 2018. [Online]. Available: <https://doi.org/10.1038/s41598-018-26836-0>
- [186] C. Potratz, "Zur Optimierung elektrostimulativer Hüftgelenksimplantate mit externer magnetischer Anregung." Ph.D. dissertation, Institute of General Electrical Engineering, University of Rostock, Rostock, Germany, 2010. [Online]. Available: [https://doi.org/10.18453/rosdok\\_id00000791](https://doi.org/10.18453/rosdok_id00000791)
- [187] J. D. Kosterich, K. R. Foster, and S. R. Pollack, "Dielectric permittivity and electrical conductivity of fluid saturated bone." *IEEE Trans. Biomed. Eng.*, no. 2, pp. 81–86, 1983. [Online]. Available: <https://doi.org/10.1109/tbme.1983.325201>
- [188] B. Amin, M. A. Elahi, A. Shahzad, E. Porter, and M. O'Halloran, "A review of the dielectric properties of the bone for low frequency medical technologies." *Biomed. Phys. Eng. Express*, vol. 5, no. 2, p. 022001, 2019. [Online]. Available: <https://doi.org/10.1088/2057-1976/aaf210>
- [189] G. T. Swanson and J. F. Lafferty, "Electrical properties of bone as a function of age, immobilization and vibration." *J. Biomech.*, vol. 5, no. 3, pp. 261–266, 1972. [Online]. Available: [https://doi.org/10.1016/0021-9290\(72\)90041-3](https://doi.org/10.1016/0021-9290(72)90041-3)

- [190] C. Gabriel, "Dielectric properties of biological tissue: variation with age." *Bioelectromagnetics*, no. S7, pp. S12–S18, 2005. [Online]. Available: <https://doi.org/10.1002/bem.20147>
- [191] A. Peyman, S. J. Holden, S. Watts, R. Perrott, and C. Gabriel, "Dielectric properties of porcine cerebrospinal tissues at microwave frequencies: in vivo, in vitro and systematic variation with age." *Phys. Med. Biol.*, vol. 52, no. 8, pp. 2229–2245, 2007. [Online]. Available: <https://doi.org/10.1088/0031-9155/52/8/013>
- [192] A. Peyman, C. Gabriel, E. H. Grant, G. Vermeeren, and L. Martens, "Variation of the dielectric properties of tissues with age: the effect on the values of SAR in children when exposed to walkie-talkie devices." *Phys. Med. Biol.*, vol. 54, no. 2, pp. 227–241, 2008. [Online]. Available: <https://doi.org/10.1088/0031-9155/54/2/004>
- [193] J. Sierpowska, J. Tyr s, M. A. Hakulinen, S. Saarakkala, J. S. Jurvelin, and R. Lappalainen, "Electrical and dielectric properties of bovine trabecular bone relationships with mechanical properties and mineral density." *Phys. Med. Biol.*, vol. 48, no. 6, pp. 775–786, 2003. [Online]. Available: <https://doi.org/10.1088/0031-9155/48/6/306>
- [194] B. Amin, M. A. Elahi, A. Shahzad, E. Parle, L. McNamara, and M. O'Halloran, "An insight into bone dielectric properties variation: a foundation for electromagnetic medical devices." in *1st World Conference on Biomedical Applications of Electromagnetic Fields (EMF-Med)*. IEEE, 2018, pp. 1–2, Split, Croatia. [Online]. Available: <https://doi.org/10.23919/EMF-MED.2018.8526050>
- [195] B. Amin, M. A. Elahi, A. Shahzad, E. Porter, B. McDermott, and M. O'Halloran, "Dielectric properties of bones for the monitoring of osteoporosis." *Med. Biol. Eng. Comput.*, vol. 57, pp. 1–13, 2019. [Online]. Available: <https://doi.org/10.1007/s11517-018-1887-z>
- [196] A. R. Liboff, R. A. Rinaldi, L. S. Lavine, and M. H. Shamos, "On electrical conduction in living bone." *Clin. Orthop. Relat. Res.*, pp. 330–335, 1975. [Online]. Available: <https://doi.org/10.1097/00003086-197501000-00045>
- [197] L. A. Geddes and L. E. Baker, "The specific resistance of biological material – a compendium of data for the biomedical engineer and physiologist." *Med. Biol. Eng.*, vol. 5, no. 3, pp. 271–293, 1967. [Online]. Available: <https://doi.org/10.1007/BF02474537>
- [198] J. Behari, S. K. Guha, and P. N. Agarwal, "Temperature dependence of the electrical conductivity of bone." *Connect. Tissue Res.*, vol. 2, no. 4, pp. 325–328, 1974. [Online]. Available: <https://doi.org/10.3109/03008207409152262>
- [199] R. Pethig, "Dielectric properties of biological materials: biophysical and medical applications." *IEEE Trans. Elect. Insulation*, vol. EI-19, no. 5, pp. 453–474, 1984. [Online]. Available: <https://doi.org/10.1109/TEI.1984.298769>

- [200] S. Saha and P. A. Williams, "Effect of various storage methods on the dielectric properties of compact bone." *Med. Biol. Eng. Comput.*, vol. 26, no. 2, pp. 199–202, 1988. [Online]. Available: <https://doi.org/10.1007/BF02442264>
- [201] C. Tang, F. You, G. Cheng, D. Gao, F. Fu, G. Yang, and X. Dong, "Correlation between structure and resistivity variations of the live human skull." *IEEE Trans. Biomed. Eng.*, no. 9, pp. 2286–2292, 2008. [Online]. Available: <https://doi.org/10.1109/tbme.2008.923919>
- [202] G. B. Reinish and A. S. Nowick, "Effect of moisture on the electrical properties of bone." *J. Electrochem. Soc.*, vol. 123, no. 10, pp. 1451–1455, 1976. [Online]. Available: <https://doi.org/10.1149/1.2132617>
- [203] D. A. Chakkalakal, M. W. Johnson, R. A. Harper, and J. L. Katz, "Dielectric properties of fluid-saturated bone." *IEEE Trans. Biomed. Eng.*, vol. BME-27, no. 2, pp. 95–100, 1980. [Online]. Available: <https://doi.org/10.1109/TBME.1980.326713>
- [204] G. N. Reddy and S. Saha, "Electrical and dielectric properties of wet bone as a function of frequency." *IEEE Trans. Biomed. Eng.*, vol. BME-31, no. 3, pp. 296–303, 1984. [Online]. Available: <https://doi.org/10.1109/TBME.1984.325268>
- [205] G. de Mercato and F. J. Garcia-Sánchez, "Dielectric properties of fluid-saturated bone: a comparison between diaphysis and epiphysis." *Med. Biol. Eng. Comput.*, vol. 26, no. 3, pp. 313–316, 1988. [Online]. Available: <https://doi.org/10.1007/BF02447087>
- [206] G. De Mercato and F. J. García Sánchez, "Variation of the electric properties along the diaphysis of bovine femoral bone." *Med. Biol. Eng. Comput.*, vol. 29, no. 4, pp. 441–446, 1991. [Online]. Available: <https://doi.org/10.1007/BF02441667>
- [207] S. Saha and P. A. Williams, "Electric and dielectric properties of wet human cancellous bone as a function of frequency." *Ann. Biomed. Eng.*, vol. 17, no. 2, pp. 143–158, 1989. [Online]. Available: <https://doi.org/10.1007/BF02368024>
- [208] J. Sierpowska, M. A. Hakulinen, J. Töyräs, J. S. Day, H. Weinans, J. S. Jurvelin, and R. Lappalainen, "Prediction of mechanical properties of human trabecular bone by electrical measurements." *Physiol. Meas.*, vol. 26, no. 2, pp. S119–S131, 2005. [Online]. Available: <https://doi.org/10.1088/0967-3334/26/2/012>
- [209] J. Sierpowska, M. J. Lammi, M. A. Hakulinen, J. S. Jurvelin, R. Lappalainen, and J. Töyräs, "Effect of human trabecular bone composition on its electrical properties." *Med. Eng. Phys.*, vol. 29, no. 8, pp. 845–852, 2007. [Online]. Available: <https://doi.org/10.1016/J.MEDENGPY.2006.09.007>
- [210] Y. Haba, A. Wurm, M. Köckerling, C. Schick, W. Mittelmeier, and R. Bader, "Characterization of human cancellous and subchondral bone with respect to electro physical properties and bone mineral density by means of impedance spectroscopy." *Med. Eng. Phys.*, vol. 45, pp. 34–41, 2017. [Online]. Available:

- <https://doi.org/10.1016/j.medengphy.2017.04.002>
- [211] S. R. Smith and K. R. Foster, "Dielectric properties of low-water-content tissues." *Phys. Med. Biol.*, vol. 30, no. 9, pp. 965–973, 1985. [Online]. Available: <https://doi.org/10.1088/0031-9155/30/9/008>
- [212] P. B. Ishai, M. S. Talary, A. Caduff, E. Levy, and Y. Feldman, "Electrode polarization in dielectric measurements: a review." *Meas. Sci. Technol.*, vol. 24, no. 10, p. 102001, 2013. [Online]. Available: <https://doi.org/10.1088/0957-0233/24/10/102001>
- [213] D. Andreuccetti, R. Fossi, and C. Petrucci, "An internet resource for the calculation of the dielectric properties of body tissues in the frequency range 10 Hz-100 GHz." *IFAC-CNR, Florence (Italy). Based on data published by C. Gabriel et al. in 1996, 1997.* [Online]. Available: <http://niremf.ifac.cnr.it/tissprop/>
- [214] U. van Rienen, Private communication, 2016.
- [215] M. H. Qvist, U. Hoeck, B. Kreilgaard, F. Madsen, and S. Frokjaer, "Evaluation of Göttingen minipig skin for transdermal in vitro permeation studies." *Eur. J. Pharm. Sci.*, vol. 11, no. 1, pp. 59–68, 2000. [Online]. Available: [https://doi.org/10.1016/S0928-0987\(00\)00091-9](https://doi.org/10.1016/S0928-0987(00)00091-9)
- [216] P. W. Kämmerer, Private communication, 2019.
- [217] M. Dau, Private communication, 2019.
- [218] P. Hasgall, F. Di Gennaro, C. Baumgartner, E. Neufeld, B. Lloyd, M. Gosselin, D. Payne, A. Klingeböck, and N. Kuster, "IT'IS Database for thermal and electromagnetic parameters of biological tissues, version 4.1." 2022. [Online]. Available: <https://doi.org/10.13099/VIP21000-04-1>
- [219] I. Lackovic and Z. Stare, "Low-frequency dielectric properties of the oral mucosa." in *13th International Conference on Electrical Bioimpedance and the 8th Conference on Electrical Impedance Tomography*. Springer, 2007. [Online]. Available: [https://doi.org/10.1007/978-3-540-73841-1\\_42](https://doi.org/10.1007/978-3-540-73841-1_42)
- [220] P. Bhardwaj, D. V. Rai, M. L. Garg, and B. P. Mohanty, "Potential of electrical impedance spectroscopy to differentiate between healthy and osteopenic bone." *Clin. Biomech.*, vol. 57, pp. 81–88, 2018. [Online]. Available: <https://doi.org/10.1016/j.clinbiomech.2018.05.014>
- [221] Y. Haba, M. Köckerling, C. Schick, W. Mittelmeier, and R. Bader, "Determination of electrophysical and structural properties of human cancellous bone and synthetic bone substitute material using impedance spectroscopy and X-ray powder diffraction." *Acta Bioeng. Biomech.*, vol. 20, pp. 11–19, 2018. [Online]. Available: <https://doi.org/10.5277/ABB-00978-2017-02>
- [222] "MatWeb web page on titanium Ti-6Al-4V (grade 5), annealed." 2019. [On-

- line]. Available: <http://www.matweb.com/search/datasheet.aspx?MatGUID=a0655d261898456b958e5f825ae85390> (accessed 21.03.2019).
- [223] “Mitsubishi chemical advanced materials web page, product data sheets.” 2019. [Online]. Available: [https://media.mcam.com/fileadmin/quadrant/documents/QEPP/Global/English/Product\\_Data\\_Sheets\\_AEP/Ketron\\_1000\\_PEEK\\_PDS\\_GLOB\\_E\\_19092016.pdf?\\_ga=2.7651570.1148302848.1554475020-1676376043.1553176436](https://media.mcam.com/fileadmin/quadrant/documents/QEPP/Global/English/Product_Data_Sheets_AEP/Ketron_1000_PEEK_PDS_GLOB_E_19092016.pdf?_ga=2.7651570.1148302848.1554475020-1676376043.1553176436) (accessed 05.04.2019).
- [224] J. W. Demmel, *Applied numerical linear algebra*. Philadelphia, PA, USA: Society for Industrial and Applied Mathematics (SIAM), 1997. [Online]. Available: <https://doi.org/10.1137/1.9781611971446>
- [225] A. Richardot and E. T. McAdams, “Harmonic analysis of low-frequency bioelectrode behavior.” *IEEE Trans. Med. Imaging*, vol. 21, pp. 604–612, 2002. [Online]. Available: <https://doi.org/10.1109/TMI.2002.800576>
- [226] W. Franks, I. Schenker, P. Schmutz, and A. Hierlemann, “Impedance characterization and modeling of electrodes for biomedical applications.” *IEEE Trans. Biomed. Eng.*, vol. 52, pp. 1295–1302, 2005. [Online]. Available: <https://doi.org/10.1109/TBME.2005.847523>
- [227] R. Lange, F. Lüthen, U. Beck, J. Rychly, A. Baumann, and B. Nebe, “Cell-extracellular matrix interaction and physico-chemical characteristics of titanium surfaces depend on the roughness of the material.” *Biomol. Eng.*, vol. 19, pp. 255–261, 2002. [Online]. Available: [https://doi.org/10.1016/S1389-0344\(02\)00047-3](https://doi.org/10.1016/S1389-0344(02)00047-3)
- [228] D. J. Rincon, E. Aguilera, and J. C. Chacón, “Numerical treatment of floating conductors based on the traditional finite element formulation,” *Adv. Electromagn.*, vol. 7, no. 3, pp. 46–55, 2018. [Online]. Available: <https://doi.org/10.7716/aem.v7i3.720>
- [229] P. K. Rajan and A. Sekar, “Linear circuit analysis.” in *The Electrical Engineering Handbook*, W.-K. Chen, Ed. Burlington: Boston, MA, USA: Elsevier/Academic Press, 2005, pp. 3–29. [Online]. Available: <https://doi.org/10.1016/B978-012170960-0/50004-9>
- [230] Y. Saad and M. H. Schultz, “GMRES: a generalized minimal residual algorithm for solving nonsymmetric linear systems.” *SIAM J. Sci. Stat. Comput.*, vol. 7, pp. 856–869, 1986. [Online]. Available: <https://doi.org/10.1137/0907058>
- [231] E. de Rocquigny, N. Devictor, and S. Tarantola, *Uncertainty in industrial practice: a guide to quantitative uncertainty management*. Chichester, England: John Wiley & Sons, 2008. [Online]. Available: <https://doi.org/10.1002/9780470770733>
- [232] I. Babuska and J. T. Oden, “Verification and validation in computational engineering and science: basic concepts.” *Comput. Methods Appl. Mech.*

- Eng.*, vol. 193, no. 36-38, pp. 4057–4066, 2004. [Online]. Available: <https://doi.org/10.1016/j.cma.2004.03.002>
- [233] D. Xiu and G. E. Karniadakis, “The Wiener–Askey polynomial chaos for stochastic differential equations.” *SIAM J. Sci. Comput.*, vol. 24, no. 2, pp. 619–644, 2002. [Online]. Available: <https://doi.org/10.1137/S1064827501387826>
- [234] D. Xiu, *Numerical methods for stochastic computations: a spectral method approach*. Princeton, NJ, USA: Princeton University Press, 2010. [Online]. Available: <https://doi.org/10.1515/9781400835348>
- [235] I. M. Sobol’, “On sensitivity estimation for nonlinear mathematical models.” *Matem. Mod.*, vol. 2, no. 1, pp. 112–118, 1990. [Online]. Available: <https://www.mathnet.ru/eng/mm2320>
- [236] B. Sudret, “Global sensitivity analysis using polynomial chaos expansions.” *Reliab. Eng. Syst. Safe.*, vol. 93, no. 7, pp. 964–979, 2008. [Online]. Available: <https://doi.org/10.1016/j.res.2007.04.002>
- [237] I. M. Sobol’, “Sensitivity estimates for nonlinear mathematical models.” *Math. Model. Comput. Exp.*, vol. 1, no. 4, pp. 407–414, 1993.
- [238] I. M. Sobol’, “Global sensitivity indices for nonlinear mathematical models and their Monte Carlo estimates.” *Math. Comput. Simulat.*, vol. 55, no. 1, pp. 271–280, 2001. [Online]. Available: [https://doi.org/10.1016/S0378-4754\(00\)00270-6](https://doi.org/10.1016/S0378-4754(00)00270-6)
- [239] G. Glen and K. Isaacs, “Estimating Sobol’ sensitivity indices using correlations.” *Environ. Model. Softw.*, vol. 37, pp. 157–166, 2012. [Online]. Available: <https://doi.org/10.1016/j.envsoft.2012.03.014>
- [240] P. D. Allison, “Testing for interaction in multiple regression.” *Am. J. Sociol.*, vol. 83, no. 1, pp. 144–153, 1977. [Online]. Available: <https://doi.org/10.1086/226510>
- [241] T. Homma and A. Saltelli, “Importance measures in global sensitivity analysis of nonlinear models.” *Reliab. Eng. Syst. Safe.*, vol. 52, no. 1, pp. 1–17, 1996. [Online]. Available: [https://doi.org/10.1016/0951-8320\(96\)00002-6](https://doi.org/10.1016/0951-8320(96)00002-6)
- [242] R. Ghanem and P. D. Spanos, “Polynomial chaos in stochastic finite elements.” *J. Appl. Mech.*, vol. 57, no. 1, pp. 197–202, 1990. [Online]. Available: <https://doi.org/10.1115/1.2888303>
- [243] T. Crestaux, O. Le Maître, and J.-M. Martinez, “Polynomial chaos expansion for sensitivity analysis.” *Reliab. Eng. Syst. Safe.*, vol. 94, no. 7, pp. 1161–1172, 2009. [Online]. Available: <https://doi.org/10.1016/j.res.2008.10.008>
- [244] N. Wiener, “The homogeneous chaos.” *Am. J. Math.*, vol. 60, no. 4, pp. 897–936, 1938. [Online]. Available: <https://doi.org/10.2307/2371268>

- [245] M. Eldred, C. Webster, and P. Constantine, "Evaluation of non-intrusive approaches for Wiener-Askey generalized polynomial chaos." in *49th AIAA/ASME/ASCE/AHS/ASC Structures, Structural Dynamics, and Materials Conference, 16th AIAA/ASME/AHS Adaptive Structures Conference, 10th AIAA Non-Deterministic Approaches Conference, 9th AIAA Gossamer Spacecraft Forum, 4th AIAA Multidisciplinary Design Optimization Specialists Conference*. AIAA, 2008, p. 1892, Schaumburg, IL, USA. [Online]. Available: <https://doi.org/10.2514/6.2008-1892>
- [246] O. G. Ernst, A. Mugler, H.-J. Starkloff, and E. Ullmann, "On the convergence of generalized polynomial chaos expansions." *ESAIM: Math. Model. Numer. Anal.*, vol. 46, no. 2, pp. 317–339, 2012. [Online]. Available: <https://doi.org/10.1051/m2an/2011045>
- [247] S. Tennøe, G. Halnes, and G. T. Einevoll, "Uncertainpy: a Python toolbox for uncertainty quantification and sensitivity analysis in computational neuroscience." *Front. Neuroinf.*, vol. 12, p. 49, 2018. [Online]. Available: <https://doi.org/10.3389/fninf.2018.00049>
- [248] T. J. Stieltjes, "Quelques recherches sur la théorie des quadratures dites mécaniques." in *Annales scientifiques de l'École Normale Supérieure*, ser. Serie 3, vol. 1, 1884, pp. 409–426. [Online]. Available: <https://doi.org/10.24033/asens.245>
- [249] W. Gautschi, *Orthogonal polynomials: computation and approximation*. Oxford, NY, USA: Oxford University Press, 2004. [Online]. Available: <https://doi.org/10.1093/oso/9780198506720.001.0001>
- [250] J. Feinberg and H. P. Langtangen, "Chaospy: an open source tool for designing methods of uncertainty quantification." *J. Comput. Sci.*, vol. 11, pp. 46–57, 2015. [Online]. Available: <https://doi.org/10.1016/j.jocs.2015.08.008>
- [251] S. Hosder, R. Walters, and M. Balch, "Efficient sampling for non-intrusive polynomial chaos applications with multiple uncertain input variables." in *48th AIAA/ASME/ASCE/AHS/ASC Structures, Structural Dynamics, and Materials Conference*. AIAA, 2007, p. 1939, Honolulu, HI, USA. [Online]. Available: <https://doi.org/10.2514/6.2007-1939>
- [252] J. M. Hammersley, "Monte Carlo methods for solving multivariable problems." *Ann. N. Y. Acad. Sci.*, vol. 86, no. 3, pp. 844–874, 1960. [Online]. Available: <https://doi.org/10.1111/j.1749-6632.1960.tb42846.x>
- [253] R. M. Rifkin and R. A. Lippert, "Notes on regularized least squares." Massachusetts Institute of Technology. Cambridge, MA, USA, Tech. Rep. MIT-CSAIL-TR-2007-025, CBCL-268, 2007. [Online]. Available: <http://hdl.handle.net/1721.1/37318>
- [254] J. Zimmermann, T. Distler, A. R. Boccaccini, and U. van Rienen,

- “Numerical simulations as means for tailoring electrically conductive hydrogels towards cartilage tissue engineering by electrical stimulation.” *Molecules*, vol. 25, no. 20, p. 4750, 2020. [Online]. Available: <https://doi.org/10.3390/molecules25204750>
- [255] J. Zimmermann, R. Altenkirch, and U. van Rienen, “Numerical study on the effect of capacitively coupled electrical stimulation on biological cells considering model uncertainties.” *Sci. Rep.*, vol. 12, no. 1, p. 4744, 2022. [Online]. Available: <https://doi.org/10.1038/s41598-022-08279-w>
- [256] K. Butenko, C. Bahls, and U. van Rienen, “Evaluation of epistemic uncertainties for bipolar deep brain stimulation in rodent models.” in *2019 41st Annual International Conference of the IEEE Engineering in Medicine and Biology Society (EMBC)*. Berlin, Germany: IEEE, 2019, pp. 2136–2140, Berlin, Germany. [Online]. Available: <https://doi.org/10.1109/EMBC.2019.8857910>
- [257] C. Schmidt, P. Grant, M. Lowery, and U. van Rienen, “Influence of uncertainties in the material properties of brain tissue on the probabilistic volume of tissue activated.” *IEEE Trans. Biomed. Eng.*, vol. 60, no. 5, pp. 1378–1387, 2013. [Online]. Available: <https://doi.org/10.1109/tbme.2012.2235835>
- [258] C. Schmidt, S. Wagner, M. Burger, U. van Rienen, and C. H. Wolters, “Impact of uncertain head tissue conductivity in the optimization of transcranial direct current stimulation for an auditory target.” *J. Neural Eng.*, vol. 12, no. 4, p. 046028, 2015. [Online]. Available: <https://doi.org/10.1088/1741-2560/12/4/046028>
- [259] U. Römer, C. Schmidt, U. van Rienen, and S. Schöps, “Low-dimensional stochastic modeling of the electrical properties of biological tissues.” *IEEE Trans. Magn.*, vol. 53, no. 6, pp. 1–4, 2017. [Online]. Available: <https://doi.org/10.1109/CEFC.2016.7816321>
- [260] N. Mangado, J. Pons-Prats, M. Coma, P. Mistrik, G. Piella, M. Ceresa, and M. A. Gonzalez Ballester, “Computational evaluation of cochlear implant surgery outcomes accounting for uncertainty and parameter variability.” *Front. Physiol.*, vol. 9, 2018. [Online]. Available: <https://doi.org/10.3389/fphys.2018.00498>
- [261] A. Narayan, Z. Liu, J. A. Bergquist, C. Charlebois, S. Rampersad, L. Rupp, D. Brooks, D. White, J. Tate, and R. S. MacLeod, “UncertainSCI: uncertainty quantification for computational models in biomedicine and bioengineering.” *Comput. Biol. Med.*, vol. 152, p. 106407, 2023. [Online]. Available: <https://doi.org/10.1016/j.compbiomed.2022.106407>
- [262] A. Olivier, D. Giovanis, B. S. Aakash, M. Chauhan, L. Vandanapu, and M. Shields, “UQpy: a general purpose Python package and development environment for uncertainty quantification.” *J. Comput. Sci.*, vol. 47, p. 101204, 2020. [Online]. Available: <https://doi.org/10.1016/j.jocs.2020.101204>



- [263] O. Le Maître and O. M. Knio, *Spectral methods for uncertainty quantification: with applications to computational fluid dynamics.*, 1st ed., ser. Scientific Computation. Dordrecht, Netherlands: Springer Science & Business Media, 2010. [Online]. Available: <https://doi.org/10.1007/978-90-481-3520-2>
- [264] V. G. Eck, W. P. Donders, J. Sturdy, J. Feinberg, T. Delhaas, L. R. Hellevik, and W. Huberts, “A guide to uncertainty quantification and sensitivity analysis for cardiovascular applications.” *Int. J. Numer. Meth. Biomed. Engng.*, vol. 32, no. 8, p. e02755, 2016. [Online]. Available: <https://doi.org/10.1002/cnm.2755>
- [265] J. Zimmermann, K. Budde, N. Arbeiter, F. Molina, A. Storch, A. M. Uhrmacher, and U. van Rienen, “Using a digital twin of an electrical stimulation device to monitor and control the electrical stimulation of cells in vitro.” *Front. Bioeng. Biotechnol.*, vol. 9, 2021. [Online]. Available: <https://doi.org/10.3389/fbioe.2021.765516>
- [266] J. Feinberg and H. P. Langtangen, “Chaospy software package for uncertainty quantification,” 2014. [Online]. Available: <https://github.com/hplgit/chaospy>
- [267] M. Schönleber, D. Klotz, and E. Ivers-Tiffée, “A method for improving the robustness of linear Kramers-Kronig validity tests.” *Electrochim. Acta*, vol. 131, pp. 20–27, 2014. [Online]. Available: <https://doi.org/10.1016/j.electacta.2014.01.034>
- [268] J. Zimmermann and L. Thiele, “j-zimmermann/impedancefitter: v2.0.3,” 2022. [Online]. Available: <https://doi.org/10.5281/zenodo.6557710>
- [269] R. Hoekema, G. H. Wieneke, F. S. S. Leijten, C. W. M. van Veelen, P. C. van Rijen, G. J. M. Huiskamp, J. Ansems, and A. C. van Huffelen, “Measurement of the conductivity of skull, temporarily removed during epilepsy surgery.” *Brain Topogr.*, vol. 16, no. 1, pp. 29–38, 2003. [Online]. Available: <https://doi.org/10.1023/A:1025606415858>
- [270] R. Köhling, Private communication, 2021.
- [271] J. A. Nelder and R. Mead, “A simplex method for function minimization.” *Comput. J.*, vol. 7, no. 4, pp. 308–313, 1965. [Online]. Available: <https://doi.org/10.1093/comjnl/7.4.308>
- [272] A. R. Conn, K. Scheinberg, and L. N. Vicente, *Introduction to derivative-free optimization.*, ser. MPS-SIAM series on optimization. Philadelphia, PA, USA: Society for Industrial and Applied Mathematics (SIAM), 2009, no. 8. [Online]. Available: <https://doi.org/10.1137/1.9780898718768>
- [273] S. F. Cogan, K. A. Ludwig, C. G. Welle, and P. Takmakov, “Tissue damage thresholds during therapeutic electrical stimulation.” *J. Neural Eng.*, vol. 13, no. 2, p. 021001, 2016. [Online]. Available: <https://doi.org/10.1088/1741-2560/13/2/021001>

- [274] IEC 60479-1: *Effects of Current on Human Beings and Livestock*, International Electrotechnical Commission Std., 2018. [Online]. Available: <https://webstore.iec.ch/publication/62980>
- [275] M. Kono, T. Takahashi, H. Nakamura, T. Miyaki, and J. Rekimoto, "Design guideline for developing safe systems that apply electricity to the human body." *ACM Trans. Comput.-Hum. Interact.*, vol. 25, no. 3, pp. 1–36, 2018. [Online]. Available: <https://doi.org/10.1145/3184743>
- [276] S. A. Leon, S. O. Asbell, H. H. Arastu, G. Edelstein, A. J. Packel, S. Sheehan, I. Daskal, G. G. Guttmann, and I. Santos, "Effects of hyperthermia on bone. II. Heating of bone in vivo and stimulation of bone growth." *Int. J. Hyperthermia*, vol. 9, pp. 77–87, 1993. [Online]. Available: <https://doi.org/10.3109/02656739309061480>
- [277] M. A. Serrat, T. J. Schlierf, M. L. Efaw, F. D. Shuler, J. Godby, L. M. Stanko, and H. L. Tamski, "Unilateral heat accelerates bone elongation and lengthens extremities of growing mice." *J. Orthop. Res.*, vol. 33, no. 5, pp. 692–698, 2015. [Online]. Available: <https://doi.org/10.1002/jor.22812>
- [278] R. A. Eriksson and T. Albrektsson, "The effect of heat on bone regeneration: an experimental study in the rabbit using the bone growth chamber." *J. Oral Maxillofac. Surg.*, vol. 42, pp. 705–711, 1984. [Online]. Available: [https://doi.org/10.1016/0278-2391\(84\)90417-8](https://doi.org/10.1016/0278-2391(84)90417-8)
- [279] M. Ellenrieder, T. Tischer, P. C. Kreuz, S. Fröhlich, A. Fritsche, and W. Mittelmeier, "Arthroscopically assisted therapy of avascular necrosis of the femoral head." *Oper. Orthop. Traumatol.*, vol. 25, pp. 85–94, 2013. [Online]. Available: <https://doi.org/10.1007/s00064-011-0072-4>
- [280] F. Plocksties, C. Niemann, R. Bader, F. Möws, H. Seitz, P. W. Kämmerer, M. Dau, V. Kamp, J. Heller, and D. Timmermann, "Requirements and design of an implant for electrical stimulation for bone regeneration in animals." in *2020 IEEE 2nd Global Conference on Life Sciences and Technologies (LifeTech)*. IEEE, 2020, pp. 157–160, Kyoto, Japan. [Online]. Available: <https://doi.org/10.1109/LifeTech48969.2020.1570619159>
- [281] F. Plocksties, M. Kober, C. Niemann, J. Heller, M. Fauser, M. Nüssel, F. Uster, D. Franz, M. Zwar, and A. Lüttig, "The software defined implantable modular platform (STELLA) for preclinical deep brain stimulation research in rodents." *J. Neural Eng.*, vol. 18, no. 5, p. 056032, 2021. [Online]. Available: <https://doi.org/10.1088/1741-2552/ac23e1>
- [282] K. Butenko, "Modeling perspective on translatability of deep brain stimulation mechanism for treating parkinsonian motor symptoms in rodent and human." Ph.D. dissertation, Institute of General Electrical Engineering, University of Rostock, Rostock, Germany, 2021. [Online]. Available: [https://doi.org/10.18453/rosdok\\_id00003623](https://doi.org/10.18453/rosdok_id00003623)

- [283] C. Schmidt, U. Zimmermann, and U. van Rienen, "Uncertainty quantification of the optimal stimulation area in an electro-stimulative hip revision system." in *2014 36th Annual International Conference of the IEEE Engineering in Medicine and Biology Society*. IEEE, 2014, pp. 824–827, Chicago, IL, USA. [Online]. Available: <https://doi.org/10.1109/embc.2014.6943718>
- [284] C. Schmidt, E. Dunn, M. Lowery, and U. van Rienen, "Uncertainty quantification of oscillation suppression during DBS in a coupled finite element and network model." *IEEE Trans. Neural Syst. Rehabil. Eng.*, vol. 26, no. 2, pp. 281–290, 2016. [Online]. Available: <https://doi.org/10.1109/tnsre.2016.2608925>
- [285] J. Vorwerk, U. Aydin, C. H. Wolters, and C. R. Butson, "Influence of head tissue conductivity uncertainties on EEG dipole reconstruction." *Front. Neurosci.*, vol. 13, p. 531, 2019. [Online]. Available: <https://doi.org/10.3389/fnins.2019.00531>
- [286] G. B. Saturnino, A. Thielscher, K. H. Madsen, T. R. Knösche, and K. Weise, "A principled approach to conductivity uncertainty analysis in electric field calculations." *NeuroImage*, vol. 188, pp. 821–834, 2018. [Online]. Available: <https://doi.org/10.1016/j.neuroimage.2018.12.053>
- [287] S. S. Shapiro and M. B. Wilk, "An analysis of variance test for normality (complete samples)." *Biometrika*, vol. 52, no. 3/4, pp. 591–611, 1965. [Online]. Available: <https://doi.org/10.2307/2333709>
- [288] S. Tamilselvi, V. Raman, and N. Rajendran, "Corrosion behaviour of Ti-6Al-7Nb and Ti-6Al-4V ELI alloys in the simulated body fluid solution by electrochemical impedance spectroscopy." *Electrochim. Acta*, vol. 52, no. 3, pp. 839–846, 2006. [Online]. Available: <https://doi.org/10.1016/j.electacta.2006.06.018>
- [289] V. Barranco, A. Jimenez-Morales, E. Peon, G. J. Hickman, C. C. Perry, and J. C. Galván, "Enhancing in vitro biocompatibility and corrosion protection of organic-inorganic hybrid sol-gel films with nanocrystalline hydroxyapatite." *J. Mater. Chem. B*, vol. 2, no. 24, pp. 3886–3896, 2014. [Online]. Available: <https://doi.org/10.1039/C4TB00173G>
- [290] F. R. García-Galván, M. A. Mezour, G. J. Hickman, I. E. Soliman, A. Jiménez-Morales, V. Barranco, J. C. Galván, and C. C. Perry, "Organic-inorganic hybrid coatings containing phosphorus precursors prepared by sol-gel on Ti6Al4V alloy: electrochemical and in-vitro biocompatibility evaluation." *Prog. Org. Coat.*, vol. 148, p. 105834, 2020. [Online]. Available: <https://doi.org/10.1016/j.porgcoat.2020.105834>
- [291] C. A. Guerra Figueroa, "Electrochemical and tribological evaluation of porous Ti alloys for orthopedic use." Ph.D. dissertation, Pontificia universidad católica de Chile - School of engineering, Santiago, Chile, 2020. [Online]. Available: <https://doi.org/10.7764/tesisUC/ING/47376>

- [292] L. P. Faverani, W. G. Assunção, P. S. P. de Carvalho, J. C.-C. Yuan, C. Sukotjo, M. T. Mathew, and V. A. Barao, "Effects of dextrose and lipopolysaccharide on the corrosion behavior of a Ti-6Al-4V alloy with a smooth surface or treated with double-acid-etching." *PLOS ONE*, vol. 9, no. 3, p. e93377, 2014. [Online]. Available: <https://doi.org/10.1371/journal.pone.0093377>
- [293] I. Ramires and A. C. Guastaldi, "Electrochemical study of the corrosion of Ti-Pd and Ti-6Al-4V electrodes in sodium chloride solutions." *Biomecânica*, vol. 9, no. 1, pp. 61–65, 2001. [Online]. Available: <http://doi.org/10.5821/sibb.v9i1.1664>
- [294] C. Schmidt and U. van Rienen, "Modelling the probabilistic neural activation in deep brain stimulation: influence of uncertainty in the parameters of the electrode-tissue-interface." in *2013 International Symposium on Electromagnetic Theory*. IEEE, 2013, pp. 365–368, Hiroshima, Japan. [Online]. Available: <https://ieeexplore.ieee.org/document/6565755>
- [295] S. Kumaravel and S. Sundaram, "Monitoring of fracture healing by electrical conduction: a new diagnostic procedure." *Indian J. Orthop.*, vol. 46, no. 4, pp. 384–390, 2012. [Online]. Available: <https://doi.org/10.4103/0019-5413.97260>
- [296] K. Gupta, P. Gupta, G. K. Singh, S. Kumar, R. K. Singh, and R. N. Srivastava, "Changes in electrical properties of bones as a diagnostic tool for measurement of fracture healing." *Hard Tissue*, vol. 2, no. (1):3, 2013. [Online]. Available: <https://doi.org/10.13172/2050-2303-2-1-316>
- [297] M. Kahn, L. B. Krone, C. Blanco-Duque, M. C. C. Guillaumin, E. O. Mann, and V. V. Vyazovskiy, "Neuronal-spiking-based closed-loop stimulation during cortical ON- and OFF-states in freely moving mice." *J. Sleep Res.*, vol. 31, no. 6, p. e13603, 2022. [Online]. Available: <https://doi.org/10.1111/jsr.13603>
- [298] D. Rozgić, V. Hokinikyan, W. Jiang, I. Akita, S. Basir-Kazeruni, H. Chandrakumar, and D. Marković, "A 0.338 cm<sup>3</sup>, artifact-free, 64-contact neuromodulation platform for simultaneous stimulation and sensing." *IEEE Trans. Biomed. Circuits Syst.*, vol. 13, no. 1, pp. 38–55, 2019. [Online]. Available: <https://doi.org/10.1109/TBCAS.2018.2889040>
- [299] D. Kumar, S. B. Alam, D. Vučinić, and C. Lacor, "Uncertainty quantification and robust optimization in engineering." in *Advances in Visualization and Optimization Techniques for Multidisciplinary Research: Trends in Modelling and Simulations for Engineering Applications*, D. Vucinic, F. Rodrigues Leta, and S. Janardhanan, Eds. Singapore, Springer Nature, 2020, pp. 63–93. [Online]. Available: [https://doi.org/10.1007/978-981-13-9806-3\\_3](https://doi.org/10.1007/978-981-13-9806-3_3)
- [300] R. Mhanna and A. Hasan, *Introduction to Tissue Engineering*. Weinheim, Germany: John Wiley & Sons, Ltd, 2017, vol. 1, ch. 1, pp. 1–34. [Online]. Available: <https://doi.org/10.1002/9783527689934.ch1>
- [301] R. Lange, Private communication, 2019.

- [302] N. Engel, M. Dau, P. W. Kämmerer, and V. Engel, “Stimulatable implant with included impedance measurement.” Deutsches Patent- und Markenamt. German Patent DE102 021 117 160A1, Jul. 02, 2021, (accessed 02.11.2023). [Online]. Available: <https://depatisnet.dpma.de/DepatisNet/depatisnet?action=bibdat&docid=DE102021117160A1>
- [303] P. S. Lee, H. Eckert, R. Hess, M. Gelinsky, D. Rancourt, R. Krawetz, G. Cuniberti, and D. Scharnweber, “Developing a customized perfusion bioreactor prototype with controlled positional variability in oxygen partial pressure for bone and cartilage tissue engineering.” *Tissue Eng. Part C Methods*, vol. 23, no. 5, pp. 286–297, 2017. [Online]. Available: <https://doi.org/10.1089/ten.tec.2016.0244>
- [304] P. S. Lee, R. Hess, J. Friedrichs, V. Haenchen, H. Eckert, G. Cuniberti, D. Rancourt, R. Krawetz, V. Hintze, and M. Gelinsky, “Recapitulating bone development events in a customised bioreactor through interplay of oxygen tension, medium pH, and systematic differentiation approaches.” *J. Tissue Eng. Regen. Med.*, vol. 13, no. 9, pp. 1672–1684, 2019.
- [305] N. Engel, C. Fechner, A. Voges, R. Ott, J. Stenzel, S. Siewert, C. Bergner, V. Khaimov, J. Liese, K.-P. Schmitz, B. J. Krause, and B. Frerich, “An optimized 3D-printed perfusion bioreactor for homogeneous cell seeding in bone substitute scaffolds for future chairside applications.” *Sci. Rep.*, vol. 11, p. 22228, 2021. [Online]. Available: <https://doi.org/10.1038/s41598-021-01516-8>
- [306] U. van Rienen, H. Raben, W. Radlof, M. Sander, M. Dau, J. Zimmermann, H. Bathel, N. Arbeiter, N. Engel, and L. Lembcke, “Patent application: Knochen-implantat sowie Verfahren und Computerprogrammprodukt zur Herstellung eines Knochenimplantats.” Deutsches Patent- und Markenamt. German Patent Official file number: 10 2024 117 508.7, 2024, submitted on 20.06.2024.
- [307] N. Narra, J. Valášek, M. Hannula, P. Marcián, G. K. Sándor, J. Hyttinen, and J. Wolff, “Finite element analysis of customized reconstruction plates for mandibular continuity defect therapy.” *J. Biomech.*, vol. 47, no. 1, pp. 264–268, 2014. [Online]. Available: <https://doi.org/10.1016/j.jbiomech.2013.11.016>
- [308] U. Zimmermann and U. van Rienen, “The impact of bone microstructure on the field distribution of electrostimulative implants.” in *Conf. Proc. IEEE Eng. Med. Biol. Soc.* IEEE, 2015, pp. 3545–3548, Milan, Italy. [Online]. Available: <https://doi.org/10.1109/EMBC.2015.7319158>
- [309] B. Chopard, J. Borgdorff, and A. G. Hoekstra, “A framework for multi-scale modelling.” *Phil. Trans. R. Soc. A.*, vol. 372, p. 20130378, 2014. [Online]. Available: <https://doi.org/10.1098/rsta.2013.0378>



# Selbstständigkeitserklärung

Ich versichere hiermit an Eides statt, dass ich die vorliegende Arbeit mit dem Titel “Modelling and simulation of the electric field distribution of electrostimulative implants for regeneration of mandibular bone defects” selbstständig angefertigt und ohne fremde Hilfe verfasst habe, keine außer den von mir angegebenen Hilfsmitteln und Quellen dazu verwendet habe und die den benutzten Werken inhaltlich und wörtlich entnommenen Stellen als solche kenntlich gemacht habe.

Rostock, 18.03.2024

Hendrikje Raben